Optimization of a Supercritical Carbon Dioxide Solar Thermal Power System

by
Ruan van der Westhuizen

Dissertation presented for the degree of Doctor of Philosophy in the Faculty of Engineering at Stellenbosch University

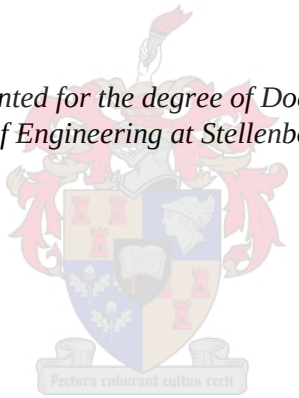

Supervisor: Prof A.A. Groenwold
Co-supervisors: Prof S.J. van der Spuy
Mr R.T. Dobson

December 2020

Declaration

By submitting this dissertation electronically, I declare that the entirety of the work contained therein is my own, original work, that I am the sole author thereof (save to the extent explicitly otherwise stated), that reproduction and publication thereof by Stellenbosch University will not infringe any third party rights and that I have not previously in its entirety or in part submitted it for obtaining any qualification.

Date: December 2020

Abstract

Optimization of a Supercritical Carbon Dioxide Solar Thermal Power System

R. van der Westhuizen

A new procedure for the optimal design of a solar thermal power system that uses a supercritical carbon dioxide (sCO_2) Brayton cycle is developed. The design procedure is compatible with different types of component models, solution methods and design constraints. The variables of the system, and the objectives and constraints of the system design, are managed through a comprehensive computational architecture. Multi-objective optimization of 23 thermodynamic-, geometric- and performance design variables of the system is achieved.

The design procedure is based on a specific series of design decisions that continually reduce the design spaces of the turbomachinery and heat exchanger sub-systems, in such a way that Pareto-optimality of the final system design is ensured. For computational expediency, initial design decisions are made based on the analysis of a thermodynamic model. It is demonstrated that the optimal thermodynamic design of the system is influenced by the performance values of the turbomachinery and recuperator.

Subsequent design decisions are made based on the independent analyses of detailed turbomachinery and heat exchanger models. The turbomachinery is modeled in Matlab® with a mean-line analytical approach that uses specified performance coefficients. Explicit constraints ensure that the turbomachinery designs are within established limits. The heat exchangers are modeled in Flownex® using a control-volume-based convection-diffusion approach that can accurately represent the internal pinch-point of the recuperator. All models make use of realistic thermodynamic properties for supercritical carbon dioxide and are extensively validated with published data.

A formal derivation shows that there are two distinct operating regions for the heat exchangers of the system. A successful system design depends on the region in which the heat exchangers function. This region can be controlled by changing the value of the nominal flow area, which is considered the most important design variable of the system.

Six designs of the same basic system, but with different objectives and constraints, are presented. These designs are evaluated and compared to each other through a detailed quantitative investigation that highlights which factors contribute most to the inefficiency of each design. The best design achieves a thermal-to-mechanical efficiency of 40% at a turbine inlet temperature of 550 °C. This efficiency is demonstrated to be near the practical maximum for an sCO_2 system that employs the recuperated cycle configuration with a linear solar receiver.

Future developments of the design procedure could consider the addition of a financial model as well as constraints to account for the structural integrity of the system.

Uittreksel

Optimering van 'n Superkritiese-koolstofdioksied Termiese-sonkragstelsel

R. van der Westhuizen

'n Nuwe prosedure vir die optimale ontwerp van 'n termiese-sonkragstelsel wat 'n superkritiese-koolstofdioksied (sCO_2) Braytonsiklus gebruik, word ontwikkel. Die ontwerpprosedure is verenigbaar met verskillende tipes komponentmodelle, oplosmetodes en ontwerpbeperkings. Die veranderlikes van die stelsel, asook die doelwitte en beperkings van die stelselontwerp, word bestuur deur middel van 'n uitgebreide berekeningsraamwerk. Multidoelwit-optimering van 23 termodinamiese-, geometriese- en verrigtingsontwerpveranderlikes van die stelsel word behaal.

Die ontwerpprosedure is gebaseer op 'n spesifieke reeks ontwerpbesluite, wat deurlopend die ontwerpruimtes van die turbomasjinerie en hitteruiler substelsels inkort, op só 'n wyse dat Pareto-optimaliteit van die finale stelselontwerp verseker word. Ter wille van berekeningsdoelmatigheid word ontwerpbesluite aanvanklik geneem op grond van die ontleding van 'n termodinamiese model. Dit word gedemonstreer dat die optimale termodinamiese ontwerp van die stelsel beïnvloed word deur die verrigtingswaardes van die turbomasjinerie en tussenverhitter.

Daaropvolgende ontwerpbesluite word geneem op grond van die onafhanklike ontleding van breedvoerige turbomasjinerie en hitteruiler modelle. Die turbomasjinerie word gemodelleer in Matlab® met 'n middellyn-analitiese benadering wat bepaalde verrigtingskoëffisiënte gebruik. Uitdruklike beperkings verseker dat die ontwerpe van die turbomasjinerie binne gevestigde grense is. Die hitteruilers word gemodelleer in Flownex® deur 'n beheervolume-konveksie-diffusie benadering wat die interne knyppunt van die tussenverhitter akkuraat kan voorstel. Al die modelle maak gebruik van realistiese termodinamiese eienskappe vir superkritiese-koolstofdioksied en word omvattend met gepubliseerde data gevalideer.

'n Formele afleiding toon dat daar twee afsonderlike bedryfsgebiede vir die hitteruilers van die stelsel is. 'n Suksesvolle stelselontwerp is afhanklik van die gebied waarin die hitteruilers funksioneer. Hierdie gebied kan beheer word deur die waarde van die nominale vloei-area te verander. Dit word gereken as die belangrikste ontwerpveranderlike van die stelsel.

Ses ontwerpe van dieselfde basiese stelsel, maar met verskillende doelwitte en beperkings, word aangebied. Hierdie ontwerpe word ge-evalueer en met mekaar vergelyk deur middel van 'n breedvoerige kwantitatiewe ondersoek wat die faktore, wat die meeste bydra tot die ondoeltreffendheid van elke ontwerp, uitlig. Wat die omskakeling van hitte na meganiese energie betref, behaal die beste ontwerp 'n doeltreffendheid van 40% teen 'n turbine-inlaattemperatuur van 550 °C. Hierdie doeltreffendheid is gedemonstreer om naby die praktiese maksimum te wees vir 'n sCO_2-stelsel wat gebruik maak van die tussenverhitte sikluskonfigurasie en 'n lineêre sonenergie-ontvanger.

Toekomstige ontwikkelinge van die ontwerpprosedure kan die byvoeging van 'n finansiële model, asook beperkings wat die strukturele integriteit van die stelsel in ag neem, oorweeg.

Acknowledgments

My three academic supervisors, Prof Albert Groenwold, Prof Johan van der Spuy and Mr Robert Dobson, thank you for your guidance and support. I am grateful that I had the opportunity to have worked with you on this topic over the past few years; each of you contributed a unique and profound perspective to my way of thinking.

Mr Dobson, the values that you uphold, the wisdom and experience that you have shared with me, your creative ways of solving problems, and the unlimited passion you have for your work are an inspiration to me as a person and as an engineer. Thank you for being my mentor in the early days of my career, for introducing me to sCO_2 power systems, and for giving me the freedom to explore this topic in the way that I envisioned.

Prof Groenwold, thank you for recognizing the unrealized potential of my early work. You introduced me to mathematical optimization, which brought clarity and organization to my work, and which allowed me to achieve research goals that would not otherwise have been possible. It was a privilege and a pleasure to have such a knowledgeable and experienced expert as my supervisor, especially one with such a selfless character.

Prof van der Spuy, thank you for your practical insight, constructive advice and keen eye for detail. Your suggestions and guidance have undoubtedly elevated the standard of my work. Thank you that you always take a sincere interest in the well-being of your students and prioritize their success above all your other professional responsibilities in the faculty.

Many of my school teachers were inspirational, but in particular I would like to thank Mrs Alayne Torres, who cultivated in me an appreciation for the sciences, and Mr Don Duffield, who through his endless enthusiasm encouraged me to ultimately pursue a career in engineering.

My parents, Sakkie and Petro, you deserve my deepest gratitude. Your love and support for me have always been without bounds. You created an environment which allowed me to learn, to grow, to prosper and to give my undivided attention to my chosen pursuits. Without the foundations that you laid, my work could certainly not have been accomplished.

To my colleagues and friends from the university, thank you that I could share the challenges and the breakthroughs of my work with you. I value your support and fellowship.

I would like to thank Flownex for kindly offering me a personal license of the software which allowed me to continue with my research off-campus.

Financial support for this research was provided by the
Centre for Renewable and Sustainable Energy Studies (CRSES)
and the
Solar Thermal Energy Research Group (STERG)
at Stellenbosch University.

In loving memory of
my grandfather

Quinten Momberg
1927 – 2017

and grandmother

Elizabeth Petronella Momberg
1930 – 2020

whose lives were a paragon of virtue and wisdom,
and who supported me to the last.

FOR OF HIM, AND THROUGH HIM, AND TO HIM,
ARE ALL THINGS: TO WHOM BE THE GLORY FOR EVER.

The Holy Bible, Romans 11:36 KJV

Table of Contents

List of Figures

List of Tables

Nomenclature

Letters

A	Area [m^2]
B ($\mathbf{B}$)	Blade velocity (vector) [m/s]
b	Blade width [m]
C_p	Static pressure recovery coefficient
c_p	Specific heat capacity at constant pressure [J/kgK]
c ($\mathbf{c}$)	Speed of sound [m/s], constant (vector)
D	Diameter [m]
E	Energy [J]
f	Objective function, function, friction factor
g ($\mathbf{g}$)	Inequality constraint (vector)
h ($\mathbf{h}$)	Specific enthalpy [J/kg], convection heat transfer coefficient [W/m^2K], height [m], equality constraint (vector)
K	Total pressure loss coefficient, secondary pressure loss coefficient
k	Thermal conductivity [W/mK]
L	Length [m]
M	Moment (or torque) [Nm]
m	Number of inequality constraints
$\dot{m}$	Mass flow rate [kg/s]
N	Number of parallel flow tubes, number of valid design vectors
n	Number of design variables, number of control volumes
P	Pressure [Pa], power system design space
p	Perimeter [m]
$\dot{Q}$	Heat rate [W]
q	Specific heat [J/kg]
$\mathbb{R}$	Real number space
R ($\mathbf{R}$)	Velocity (vector) in the relative frame of reference [m/s]
r	Radius [m], number of equality constraints
s	Entropy [J/kgK]
T	Temperature [°C, K], thermal system design space
t	Thickness [m]
V ($\mathbf{V}$)	Velocity (vector) in the stationary frame of reference [m/s]
v	Specific volume [m^3/kg]
$\dot{W}$	Work rate (or power) [W]
w	Specific work [J/kg], width [m]
X	Complete system design space
x ($\mathbf{x}$)	Design variable (vector)
y	Response variable
Z	Extended design space
z ($\mathbf{z}$)	Variable (vector) in an extended design space

Symbols

α	Angle of the flow in the stationary frame of reference [°]
β	Angle of the flow in the relative frame of reference [°]
γ	Weighting factor
Δ	Change
ε	Emissivity
ϵ	Recuperator effectiveness, surface roughness [m]
η	Efficiency
λ	Incidence factor
μ	Dynamic viscosity [kg/ms]
ρ	Density [kg/m^3]
σ	Slip factor
τ	Temperature difference between fluid and channel [°C, K]
Ω	Rotational speed [rpm]
ω	Angular velocity [rad/s]

Abbreviations and Acronyms

AR	Area Ratio
BWR	Back-work Ratio
CAPEX	Capital Expenditure
CFD	Computational Fluid Dynamics
CO_2	Carbon Dioxide
CR	Concentration Ratio
CSP	Concentrated Solar Power
DNI	Direct Normal Irradiation
DNS	Direct Numerical Simulation
MDO	Multidisciplinary Design Optimization
NP	Non-deterministic Polynomial
OPEX	Operating Expenditure
PCHE	Printed Circuit Heat Exchanger
PR	Pressure Ratio
RSM	Response Surface Model
SAURAN	Southern African Universities Radiometric Network
sCO_2	Supercritical Carbon Dioxide
SDR	Sequential Design-space Reduction

Dimensionless Groups

Ma	Mach Number
Nu	Nusselt Number
Pr	Prandtl Number
Re	Reynolds Number

Superscripts

n	Number of design variables, coefficient in Dittus-Boelter correlation
T	Transpose

Subscripts

C	Compressor, cold
CV	Control volume
c	Cross-sectional, channel
conv.	Convection
D	Diffuser
F	Fluid, fins
G	Glass
H	Heat sink, high, hot
i	Index, ideal, inner
j	Index
L	Low
Mech.	Mechanical
m	Meridional direction
N	Nominal, nozzle
N	Number of valid design vectors
n	Number of design variables
o	Outer
P	Power system
Para.	Parasitic
p	Associated exclusively with the power system
R	Recuperator
r	Radial direction
rad.	Radiation
S	Solar receiver, steel
s	Associated with both the power system and the thermal system, isentropic, surface
shd	Shroud
T	Thermal system, turbine, tube
Therm.	Thermodynamic
t	Associated exclusively with the thermal system, tangential direction
th	Thermal
V	Vacuum
W, w	Wall
x	Axial direction
0	Stagnation
∞	Ambient

Diacritics

$\check{\square}$	Lower bound
$\hat{\square}$	Upper bound
$\square^{\star}$	Valid
$\tilde{\square}$	Pseudo-
$\underset{\sim}{\square}$	Related to the surrogate problem
$\bar{\square}$	Average
$\underline{\square}$	Key-
$\square'$	Zero-slip or perfect incidence case, per unit length
$\square''$	Per unit area

Mathematical Symbols

$\mid$	Such that
$\subset$	Sub set
$\supset$	Super set
$\in$	In
$\cap$	Intersection
$\rightarrow$	Tends to
$\forall$	For all
$\approx$	Approximately equal
$\sim$	Approximately
$\propto$	Proportional to
O	Of order

1. Introduction

1.1. Background

As the world continues to experience accelerated growth and improvement across an expansive range of metrics (Pinker, 2018), electricity consumption is bound to increase. Since 1990, global electricity consumption has more than doubled and global electricity consumption *per capita* has increased by more than 50% (International Energy Agency, 2020). These trends are even greater when developing countries actively industrialize: at present China consumes more than *ten times* as much electricity as it did thirty years ago.

The majority of the global electricity supply is produced by means of a *thermal power system*. A thermal power system facilitates the conversion of thermal energy to mechanical energy by means of a thermodynamic cycle, and subsequently the conversion of mechanical energy to electrical energy by means of an electromagnetic induction generator.

Statistics from the International Energy Agency (2020) reveal that the combustion of fossil fuels accounts for more than 80% of thermal energy sources for thermal power systems. A consequence of fossil fuel combustion is that pollutants are released into the atmosphere. Some of these pollutants, termed *greenhouse gases*, are known to trap heat from the sun in the atmosphere and therefore, as the concentration of greenhouse gases increases, the average global temperature rises. Correlated with rising temperatures are melting polar ice, higher sea levels, an increase in the severity and duration of short-term extreme weather events, a loss of biodiversity, threats to water and food supply, and an increase in geo-political tensions and conflict. Unrestrained emissions of greenhouse gases are therefore, without doubt, unsustainable. The United Nations (2020) proclaim that

> *climate change is the defining issue of our time and we are at a defining moment... the impacts of climate change are global in scope and unprecedented in scale. Without drastic action today, adapting to these impacts in the future will be more difficult and costly.*

A solution to reducing greenhouse gas emissions is to shift from fossil fuel combustion to alternative forms of thermal energy for thermal power systems. The most obvious, simplest and cleanest source of thermal energy is the thermal energy generated by the sun, which reaches the earth through electromagnetic radiation. This energy is freely available, practically unlimited and can be exploited without harming the environment. Solar energy therefore seems to be an ideal choice for a thermal energy source, but at present solar thermal energy contributes less than 1% to global electrical power production (International Energy Agency, 2020).

Solar Energy

Harnessing energy from the sun on the surface of the planet is not as convenient as it may appear to be: not only is the energy density of sunlight relatively low, but the energy available at a given point on earth perpetually varies as the earth rotates and as the sun is obscured by clouds (Stine and Geyer, 2001). This makes producing a consistent and predictable energy supply challenging. Developing methods and technology to effectively harness solar energy therefore remains an ongoing effort and an active research area.

The focus of the current research is on the intermediate part of a solar thermal power system: the thermodynamic cycle and its components.

Thermodynamic Cycles

Two types of thermodynamic cycles that have historically been used in electrical power generation applications are the Rankine cycle and the Brayton cycle (Dennis *et al.*, 2017). Fundamentally, both the Rankine cycle and the Brayton cycle work in the same way (Borgnakke and Sonntag, 2014). Both have a working fluid that changes between thermodynamic states as it passes through three stages: a compression stage, a heat addition stage, and an expansion stage. The changes in thermodynamic state of the fluid means that ultimately there is a favorable net difference between the magnitude of the mechanical work needed to compress the cold fluid in the first stage, and the magnitude of the mechanical work that can be extracted from the hot fluid in the third stage.

The Rankine cycle is preferred over the Brayton cycle from the perspective of the efficiency with which it converts thermal energy to mechanical energy (Borgnakke and Sonntag, 2014). In the Rankine cycle, the compression stage requires comparatively little work because the fluid is condensed from a gas-state to a liquid-state before its pressure is increased by means of a pump. The Brayton cycle does not condense the fluid but increases its pressure in the gas-state using a compressor. This requires comparatively more work and therefore the Brayton cycle is, in general, less efficient than the Rankine cycle.

Components of the Brayton cycle are generally more robust and reliable than the components of the Rankine cycle when operating under transient conditions and in applications (such as solar thermal power) in which daily start-up and shut-down cycling occurs (Muñoz-Antón *et al.*, 2015).

The Rankine cycle is traditionally operated using a configuration which consists of a fixed amount of working fluid, usually water (steam), that continually circulates between these three stages in a closed-loop. A heat rejection stage is added between the third and first stages of the cycle in order to return the fluid to its original thermodynamic state. The Brayton cycle is traditionally operated with an open-loop configuration in which new working fluid, usually atmospheric air, enters the cycle before the first stage and leaves the cycle after the third stage.

Early History of the sCO_2 Cycle

In the 1960's it was proposed by Angelino (1968) and independently also by Feher (1968) that a closed-loop configuration of the Brayton cycle that is operated with a fluid in its supercritical state could be a viable alternative to the traditional thermodynamic cycles. A *supercritical* Brayton cycle can be more efficient than the traditional Brayton cycle because the compression work can be significantly reduced, and it can be simpler than the Rankine cycle because the fluid does not need to be condensed to its liquid state.

Investigations of the supercritical Brayton cycle identified carbon dioxide (CO_2) as a suitable working fluid, because it maintains the same advantages of air and water (it is abundant, inexpensive, inert and non-toxic) and its thermodynamic properties are well-documented (Feher, 1968). Moreover, the critical temperature of carbon dioxide is near room temperature. This means that the heat rejection temperature of the cycle can be low enough to offer an acceptable cycle efficiency without requiring the fluid to be condensed (Dostal *et al.*, 2004). The critical pressure of carbon dioxide allows the cycle to operate at pressures that are low enough to be practical, but high enough that fractional pressure drops in the cycle can be small (Dostal *et al.*, 2004).

Feher (1968) acknowledged the benefits of this new supercritical carbon dioxide (sCO_2) cycle and proposed that it could be applied to many fields, from terrestrial power plants to space and marine applications. Although the continued commercial and industrial success of the traditional cycles provided little incentive to pursue this alternative cycle in the past, modern emissions regulations, environmental concerns and economic pressures have brought about renewed interest in the sCO_2 cycle.

The Modern Era of sCO_2 Cycle Research

The first major contribution in the modern era of sCO_2 cycle research and the one which invigorated the global resurgence of interest is that by Dostal *et al.* (2004). In the subsequent years, research on the sCO_2 cycle has expanded dramatically and at present virtually all aspects of sCO_2 cycle research have been covered to a greater or lesser extent in literature.

Notwithstanding this, the sCO_2 industry is still in its infancy and sCO_2 cycles do not have a commercial or industrial track record. Challenges still remain before the sCO_2 cycle can be considered as a serious competitor to the significantly more mature steam-Rankine and air-Brayton cycles.

A major impediment to the proliferation of the sCO_2 cycle is that off-the-shelf components are not available. The methods and techniques with which such components can be designed are also not well-established, because the theory used to analyze and design the components is not only different, but also more complicated than the equivalent theory of the traditional cycles (Musgrove and Wright, 2017; Bennett *et al.*, 2017).

1.2. Context

From a technical perspective, the research on sCO_2 cycles can be classified into four areas: *Analysis*, *Simulation*, *Experimentation* and *Design*.

1.2.1. Analysis

The objectives of analyzing sCO_2 cycles are to compare sCO_2 with other working fluids, to consider different configurations of the cycle and what the effects of changing the thermodynamic operating conditions of the cycle are.

Comparison of sCO_2 to Other Working Fluids

The first topic to consider is whether sCO_2 is worth pursuing over the traditional working fluids such as steam and air, especially since these fluids have a considerable head-start in terms of research, development, and commercial and industrial adoption.

A techno-economic study by Cheang *et al.* (2015) showed that for concentrated solar power (CSP) applications, the sCO_2 Brayton cycle is neither more efficient nor more cost-effective than the traditional steam Rankine cycle. They attribute this in part to the maximum temperature of the thermodynamic cycle in a CSP system being relatively low, typically 550 °C to 565 °C, because of the limit imposed by the molten salt in the storage tanks. This limitation would not be present in nuclear power applications and higher temperatures can be supported, in which case sCO_2 may be the preferred working fluid. This finding is confirmed by Dostal *et al.* (2004), who report that the point where the sCO_2 cycle efficiency begins to exceed the steam Rankine cycle efficiency is 550 °C.

Nevertheless, Dostal *et al.* (2004) argue that there are other advantages associated with choosing sCO_2 over steam, not the least of which is that a simple sCO_2 cycle configuration can have a similar thermal efficiency than a more complicated configuration of the steam cycle. The high density of CO_2 in its supercritical region also means that the turbomachinery and heat exchangers that form part of the cycle can be made physically smaller, compared to equivalent steam cycle components, whilst still maintaining similar performance. As such, the power output and efficiency of small-scale sCO_2 cycles can compare favorably with large-scale steam cycles (Dostal *et al.*, 2004). An sCO_2 Brayton cycle can provide the same power output as a steam Rankine cycle whilst occupying up to 30 times less volume (DOE/Sandia National Laboratories, 2011).

Smaller thermal power systems are preferred over larger thermal power systems in developed countries (Musgrove and Wright, 2017), whereas developing countries can benefit from the rapid deployment of smaller systems, particularly in rural areas or in off-grid applications (Li *et al.*, 2020).

Apart from physically smaller equipment, potentially improved efficiency and a simpler cycle configuration, other advantages of the sCO_2 cycle are that it integrates well with dry-cooling, the operating pressures are the same or lower than the pressures in steam cycles, the cycle is versatile in terms of its ability to work with different heat sources across a wide range of temperatures, and sCO_2 maintains all the advantageous factors that are associated with the traditional working fluids of water and air (Dostal *et al.*, 2004; Wright and Anderson, 2017).

A disadvantage of the sCO_2 cycle is the necessity of using advanced materials that can withstand the corrosiveness of CO_2 (Cheang *et al.*, 2015). The substantial changes in the specific heat capacity of CO_2 near the critical point also make heat exchanger design challenging (Stein and Buck, 2017). A risk factor is that the high power rating but small size of the turbine could reduce its reliability (Wright and Anderson, 2017).

Working fluids other than CO_2 have also been considered for application in supercritical power cycles. As an example, a nitrogen cycle is shown to perform similarly to a CO_2 cycle, but a CO_2 cycle is more efficient at higher turbine inlet pressures (Coco-Enríquez *et al.*, 2017).

Cycle Configurations and Thermodynamic Operating Conditions

With a given set of thermodynamic conditions and pressure drops, Milani *et al.* (2017) and Luu *et al.* (2017a) analyzed several different configurations of the sCO_2 cycle which have different numbers of turbomachines and heat exchangers, arranged in different ways. In general, more complicated cycle configurations have improved thermal efficiency values, smaller heat exchanger areas, lower cooling duties and lower water usage. Based on these metrics, the "combined cycle" configuration (which is a recompression cycle with the addition of intercooling and reheating) is the best, but comes at the cost of complexity. This configuration requires five turbomachines and six heat exchangers, as opposed to only two turbomachines and three heat exchangers for the simple recuperated cycle configuration.

A more detailed thermodynamic analysis can be achieved through a parametric variation of key variables (Sarkar and Bhattacharyya, 2009; Milani *et al.*, 2017; Wang and He, 2017).

The risk associated with using a set of given thermodynamic conditions and assumed pressure drops is that the results of the study are subject to the validity of these conditions and assumptions. The analyzed configurations may perform differently at different thermodynamic operating conditions or pressure drops.

An approach that overcomes this is to concurrently analyze different cycle configurations and the effect of thermodynamic operating conditions on the performance of each of those configurations – as demonstrated by Battisti *et al.* (2015) and Wang *et al.* (2018). The general performance trends exhibited by the different cycle configurations with respect to changing thermodynamic operating conditions are similar and differ only by two to three percentage points at most (Wang *et al.*, 2018). Furthermore, the thermodynamic operating conditions strongly dominate over cycle configuration in terms of cycle efficiency. Cycle configuration can therefore be seen to be of secondary importance compared to the effect of major thermodynamic operating conditions of the cycle such as turbine inlet temperature and compressor outlet pressure.

1.2.2. Simulation

Simulation differs from *Analysis* in that the purpose is to gain a deeper understanding of how a particular system operates rather than just a broad overview. The following elements of sCO_2 system simulation are discussed: the different types of simulations, the relationship between modeling and simulation – particularly how the accuracy of the modeling affects the relevance of the simulation results – and the different computational environments that have been used to model and simulate sCO_2 systems.

Classification of Simulation Types

Simulation work can be classified into three broad types: a *steady-state design-point simulation* is a study of the system as it is meant to be operated at under ideal environmental and control conditions, similar to the research contributions on cycle analysis presented in Section 1.2.1. A *steady-state off-design simulation* allows the system to be studied under environmental or control conditions that differ from the design conditions but that are independent of time; and a *transient simulation* allows the system to be studied as the environmental or control conditions vary with time.

The latter two types of simulations need to be clearly distinguished. For example, Berthet Couso *et al.* (2017) present a so-called transient simulation even though it is actually a steady-state off-design simulation conducted at a series of 15 minute intervals. *Bona fide* transient simulations such as the work by Hexemer and Rahner (2011) simulate the system in time steps that are of the order of seconds. This allows robust real-time control strategies to be developed for the system which is not possible using only steady-state off-design simulations.

Modeling and Modeling Accuracy

Simulations are based on models of the thermodynamic cycle and its components. The accuracy of any simulation is therefore inextricably related to the accuracy of its underlying models and as such these models need to be realistic to a level that is commensurate with the expectations of how the simulations are to be applied.

For the purposes of analyzing a system as discussed in Section 1.2.1, general trends and qualitative insights are usually expected and therefore the modeling accuracy is not of primary concern. The research methodologies applied in cycle analysis usually make use of many significant assumptions and simplifications because the purpose is to get a broad overview of a wide range of aspects about the cycle.

Whilst simulation work may also strive to obtain qualitative insights, the focus is often more towards quantitative results which are by nature only meaningful if they are realistic. Even so, it is often the case that simulation models are founded on precarious assumptions about the performance of the components, either for the purposes of computational expediency or out of necessity resulting from a lack of appropriate data or theory. It is therefore prudent to carefully consider which assumptions have been made in the underlying models when evaluating the quantitative results of such simulations.

Some examples of simplifying assumptions in prior simulation work are as follows:

- It is a well-motivated and common practice to assume that the recuperator(s) and turbomachines do not lose heat to the environment; but making the same assumption with regard to the primary heat exchanger between the cycle and the heat source, as shown by Battisti *et al.* (2015), requires careful consideration.

  For a heat source such as a coal-fired boiler or nuclear reactor, this assumption is sensible because the heat source is separate from the environment. The heat loss that occurs is therefore from the heat source itself and not from the primary heat exchanger that accepts the heat. For a heat source such as concentrated solar power though, the heat source *is* the environment and therefore the heat loss that occurs is from the solar receiver (the primary heat exchanger) and not from the heat source.

  In solar tower-type CSP systems, the heat loss can be mitigated to some extent by using cavity receivers (Stein and Buck, 2017) which shield the hot receiver surface from radiation and convection losses. In parabolic-trough CSP systems though, the receiver is entirely exposed to the ambient air and therefore radiation and convection heat losses should be considered as a fundamental part of the modeling.

- In some studies, the pressure drop in the heat exchangers is completely neglected (Berthet Couso *et al.*, 2017) or is assumed to be a constant value (Milani *et al.*, 2017). This may be a permissible assumption to make or it may be completely inaccurate – the only way to ascertain this is by doing a full analysis of the heat exchangers.

- To analyze the heat exchangers, Berthet Couso *et al.* (2017) used the effectiveness-NTU method. This is a common method for traditional heat exchanger analysis and is applicable under certain cases for sCO_2 heat exchangers as well, but Dostal *et al.* (2004) explain that the change in specific heat capacity of CO_2 near its critical point make this an unsuitable method for sCO_2 heat exchanger analysis in general.

  A more appropriate method is to sub-divide the heat exchanger into many smaller elements (control volumes) and to evaluate the heat transfer within each element separately. Using this method also avoids the so-called "internal pinch point problem" (Friedman and Anderson, 2017) where the temperature difference between the hot and cold streams of a recuperator is minimized somewhere in the middle of the recuperator and not at one of the boundaries as might be expected.

- Modeling the performance of a turbomachine, particularly under off-design conditions, is not a trivial task. In reality, the efficiency of a turbomachine with a known geometry and working fluid is a complicated function of its inlet conditions, shaft speed and mass flow rate. This relationship is usually presented on multi-dimensional performance maps after the machine has been experimentally tested (Dixon and Hall, 2014).

  To simplify the modeling of the turbomachines, a constant efficiency can be assumed (Milani *et al.*, 2017) or the efficiency can be assumed to vary as a polynomial function of the flow coefficient or flow-to-blade velocity ratio (Dyreby, 2014). For off-design or transient simulations, the efficiency can be viewed as being independent of the shaft speed (Trinh, 2009) or it can be approximated as discussed by Singh *et al.* (2013).

Computational Environments

A wide range of computational environments have been successfully employed to model and simulate sCO_2 systems. Some researchers have elected to develop their own models and solution procedures. This has the advantage that the researcher has complete flexibility with regards to the modeling approach and details, but it requires increased coding time and there is also a higher risk of coding and logical errors. Computer programming languages such as Fortran (Iverson *et al.*, 2013; Dyreby, 2014) and MATLAB® (Osorio *et al.*, 2016a; Rao *et al.*, 2019) have been used in such cases.

Other researchers have used existing commercial software for modeling and simulation work (Cheang *et al.*, 2015; Luu *et al.*, 2017b; Avadhanula and Held, 2017), while some research institutions have specialized in-house developed simulation codes (Hexemer and Rahner, 2011; Kim *et al.*, 2017).

Combinations of computational environments have also been used; Dostal *et al.* (2004) for example used custom-developed models in Fortran in addition to commercial turbomachinery design software by Concepts NREC.

1.2.3. Experimentation

Experimental work on sCO_2 cycles is expensive and time-consuming, yet it is an essential part of validating theoretical analysis and simulation work, and it is the final step before sCO_2 cycles can be implemented in real-world applications. Experimental work on sCO_2 cycles have been limited to large, well-funded research groups in which there is a collaboration between academia and industry.

The United States has an enviable track record in the field of experimental sCO_2 research. Ashcroft *et al.* (2009) discuss the collaboration between 16 research organizations and companies on experimental sCO_2 programs. Two complete sCO_2 cycles in the United States are at Sandia National Laboratories (Wright *et al.*, 2010) and at the Bettis Atomic Power Laboratory (Clementoni *et al.*, 2014).

In Japan, the Tokyo Institute of Technology, the Institute of Applied Energy and the Thermal Engineering & Development Co. Ltd. collaborated to develop an experimental facility with the focus on investigating the sCO_2 Brayton cycle for use in thermal power systems with waste heat from an industrial process as the heat source (Utamura *et al.*, 2010).

An experimental test program was also developed in Daejeon, South Korea, with inputs from the Korea Atomic Energy Research Institute, the Korea Advanced Institute of Science and Technology, the Korea Institute of Energy Research and Jinsol Turbo (Ahn *et al.*, 2015; Cho *et al.*, 2016). The program consisted of a number of different sCO_2 loops, each developed with different research objectives in mind.

Another test loop is at the Indian Institute of Science in Bangalore (Ginley and Chattopadhyay, 2020).

All of these experimental facilities are small scale, with heat sources less than 1 MW_t. In 2018, construction started on a 10 MW_e sCO_2 pilot power plant in the United States (Gas Technology Institute, 2018). The project is a collaboration between the Gas Technology Institute, the Southwest Research Institute, General Electric and the United States Department of Energy, amongst others. The project is estimated to cost $119 million (approximately two billion South African Rand).

The construction of another 10 MW_e experimental project is underway in China. The French utility company EDF and the Chinese CSP technology manufacturer Shouhang are collaborating to convert the power block of an existing CSP plant to run on sCO_2 (Le Moullec *et al.*, 2018).

In Europe, there are two significant projects on sCO_2 systems. Both projects are a collaboration between multiple nations, research institutions and corporations. The sCO_2-HeRo project (European Commission, 2017), which concluded in 2018, was a project to test the feasibility of using an sCO_2 system to passively remove residual heat from a nuclear reactor. The sCO_2-Flex project (European Commission, 2019) is ongoing; it considers the design and simulation of a 25 MW_e sCO_2 system as a springboard for an experimental demonstration project.

The first commercially available sCO_2 system, which is for waste heat applications, is the EPS100 system by Echogen (Held, 2014).

1.2.4. Design

It is useful to make the distinction between an sCO_2 *cycle* and an sCO_2 *system*. Analysis work, as discussed in Section 1.2.1, is concerned only with the operating conditions and configuration of the thermodynamic *cycle* and not with the details of the overall *system* which includes details such as the sizes and specifications of the components.

On the other hand, simulation work (as discussed in Section 1.2.2) and experimentation work (as discussed in Section 1.2.3) deal with the overall system, but assume that the details of this system are already known.

Between these two extremes lies the domain of *Design*, in which the objective is to find the sizes and specifications of the components so that a theoretical thermodynamic cycle can be evolved into a complete system that can be simulated, or constructed and tested experimentally.

The context of the current research is in design. The point of departure is therefore a given cycle configuration and working fluid, the end result a list of detailed specifications that fully describe the system.

It is arguably not sufficient for any designer to merely propose a working design for the system. Rather, an *optimized* design that performs objectively well with regards to one or more metrics is expected. Within the context of design, design *optimization* is a key aspect and the focus of the current research is on this.

Design Optimization Challenges

The optimal design of a thermal power system is a challenging engineering problem. At its core, it is a multi-physics problem, involving at least the fields of thermodynamics, fluid mechanics and heat transfer. Analytical solutions for a detailed thermal power system model do not exist and therefore numerical solution procedures are essential. The inherently non-convex and non-linear physics of the underlying models make them computationally expensive to solve (Manninen and Zhu, 1998). In particular, sCO_2 systems require even more computationally expensive models, given that real fluid properties must be used and the simplifications used to model traditional steam-Rankine and air-Brayton systems are not appropriate for sCO_2 systems (Musgrove and Wright, 2017).

This research considers the design of the system with 23 design variables. This is the number of variables for which valid numerical values must be found in order to complete the design of the system. System design problems with more than 100 design variables have been solved before (Kler *et al.*, 2020), whilst the total number of variables in a thermal power system (including the current design problem) is of the order of several thousand. The scale of the problem is also large, with design variable values that can cover several orders of magnitude.

The number of design variables is a significant consideration because multidisciplinary design optimization problems are generally classed as *NP-hard* or *(non-deterministic polynomial)-hard* problems (Ausiello *et al.*, 1995). This refers to the notion that a solution to the problem (i.e. to find the optimal design of the system) cannot be achieved using any problem-solving algorithm in an amount of time of order $O(n^c)$, but instead requires an amount of time of order $O(c^n)$, where n is the input length (i.e. number of design variables) and c is a constant (Garey and Johnson, 1979).

Multidisciplinary optimization problems are therefore solved in *exponential* time rather than in *polynomial* time. Garey and Johnson (1979) demonstrate the effect that this distinction has on real computing time, revealing that even if the underlying model of the problem takes mere microseconds to analyze, and even if computing power could increase by several orders of magnitude, the input length (n) for problems that can be solved in a practical amount of time is small.

As a result of the extreme inherent computational expense of system design optimization, "finding the global optimum is a lofty goal that is seldom realized in practice" (Papalambros and Wilde, 2017). The primary challenge therefore is to find a way to achieve a near-optimal system design in a reasonable amount of time (Bejan *et al.*, 1996).

1.3. System Overview

A schematic diagram of the solar thermal power system to be designed in this research is presented in Figure 1. This a closed configuration of the Brayton cycle, known as the *regenerative* or the *recuperated* cycle. It consists of two turbomachines (the compressor and the turbine) and three heat exchangers (the solar receiver, the recuperator and the heat sink). The recuperator can also be referred to as the *regenerator*, and the heat sink can also be referred to as the *precooler*.

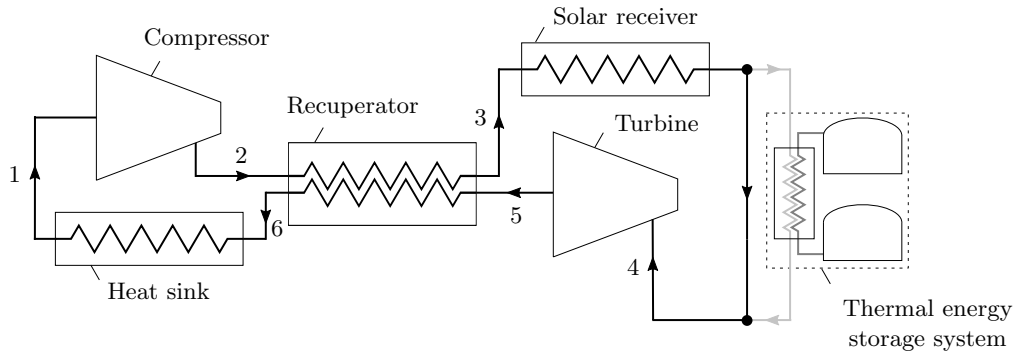

Figure 1: Schematic diagram of the system

The recuperated Brayton cycle is a simple configuration and indeed there are many more elaborate configurations available (Milani *et al.*, 2017). However, this cycle contains all of the component types that are necessary to construct any of the more advanced cycles.

The function of the recuperator is to transfer heat from the hot fluid that leaves the turbine, to the cold fluid that leaves the compressor. This reduces the sizes of the solar receiver and heat sink (because less heat has to be transferred between the cycle and the environment) and also increases the theoretical efficiency of the cycle.

Flow Stations

The path of the working fluid through the components is indicated by the thicker lines in Figure 1, the direction of flow is indicated by the arrows. There are six *stations* at the interfaces between the five components of the cycle, as indicated by the numbers. The fluid passes through each component once per cycle, except for the recuperator which the fluid passes through twice per cycle: once on the heat addition side (where the fluid gains temperature) and once on the heat rejection side (where the fluid loses temperature). A summary of the flow stations is presented in Table 1.

Table 1: Flow stations

Component	Inlet Station	Outlet Station
Compressor	1	2
Recuperator, heat addition side	2	3
Solar receiver	3	4
Turbine	4	5
Recuperator, heat rejection side	5	6
Heat sink	6	1

Nominal Flow Area

The flow areas at the interfaces between the five components (i.e. at the six stations) are the same as each other. This flow area is termed the *nominal flow area*, A_{N}, and it guarantees geometric compatibility between all of the components. Within the components themselves, the flow area can be different from the nominal flow area.

Thermal Energy Storage System

In a solar thermal power system, a *thermal energy storage system* is usually installed between the outlet of the solar receiver and the inlet of the turbine. The most common configuration of thermal energy storage at present consists of a heat exchanger which connects to the main cycle, and another loop which connects this heat exchanger and two storage tanks (Neises and Turchi, 2019). The storage system is "charged" by circulating molten salt from the "cold" tank through the heat exchanger. Heat is removed from the main cycle and is stored in the "hot" tank. The system is "discharged" by reversing the direction of molten salt flow – from the hot tank through the heat exchanger to the cold tank. As the salt flows through the heat exchanger, heat is transferred back to the main cycle.

A thermal energy storage system is an indispensable part of a solar thermal power system as it smooths out the inherent variability of the solar energy source. This provides the system with predictability and allows it to provide electrical power for an extended time even when the sun is not shining. However, because the thermal energy storage system is only relevant for controlling the system under transient, off-design conditions, it will not be considered in the current research which is concerned only with the design of the system for working under a particular set of design-point conditions at steady-state.

System Decomposition

Re-arrangement of the components as shown in Figure 2 demonstrates that the complete system (excluding the thermal energy storage system) can be represented as two interacting sub-systems; namely the *power system* which includes the turbomachinery, and the *thermal system* which includes the heat exchangers.

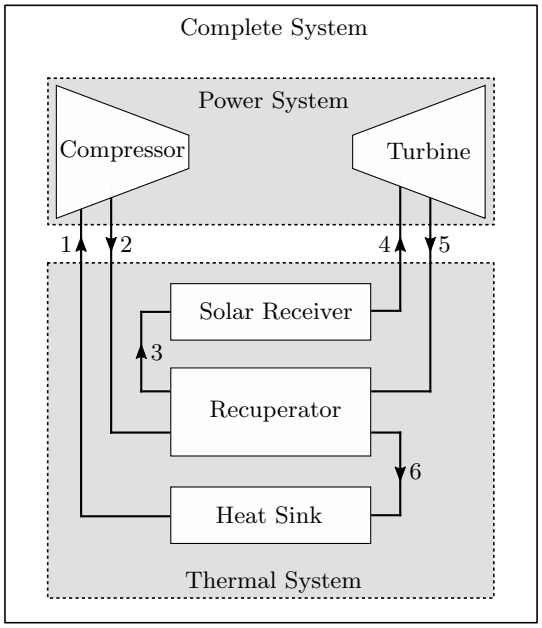

Figure 2: Schematic diagram of the complete system represented as two sub-systems

The physics that govern the operation of the components within the power system and thermal system are sufficiently different from each other, to the extent that each of the sub-systems can be considered as a specialized *discipline* on its own. The variables within each discipline are said to interact *strongly* with each other, but interact only *weakly* with the variables of the other discipline (Haftka and Gürdal, 1992). Each discipline requires its own specialized modeling approach and solution procedure. As a result, the complete thermal power system is *multidisciplinary*, and can only be modeled, analyzed, simulated, designed or optimized as an assembly of its interacting disciplines.

A system is considered *separable* if none of the variables are shared by the disciplines, and if the optimization objective and design constraints can be expressed as the summation of the functions of one discipline (Haftka and Gürdal, 1992). It is *quasi-separable* if some of the variables are shared between the disciplines, but the optimization objective and design constraints can still be expressed as for a separable system (Tosserams *et al.*, 2010). The system in the current research is *non-separable*: some variables are shared between the disciplines, and the optimization objective is a non-separable function of both disciplines.

1.4. Classical System Design Procedures

To develop an *ab initio* design (that is, starting with all design variables free to vary and excluding the possibility of pre-designed components) of the system in Figure 1 requires the use of a practical design procedure. For the detailed design of sCO_2 systems, two distinctive design procedures have been proposed:

- Dostal *et al.* (2004) separate the overall design problem into a series of smaller, independent design problems. The key operating conditions of the cycle, which include the turbine inlet temperature, compressor inlet temperature, compressor outlet pressure and the magnitude of the thermal power input are determined in the first part. The lengths and volumes of the heat exchangers and the cycle pressure ratio are determined next. Finally, the detailed design of the heat exchangers and turbomachines using dedicated models of the components are performed using the inputs that were determined previously.
- Saeed *et al.* (2019) separate the design of the system into the design of its components only; each component is described by a detailed model. The procedure starts with given inputs including the compressor inlet temperature, compressor inlet pressure and cycle pressure ratio, after which the component models are solved using an iterative scheme. Each model is analyzed more than once per iteration, and each model also contains internal iterations. The design procedure is completed once a specified error tolerance level is achieved.

A significant drawback of these existing design procedures is that they do not facilitate optimization of the system design. In both procedures, the values of the variables that are supplied to the detailed component models can only be varied using a parametric study scheme, which is only practical for optimizing the design of the system with a small number of design variables. A different type of design procedure, which uses a different computational architecture, is required if an optimal design with many design variables is sought.

For the purposes of this research, the term *extensive* optimization is used with reference to this type of "all-inclusive" design procedure, which is distinct from the above-mentioned classical design procedures that only facilitate *parametric* optimization of the design. Therefore, a design procedure with the feature of *extensive optimization* refers to one which allows an optimal (or near-optimal) design of the system to be found, where *all* of its design variables, as opposed to only a few, are initially free to vary.

Multidisciplinary Design Optimization (MDO) is a *bona fide* field within applied mathematics that specifically deals with design optimization problems which require different disciplines to be analyzed, and where the performance of the complete system is governed by the interaction between the separate disciplines (Sobieszczanski-Sobieski and Haftka, 1997).

Although there are many different MDO architectures available (Martins and Lambe, 2013), they all share the same fundamental approach: all MDO architectures have an overarching optimization algorithm which manages the constraints placed on the system and dictates when and how discipline-specific models are analyzed throughout the design process.

The main drawback of MDO is the long implementation time required. This is as a consequence of needing to develop an optimization algorithm that can communicate with the independent solvers of the different disciplines.

The execution time of an MDO procedure is also relatively long. The optimization algorithm must numerically find a set of design variables that is valid for all disciplines, but it can only analyze the disciplines independently. The execution time of a basic MDO procedure can be shortened by modifying the design problem in one of two ways:

- A set of filters can be applied before the optimization procedure commences, in order to reduce the number of unknown variables and in so doing solve a reduced optimization problem. Manninen and Zhu (1998) demonstrate this method for the thermo-economic optimization of a thermal power system, and Liang *et al.* (2020) demonstrate this method for the thermodynamic optimization of a hybrid sCO_2 Brayton cycle and organic Rankine cycle CSP system.
- A surrogate model can be introduced and optimized instead of the actual model of the system. A surrogate model is computationally less expensive to analyze than the actual multidisciplinary system model, whilst still maintaining most of its features (Wang *et al.*, 2014a). A surrogate model is typically constructed from several analyses of the actual system model (Forrester and Keane, 2009). Various types of surrogate models have been proposed, from simple polynomial expressions to neural networks and frequency domain approximations (Barton, 1998). Neural networks in particular have successfully been used before to optimize CSP systems (Richter *et al.*, 2011).

Whilst these two modifications improve the execution speed of MDO, the implementation time remains considerable. Advances such as the Dakota toolkit (Sandia National Laboratories, 2020) and the OpenMDAO framework (Gray *et al.*, 2019) have broadened the appeal and reduced the implementation effort of MDO by offering an existing framework and set of optimization tools to users, but bi-directional communication between the independent solvers of the disciplines and the optimization algorithm must still be facilitated before these tools can be used.

An alternative multidisciplinary design optimization procedure is that of *set-based design*, in which the disciplines of the system are optimized separately (Singer *et al.*, 2009). A set-matching process attempts to find a design for the system based on the results of the optimized disciplines. Although bi-directional communication between the disciplines and the need for an overarching optimization algorithm are both eliminated in set-based design, global optimization is not possible because not all possible system designs are considered. It is also unlikely that the optimal design for each discipline also corresponds to the optimal design of the complete system. An advanced application of set-based design has been proposed (Hannapel and Vlahopoulos, 2014) that offers a mathematically rigorous approach to global optimization, but at the cost of increased complexity in its implementation.

1.5. Motivation

The transition to cleaner and more sustainable thermal power systems is essential for meeting the incessantly growing global demand for electricity whilst simultaneously reducing greenhouse gas emissions. Solar thermal energy is a proven alternative to fossil fuel combustion, but is yet to see widespread global adoption. The sCO_2 Brayton cycle can add value to solar thermal power systems because it offers an improved thermal efficiency, smaller components and simpler cycle configurations compared to a traditional steam Rankine power cycle.

The special characteristics of sCO_2 systems require specialized and detailed turbomachinery and heat exchanger models to be analyzed for the design of new systems. Not only are these models inherently computationally expensive to analyze, but the computational expense scales exponentially with the number of design variables that are considered in the optimization of the system design.

Existing procedures for developing an *ab initio* design of an sCO_2 thermal power system do not facilitate extensive optimization of the design, whereas classical MDO procedures require a considerable amount of time to implement or to execute.

The implementation time of classical MDO can be shortened by eliminating an overarching optimization algorithm and bi-directional communication between disciplines, by using a method such as set-based design, although global optimization is then no longer possible. The execution time of classical MDO can be shortened by using pre-optimization design-space filtering and surrogate-based modeling, but then the implementation time of the design procedure remains considerable.

A novel opportunity therefore exists to develop a practical design procedure – specifically for an sCO_2 solar thermal power system – which can be implemented in a short amount of time, is computationally efficient and which facilitates extensive optimization of the system design.

1.6. Objectives

Objective 1: Development of a New Design Procedure

The primary objective of this research is to develop a comprehensive, practical procedure for the *ab initio* design optimization of a thermal power system. The procedure must have the following features:

- Both the thermodynamic design of the cycle and the detailed design of the components of the system must be completed.
- Multi-objective *extensive optimization* (as distinct from *parametric optimization*) of the system design must be possible.
- It must be relatively fast to implement and execute. Neither an overarching optimization algorithm nor explicit bi-directional communication between the disciplines of the system should be required.
- It must be flexible with regards to the types of models and solvers used for the disciplines of the system. This is to allow designers to select familiar models and solvers which are appropriate for a particular application.
- It must be flexible with regards to the constraints that can be placed on the system so that different design applications can be facilitated with the same general procedure.

Objective 2: Application and Demonstration of the Design Procedure

The second objective of this research is to apply the newly developed procedure by designing the sCO_2 solar thermal power system presented in Figure 1, and concomitantly to demonstrate the flexibility of the procedure in handling different design objectives and constraints for this system.

Objective 3: Development of Models

As a pre-requisite for the second objective, analytical models of the system (as an assembly of its separate disciplines) must be developed.

Objective 4: Development of a Computational Architecture

In order for the proposed design procedure to yield maximum utility for future applications, it must be based on a computational architecture that is clear, unambiguous and sufficiently general. Objectives, constraints and variables must be explicitly managed throughout the entire design process.

1.7. System Details

For the purposes of the current research, the net power output and component technologies of the system are fixed before the modeling and design of the system commences. These details discussed in the following sections.

Net Power Output

The net mechanical power output of the system is chosen to be 10 MW. This power rating is selected based on the recommendation of Sienicki *et al.* (2011). An sCO_2 thermal power system of this scale is the most flexible with regards to technology options, and a system of this scale will give an accurate representation of all the features associated with larger power systems (of the order of 100 MW and higher). This is also the power rating selected for the first major sCO_2 demonstration project in the world, which is currently underway in the United States (Gas Technology Institute, 2018).

Turbomachinery Technology

The system uses a centrifugal compressor and a radial inflow turbine. Both are single-stage machines. Radial-type turbomachines are generally preferred over axial-type turbomachines for small-scale power systems (Sienicki *et al.*, 2011) and in applications with relatively high pressure ratios or relatively low mass flow rates (Boyce, 2012).

Solar Receiver Technology

The solar receiver is an evacuated tubular receiver, which works in conjunction with a parabolic trough solar collector field (the latter is not studied as part of the current research). Although modern CSP research is mostly skewed towards *point-focus* solar receivers where the solar receiver is placed on a tower that is surrounded by a field of heliostats, this more established *line-focus* technology nevertheless has advantages.

One advantage is that line-focus systems are considerably less expensive than point-focus systems (Peinado Gonzalo *et al.*, 2019). Another advantage is that the line-focus industry is significantly more established with a proven track record and with commercially available technology. At the start of the previous decade, 96% of all operational CSP capacity was from parabolic trough plants (Llorente García *et al.*, 2011). Despite solar tower systems seeing increased installation, at present parabolic trough plants maintain a considerable lead, representing 85% of the operational CSP capacity (Achkari and El Fadar, 2020). More parabolic trough plants are also under development.

Disadvantages of line-focus technology compared to point-focus technology are a lower possible solar concentration ratio (Breeze, 2014), and single-axis as opposed to dual-axis tracking of the sun impacts the annual solar collection efficiency of the system (Stine and Geyer, 2001).

Compared to other working fluids, carbon dioxide is the most suitable for application in high-temperature parabolic trough systems, both from an efficiency perspective and from an economics perspective (Bellos *et al.*, 2016; Biencinto *et al.*, 2019).

Heat Sink Technology

Concentrated solar power plants are located in geographical regions where the direct normal irradiation (DNI) is high throughout the year. Unfortunately, these places are usually dry and arid, which makes water consumption of the power plant an important consideration.

If an abundant natural supply of water is available, then a *wet-cooled* heat sink, where the working fluid of the cycle is cooled down using water, is the preferred technology both from a technical perspective and from an economics perspective (Owen, 2013). An alternative solution is to have a *dry-cooled* heat sink, where the working fluid is cooled down using atmospheric air. Two fundamental limitations of a dry-cooled heat sink are that the compressor inlet temperature cannot be lower than the ambient temperature (plus an approach temperature) and that the performance of the heat sink (and therefore the compressor inlet temperature) fluctuates if the ambient temperature fluctuates.

At the cost of introducing a parasitic energy demand to the overall system, a dry-cooled heat sink can be enhanced using fans (Owen, 2013), but the current research will instead consider a *natural cooling* arrangement where the heat sink is cooled exclusively by radiation to the environment and convection heat loss to the ambient air (which is at the ambient wind speed).

A *hybrid* cooling solution achieves a balance between the advantages of wet- and dry-cooled heat sinks whilst minimizing the drawbacks of each type of technology. This is the recommended technology for sCO_2 systems in general (Gavic, 2012), but it is not considered in the current research because a naturally dry-cooled heat sink has fewer design variables and is sufficient to demonstrate the design procedure.

Recuperator Technology

A printed circuit heat exchanger (PCHE) is used as the recuperator technology for the system in this research. A PCHE is a *compact* heat exchanger, which means that it has a high ratio of heat transfer surface area to total volume (Çengel and Ghajar, 2015).

It is the preferred recuperator technology in sCO_2 thermal power systems because its compact nature allows material volume to be reduced, and because other heat exchanger technologies either cannot withstand the high pressures experienced in sCO_2 cycles or are more challenging to manufacture (Dostal *et al.*, 2004).

A PCHE consists of a series of metal plates into which small channels are chemically etched. The plates are then stacked together and diffusion bonded (Çengel and Ghajar, 2015). This forms the so-called *core* of the heat exchanger, onto which headers are welded to complete the heat exchanger (Musgrove *et al.*, 2017b). This technology is easily scalable.

A counter-current flow configuration is used because it will always have a higher log mean temperature difference (and is therefore smaller) compared to the parallel-flow configuration (Çengel and Ghajar, 2015)

1.8. Design Optimization Objectives

From a technical perspective, two common optimization objectives are to maximize the *thermal efficiency* or the *exergy efficiency* of the system (Wang *et al.*, 2018). The thermal efficiency relates to the first law of thermodynamics and is a measure of how efficiently the system is able to convert a thermal energy input to a net mechanical energy output. The overall *solar-to-electric* conversion efficiency of the system is less than the thermal efficiency, but because the solar field is not studied in the current research, this is not an appropriate objective.

The exergy efficiency relates to the second law of thermodynamics (Le Roux *et al.*, 2013). As energy is converted from one form to another in a real process, entropy is generated. This gives rise to the phenomenon that *exergy* (which is the potential for energy to be converted) is destroyed. Dunbar *et al.* (1995) argues that it is more important to maximize the *conservation of exergy* as opposed to the *conversion of energy*.

Maximum cycle work output is another possible optimization objective. It is not achieved at either of the points of maximum cycle first- or second law efficiency (Haseli, 2013).

From a financial perspective, three possible optimization objectives are to minimize:

- the *cost of electricity* (Wang *et al.*, 2014b), typically expressed in \$/kWh,
- the *cost of capacity* (Kler *et al.*, 2019), typically expressed in \$/kW, or
- simply the overall *cost* (Rao *et al.*, 2019), typically expressed in \$.

The latter objective is only useful if relevant constraints are provided – for example that the system must provide a certain net power output. This highlights the important link between objectives and constraints: optimality must be assessed not only on the basis of the objective function value, but also in light of the constraints under which that value is achieved.

Another financial optimization objective is to maximize the *internal rate of return,* which is typically compared to the interest rate to help investors decide whether the project is likely to be profitable (Wright and Scammell, 2017).

Beyond technical and financial considerations, optimization objectives can also be related to environmental, safety and reliability aspects (Bejan *et al.*, 1996). Although non-technical aspects are invariably an essential part of thermal power system design and optimization, they will not be explicitly considered in the current research. The reason for this is two-fold: firstly, non-technical aspects such as financial considerations are necessarily based on many assumptions (Wang *et al.*, 2014b) and can vary significantly between applications. Costs of components are different depending on whether the system is first-of-a-kind or n-th-of-a-kind; estimates for first-of-a-kind sCO_2 components can vary by as much as 80% from their nominal values (Wright and Scammell, 2017).

Secondly, non-technical aspects are weakly coupled to the technical aspects (as opposed to the power and thermal sub-systems which are strongly coupled). This means that the non-technical models are correlated to a technical design of the system, but the technical design itself is unaffected by the non-technical aspects. For example, the cost of the system is a function of its design, but its design is not a function of its cost. It would therefore be relatively straightforward to make non-technical aspects part of the design procedure.

The presence of non-technical models only change the design objectives and the criteria on which design decisions are made; not the design procedure itself. The same is true for the technical objectives of the optimization: regardless of whether thermal efficiency or exergy efficiency is the preferred technical optimization objective, the design procedure itself does not change, only the basis on which optimality is assessed changes. For the purposes of this research, design objectives that are based purely on technical grounds – any technical grounds – are sufficient. In this research, maximization of the thermal efficiency of the system, η_{th}, is chosen as an objective.

Notwithstanding the arguments for excluding non-technical design objectives, some purely technical design objectives can be motivated from a non-technical perspective, especially from an economics perspective:

- The highest pressure in the cycle (the compressor outlet pressure P_2) should be relatively low because higher fluid pressures demand greater mechanical strength and therefore necessitate thicker flow channel walls, which make the system more expensive.
- The highest temperature in the cycle (the turbine inlet temperature T_4) should be relatively low because higher temperatures require more advanced materials that are more expensive.
- If the nominal flow area A_{N} is large, then the perimeter of the flow channels is also large, and more material would be required. A small nominal flow area is therefore preferred in order to minimize the cost of materials.
- A reduction of the nominal flow area is associated with an increase in the velocity of the flow. Given that frictional pressure drop (which reduces cycle efficiency) is exponentially related to fluid velocity (and therefore to mass flow rate $\dot{m}$), minimizing mass flow rate must be a concomitant objective with the objective of minimizing the nominal flow area.

These five design optimization objectives are summarized in Table 2.

Table 2: Design optimization objectives (Key: $\uparrow$ = maximize, $\downarrow$ = minimize)

Objective	Variable	Target	Motivation
f_1	η_{th}	$\uparrow$	Overall measure of system performance
f_2	P_2	$\downarrow$	Thinner flow channel walls, less expensive
f_3	T_4	$\downarrow$	Less advanced materials, less expensive
f_4	A_{N}	$\downarrow$	Smaller heat exchanger volumes, less expensive
f_5	$\dot{m}$	$\downarrow$	Lower flow velocity, lower pressure drop

Conceptually, the objective of the system design optimization is to *minimize*

$$f \;=\; -\gamma_1 f_1 \;+\; \gamma_2 f_2 \;+\; \gamma_3 f_3 \;+\; \gamma_4 f_4 \;+\; \gamma_5 f_5 \;, \tag{1}$$

where $\gamma_1, \gamma_2, \gamma_3, \gamma_4$ and γ_5 are appropriate weighting factors that make the objectives additive and ascribe relative importance to them. However, this weighting factor concept will not be applied formally in the current research, given the subjective nature of such weighting factors. It is introduced here merely for the sake of clarity.

Instead, in the current research, it is proposed that a pair of objectives be optimized one at a time. This is a pragmatic approach and it is not suggested to be mathematically equivalent to minimizing Equation (1). Although the application of the proposed design procedure is demonstrated in detail in Chapter 6, essentially it minimizes Equation (1) as follows:

- The system is analyzed with the exclusive intention of finding the trade-off between objectives f_1 and f_3. The designer selects an appropriate value for T_4 (or f_3), which then establishes the relationship between objectives f_1 and f_3.
- With T_4 (or f_3) fixed, the system is analyzed with the exclusive intention of finding the trade-off between objectives f_1 and f_2. The designer selects an appropriate value for P_2 (or f_2), which then establishes the relationship between objectives f_1, f_2 and f_3.
- With T_4 (or f_3) and P_2 (or f_2) fixed, the system is analyzed with the exclusive intention of finding the trade-off between objectives f_1 and f_5. The designer selects an appropriate value for $\dot{m}$ (or f_5), which then establishes the relationship between objectives f_1, f_2, f_3 and f_5.
- Finally, objective f_4 is met by determining the smallest allowable value of A_{N}.

1.9. Organization

A design optimization problem consists of various successive tasks, as demonstrated in Figure 3. The organization of the dissertation is structured around this logic.

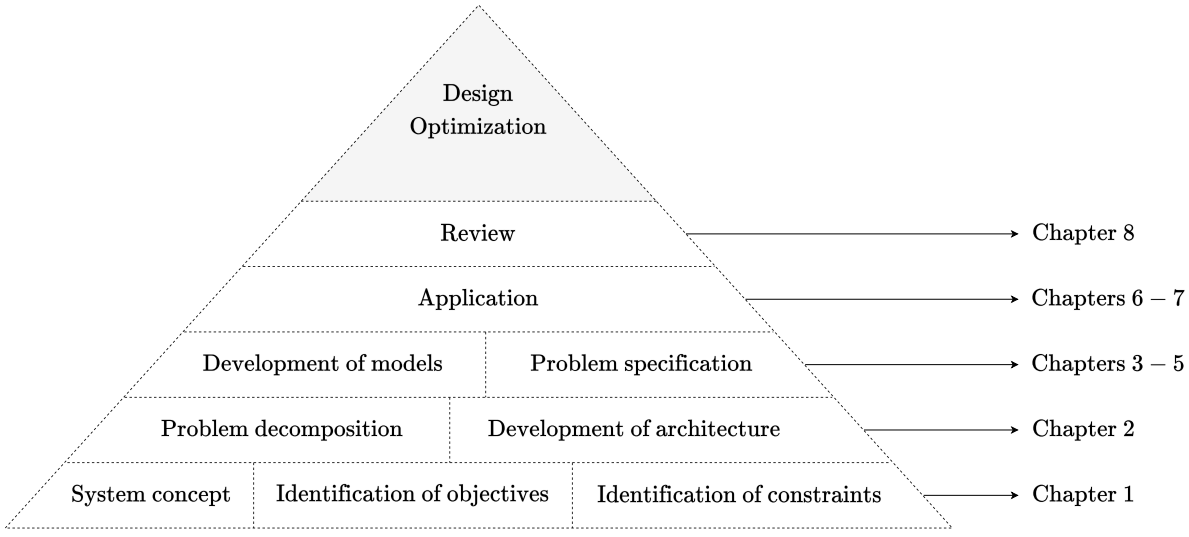

Figure 3: Topics in a design optimization problem and organization of the dissertation

In Chapter 1, the basic configuration of the system and its component technology types are introduced, the objectives of the design optimization are discussed, and the main constraint of the system (which is that it is to produce a net mechanical power output of 10 MW) is identified.

With the problem to be solved clearly defined, a way to solve the problem is considered next. It has been discussed how the complete system can be separated into its disciplines, but to apply this in practice requires a formal computational architecture with a rigorous mathematical foundation. This is the topic of Chapter 2 of the dissertation.

The design procedure introduced in this work requires models of the two disciplines of the system (the power system and the thermal system) as well as a separate surrogate model, which is a model of the Brayton cycle thermodynamics. These models are developed in Chapters 3, 4 and 5. The variables that are present in each model are also identified and categorized so that the problem can be fully specified in a mathematically rigorous way.

In Chapter 6, the actual application of the design procedure is presented. The full *ab initio* design of the system is demonstrated. This is a conventional design, with no unusual constraints placed on the system. In contrast, Chapter 7 demonstrates how the proposed design procedure could be adapted if there are special constraints placed on the system.

Finally, a review of the design optimization results and the procedure itself is presented in Chapter 8. Various insights are provided that could be meaningful beyond the boundaries of the current research objectives.

2. Computational Architecture

The computational architecture on which the design optimization procedure relies is presented in this chapter. The computational architecture is based on the principles, nomenclature and terminology of mathematical optimization (Snyman, 2004). These elements are discussed first, followed by a detailed discussion of the concept of the *design space*. The formulation of the surrogate problem is introduced and its relationship to the actual problem is explained next. Finally, the implementation of this architecture is described.

2.1. Elements of Mathematical Optimization

A design optimization problem can be mathematically formulated as:

$$\begin{array}{l}\text{Find } \mathbf{x} \text{ such that } f(\mathbf{c},\mathbf{x}) \text{ is minimized, subject to the constraints}\\ \check{\mathbf{x}} \leq \mathbf{x} \leq \hat{\mathbf{x}},\\ \mathbf{g} = g_i(\mathbf{c},\mathbf{x}) \leq 0, \quad \text{with } i = 1,2,\ldots,m, \text{ and}\\ \mathbf{h} = h_j(\mathbf{c},\mathbf{x}) = 0, \quad \text{with } j = 1,2,\ldots,r\ .\end{array} \tag{2}$$

This formulation has several elements, which are discussed in detail in the following sections. Essentially it has *variables*, which are represented by the vectors $\mathbf{c}$, $\mathbf{x}$, $\check{\mathbf{x}}$ and $\hat{\mathbf{x}}$, and *functions*, of which there is a single function f and any number of functions g and h. The variables represent some physical characteristic of the system and the functions represent some relationship between the variables of the system.

2.1.1. Constants

The *constants* of the problem,

$$\mathbf{c} = [c_1, c_2, \ldots]^{\mathrm{T}}\ , \tag{3}$$

have fixed numerical values from the outset of the design process. For the current system, this would be factors such as the ambient temperature, the ambient wind speed, the level of incident solar energy, etc. These factors are usually beyond the control of the designer.

A more appropriate term for these variables is *pseudo-constants* because their values can be different in different design scenarios (as opposed to a universal physical constant like the speed of light in a vacuum). No distinction is made regarding how such variables are managed though.

2.1.2. Design Variables

Design variables are unknown at the start of the design process, and the aim of the design process is to find a suitable set of values for all of the design variables.

A single design variable is denoted by x_i and the column vector of all design variables in the system is denoted by $\mathbf{x}$, such that

$$\mathbf{x} = [x_1, x_2, \ldots, x_n]^{\mathrm{T}} \in \mathbb{R}^n \ . \tag{4}$$

This is the so-called *design* of the system.

There are n design variables, so the design problem is said to be n-dimensional. The design variables are also all assumed to be real numbers.

Design variables for the current system include thermodynamic operating conditions, component geometry and component performance characteristics. All of the design variables are listed in the tables in Appendix A.

For a design optimization problem that only has a single discipline, there is no need to differentiate between different types of design variables. However, a multidisciplinary design optimization problem can benefit from making this distinction.

Given the sub-systems introduced in Figure 2, the design of the complete system can be represented as a multidisciplinary design problem of two disciplines. It is therefore useful to consider the design vector as consisting of three parts, such that

$$\begin{aligned} \mathbf{x} &= [\mathbf{x}_{\mathrm{s}}, \mathbf{x}_{\mathrm{p}}, \mathbf{x}_{\mathrm{t}}]^{\mathrm{T}} \\ &= [x_{\mathrm{s}1}, x_{\mathrm{s}2}, \ldots, x_{\mathrm{p}1}, x_{\mathrm{p}2}, \ldots, x_{\mathrm{t}1}, x_{\mathrm{t}2}, \ldots]^{\mathrm{T}} \ , \end{aligned} \tag{5}$$

where $\mathbf{x}_{\mathrm{s}}$ is the design variables that appear in both the power system discipline and in the thermal system discipline, $\mathbf{x}_{\mathrm{p}}$ is the design variables that appear only in the power system discipline, and $\mathbf{x}_{\mathrm{t}}$ is the design variables that appear only in the thermal system discipline.

The power system can therefore be independently designed by finding the vector

$$\mathbf{x}_{\mathrm{P}} = [\mathbf{x}_{\mathrm{s}}, \mathbf{x}_{\mathrm{p}}]^{\mathrm{T}} \tag{6}$$

and the thermal system can therefore be independently designed by finding the vector

$$\mathbf{x}_{\mathrm{T}} = [\mathbf{x}_{\mathrm{s}}, \mathbf{x}_{\mathrm{t}}]^{\mathrm{T}} \ . \tag{7}$$

2.1.3. Response Variables

The *response variables* of the problem are calculated (implicitly or explicitly) as a function of one or more of the constants or design variables, such that for each response variable,

$$y = y(\mathbf{c}, \mathbf{x}) \ . \tag{8}$$

There are many response variables in the problem; some are practically meaningful, such as the thermal efficiency of the system, whilst others are required purely as part of the solution process. An example of the latter is the heat transfer coefficient in a control volume of one of the heat exchanger flow channels. A selection of noteworthy response variables is provided in Table 31 in Appendix A.6.

2.1.4. Bound Constraints

Explicit control over the range of allowable values for the design variables is implemented through the *bound constraints* of the problem. The *lower bound* on a design variable is denoted by $\check{x}_i$ and the *upper bound* on a design variable is denoted by $\hat{x}_i$. Thus, for all of the design variables, the notation is

$$\begin{bmatrix} \check{x}_1 \\ \check{x}_2 \\ \vdots \\ \check{x}_n \end{bmatrix} \leq \begin{bmatrix} x_1 \\ x_2 \\ \vdots \\ x_n \end{bmatrix} \leq \begin{bmatrix} \hat{x}_1 \\ \hat{x}_2 \\ \vdots \\ \hat{x}_n \end{bmatrix} , \tag{9}$$

which can be written compactly in vector form as $\check{\mathbf{x}} \leq \mathbf{x} \leq \hat{\mathbf{x}}$.

In the special case where the lower and upper bounds on a design variable are equal, that design variable then becomes a constant, i.e.

$$\check{x} = \hat{x} \iff x = c \, . \tag{10}$$

It is best practice to assign lower and upper bounds to all design variables at the start of the design process. If this is not done, optimization algorithms will usually introduce artificial bounds (Schichl *et al.*, 2013). The range between the lower and upper bounds should not be so small that meaningful solutions are excluded, but should not be excessively large that solving the problem becomes inefficient.

The (default) lower and upper bounds for the design variables in this research are available in the tables in Appendix A.

2.1.5. Inequality Constraints

There are m so-called *inequality constraints* $g(\mathbf{c}, \mathbf{x})$ in (2). Each inequality constraint is a function of one or more constants or design variables (either explicitly, or implicitly through response variables); and the evaluation of this function should be a negative scalar value for a valid design of the system.

An example of an inequality constraint placed on the system is the local Mach number of the flow in the turbomachines, which should be less than one to prevent choking in the machine at its design point.

Although it is a theoretical possibility to have multidisciplinary inequality constraints, such constraints are not encountered in the current design problem and are thus not explicitly catered for. It is therefore assumed that all inequality constraints placed on the system are either placed only on the power system or only on the thermal system. As such, a power system inequality constraint is

$$g_{\mathrm{p}} = g_{\mathrm{p}}(\mathbf{c}, \mathbf{x}_{\mathrm{s}}, \mathbf{x}_{\mathrm{p}}) \tag{11}$$

and a thermal system inequality constraint is

$$g_{\mathrm{t}} = g_{\mathrm{t}}(\mathbf{c}, \mathbf{x}_{\mathrm{s}}, \mathbf{x}_{\mathrm{t}}) \ . \tag{12}$$

2.1.6. Equality Constraints

There are r so-called *equality constraints* $h(\mathbf{c}, \mathbf{x})$ in (2). Each equality constraint is a function of one or more constants or design variables (either explicitly, or implicitly through response variables); and the evaluation of this function should be equal to zero for a valid design of the system.

An example of an equality constraint placed on the system is its net mechanical power output.

As with the inequality constraints, it is assumed that all equality constraints placed on the system are either placed only on the power system or only on the thermal system.

As such, a power system equality constraint is

$$h_{\mathrm{p}} = h_{\mathrm{p}}(\mathbf{c}, \mathbf{x}_{\mathrm{s}}, \mathbf{x}_{\mathrm{p}}) \tag{13}$$

and a thermal system equality constraint is

$$h_{\mathrm{t}} = h_{\mathrm{t}}(\mathbf{c}, \mathbf{x}_{\mathrm{s}}, \mathbf{x}_{\mathrm{t}}) \ . \tag{14}$$

2.1.7. Objective Function

The difference between a design problem and a design *optimization* problem is the presence of the *objective function*, f. A design problem is solved by finding any design vector that satisfies the constraints, whereas a design optimization problem is solved by finding not only a design vector that satisfies the constraints, but one that also minimizes the scalar value of the objective function evaluation.

It is typical to express the objective function such that smaller values of f represent better performance as compared to larger values of f, and therefore the value of the objective function should be minimized.

2.2. Design Spaces

The set of all design variable values between the lower bounds and upper bounds is the so-called *design space*. There are different types of design spaces that are encountered throughout the design process; these are delineated in this section. The solution and interpretation of design spaces are aspects that are also discussed.

2.2.1. Types of Design Spaces

Initial Design Space

At the start of the design process, the lower and upper bounds are defined by the designer. This *initial* design space is

$$X = \{\mathbf{x} \mid \check{\mathbf{x}} \leq \mathbf{x} \leq \hat{\mathbf{x}}\}\,,\ X \subset \mathbb{R}^n\,. \tag{15}$$

Valid Design Space

The initial design space does not take into account the constraints placed on the system. As the system models are analyzed, some of the variables would likely only be valid within a smaller range of values than the initial range. This *solution-defined* or *valid* design space is therefore

$$X \supset X^\star = \{\mathbf{x}^\star \mid \check{\mathbf{x}}^\star \leq \mathbf{x}^\star \leq \hat{\mathbf{x}}^\star\}\ , \tag{16}$$

where $\mathbf{x}^\star$ is a design vector that satisfies all of the constraints of the problem, i.e. $\mathbf{g}$ and $\mathbf{h}$. In other words, $X^\star$ the set of all design vectors $\mathbf{x}$ that satisfy $\mathbf{g}$ and $\mathbf{h}$.

The solution-defined vector of lower bounds on the design variables is $\check{\mathbf{x}}^\star$, and the solution-defined vector of upper bounds on the design variables is $\hat{\mathbf{x}}^\star$.

The initial design space for a two-dimensional problem is depicted in Figure 4, and Figure 5 shows how the valid design space relates to it. Notice that the initial design space always has straight sides representative of the continuum of values between the lower and upper bounds, whereas the valid design space may have irregular sides as a result of the constraints placed on the system.

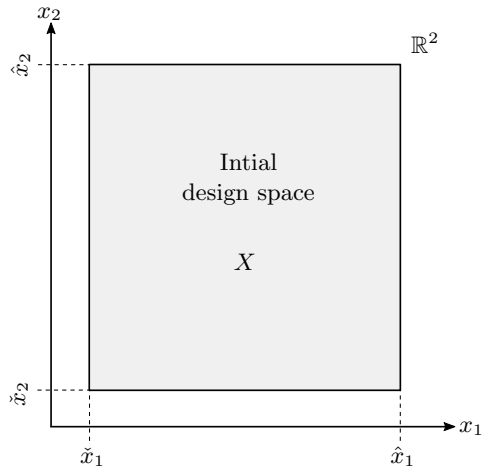

Figure 4: Initial design space of a two-dimensional problem

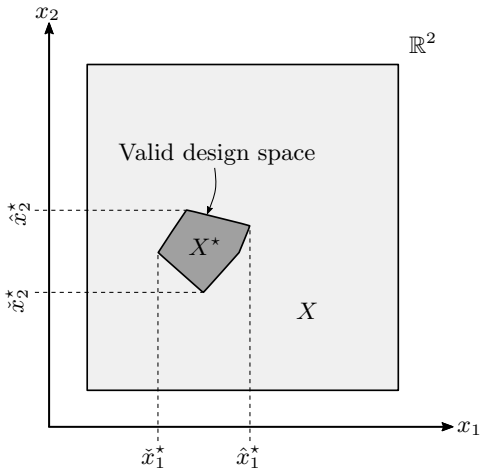

Figure 5: Valid design space of a two-dimensional problem

Discipline-valid Design Spaces

In a multidisciplinary design optimization problem, $X^\star$ represents the valid design space of the complete system. It is also possible to identify *discipline-valid* design spaces which are the valid design spaces of each of the disciplines separately. The current system has two disciplines; the valid power system design space is denoted by $P^\star$ and the valid thermal system design space is denoted by $T^\star$.

Analogous to Equation (16), the valid power system design space is defined as

$$X \supset P^\star = \{\mathbf{x}_\mathrm{P}^\star \mid \check{\mathbf{x}}_\mathrm{P}^\star \leq \mathbf{x}_\mathrm{P}^\star \leq \hat{\mathbf{x}}_\mathrm{P}^\star\} \ , \tag{17}$$

where $\mathbf{x}_\mathrm{P}^\star$ is a valid design vector for the power system, $\check{\mathbf{x}}_\mathrm{P}^\star$ is the solution-defined vector of lower bounds on the power system, and $\hat{\mathbf{x}}_\mathrm{P}^\star$ is the solution-defined vector of upper bounds on the power system.

Similarly, the valid thermal system design space is defined as

$$X \supset T^\star = \{\mathbf{x}_\mathrm{T}^\star \mid \check{\mathbf{x}}_\mathrm{T}^\star \leq \mathbf{x}_\mathrm{T}^\star \leq \hat{\mathbf{x}}_\mathrm{T}^\star\} \ , \tag{18}$$

where $\mathbf{x}_\mathrm{T}^\star$ is a valid design vector for the thermal system, $\check{\mathbf{x}}_\mathrm{T}^\star$ is the solution-defined vector of lower bounds on the thermal system, and $\hat{\mathbf{x}}_\mathrm{T}^\star$ is the solution-defined vector of upper bounds on the thermal system.

Figure 6 shows the valid power system design space and the valid thermal system design space, both as a subset of the initial design space. The two discipline-valid design spaces could – and indeed should – overlap with each other in some region, because this intersection of the two discipline-valid design spaces is the valid design space of the complete system,

$$X^\star = P^\star \cap T^\star \ . \tag{19}$$

This concept is clarified in Figure 7.

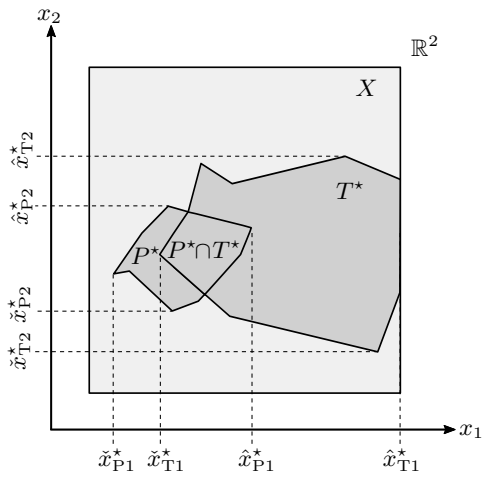

Figure 6: Valid sub-system design spaces

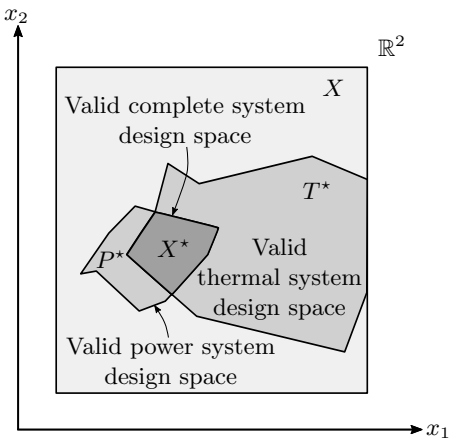

Figure 7: Valid system and sub-system design spaces

2.2.2. Design Space Discovery

The process of discovering the shape and size of a valid design space involves solving the model to find the set of all design vectors that satisfy the constraints. Four methods of discovering the design space are discussed below. Two of these methods (parametric variation and Monte Carlo simulation) are direct enumeration methods, which means that a given design vector is supplied as input to the model and the model is solved, with no check on optimality and not necessarily with a check on constraints either. The other two methods are optimization methods, and therefore explicitly check constraint satisfaction and attempt to optimize the objective function, before reporting a solution.

Parametric Variation

The simplest way to find the design space is to solve the model with a given list of discrete values for each unknown design variable. This is a satisfactory approach for a very small number of variables (two or three) but is unsuitable for larger numbers of variables. The computational cost to achieve a satisfactory prediction of the full design space is extremely high for higher dimensional problems, since it essentially requires the analysis of the model to be done using nested *for*-loops. Furthermore, the given values are discrete and therefore careful consideration of the intervals between successive values of each parameter is required.

Monte Carlo Simulation

A Monte Carlo simulation is the process of using a number of *random* input values to evaluate a model (O'Connor and Kleyner, 2012). It differs from parametric variation in that the inputs are randomly sampled from a given probability distribution (which is uniform unless some additional information about the actual distribution is available) as opposed to being explicitly specified. Monte Carlo simulations are not solved using nested *for*-loops; instead the design vectors for the simulations are compiled *a priori*. Since the sampling is random, multiple trials using the same number of samples will yield different results.

Gradient-based Algorithms

A gradient-based optimization algorithm uses first- (and occasionally also second-) derivatives of the objective and constraint functions in order to predict a direction in which the objective function can be minimized (Nocedal and Wright, 2006). The algorithm starts with a given initial design vector and attempts to minimize the value of the objective function whilst maintaining constraint satisfaction. Once the value of the objective function can no longer be reduced, the result is reported and is termed a *local minimum*. Gradient-based algorithms are therefore local optimization algorithms. Different initial design vectors may converge to different local minima, and therefore in order to have a good approximation of the global minimum, a large number of different initial design vectors need to be analyzed.

Non-gradient-based Algorithms

Many optimization approaches are available that do not exploit gradient information; some common ones are Genetic Algorithms, Simulated Annealing and Particle Swarm optimization (Papalambros and Wilde, 2017). The combination of Genetic Algorithms and Neural Networks (as a surrogate model) have been successfully used before to optimize CSP systems in particular (Richter *et al.*, 2011). Unfortunately, non-gradient-based algorithms are not effective if the system has a large number of design variables. Gradient-based optimization algorithms are the only effective method to use when the number of design variables is more than about 15 (Kler *et al.*, 2019). The current research considers a system with 23 design variables.

2.2.3. Design Space Evolution

In theory, the valid design space $X^\star$ defined by Equation (16) is a continuous volume in the n-dimensional real space. In reality however, the solution of the problem is numerical and therefore the design space is made up of valid design vectors which are discrete, i.e.

$$X^\star = [\mathbf{x}_1^\star, \mathbf{x}_2^\star, \dots] \ . \tag{20}$$

An approximation to the valid design space is a *pseudo* design space,

$$\tilde{X}^\star \approx [\mathbf{x}_1^\star, \mathbf{x}_2^\star, \dots, \mathbf{x}_N^\star] \ , \tag{21}$$

where

$$\tilde{X}^\star \to X^\star \quad \text{if} \quad N \to \infty \ . \tag{22}$$

For all intents and purposes, this is equivalent to

$$\tilde{X}^\star \to X^\star \quad \text{if} \quad N \gg 0 \ , \tag{23}$$

which is a necessary assumption to make in order to solve the optimization problem using numerical methods. What this means is that a pseudo design space, as defined by a discrete collection of several valid design vectors, approaches the continuous true design space, provided that the number of valid design vectors in the pseudo design space is large.

As a demonstration of this, consider the evolution of a pseudo design space for an arbitrary optimization problem of two variables, as presented in Figures 8 through 11. Each valid solution of the problem appears as a discrete point at the co-ordinates (z_1, z_2) in this two-dimensional example.

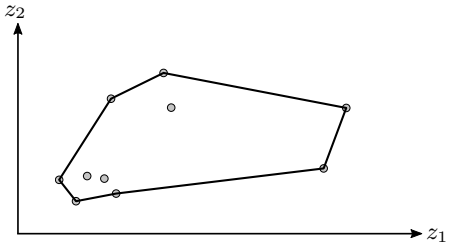

Figure 8: Pseudo design space with $N = 10$ valid designs

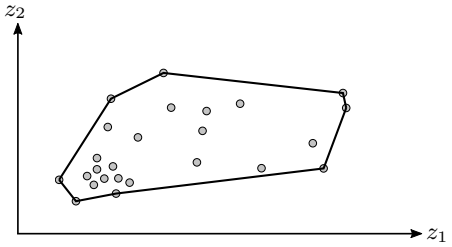

Figure 9: Pseudo design space with $N = 25$ valid designs

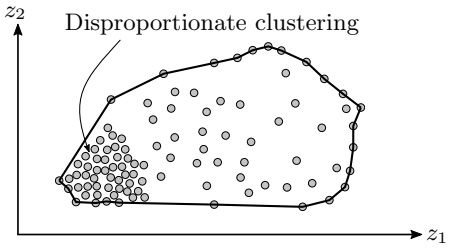

Figure 10: Pseudo design space with $N = 100$ valid designs

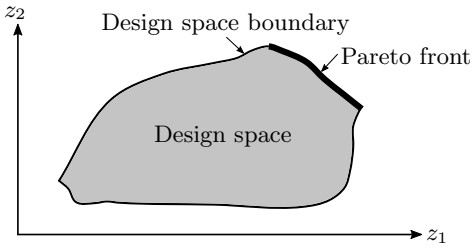

Figure 11: Approximation of the true design space with a large number of valid designs

The boundaries of the design space are found by connecting the outer points together. Although there are formal mathematical approaches to do this (Hu *et al.*, 2013), it can also be effectively accomplished by inspection in which the outer points are manually connected with line segments using graphics-editing software such as Inkscape (2020). This is the approach followed in the current research.

Regardless of which method is used to determine the boundaries of the design space, the approximation is necessarily inaccurate with a small number of valid designs. As Figure 8 demonstrates, after ten valid designs have been found, the design space is not well-defined. The line segments between the boundary points are long, which is indicative of considerable uncertainty regarding the boundaries because of the sparseness of the data. As more valid designs are found, the design space and its boundaries become more resolved, and the line segments between boundary points become shorter. This can be seen in Figures 9 and 10 with 25 and 100 valid designs, respectively.

Finally, after a large number of valid designs have been found, the data points would be so densely packed that together they approximate a continuous surface, as demonstrated by the shaded area in Figure 11.

2.2.4. Pareto Optimality

It is unlikely that a single optimal design of a system exists, for the reason that most design optimization problems in practice are *multi-objective* optimization problems with more than one possible definition of what the *optimal* design entails.

A solution to making a multi-objective optimization problem a single-objective optimization problem is to assign a relative weighting factor to each objective and to optimize then for the summation of the various weighted objectives as indicated in Equation (1), or alternatively to use the game theory approach (Rao, 1987).

A simpler alternative is to present the full design space as *the* solution to the optimization problem (Wang *et al.*, 2014b). From this, the designer can conveniently determine the global optimum or see the trade-offs between the different objectives so that a satisfactory design choice can be made.

A *Pareto-optimal* design is one for which the optimality with regards to one objective cannot be improved unless the optimality with regards to another objective is reduced. The *Pareto-optimal set* or *Pareto front* is all the valid designs which meet this criterion (Rao, 1987). For example, if the optimization objectives are to maximize z_1 and to maximize z_2, the Pareto front would be as indicated in Figure 11. All the designs on the Pareto front are considered to be equally optimal.

A typical Pareto front example is for the dual-objective optimization problem of minimizing the cost of electricity and maximizing the thermal efficiency of a thermal power system. In this case the Pareto front turns out to be a smooth curve with the cost being the highest at the lowest efficiency, then reducing to some minimum cost at some intermediate efficiency, and finally the cost increases again at higher efficiencies (Wang *et al.*, 2014b). It remains a subjective matter to decide which design is best on a Pareto front, but various equivalently optimal designs can be identified which are superior over many other designs.

2.2.5. Design Space Extension

Design spaces are at least n-dimensional (because there are n design variables in the system) but they can easily be extended to include the values of response variables or the value of the objective function that corresponds to the valid design vectors. Whereas a standard design space is the collection of valid design vectors as defined in Equation (20), an *extended design space* is defined as

$$Z = [\mathbf{z}_1, \mathbf{z}_2, \dots] \ , \tag{24}$$

with an *extended design vector* defined as

$$\mathbf{z} = [z_1, z_2, \dots]^{\mathrm{T}} \ . \tag{25}$$

Each scalar z_i in an extended design vector can be the value of:

- a design variable, in which case $z_i = x_j$,
- a response variable (corresponding to the design vector), in which case $z_i = y(\mathbf{c}, \mathbf{x})$, or
- the objective function (corresponding to the design vector), in which case $z_i = f(\mathbf{c}, \mathbf{x})$.

The introduction of the concept of the extended design space allows plots like Figure 11 to be presented in a consistent manner, regardless of whether variables or objective function values are plotted on the axes. This allows trade-offs between one variable and another variable, and between one variable and an objective function, to be investigated in exactly the same way as in a Pareto trade-off which is traditionally only between one objective function and another objective function. For the remainder of the dissertation, the term *design space* should be taken to refer to what is actually a *pseudo-* and an *extended* design space.

2.2.6. Search Termination

When to terminate the search for new valid design vectors (after how many valid design vectors N have been found) is an important consideration. Three possible termination criteria (i.e. when to stop searching for more valid design vectors) are as follows.

Classical Convergence

A technique used to check the convergence of a solution in computational fluid dynamics (CFD) simulations – which is based on a grid of nodes – is to use successively more refined grids, solve the model and compare the calculated result of some metric with the same result achieved using the previous, less-refined grid (Versteeg and Malalasekera, 2007). The solution is then considered to be independent of the grid resolution once successively refined grids yield results that differ by less than a pre-defined margin.

The same technique can, in principle, be extended to optimization problems. In this case a natural metric to use is the objective function value, and the number of valid design vectors to be sought before terminating the solution is the analogy to the CFD grid.

Statistical Criterion

Bolton *et al.* (2004) proposed a termination criterion that is based on Bayesian statistics. A confidence level can be specified, and new design vectors are continuously analyzed until the confidence level is reached.

The validity of this criterion is based on the assumption that the probability of convergence to the global minimum is at least as large as the convergence to any local minimum. It is a valid assumption in some problems, for example in structural engineering, but not for the problem of designing a thermal power system.

This can be confirmed through the inspection of the design space: the results in this research tend to appear as demonstrated in Figure 10. Although merely a simplistic example, it is clear that there is disproportionate clustering of the results. This can be observed in the current problem regardless of how many independent trials are performed.

For initial design vectors sampled from a uniform distribution, clustering in the same region across multiple trials is not expected. If the probability of converging to local minima were equal, then the results would be randomly spread out across the entire design space. This is not the case for the current problem and therefore this termination criterion is not suitable.

Visual Inspection

Of the available design space discovery methods discussed in Section 2.2.2, all of them can be configured to have multiple, independent trials. For example, a trial with a given set of (initial) design vectors is independent from the same trial performed with a different set of (initial) design vectors.

After the completion of each trial, the design space can be re-plotted as in Figures 8 to 10. With each successive trial, the design space is therefore increasingly resolved. The designer can then decide if another trial should be performed in order to find more valid design vectors to add to the known design space, thereby resolving it further, or if the design space is sufficiently well resolved to be meaningful.

Although it is fundamentally a subjective criterion, the significance of this fact is entirely academic. Once the design space takes on a clearly-defined shape as in Figure 11, any additional resolution would be superfluous.

Unfortunately, given the nature of the problem at hand, and the disproportionate clustering of the solutions in some regions of the design space, a large number of trials have to be completed to resolve the full design space to look like Figure 11. Even just resolving the Pareto front is computationally expensive because, the vast majority of initial design vectors end up converging to solutions that lie elsewhere. Consider as an example the location of the Pareto front (the top right hand side of the design space) in Figure 11 compared to the location where most initial design vectors converge to (the bottom left hand corner of the design space).

2.3. Surrogate Problem

The elements of mathematical optimization can be re-formulated to apply to a surrogate problem as well. The surrogate problem can be mathematically formulated as:

$$\begin{aligned}
&\text{Find } \underset{\sim}{\mathbf{x}} \text{ such that } \underset{\sim}{f}(\underset{\sim}{\mathbf{c}}, \underset{\sim}{\mathbf{x}}) \text{ is minimized, subject to the constraints} \\
&\check{\underset{\sim}{\mathbf{x}}} \leq \underset{\sim}{\mathbf{x}} \leq \hat{\underset{\sim}{\mathbf{x}}}, \\
&\underset{\sim}{\mathbf{g}} = \underset{\sim}{g}_i(\underset{\sim}{\mathbf{c}}, \underset{\sim}{\mathbf{x}}) \leq 0, \quad \text{with } i = 1, 2, \ldots, m, \text{ and} \\
&\underset{\sim}{\mathbf{h}} = \underset{\sim}{h}_j(\underset{\sim}{\mathbf{c}}, \underset{\sim}{\mathbf{x}}) = 0, \quad \text{with } j = 1, 2, \ldots, r \, .
\end{aligned} \tag{26}$$

Even though it has a similar structure, the surrogate problem is a different problem from the actual problem as presented in (2). To differentiate the symbols used in the surrogate problem from the symbols used in the actual problem, all the symbols that are related to the surrogate problem are supplemented with a tilde ($\sim$) underneath.

The design variables of the surrogate problem are

$$\underset{\sim}{\mathbf{x}} = [\underset{\sim}{x}_1, \underset{\sim}{x}_2, \ldots, \underset{\sim}{x}_{\underset{\sim}{n}}]^{\mathrm{T}} \in \mathbb{R}^{\underset{\sim}{n}} \, . \tag{27}$$

Again, the aim is to find valid design vectors $\underset{\sim}{\mathbf{x}}^{\star}$, and especially the valid design vector that minimizes the objective function $\underset{\sim}{f}$.

Surrogate Problem vs Actual Problem: Differences

The sole reason for introducing a surrogate problem is because the actual problem is too computationally expensive to solve. There are two reasons why the surrogate model is faster to solve than the actual problem. Firstly, the surrogate problem has fewer design variables, such that $\underset{\sim}{n} < n$. The dimensionality of the surrogate problem is therefore less than the dimensionality of the actual problem.

Secondly, the function evaluations of the surrogate problem are less complicated and therefore take less time to evaluate. In other words, it is faster to evaluate $\underset{\sim}{f}$, $\underset{\sim}{\mathbf{g}}$ and $\underset{\sim}{\mathbf{h}}$ as compared to f, $\mathbf{g}$ and $\mathbf{h}$.

The surrogate problem is also a problem of only a single discipline, whereas the actual problem is multidisciplinary.

Surrogate Problem vs Actual Problem: Similarities

As two independent problems, the real problem is solved when valid values for the design variables in $\mathbf{x}$ are found based on the analyses of the detailed multidisciplinary models, and the surrogate problem is solved when valid values for the design variables in $\underset{\sim}{\mathbf{x}}$ are found based on the analysis of the surrogate model. For the actual problem to be *replaced* (in part) by the surrogate problem, requires some qualifications in that the surrogate problem has to resemble the actual problem in two key ways.

Firstly, even though the surrogate problem can contain unique design variables that are not the same as the design variables in the actual problem and vice versa, some of the design variables in the surrogate problem must be the same as in the actual problem. This allows the value of a design variable in the actual problem to be fixed once its value in the surrogate problem is fixed. These variables can be termed *key* design variables and are denoted by an underlined symbol. For a key design variable,

$$\underline{x} = x = \underset{\sim}{x} \, . \tag{28}$$

The key design variables for the current research are those which are underlined in the tables in Appendix A.

Secondly, with regards to these key design variables, the objective function of the surrogate problem must behave similarly to the objective function of the actual problem across all values of the key design variables. In other words,

$$\underset{\sim}{f}(\underline{\mathbf{x}}) \sim f(\underline{\mathbf{x}}) \; \forall \; \underline{\mathbf{x}} \, . \tag{29}$$

2.4. Implementation in MATLAB®

The design spaces of the thermodynamic model (developed in Chapter 3) and the power system model (developed in Chapter 4) are found using the scientific computing package MATLAB® (MathWorks, 2019). Before the models can be analyzed, the following need to be prepared:

- A table of the lower bounds $\check{\mathbf{x}}$ and upper bounds $\hat{\mathbf{x}}$ for all the design variables. A convenient way to manage this is to create the table in a spreadsheet format, with the variable names, values of the lower bounds and values of the upper bounds stored in successive columns of the spreadsheet. The variables and default values of the bounds are presented in the tables in Appendix A.
- A function which accepts a given vector of design variables $\mathbf{x}$, and returns the scalar value of the objective function f when evaluated at $\mathbf{x}$.
- A function which accepts a given vector of design variables $\mathbf{x}$, and returns two other vectors. The first vector to be returned is $\mathbf{g}$, which is the evaluation of all the inequality constraints placed on the model. The second vector to be returned is $\mathbf{h}$, which is the evaluation of all the equality constraints placed on the model.

  Most of the constraints in the models are functions of response variables rather than purely design variables or constants. Therefore, a series of logical calculations must first take place to calculate the response variables from the design variables and constants, before $\mathbf{g}$ and $\mathbf{h}$ can be returned.

  The logical calculations, inequality constraints and equality constraints are presented in the tables in Appendix B for the thermodynamic model and in Appendix C for the power system model.

Once the pre-requisite table of bounds and the functions have been created, the following procedure is used to analyze the models:

1. The spreadsheet containing the values of the lower bounds and the upper bounds is read into MATLAB® at the start of the analysis. The values of the bounds are assigned to $\check{\mathbf{x}}$ and $\hat{\mathbf{x}}$, which then become enumerated column vectors in MATLAB®.
2. The MATLAB® optimization options are specified. Key options to be specified are which gradient-based optimization algorithm to use, the constraint tolerance level, the maximum numbers of iterations or function evaluations, and how the gradients of the objectives and constraints should be calculated.

   There is no definitive guide as to which options are best and, as with all design optimization problems in general, it is up to the designer to find which combination of options works best for the particular problem and software. It is advised that the user be familiar with the appropriate MATLAB® documentation to understand the various concepts and how they are applied.

From experience with the current problem, the *Sequential Quadratic Programming* (SQP) algorithm with a maximum of 2 000 function evaluations can be recommended. This allows most of the initial starting vectors to converge to local minima whilst still terminating reasonably quickly in the case of potentially infeasible designs.

A constraint tolerance level of 0.001 is used in this research. However, since the constraint tolerance is a *relative* tolerance level (MathWorks, 2019), a significantly finer tolerance level such as 1×10^{-9} should be specified, in order to ensure that the *absolute* tolerance level of 0.001 has a high likelihood of being achieved. The absolute tolerance level is checked by manually evaluating the constraints function with each design vector reported as valid by the optimization algorithm. Design vectors that do not meet the absolute tolerance level are discarded.

Although MATLAB® supports the option to supply manually-computed gradients to the optimization algorithm, it can also automatically evaluate the gradients using finite differences. Manually-computed gradients are generally preferred for the sake of robustness and computational speed. However, for the current problem, the automated finite-differences approach is robust and only marginally slower than using manually-computed gradients. It is therefore an acceptable approach.

3. A number of random design vectors are generated in MATLAB®, with values for each of the design variables that are between the lower and upper bounds. It does not matter how many design vectors are specified to be generated at a time because many independent runs will be performed; a few hundred initial design vectors per run is reasonable.

   Different sampling techniques such as *Stratified* sampling or *Latin Hypercube* sampling (McKay *et al.*, 1979) can be used as opposed to purely random sampling. However, random sampling is the easiest to implement because MATLAB® has this capability as a built-in function (*RandomStartPointSet*). Furthermore, the computational time required to find the full design space is low enough that a more advanced sampling method will not yield a significant benefit.

4. The MATLAB® built-in function *fmincon* accepts the pre-defined functions which were created. It takes each of the generated random design vectors and automatically adjusts the values of the design variables such that f is minimized, whilst attempting to ensure that $\mathbf{g}$ and $\mathbf{h}$ are satisfied to within the given tolerance level.

   In this research, there is not an explicit objective function for any of the analyses, because the aim is to find the *full* design space from which the Pareto front is then inferred. The objective function is therefore set to return an arbitrary constant value, which means that the optimization algorithm operates as a numerical solver but with explicit checks on the constraints.

5. If valid design vectors have been found from the initial random starting points, they can be saved and plotted as shown in Figures 8 through 11 to reveal the design space.

6. Steps 3 through 5 are repeated until the designer ends the analysis based on an appropriate stopping criterion, as discussed in Section 2.2.6. The *visual inspection* stopping criteria is used in this research.

3. Thermodynamic Model

A thermodynamic model of the Brayton cycle is used as a surrogate model during the design of the system. The surrogate model is a representation of the actual system model (as comprised of the detailed multidisciplinary sub-system models) that is simpler and faster to analyze. This chapter discusses the motivation, development and validation of the thermodynamic model.

3.1. Purpose of the Thermodynamic Model

The thermodynamic model should provide a computationally inexpensive way to:

- estimate the thermal efficiency of the Brayton cycle,
- evaluate trade-offs between variables,
- study effects such as component inefficiencies and pressure drop on the performance of the cycle.

This will allow the thermodynamic model to be used to decide on values for some of the key design variables, so that these variables can be treated as constants when the more computationally expensive detailed turbomachinery and heat exchanger models are analyzed.

Some of the differences between the thermodynamic model and the detailed sub-system models are that the thermodynamic model does not take into account the geometry (size and shape) of the components, nor does it take into account component technology types, nor does it attempt to capture any physics beyond the basic thermodynamic processes.

The thermodynamic model of this research is based on fundamental thermodynamic concepts (Borgnakke and Sonntag, 2014), but it differs from other Brayton cycle optimization studies (Haseli, 2013; Meas and Bello-Ochende, 2017) in that real thermodynamic properties for sCO_2 are used. The optimization in the current research is also performed using a single optimization algorithm (as discussed in Section 2.4) rather than with the multi-layered iterative optimization approach proposed by Battisti *et al.* (2016).

3.2. Cycle Thermodynamics

The thermodynamic processes of the closed-loop Brayton cycle are presented on a temperature-entropy (Ts) diagram in Figure 12. Lines of constant pressure (isobars) are added. The numbers in this diagram correspond to the stations identified in Figure 1.

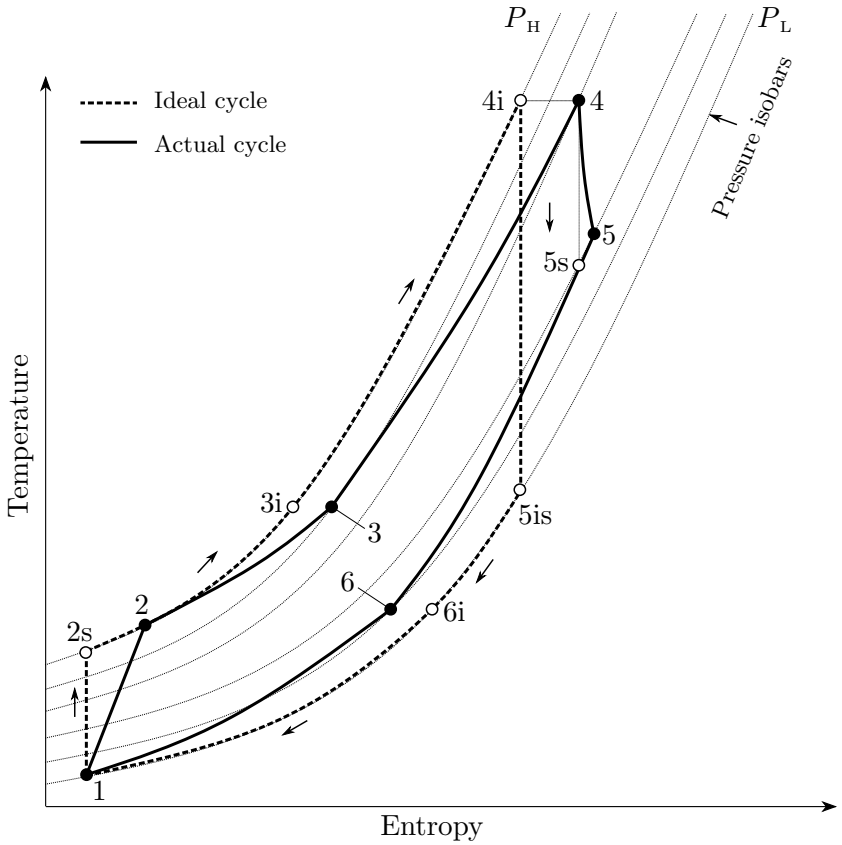

Figure 12: Diagram of actual and ideal cycle thermodynamics

Ideal Simple Cycle Thermodynamics

With reference to Figure 12, the ideal simple (without recuperation) cycle consists of four processes: compression between states 1 and 2s, heat addition between state 2s and 4i, expansion between state 4i and state 5is, and heat rejection between states 5is and 1. The basic ideal cycle therefore follows the dotted lines in the loop 1-2s-4i-5is-1. In the ideal cycle, the heat addition process occurs at a constant high pressure P_H, the heat rejection process occurs at a constant low pressure P_L, and the compression and expansion processes occur at constant entropy.

Ideal Recuperated Cycle Thermodynamics

In the ideal recuperated cycle, the heat addition process occurs between states 3i and 4i, and the heat rejection process occurs between states 6i and 1. Recuperative heat transfer occurs between states 5is and 6i for the heat rejection side, and between states 2s and 3i for the heat addition side. The ideal recuperated cycle therefore follows the dotted lines in the loop 1-2s-3i-4i-5is-6i-1 in Figure 12.

Actual Recuperated Cycle Thermodynamics

In contrast to the ideal cycle, in the actual implementation of the recuperated cycle the heat addition and rejection processes do not occur at constant pressure because there is a frictional pressure drop in the heat exchangers in the direction of fluid flow. Furthermore, the compression and expansion processes are not isentropic because of irreversible energy transfer in the turbomachines. The solid lines in Figure 12 demonstrate how the thermodynamics of the cycle are affected by these changes:

- Starting at state 1, the actual compression process ends at state 2, which is at a higher temperature and entropy than state 2s.
- Pressure drop on the heat addition side of the recuperator results in the outlet being at state 3, which is at a lower pressure but higher entropy than state 3i.
- Pressure drop in the solar receiver results in the outlet being at state 4, which is at a lower pressure and higher entropy than state 4i.
- The actual expansion process ends at state 5, which is at a higher temperature and higher entropy than both state 5is and state 5s.
- The outlet of the recuperator is at state 6, which is at a lower pressure than state 5 and a higher pressure than state 6i.
- At state 1, the pressure is lower than at state 6 because of pressure drop in the heat sink.

In the actual cycle, the highest pressure P_{H} occurs at the outlet of the compressor at state 2, and the pressures at states 3 and 4 are both lower than P_{H}. Similarly, the lowest pressure in the cycle P_{L} occurs at the inlet of the compressor at state 1, and the pressure at states 5 and 6 are both higher than P_{L}. The order of pressures in the actual cycle sorted from lowest to highest is therefore

$$P_1 \leq P_6 \leq P_5 \leq P_4 \leq P_3 \leq P_2 \, . \tag{30}$$

Concomitantly, in the actual cycle the compression pressure ratio (P_2/P_1) is higher than the expansion pressure ratio (P_4/P_5). In the ideal cycle, these two pressure ratios are the same.

As depicted in Figure 12, the order of temperatures in the cycle sorted from lowest to highest is

$$T_1 \leq T_2 \leq T_6 \leq T_3 \leq T_5 \leq T_4 \, . \tag{31}$$

3.3. Simplifying Assumptions

Adiabatic Turbomachinery

The compression and expansion processes are assumed to be adiabatic – or that no heat transfer occurs to or from the fluid and the environment.

This is a reasonable assumption to make, in general, because the turbomachines are physically small components (compared to the heat exchangers) and the flow velocity through the turbomachines is typically high. Both of these factors result in that, per unit of mass flow through the machines, there is little surface area and little time for heat transfer to take place.

Compared to the shaft work component, heat transfer in the turbomachines is thus assumed to be negligible.

Negligible Gravitational Potential Energy Difference

The difference of gravitational potential energy between the stations is considered as negligible, because it is assumed that the system flow path is at the same level of elevation. Gravitational potential energy is therefore just an arbitrary numerical value that would be constant at all points in the system.

Negligible Kinetic Energy Difference

The kinetic energy of the flow (which is related to the flow velocity) at the stations of interest is assumed to be of a similar magnitude, and therefore the difference of kinetic energy between the stations can be considered as negligible.

This assumption means that it is not necessary to distinguish between stagnation and static thermodynamic properties in the thermodynamic model. Note that this assumption is not applied in the detailed model of the power system which is developed in Chapter 4.

Insulated Recuperator

The recuperator is assumed to be perfectly insulated to the environment; the only heat transfer that occurs is from the hot stream to the cold stream.

This is a reasonable assumption to make given that there is a significant temperature gradient between the hot and cold streams, and good insulating material is widely available and easy to install on the outside of a recuperator housing.

3.4. Theoretical Analysis

Three aspects of the cycle are considered in its theoretical analysis: the transfer of energy between the cycle and its external environment, the efficiency of the turbomachinery, and the details of the recuperation process.

External Energy Transfers

As described by the following equations, the transfer of energy in the thermodynamic cycle, either as heat q or as mechanical work w, is evaluated as the difference in enthalpy between the start and end states of the process:

Compression process:	$w_{\mathrm{C}} = h_2 - h_1$	(32)
Isentropic compression process:	$w_{\mathrm{C,s}} = h_{2\mathrm{s}} - h_1$	(33)
Expansion process:	$w_{\mathrm{T}} = h_4 - h_5$	(34)
Isentropic expansion process:	$w_{\mathrm{T,s}} = h_4 - h_{5\mathrm{s}}$	(35)
Heat addition process:	$q_{\mathrm{S}} = h_4 - h_3$	(36)
Heat rejection process:	$q_{\mathrm{H}} = h_6 - h_1$	(37)

Isentropic Efficiency of the Turbomachinery

The ratio between the work required for the isentropic compression process and actual compression process,

$$\eta_{\mathrm{C}} = \frac{w_{\mathrm{C,s}}}{w_{\mathrm{C}}} \ , \tag{38}$$

is termed the *isentropic efficiency* of the compressor. Similarly, the ratio between the actual work output and the isentropic work output from the isentropic expansion process,

$$\eta_{\mathrm{T}} = \frac{w_{\mathrm{T}}}{w_{\mathrm{T,s}}} \ , \tag{39}$$

is termed the *isentropic efficiency* of the turbine.

Analysis of the Recuperation Process

The temperature change on the heat rejection side of the recuperator is

$$\Delta T_{\mathrm{hot}} = T_5 - T_6 \ , \tag{40}$$

and the temperature change on the heat addition side of the recuperator is

$$\Delta T_{\mathrm{cold}} = T_3 - T_2 \ . \tag{41}$$

The heat rejection side can supply heat only until the temperature at state 6 equals the temperature at state 2, or

$$T_{\mathrm{hot,limit}} = T_6 = T_2 \ . \tag{42}$$

Similarly, the heat addition side can accept heat only until the temperature at state 3 equals the temperature at state 5, or

$$T_{\text{cold,limit}} = T_3 = T_5 \ . \tag{43}$$

It is therefore not possible for any side of the recuperator to have a temperature change that is greater than the temperature difference between states 2 and 5, or

$$\Delta T_{\max} = T_5 - T_2 \ . \tag{44}$$

In an insulated recuperator, the energy that is transferred (as evaluated by the enthalpy difference) from the heat rejection side between states 5 and 6 is the same as the energy that is transferred to the heat addition side between states 2 and 3, or

$$q_{\text{R}} = h_5 - h_6 = h_3 - h_2 \ . \tag{45}$$

The *effectiveness* of a heat exchanger is a measure of its performance. The effectiveness can be defined in two ways: as the ratio of the actual heat transfer to the maximum possible heat transfer (Çengel and Ghajar, 2015) or as the ratio of the actual temperature change to the maximum possible temperature change on one side of the recuperator (Uusitalo *et al.*, 2019). Choosing the heat rejection side as the reference side,

$$\epsilon = \frac{\Delta T_{\text{hot}}}{\Delta T_{\max}} = \frac{T_5 - T_6}{T_5 - T_2} \ . \tag{46}$$

If the heat addition side is used as the reference side instead, a different value for effectiveness would result. This is because the average specific heat capacity of the fluid is not necessarily the same on both sides of the recuperator.

However, it is inconsequential as to which side of the recuperator is selected as the reference side, because the actual performance of the recuperator does not change. Regardless of the definition of effectiveness, higher values of effectiveness represent greater temperature changes for both sides and therefore better recuperator performance. Furthermore, because the maximum temperature difference on both sides is the same, recuperator effectiveness is always between zero and 100% regardless of which definition is used.

3.5. Performance of the Cycle

The performance of the cycle is related to the principle of the *conservation of energy*, and it can be measured by two basic metrics: its *net power output* and its *thermal efficiency*.

Conservation of Energy

Fundamentally, the energy E that the cycle accepts as input from its environment must equal the energy that the cycle produces as output to its environment, or

$$E_{\text{in}} = E_{\text{out}} \implies q_{\text{S}} + w_{\text{C}} = q_{\text{H}} + w_{\text{T}} \ . \tag{47}$$

A thermodynamic cycle is a thermal-mechanical energy-conversion device. This means that the *ratio* between thermal and mechanical energy on the input and output sides are intended to be different, even though the sum of each side must remain the same.

Net Power Output

The basic thermodynamic energy transfers of the cycle are expressed in specific (per unit mass) terms. A specific heat transfer process can be converted into a heat rate by multiplying by the cycle mass flow rate as

$$\dot{Q} = \dot{m}\, q \ , \tag{48}$$

and a specific work transfer process can be converted into a work rate (or *power*) by multiplying by the cycle mass flow rate as

$$\dot{W} = \dot{m}\, w \ . \tag{49}$$

The net mechanical power output of the system,

$$\dot{W}_{\text{net}} = \dot{W}_{\text{T}} - \dot{W}_{\text{C}} \ , \tag{50}$$

is evaluated as the difference between the power developed by the turbine and the power required by the compressor.

Such is the significance of the net power output rating to the scale of the system and the feasible technology options, that deciding how much power to produce should probably be one of the first decisions to make in the design of any thermal power system. Nevertheless, the mass flow rate is the only thermodynamic variable that is affected by different power ratings.

Thermal Efficiency

A measure of how efficiently a thermal power system produces this net power is the *thermal efficiency*. It is the fraction of the thermal energy input that is converted into a net mechanical work output, or

$$\eta_{\text{th}} = \frac{w_{\text{net}}}{q_{\text{S}}} = \frac{\dot{W}_{\text{net}}}{\dot{Q}_{\text{S}}} \ . \tag{51}$$

3.6. Representation of Thermodynamic Properties

Real thermodynamic properties are used in the thermodynamic model and in the detailed turbomachinery and heat exchanger models. The thermodynamic properties vary greatly near the critical point of the fluid, which means that assumptions such as incompressibility, ideal gas behavior or constant specific heat capacity are unsuitable. These variations in the thermodynamic properties must be exploited for the sCO_2 cycle to be efficient, but it requires the use of a more complicated thermodynamic property model (Musgrove *et al.*, 2017a).

In order to characterize the thermodynamic state of a fluid, only two thermodynamic properties of the fluid need to be known (White, 2011). All other thermodynamic properties can then be determined as a function of these two properties. Any pair of thermodynamic properties can be used, but temperature and pressure are the two most familiar quantities and they have a practical, identifiable meaning.

There are three common methods of calculating the other thermodynamic properties from a given pair:

- through an equation-of-state,
- through the interpolation of tables of stored thermodynamic data, or
- through a function with coefficients determined from a statistical regression analysis of the tabulated data.

These three methods are listed in the order of (generally) most accurate to least accurate, and from the slowest to evaluate to the fastest to evaluate.

The most accurate and widely used equation-of-state for carbon dioxide was developed by Span and Wagner (1996). This equation-of-state is also the reference equation-of-state that is used to evaluate the thermodynamic properties for carbon dioxide in the NIST database (NIST, 2020). The data in this database is available free of charge and can be downloaded as a series of tables. This is the data set for the thermodynamic properties of carbon dioxide used in both the thermodynamic model and the power system model of this research.

The tables can be in multiple formats, but a sensible format is the isobaric format (i.e. each table has data at the same pressure) and the data is arranged from a minimum temperature to a maximum temperature at a constant spacing.

For the current models, tables with data at the critical pressure of 7.38 MPa, and for each pressure value from 7.50 MPa to 30.0 MPa in steps of 500 kPa are used. In each table, the minimum temperature is 305 K (or 32 °C, which is one degree above the critical temperature of carbon dioxide) and the maximum temperature is 975 K (which is just above 700 °C). The temperature spacing is 5 K.

A function to interpolate the thermodynamic tables has been created in MATLAB® (MathWorks, 2019). It keeps the data tables in computer memory so that subsequent evaluations of thermodynamic property data can be expedited. The interpolation scheme between the data points is linear.

For the current application, the evaluation of the thermodynamic properties to within 5 K and 500 kPa is a reasonable trade-off between accuracy and computational expense. If greater accuracy is desired, the resolution of the tables can be increased but a corresponding increase in computation time should then be expected.

3.7. Validation of the Model

Validation of the developed thermodynamic model is performed by comparing the cycle efficiency at a given operating point, with the cycle efficiency of three models from literature at that same operating point. The cycle efficiency is the most comprehensive measure of the accuracy of the model because it is a function of all the underlying physics. Details of this validation study are available in Appendix E.1. The results show that the developed model matches the models from literature well.

4. Power System Model

This chapter on the development of the power system model begins with a discussion on some of the different approaches that can be used to model turbomachines. The physical geometry of the turbomachines and their basic principles of operation are then introduced, followed by the fundamental theory of the chosen modeling approach. Finally, the turbomachinery models are verified and validated.

4.1. A Review of Different Modeling Approaches

The relationships between the geometry, thermodynamics, fluid dynamics and performance parameters of a turbomachine are complicated, especially if the working fluid is sCO_2. Traditional modeling assumptions such as incompressibility and ideal gas behavior are generally unacceptable (Bennett *et al.*, 2017), and therefore careful consideration is required before selecting a modeling approach for sCO_2 turbomachinery. Four common turbomachinery modeling approaches are discussed below.

Scaling and Similitude

The concept of *similitude* argues that if the flow conditions and geometry of two turbomachines have the same dimensionless numbers, then their performance will be similar (Korpela, 2011). Similitude allows a successful turbomachine design to be duplicated at different scales provided that a series of dimensionless groups of variables remain unchanged (Japikse and Baines, 1994). In theory this means that a single basic design can be used in many different applications. In the context of the current research, scaling is however an unsuitable modeling method as motivated by several reasons:

- Similarity works only if all of the dimensionless variables remain constant. One of the dimensionless variables that need to be considered is the Reynolds number, which in practice is usually not possible to keep constant at different scales if the same fluid and speed ratios are used (Japikse and Baines, 1994).
- There are limits to how great the difference in scale between the reference design and the new design can be, because various geometrical features such as surface roughness, blade thickness and clearances do not scale well (Japikse and Baines, 1994).
- Although scaling works well if the working fluid is changed from one ideal gas to another, as demonstrated by von Backström (2008), scaling from an ideal gas to a real fluid or from an incompressible fluid to a compressible fluid cannot be achieved with the same degree of accuracy (Japikse and Baines, 1994).

- Exploration of the full design space (i.e. global optimization of all the variables of the turbomachine) is not possible. The performance of the new design can only be as good as or similar to the performance of the reference design.

Analytical Modeling

Using the basic principles of the conservation of mass, momentum and energy, a series of equations that capture the salient relationships between the many variables of a turbomachine can be developed. Different analytical modeling approaches have been proposed, including the *single-zone* approach, the *jet-wake* approach and the *two-zone* approach (Japikse, 1985). These approaches primarily focus on predicting the outlet conditions of the turbomachine.

The most widely applied analytical modeling approach is the single-zone, *mean-line* approach in which it is assumed that the flow conditions on a streamline at a mean radius is representative of the flow conditions at all radii (Dixon and Hall, 2014). A few key points along the streamline are then identified and the flow is analyzed only at these key points.

Most textbooks on turbomachinery cover this approach to some extent, but there is no "universal" single-zone mean-line model for turbomachines. The approach offers a great deal of freedom of interpretation with regards to assumptions or simplifications, loss modeling, and at which points along the streamline the flow is analyzed at. It is therefore a flexible and customizable modeling approach.

Computational Fluid Dynamics

In computational fluid dynamics (CFD), the full, discretized flow field is numerically resolved from the basic transport equations. It can be considered as the most accurate type of turbomachinery modeling approach, but CFD has some drawbacks that need to be taken into account:

- Significant turbulence occurs in the flow through a turbomachine stage (Tucker, 2013). Accurate performance prediction therefore necessitates accurate turbulence modeling. In lieu of direct numerical simulation (DNS) which is computationally very expensive, careful consideration should be given to the selection of wall functions and turbulence models, as these can drastically affect the results of the simulation (Tucker, 2011).
- Even without DNS, CFD is still a computationally expensive tool and all the more so for design optimization where it is required that the mesh be updated and the flow field be resolved for each design case. Optimization using CFD can be sped-up through the use of a response surface model (RSM) – which is a surrogate model where the results of a few CFD simulations are used to create a representation of the effect of the design variables on the objective function (Li and Zheng, 2017). The quality of the simulation and optimization results is however dependent on the quality of the RSM.
- For sCO_2, high resolution tables of thermodynamic property data need to be used in the CFD analysis. This can significantly slow down the analysis (Schuster *et al.*, 2016).

Holistic Modeling

A combination of modeling methods is always superior to only a single method. Hacks *et al.* (2018a) and Holaind *et al.* (2017) demonstrate how scaling and similitude can be used as the basis for a CFD model, whereas Zhou *et al.* (2018) demonstrate how an analytical mean-line approach is used as the basis for a CFD model.

Commercial turbomachinery modeling is usually done using a holistic approach where one-dimensional mean-line models, two- and three-dimensional CFD models, finite element structural models and computer-aided manufacturing models are integrated. This approach is discussed by Qiu *et al.* (2010).

4.2. Geometry and Principles of Operation

A typical *stage* of a turbomachine consists of three main sections:

- The first section, termed the *nozzle* section, is located at the upstream interface between the turbomachine and the rest of the system. It is a converging flow channel that accelerates the flow. For a centrifugal compressor, this can also be referred to as the *inducer* section or, for a radial inflow turbine, the *scroll* section. Stator blades or *vanes* are installed to change the direction of the flow before it leaves this section.
- The second section consists of a set of blades that rotate on the shaft of the turbomachine. This is termed the *rotor*, or also – in the case of a centrifugal compressor – the *impeller*.
- The third section is located at the downstream interface between the turbomachine and the rest of the system. This is a diverging flow channel that decelerates the flow. It is termed a *diffuser*, or also a *collector scroll* or *volute*.

A schematic diagram of a radial turbomachine stage (which can represent both a centrifugal compressor and a radial inflow turbine) is shown in Figure 13. The numbers correspond to the flow stations identified in Figures 1 and 12.

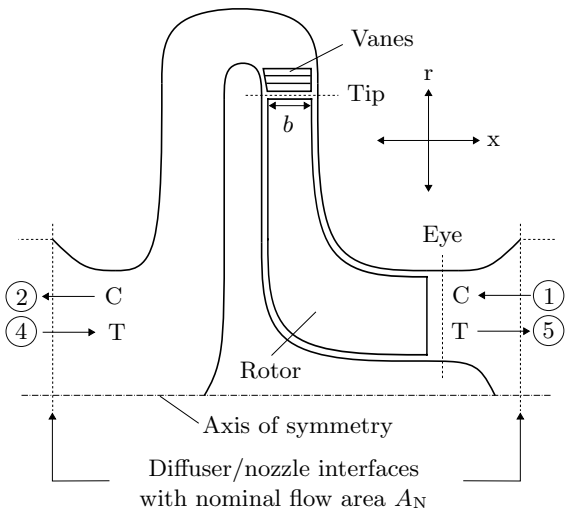

Figure 13: Schematic representation of the profile of a radial turbomachine stage

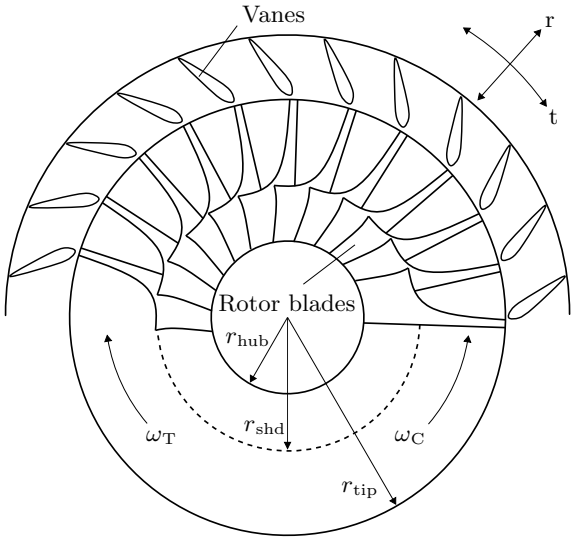

Figure 14: Schematic representation of the blades of a radial turbomachine

For the case of a centrifugal compressor, the flow is from right to left (as indicated by the arrows labeled "C"). The flow enters the stage at station 1. It passes through the nozzle section axially but is turned to leave the rotor section radially. A series of exit vanes and the shape of the diffuser channel then returns the flow to the axial direction by the time it exits the stage at station 2.

For the case of a radial inflow turbine, the flow is from left to right (as indicated by the arrows labeled "T"). The flow enters the nozzle section axially at station 4 and is then rotated by the shape of the channel and a series of guide vanes so that it enters the rotor section in the radial direction. In the rotor section the flow is again turned back into the axial direction, after which it leaves through the diffuser at station 5.

For convenient reference, a summary of the above information is provided in Table 3.

Table 3: Summary of turbomachinery flow directions and stations

Compressor:	Nozzle (1)	→	Eye	→	Tip	→	Diffuser (2)
Turbine:	Nozzle (4)	→	Tip	→	Eye	→	Diffuser (5)

The top of the rotor near the vanes is referred to as the *tip* of the rotor. The rotor geometry here can be characterized by the tip radius r_{tip} and the blade width b. The other end of the rotor section where the flow is axial is referred to as the *eye* and the geometry of the rotor here can be characterized by the hub radius r_{hub} and shroud radius r_{shd}. These radii are indicated in Figure 14 (note that only the top half of the blades and vanes are shown).

The direction of rotation of the blades is opposite for a turbine and a compressor, as indicated in Figure 14. The direction of rotation of the turbine is indicated by ω_T, and the direction of rotation of the compressor is indicated by ω_C.

4.3. Turbomachinery Mean-line Analysis Theory

A one-dimensional mean-line approach is followed to model the turbomachinery for the current research. The theory is introduced in this section. The aim is to use this theory to develop a model of the power system that can be practically applied in the optimization of the complete system, and to provide a basis on which more advanced turbomachinery models (such as those based on CFD) can be developed.

4.3.1. Geometrical Relations

The inlet of the nozzle and outlet of the diffuser for both the compressor and turbine (i.e. stations 1, 2, 4 and 5) are where the turbomachines interface with the other components of the system and therefore, by definition, the flow area here is equal to the nominal flow area A_{N}. This is the largest cross-sectional flow area, and the flow area is smaller in the direction of the rotor. At the tip of the rotor, the radial flow area

$$A_{\mathrm{tip,r}} = 2\,\pi\,r_{\mathrm{tip}}\,b \tag{52}$$

is the circumference of the rotor disk multiplied by the blade width. At the eye of the rotor, the axial flow area

$$A_{\mathrm{eye,x}} = \pi\left(r_{\mathrm{shd}}^2 - r_{\mathrm{hub}}^2\right) \tag{53}$$

is the annulus between the shroud and the hub.

These areas are the *mixed-out* flow areas and therefore the thickness of the rotor blades are not taken into consideration.

The flow conditions at the eye are analyzed at

$$r_{\mathrm{eye}} = \frac{r_{\mathrm{shd}} + r_{\mathrm{hub}}}{2}\ , \tag{54}$$

which is the mean radius between the shroud and the hub.

4.3.2. Conservation of Mass

The direction in which mass is conveyed through the stage can be referred to as the *meridional* (m) direction. The velocity vector in that direction is therefore the meridional velocity V_{m} and the flow area which is normal to this velocity is the meridional area A_{m}.

At the tip of the rotor, the meridional direction is the radial (r) direction. At the eye of the rotor, the meridional direction is the axial (x) direction.

The product of the local density ρ, local meridional velocity and meridional area is defined as the *mass flow rate*,

$$\dot{m} = \rho\,V_{\mathrm{m}}\,A_{\mathrm{m}}\ . \tag{55}$$

Under steady-state conditions, the mass flow rate throughout the stage is the same, which therefore implicitly ensures that mass is conserved.

4.3.3. Velocity Vector Analysis

At both the tip and the eye of the rotor section, the flow is not purely in the meridional direction but instead has a component in the tangential (t) direction as well. Furthermore, since the blades are rotating, the flow must be analyzed both in an absolute (stationary) frame of reference and in a relative (moving) frame of reference. The two frames of reference must be consolidated. A convenient way to analyze the different velocity vectors and their components in the two frames of reference is through a *velocity triangle*.

Velocity Vectors and Components

In a velocity triangle, there are three velocity vectors: the absolute velocity vector $\mathbf{V}$ that corresponds to the absolute frame of reference, the relative velocity vector $\mathbf{R}$ that corresponds to the relative frame of reference, and the blade velocity vector $\mathbf{B}$. The relative velocity vector is defined as the vector subtraction of the blade velocity from the absolute velocity, or

$$\mathbf{R} = \mathbf{V} - \mathbf{B} \, . \tag{56}$$

At the tip, the flow velocity vectors ($\mathbf{V}$ and $\mathbf{R}$) have components in the radial and tangential directions; at the eye they have components in the axial and tangential directions. The blade velocity ($\mathbf{B}$) is necessarily tangential to the direction of rotation and therefore only has a tangential component.

Sign Convention

The adopted sign convention for the velocity triangles is that a vector component is considered positive if it is in the same direction as the blade velocity and negative if it is in the opposite direction.

The angle α that the absolute velocity vector $\mathbf{V}$ makes with the meridional direction reference line is considered as positive if the angle is measured towards the positive tangential direction and negative if the angle is measured in the opposite direction. The same sign convention also applies to the angle β that the relative velocity vector $\mathbf{R}$ makes with the meridional direction reference line.

Velocity Triangle at the Eye of the Rotor

The flow that enters the eye of the compressor is always in the axial direction and therefore the absolute flow angle at the eye is always zero ($\alpha_{\text{eye}} = 0°$). This is not the case with the flow that leaves the rotor at the eye of a turbine because the flow follows the turbine blades. Notwithstanding this, the turbine can specifically be designed to have $\alpha_{\text{eye}} = 0°$. This is the so-called *nominal design* condition and it will be implemented in the current model. If $\alpha_{\text{eye}} = 0°$, then the analysis of the design-point velocity triangles at the eye are the same for both the compressor and the turbine. This design-point velocity triangle is depicted in Figure 15.

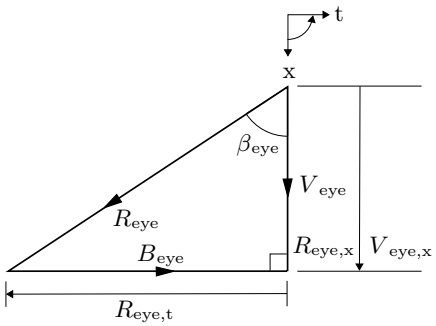

Figure 15: Velocity triangle at the eye of rotor under design-point conditions

The blade velocity at the eye,

$$B_{\text{eye}} = \omega\, r_{\text{eye}} \ , \tag{57}$$

is the product of the *angular velocity* of the shaft, ω, and the mean radius at the eye. The angular velocity ω is measured in radians-per-second, whereas the more commonly used *rotational speed* of the shaft, Ω, is typically measured in revolutions-per-minute.

Since the absolute flow angle at the eye is zero, there is no tangential absolute velocity component at the eye and therefore

$$V_{\text{eye}} = V_{\text{eye,x}} = R_{\text{eye,x}} \ . \tag{58}$$

Furthermore, with no absolute tangential velocity component, it follows from the definition in Equation (56) that

$$R_{\text{eye,t}} = -B_{\text{eye}} \ . \tag{59}$$

The magnitude of the relative velocity vector is calculated from the basic geometry as

$$R_{\text{eye}} = \sqrt{R_{\text{eye,t}}^2 + R_{\text{eye,x}}^2} \ . \tag{60}$$

The Concepts of Slip and Incidence

At the tip of the rotor the flow situation is significantly more complicated than at the eye. Considering that a centrifugal compressor has a finite number of blades, the flow experiences a relative eddy (i.e. relative to the rotating blades) in the inter-blade channels. Invariably, the physics of this process cause the flow to leave at the relative angle β_{tip} rather than the physical blade angle β'_{tip} (Japikse and Baines, 1994). This phenomenon is termed *slip*. Slip is unavoidable and cannot be eliminated from the design of the compressor.

The effect of slip is that the absolute tangential velocity $V_{\text{tip,t}}$ is reduced from its zero-slip equivalent $V'_{\text{tip,t}}$, and the relative tangential velocity component $R_{\text{tip,t}}$ is increased from its zero-slip equivalent $R'_{\text{tip,t}}$.

To characterize the amount of slip in a compressor, the *slip factor*

$$\sigma = \frac{V_{\text{tip,t}}}{V'_{\text{tip,t}}} \tag{61}$$

can be introduced, which represents slip as the fraction with which the absolute tangential velocity component is reduced from the zero-slip case.

Similar physics are encountered in a radial inflow turbine, which ultimately mean that the optimal incidence angle is β_{tip} rather than the physical blade angle β'_{tip} (Dixon and Hall, 2014). The incidence angle can be specifically controlled under design-point conditions by specifying an appropriate inlet guide vane angle α_{tip}.

As with compressor slip, to characterize how much the optimal incidence angle differs from the physical blade angle, the *incidence factor*

$$\lambda = \frac{V_{\text{tip,t}}}{V'_{\text{tip,t}}} \tag{62}$$

can be introduced (Whitfield and Baines, 1990). The incidence factor relates the absolute tangential velocity component to its equivalent in the hypothetical perfect-incidence scenario where the optimal incidence angle is also the physical blade angle.

Radial turbomachines are usually designed with straight blades in order to reduce material stress (Dixon and Hall, 2014). This means that $\beta'_{\text{tip}} = 0°$.

To a good approximation, the slip factor of a centrifugal compressor is the same as the incidence factor of a radial inflow turbine, if the rotors of both machines have straight blades and have the same number of vanes (Dixon and Hall, 2014).

Velocity Triangle at the Tip of the Rotor

The velocity triangle at the tip of the rotor is depicted in Figure 16. The dotted lines indicate the hypothetical scenario where there is no slip in the compressor, and for the turbine, the hypothetical scenario where the optimal incidence angle is also the physical blade angle. The actual flow scenario is indicated by the solid lines.

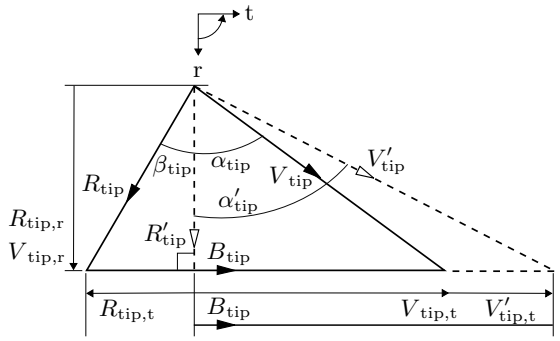

Figure 16: Velocity triangle at the tip of rotor under design-point conditions

The blade velocity at the tip,

$$B_{\text{tip}} = \omega\, r_{\text{tip}} \ , \tag{63}$$

is the product of the angular velocity of the shaft and the tip radius.

For straight blades, $\beta'_{\text{tip}} = 0°$ implies that there is no tangential component of the relative velocity vector in the hypothetical scenario, i.e. $R'_{\text{tip,t}} = 0$. It then follows from the definition of the relative velocity vector in Equation (56) that

$$V'_{\text{tip,t}} = B_{\text{tip}} \ . \tag{64}$$

The definition of the slip factor in Equation (61) or the incidence factor in Equation (62) can be used to relate $V_{\text{tip,t}}$ to $V'_{\text{tip,t}}$. Once the magnitude of the components are known, the magnitude of the absolute velocity vector is calculated from the basic geometry as

$$V_{\text{tip}} = \sqrt{V^2_{\text{tip,t}} + V^2_{\text{tip,r}}} \ . \tag{65}$$

With

$$R_{\text{tip,t}} = V_{\text{tip,t}} - B_{\text{tip}} \tag{66}$$

from the definition of the relative velocity vector in Equation (56), and with

$$R_{\text{tip,r}} = V_{\text{tip,r}} \tag{67}$$

from Figure 16, the magnitude of the relative velocity vector is calculated from the basic geometry as

$$R_{\text{tip}} = \sqrt{R^2_{\text{tip,t}} + R^2_{\text{tip,r}}} \ . \tag{68}$$

4.3.4. Conservation of Angular Momentum

The moving fluid exerts a torque on the blades of a turbine, causing the shaft to rotate and thus transferring momentum from the fluid to the shaft. Similarly, an external torque is required to rotate the shaft, causing the blades of a compressor to act on the fluid and thus transferring momentum from the shaft to the fluid.

Derivation of the conservation of angular momentum (Korpela, 2011) shows that under steady conditions the torque or *moment* is

$$M = \dot{m}\left(r_{\text{tip}} V_{\text{tip,t}} - r_{\text{eye}} V_{\text{eye,t}}\right) \ . \tag{69}$$

This is purely the momentum transferred between the shaft and the fluid – it does not take into account any additional loss factors.

The moment is defined as positive in the direction of rotation of the shaft. A positive result for Equation (69) when applied to a turbine implies that the transfer of momentum is from the fluid to the blades; whereas a positive result for Equation (69) when applied to a compressor implies that the transfer of momentum is from the blades to the fluid.

Based on Figure 15, it can be observed that under design-point conditions the absolute velocity at the eye does not have a tangential component. Equation (69) can thus be simplified as

$$M = \dot{m}\left(r_{\text{tip}} V_{\text{tip,t}}\right) \ . \tag{70}$$

4.3.5. Conservation of Energy

The conservation of energy in a turbomachine stage is best analyzed by studying the mechanical, thermodynamic and parasitic energy transfers independently.

Mechanical Energy Transfer

The *mechanical power* or *dynamic power* originates from the conservation of angular momentum and is determined by multiplying the moment by the shaft speed as

$$\dot{W}_{\text{Mech.}} = M\,\omega\ . \tag{71}$$

Thermodynamic Energy Transfer

The *thermodynamic power*, which originates from application of the first law of thermodynamics (Dixon and Hall, 2014), is

$$\dot{W}_{\text{Therm.}} = \dot{m}\,w_0 = \dot{m}\,(h_{0,\text{tip}} - h_{0,\text{eye}})\ . \tag{72}$$

Since the energy at the tip is always higher than the energy at the eye – for both a compressor and a turbine – this is always a positive quantity.

Note that, unlike the similar equations introduced in Section 3.4, in this case the kinetic energy is not assumed to be negligible, hence stagnation enthalpy rather than static enthalpy is considered here.

Parasitic Energy Transfer

It is important to make the distinction between the mechanical power and the thermodynamic power because in a real turbomachine, the mechanical power and the thermodynamic power is not the same (Japikse, 1996). The dynamic power only considers the interaction between the flow and the shaft, whereas the thermodynamic power considers the action of every phenomenon that occurs in the machine.

The imbalance between the results of Equations (71) and (72) can be attributed to the *parasitic losses* in the machine and termed the *parasitic work* (or *power*) as

$$\dot{W}_{\text{Para.}} = \left|\dot{W}_{\text{Mech.}} - \dot{W}_{\text{Therm.}}\right|\ . \tag{73}$$

The absolute value in Equation (73) ensures that the parasitic work term is always treated as a positive value: in a compressor, the power that is transferred to the fluid is less than the required shaft power, and in a turbine the usable power available on the shaft is less than the fluid power.

The parasitic work term at the design point of a turbomachine should be relatively small. In the current model it is thus assumed that

$$\dot{W}_{\text{Para.}} = 0\ , \tag{74}$$

such that

$$\dot{W}_{\text{Mech.}} = \dot{W}_{\text{Therm.}} = \dot{W}\ . \tag{75}$$

Nozzle and Diffuser Sections

With the observation that no mechanical energy transfer takes place in the nozzle and diffuser sections, and with the assumption of these sections being adiabatic, the stagnation enthalpy remains constant. Table 4 shows these relationships for the compressor and turbine.

Table 4: Conservation of energy in the nozzle and diffuser sections

	Nozzle	Diffuser
Compressor:	$h_{0,1} = h_{0,\text{eye}}$	$h_{0,\text{tip}} = h_{0,2}$
Turbine:	$h_{0,4} = h_{0,\text{tip}}$	$h_{0,\text{eye}} = h_{0,5}$

4.3.6. Rotor Performance Modeling

Definitions of Efficiency

The performance of the rotor is typically assessed in terms of entropy generation during the expansion or compression process. An isentropic process is therefore defined as the baseline process to which the actual process can be compared.

For the compressor, the baseline specific energy transferred to the fluid is

$$w_{0,\text{s}} = h_{0,\text{tip,s}} - h_{0,\text{eye}} \ , \tag{76}$$

where $h_{0,\text{eye}}$ is the actual stagnation enthalpy at the eye, and $h_{0,\text{tip,s}}$ is the stagnation enthalpy at the tip that is achieved in an isentropic compression process.

For the turbine, the baseline specific energy transferred from the fluid is

$$w_{0,\text{s}} = h_{0,\text{tip}} - h_{0,\text{eye,s}} \ , \tag{77}$$

where $h_{0,\text{tip}}$ is the actual stagnation enthalpy at the tip, and $h_{0,\text{eye,s}}$ is the stagnation enthalpy at the eye that is achieved in an isentropic expansion process.

The ratio between the actual expansion or compression processes and the defined baseline processes gives rise to the concept of the *isentropic efficiency* of the rotor – or more specifically – the *total-to-total* isentropic efficiency of the rotor. The efficiency is always between zero and 100%, where the latter represents the isentropic (best possible) case.

The total-to-total isentropic efficiency for a compressor rotor is

$$\eta_{\text{R}} = \frac{w_{0,\text{s}}}{w_0} \ , \tag{78}$$

and the total-to-total isentropic efficiency for a turbine rotor is

$$\eta_{\text{R}} = \frac{w_0}{w_{0,\text{s}}} \ . \tag{79}$$

The total-to-total isentropic efficiency definition is used instead of the *total-to-static* definition because the kinetic energy in the fluid after the rotor section is still useful (Dixon and Hall, 2014). It will be recovered in the diffuser to contribute to a static pressure rise.

The baseline isentropic work $w_{0,s}$ can be calculated once the inlet thermodynamic conditions and outlet pressure of the rotor are known, and with knowledge of the efficiency, the actual work w_0 can then subsequently be calculated. Four options for finding the efficiency of the rotor are discussed below;the *design space restriction* approach is used in this research.

Constant Efficiency Approach

One option is to assume a constant value for the efficiency. This is useful when doing basic thermodynamic cycle calculations and for preliminary system design work. Often the performance of the nozzle and diffuser sections are lumped together and the rotor efficiency is treated as the stage efficiency.

However, this approach completely decouples the thermodynamic performance of the rotor from its physical design and therefore assumes that any rotor design is capable of achieving the proposed efficiency. As such, this method is unsuitable for detailed design work.

Performance Correlation Approach

An alternative approach to predicting the performance of a rotor is to consider correlations where the efficiency is given as a function of a dimensionless variable or as a contour plot against two dimensionless variables.

Many different efficiency correlations are available in literature; some are based on analytical or theoretical principles whilst others are correlated directly from empirical data. Typical examples include various specific-speed diagrams (including the Cordier diagram) or specific-speed vs specific-diameter diagrams, correlations against flow coefficient and correlations against blade velocity ratios (Japikse and Baines, 1994; Aungier, 2000, 2006).

Although these correlations are by their nature general, they are not universally accurate. Balje (1981) mentions that these correlations apply only to specific types of rotor designs (i.e. that have particular geometrical ratios) and are valid only under particular conditions, such as for a given Reynolds number. Furthermore, the exact efficiencies are largely dependent on the quality and state-of-the art of the manufacturing process and the development time involved in refining the design of the machine.

Deterministic Modeling Approach

A more rigorous approach is to deterministically calculate what the efficiency should be, by identifying and subsequently modeling the various physical phenomena that cause entropy generation in the rotor section. Persky and Sauret (2019) have identified the main causes as being:

- an *incidence loss* which accounts for inter-blade vorticity,
- a *passage loss* which accounts for blockage, viscous shear, mixing and secondary flows,
- a *trailing edge loss* which accounts for the expansion of the passageway as the flow leaves the rotor,
- a *clearance loss* which occurs as a result of there being a gap between the rotor and the housing of the machine through which fluid can leak and recirculate,

- a *windage loss* which is as a result of the back of the rotor rotating against the air in the stationery housing of the machine, and
- an *exit energy loss* which accounts for the mutual interaction between the fluid dynamics of the diffuser and the rotor exit.

A wide selection of analytical equations that predict the magnitude of each factor is available (Persky and Sauret, 2019). Unfortunately, there are more than 1.5 million different ways in which these equations can be combined, which means that there is no "universal" loss model for the rotor section.

Furthermore, Japikse and Baines (1994) mention that what constitutes an *internal loss*, i.e. the losses associated with the actual flow process, and what constitutes an *external loss*, i.e. the losses not associated with the actual flow process and which appear in the parasitic work term of Equation (73), is largely a matter of industry convention or preference rather than being based on theory.

A further issue with this approach is that the equations make use of *loss coefficients* which are based on correlations with empirical data, usually for air turbomachines. The use of these coefficients to model sCO_2 turbomachinery therefore requires careful consideration.

Even for the same working fluid, the values of the loss coefficients are not necessarily universally applicable and can be dependent on local thermodynamic properties, flow conditions and machine geometry. If an experiment was performed with one machine design and at one operating point, then the loss coefficient values are only validated for that single case. Even if experiments are then performed for one design at many operating points, the coefficient values are still only validated for that single design. Ideally, many different machine designs should be tested at many different operating points in order to develop a substantial database with coefficient values. The coefficient values should then be correlated against dimensionless flow and geometrical parameters if they are to be generally applicable.

Alshammari *et al.* (2018) demonstrate this method of using loss coefficients for off-design performance prediction of turbines, but with air and R123 as working fluids.

Design Space Restriction Approach

A fourth method that can be used to model the performance of the rotor is to restrict its design space to a region that is known to yield efficient designs, and then to assume that the efficiency of the design in that region is a reasonably high constant value. Logan (1981) provides typical design ranges for many of the variables, including angles, blade geometry ratios and velocity ratios. If the design space is restricted to fall within these ranges, then a reasonably high efficiency can be expected.

This is the approach that will be employed in the current models of the turbine and compressor, for two reasons. Firstly, restricting the design space to a region that is known to provide efficient and stable operation is good practice as it will help to avoid unusual, extreme or impractical designs. Secondly, design space restriction is the natural purpose of inequality constraints and therefore this approach is easily implemented in a computational architecture based on mathematical optimization.

4.3.7. Nozzle and Diffuser Performance Modeling

It is not sensible to define loss coefficients for the nozzle and diffuser sections in terms of an entropy increase because the main function of these sections is to facilitate an interconversion of static pressure and flow velocity. The increase of entropy is therefore not as relevant as compared to a thermodynamic process in which energy is transferred.

Static, Stagnation and Dynamic Pressure Concepts

Static pressure P, static temperature T and static enthalpy h are thermodynamic properties of the fluid. A thermodynamic property lookup table or equation-of-state denominated in temperature and pressure allows the static enthalpy to be calculated as

$$h = f(T, P) \ . \tag{80}$$

The static enthalpy and kinetic energy of the fluid can be combined to form the *stagnation enthalpy* (Borgnakke and Sonntag, 2014),

$$h_0 = h + \tfrac{1}{2}V^2 \ . \tag{81}$$

By analogy to Equation (80), it can be claimed that

$$h_0 = f(T_0, P_0) \ , \tag{82}$$

where T_0 is the stagnation temperature and P_0 is the stagnation pressure – the thermodynamic properties associated with the stagnation enthalpy.

For modeling and simulation purposes, the use of static thermodynamic properties and velocity as separate variables is sufficient. On the contrary, much if not all experimental work on turbomachines is done using stagnation values, and hence the correlations derived from the experimental data are also expressed as stagnation values.

The interconversion between static and stagnation temperature and pressure should ideally be done on the basis of Equations (80) through (82), a thermodynamic property table or equation-of-state, and exploiting the fact that the entropy is the same in both the static and stagnation cases (Dixon and Hall, 2014).

A simpler alternative is to assume that the fluid is incompressible, in which case the stagnation pressure can be converted directly from the static pressure as

$$P_0 = P + \tfrac{1}{2}\rho V^2 \ , \tag{83}$$

where the $\frac{1}{2}\rho V^2$ term is referred to as the *dynamic pressure* (White, 2011).

In the current models, the stagnation pressure is only applied in the evaluation of the performance of the diffuser and nozzle sections – as will be discussed in the following sections. Given that the performance modeling of these sections is fundamentally coarse (because only a single coefficient is used to describe the performance), the small error that is made by assuming that the fluid is incompressible in the calculation of the stagnation pressure is considered inconsequential.

Diffuser Performance

The main function of the diffuser section is to slow the flow velocity and increase its static pressure. The *static pressure recovery coefficient* (Japikse and Baines, 1994) of a diffuser,

$$C_{\mathrm{p}} = \frac{P_{\mathrm{out}} - P_{\mathrm{in}}}{P_{0,\mathrm{in}} - P_{\mathrm{in}}} = \frac{P_{\mathrm{out}} - P_{\mathrm{in}}}{\frac{1}{2}\rho_{\mathrm{in}} {V_{\mathrm{in}}}^2} \ , \tag{84}$$

represents the fraction of the dynamic pressure available at the inlet that is converted to a static pressure rise at the outlet. The *ideal* static pressure recovery coefficient,

$$C_{\mathrm{p,i}} = 1 - (\mathrm{AR})^2 \ , \tag{85}$$

is only a function of the diffuser area ratio,

$$\mathrm{AR} = \frac{A_{\mathrm{in}}}{A_{\mathrm{out}}} \quad . \tag{86}$$

The ratio of the actual pressure recovery coefficient to the ideal pressure recovery coefficient is the *diffuser effectiveness* or *diffuser efficiency*,

$$\eta_{\mathrm{D}} = \frac{C_{\mathrm{p}}}{C_{\mathrm{p,i}}} \quad . \tag{87}$$

Nozzle Performance

The nozzle section increases the flow velocity whilst sacrificing static pressure. Its performance can be expressed in the form of a *total pressure loss coefficient*,

$$K_{\mathrm{N}} = \frac{P_{0,\mathrm{in}} - P_{0,\mathrm{out}}}{P_{0,\mathrm{in}} - P_{\mathrm{in}}} = \frac{\left(P_{\mathrm{in}} + \frac{1}{2}\rho_{\mathrm{in}} {V_{\mathrm{in}}}^2\right) - \left(P_{\mathrm{out}} + \frac{1}{2}\rho_{\mathrm{out}} {V_{\mathrm{out}}}^2\right)}{\frac{1}{2}\rho_{\mathrm{in}} {V_{\mathrm{in}}}^2} \ , \tag{88}$$

which is the ratio of the total pressure drop between the inlet and outlet as a ratio to the dynamic pressure at the inlet (Japikse and Baines, 1994).

The nozzle section for a compressor does not have any guide vanes and therefore the loss coefficient will be lower, as compared to the nozzle section for the turbine which has a flow path that includes guide vanes.

4.3.8. Model Coefficients

Four coefficients must be specified for each turbomachine in order to functionally complete the model. These coefficients are the slip or incidence factor, rotor isentropic efficiency, diffuser efficiency and nozzle total pressure loss coefficient. The definitions of these coefficients have already been introduced in the current chapter.

In the subsequent chapters of the dissertation, four conservative designs of the system are completed (Designs A, B, C and A^{+}) and two optimistic designs of the system are completed (Designs A^{++} and X). The values used for the coefficients in the conservative designs are less favorable than for the optimistic designs. The numerical values for the coefficients used for each design are summarized in Table 30 in Appendix A.5, but are motivated as follows:

- For a turbomachine with straight blades ($\beta'_{\text{tip}} = 0°$), Stanitz's correlation for slip factor reduces to a simple function of the number of vanes (Dixon and Hall, 2014). Assuming that the number of vanes is 12, Stanitz's correlation gives a value of $\sigma = 0.84$. This value is used for the conservative designs. For the optimistic designs it is assumed that there are three times as many vanes, giving a value of $\sigma = 0.95$. The value of the incidence factor is the same as the slip factor.
- After reviewing several other studies, Uusitalo *et al.* (2019) recommend turbomachine isentropic efficiencies of 85% as a guideline for sCO_2 cycle simulations. For the conservative designs, a value of 80% is used for rotor isentropic efficiency. This is because the design space restriction approach that is followed in the models (as discussed in Section 4.3.6) has not yet been proven to apply to sCO_2 turbomachinery, and thus some uncertainty exists. For the optimistic designs, a value of 90% is used instead.
- Based on the recommendations of Japikse and Baines (1994), the diffuser section is assumed to have an efficiency of 80% for the conservative designs and 90% for the optimistic designs.
- Based on the recommendations of Japikse and Baines (1994), the compressor nozzle section is assumed to have a total pressure loss coefficient of 5% for the conservative designs and 3% for the optimistic designs; and the turbine nozzle section is assumed to have a total pressure loss coefficient of 10% for the conservative designs and 7% for the optimistic designs.

4.3.9. Other Design Considerations

Area Ratios

The area ratio of the nozzle section is always converging and the area ratio of the diffuser section is always diverging. This is enforced by inequality constraints on the area ratio between the nominal flow area (which is also the nozzle inlet area and the diffuser outlet area), and the meridional areas at the tip and at the eye of the rotor section.

Choke Margin

When the flow through some section of the turbomachine stage reaches the speed of sound, no further increase in mass flow is possible. Under these conditions the machine is said to be *choked* (Dixon and Hall, 2014). The *Mach number*,

$$\text{Ma} = \frac{V}{c} , \tag{89}$$

is defined as the ratio of the local velocity V to the local speed of sound c. A Mach number of one means that the flow has reached the speed of sound and that the stage is thus choked.

To ensure that choking does not occur at the design point of the machines, the inequality constraint

$$\text{Ma} \leq 0.95 \tag{90}$$

will be checked for all absolute and relative flow velocity vectors in the stage.

4.4. Qualitative Verification

In order to fully define the operating point of a compressible turbomachine with a known geometry and working fluid, four independent variables must be specified (Dixon and Hall, 2014). Usually, this is the mass flow rate, rotational speed, and inlet temperature and pressure, although other combinations are also possible, such as outlet pressure instead of mass flow rate. If these four variables are fixed in an experimental test, all the other variables will be uniquely determined. A numerical model that aims to replicate a physical machine therefore needs to have this same characteristic.

Provided that values for the coefficients in Section 4.3.8 are specified, the developed turbomachinery models will provide a unique solution. The models are therefore capable of capturing the fundamental relationships between the variables.

4.5. Quantitative Validation

To determine the numerical accuracy of the models, they must be validated using data. In addition to the measured performance data and thermodynamic operating conditions, the data sets must also include sufficient geometric data to allow the actual machine to be replicated in the modeling environment. Unfortunately, the availability of such data sets for sCO_2 components, in particular radial inflow turbines and centrifugal compressors, is limited.

Furthermore, the performance of the compressor is more uncertain compared to the turbine, given that the fluid typically enters the compressor near the critical point. Experimental work therefore tends to focus on the sCO_2 compressor rather than on the sCO_2 turbine.

The developed compressor model is validated with two sets of experimental data. The first validation study (details in Appendix E.2) is with data from the sCO_2-HeRo project (Hacks *et al.*, 2018a,b) and the second validation study (details in Appendix E.3) is with data from the Sandia project (Wright *et al.*, 2010). The turbine is validated with data from a CFD simulation (Zhou *et al.*, 2018); details are available in Appendix E.4.

In all three studies, the turbomachines are validated at (or close to) their respective design points. The two compressor experiments did not include a nozzle section, but included a diffuser section, whereas the turbine study did not include a diffuser section but included a nozzle section.

As confirmed by the good agreement between the reference results and the calculated results in these validation studies, the developed compressor and turbine models are accurate. The biggest difference in results is a 10% under-prediction of the turbine power output. However, this is to be expected and it is essentially so by design – given the conservative values of the model coefficients in Section 4.3.8. The reference turbine had a higher efficiency than the value assumed in the current models and therefore a higher power output was observed.

By iteratively changing the model coefficients in Section 4.3.8, it is possible to tune the models to be in perfect agreement with the reference results.

However, this *tuning* of the models is discouraged. Although it has been shown that the one-dimensional mean-line models in this work – even with un-tuned coefficients – produce reasonable and meaningful results, this approach has its limitations. If significantly more accurate results are needed then a more advanced modeling approach should be followed, as opposed to tuning the one-dimensional mean-line model to fit a particular data set. Tuning only makes the model more accurate for that specific case, but is not guaranteed to make the model more accurate for all cases.

5. Thermal System Model

The three heat exchangers, namely the solar receiver, recuperator and heat sink are modeled together as the *thermal system*. This chapter starts with a discussion of the important features of the thermal system. The modeling software environment is introduced next, followed by a discussion of the ambient conditions under which the system operates. Discretization of the heat exchangers into several parallel flow channels and a series of control volumes is graphically illustrated in the next section. Following this, four sections are dedicated to describing the details of the models. The validation of the thermal system model is presented in the concluding section of this chapter.

5.1. Features of the Thermal System Model

Control-volume-based Approach

The variation in the specific heat of carbon dioxide near its critical point introduces the possibility of encountering an *internal pinch point* in the recuperator. This happens when the temperature difference between the hot and cold streams approaches zero somewhere in the middle of the recuperator. Consequently the heat transfer approaches zero. If the heat exchangers are modeled only in terms of their inlet and outlet temperatures, this internal pinch point cannot be captured and the heat transfer would be over-predicted (Friedman and Anderson, 2017).

A solution to the internal pinch point problem is to subdivide the heat exchangers into a number of control volumes, and to solve it as a *convection-diffusion* problem where the conservation equations are applied to the fluid in each control volume and heat transfer occurs perpendicular to the direction of fluid flow.

Realistic Thermodynamic Properties

As a result of the large variation of the thermodynamic properties near the critical point of the fluid, accurate modeling of the thermodynamic properties is an essential feature of the thermal system model.

Simplifying Assumptions

Two simplifying assumptions in the thermal system model are as follows:

- The fluid flow is treated as one-dimensional in the axial (longitudinal) direction of the heat exchanger flow channels. The flow velocity and all thermodynamic properties are assumed to refer to the *bulk* or *cup-mixing* average values (Bird *et al.*, 2002). The cross-sectional velocity profile is not taken into account.
- Heat transfer is one-dimensional: planar in the case of the recuperator, and axi-symmetric in the case of the solar receiver and heat sink.

5.2. The Flownex® Simulation Environment

Introduction to Flownex®

A control-volume-based approach to solving the conservation of mass, momentum and energy equations, whilst taking into account real fluid behavior, is within the proven capabilities of the Flownex® Simulation Environment which will be used to model the thermal system model for this research.

Flownex® is a commercial software package for the simulation of thermo-fluid systems. The software has historically been applied in the nuclear industry, where it has been "extensively validated and verified" insofar as it "is the only software of its kind to hold a nuclear accreditation" (Flownex Simulation Environment, 2020a). Flownex® has been successfully applied to simulate supercritical carbon dioxide cycles previously. Most notably, Flownex® is used by the Gas Technology Institute for the simulation work of the 10 MW sCO_2 project in the United States (Flownex Simulation Environment, 2020b; Gas Technology Institute, 2018).

Modeling in Flownex®

Flownex® offers a library of pre-developed models, including physical elements (such as flow channels) and heat transfer elements (such as conduction, convection and radiation elements). Each element has its own set of input values which can include aspects such as geometrical specifications, material, number of control volumes, or options regarding which pressure drop formulation or heat transfer correlation should be used.

The elements are connected together in a network, where inlet and outlet boundary conditions must be specified for the network. Temperature and pressure values are usually supplied as inlet boundary conditions, and mass flow rate is usually supplied as the outlet boundary condition. The boundaries between the elements that are in the interior of the network (called *nodes*) need not be specified because their values result from the solution of the network.

Heat transfer modeling in Flownex® is based on the thermal resistance concept (Çengel and Ghajar, 2015).

Solution of a Flownex® Network

The Flownex® solver is a direct-enumeration solver, which means that it can only solve the network if all the required input variables have numerical values. Variables with known values must be entered as constants before the start of the analysis, while variables with unknown values can be treated with a user-supplied parameter table or with the built-in Monte Carlo simulation tool. After convergence has been achieved, Flownex® will report the solution of the network. Results can then be exported for post-processing.

5.3. Ambient Conditions

The thermal system is the sub-system that interacts with the natural environment and therefore the ambient conditions play a vital role in its performance.

The geographic location of the system is chosen to be near the town of Stellenbosch, in the Western Cape province of South Africa. The climate in this region is Mediterranean, with dry summers and wet winters. As a result, the yearly average solar irradiation (DNI) in this region is about $2\,300\,\mathrm{kWh/m^2}$, which is an average value both for South Africa and for the world (The World Bank and Solargis, 2019).

A meteorological measurement station is installed at Stellenbosch University which provides accurate local solar irradiation, ambient temperature and ambient wind speed data. This meteorological data is available free of charge from SAURAN – the *Southern African Universities Radiometric Network* (Brooks *et al.*, 2015).

Excerpts from the SAURAN database for the Stellenbosch University station over the three year period from beginning 2017 to end 2019 are presented in Figures 17, 18 and 19.

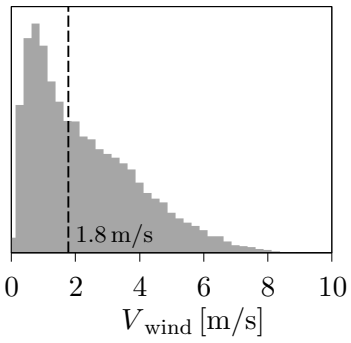

Figure 17: Relative frequency of wind speed measurements (Brooks *et al.*, 2015)

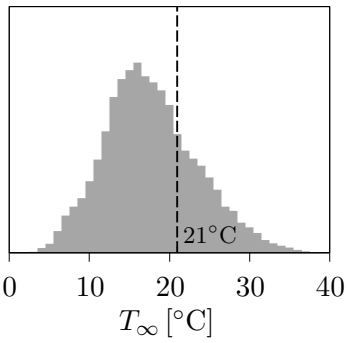

Figure 18: Relative frequency of air temperature measurements (Brooks *et al.*, 2015)

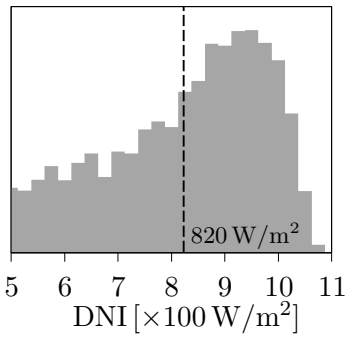

Figure 19: Relative frequency of solar radiation measurements (Brooks *et al.*, 2015)

The value of these conditions change on an intra-day as well as on a seasonal basis. Typical values are specified for the models of the current research.

Wind Speed

Figure 17 is a relative frequency histogram of wind speed measurements. The measurements approximate a beta distribution, with most values clustered around the lower wind speed values. The median wind speed of $V_{\text{wind}} = 1.8\,\text{m/s}$ as indicated is applied in this research.

Ambient Air Temperature

Figure 18 is a relative frequency histogram of ambient air temperature measurements. The measurements approximate a normal distribution, with the minimum observed temperature just above 0 °C and the maximum observed temperature just below 40 °C. The mean air temperature is around 17 °C, but this also includes night-time temperature measurements. In this research, the 75th percentile, which is $T_\infty = 21\,°\text{C}$ as indicated, is used as the ambient air temperature specification.

Solar Radiation

Figure 19 is a relative frequency histogram of the observed direct normal irradiation (DNI). The DNI represents the light that falls in a straight line from the sun and is therefore available for concentration. It excludes diffuse light, such as light that passes through clouds.

The maximum observed DNI is $1\,070\,\text{W/m}^2$ and the minimum is zero every night after the sun sets and whenever the sun is blocked by clouds. In this research, the DNI specification is chosen to be $820\,\text{W/m}^2$, which is calculated as the average DNI value of all DNI observations that are above $500\,\text{W/m}^2$ (below $500\,\text{W/m}^2$ the system is assumed to be inactive).

The DNI is the energy that is available per unit area of the parabolic trough collectors. The parabolic troughs are curved and their reflective surfaces focus all of this energy onto the surface of the solar receiver absorber tube, as indicated in Figure 20.

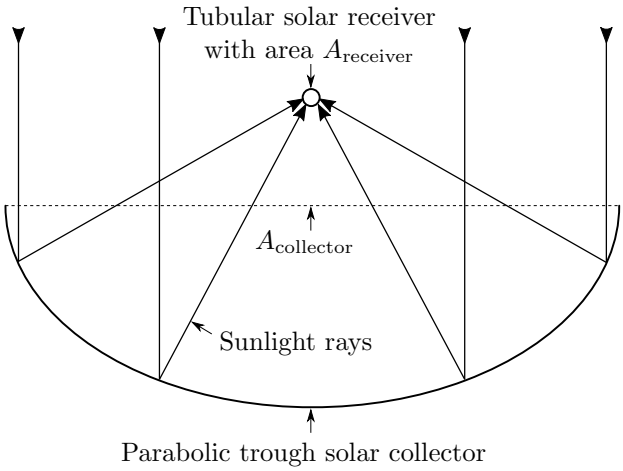

Figure 20: Schematic diagram of the solar collector and receiver

Since the surface area of the absorber tube is much smaller than the surface area of the collectors, the energy per unit area is significantly increased.

The *geometric concentration ratio*,

$$\mathrm{CR} = \frac{A_{\mathrm{collector}}}{A_{\mathrm{receiver}}} \ , \tag{91}$$

is the ratio between the aperture of the solar collector and the solar receiver (Stine and Geyer, 2001). For parabolic trough systems, this is typically between 60 and 100 times (Breeze, 2014). The average value of CR = 80 times is applied in the current research.

To calculate the energy input per unit area of the solar receiver, the DNI is multiplied by the concentration ratio such that

$$\dot{q}''_{\mathrm{S}} = \mathrm{DNI} \times \mathrm{CR} \ . \tag{92}$$

To calculate the total energy input for the whole solar receiver, this value is multiplied by the total surface area, such that

$$\dot{Q}_{\mathrm{S}} = \dot{q}''_{\mathrm{S}} \times A_{\mathrm{s,S,o}} \ . \tag{93}$$

Effective Sky Temperature

For calculations regarding radiation to the environment, the effective atmospheric temperature or *effective sky temperature*, T_{sky}, is usually between $-43\,^{\circ}\mathrm{C}$ and $12\,^{\circ}\mathrm{C}$ (Çengel and Ghajar, 2015). In this research the average value of $T_{\mathrm{sky}} = -16\,^{\circ}\mathrm{C}$ is applied.

Atmospheric Emissivity

For calculations regarding radiation to the environment, the atmospheric- or sky emissivity can be estimated using correlations that account for various atmospheric conditions, such as cloud cover, dew point temperature and particulate matter (Mills, 1999). A typical value for clear sky conditions is $\varepsilon_{\mathrm{sky}} = 0.8$.

5.4. Heat Exchanger Branching and Control Volumes

Geometric compatibility between the components is assured through the nominal flow area A_N, which is the same at the interfaces between all the components. However, unlike in the power system model where the flow is accelerated in the nozzle section and decelerated in the diffuser section, the heat exchangers do not benefit from a change in area. The heat exchangers therefore maintain this nominal flow area throughout.

A heat exchanger with several parallel flow channels as depicted in Figure 21 is more practical than a heat exchanger consisting of only a single long flow channel. From the upstream direction, the flow branches from a single large channel into N smaller flow channels through a *header*, and at the downstream side the N channels are collected back into a single channel through a *manifold*. The header and manifold sections are assumed to be adiabatic; only the *active zone* of the heat exchanger participates in the heat transfer.

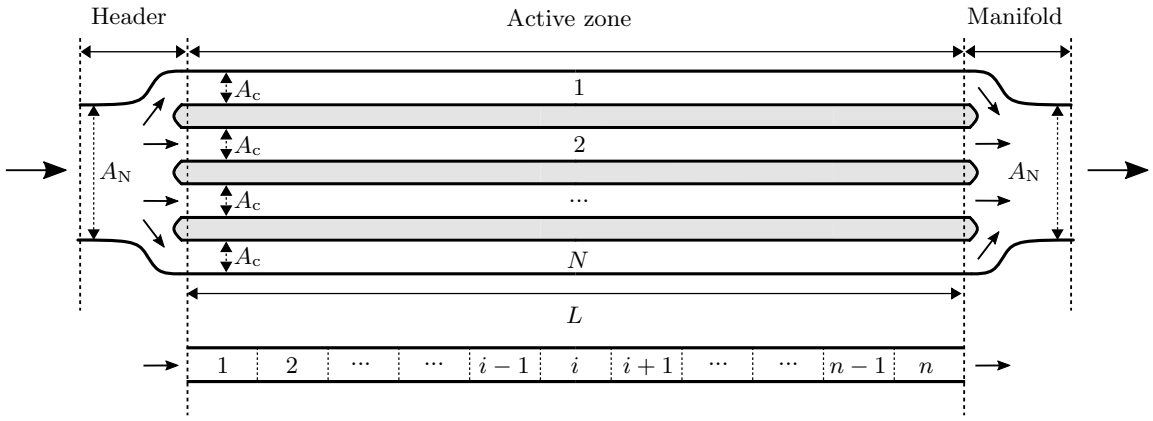

Figure 21: Schematic diagram of heat exchanger branching and control volumes

The cross-sectional flow area of each channel in Figure 21 is the nominal flow area divided by the number of flow channels, or

$$A_c = \frac{A_N}{N} \, . \tag{94}$$

The mass flow rate in each channel is the total cycle mass flow rate divided by the number of channels, or

$$\dot{m}_c = \frac{\dot{m}}{N} \, . \tag{95}$$

Each flow channel is identical to every other flow channel in the heat exchanger. Therefore, the fluid dynamics and heat transfer equations only need to be solved for the active zone of a single flow channel.

The active zone is divided into n identically-sized control volumes, as indicated in the bottom part of Figure 21. By definition, the fluid velocity, thermodynamic properties and heat transfer characteristics are invariant within a control volume.

5.5. Model of the Complete Thermal System

The Flownex® model of the complete thermal system is presented in Figure 22. It consists of four flow elements:

- the heat sink flow channel,
- the flow channel of the heat addition (cold) side of the recuperator,
- the flow channel of the heat rejection (hot) side of the recuperator, and
- the solar receiver flow channel.

The model also contains six heat transfer elements:

- one element to model the heat transfer in the heat sink ($\dot{Q}_{\mathrm{H}}$),
- one element to model the heat transfer in the recuperator ($\dot{Q}_{\mathrm{R}}$), and
- four elements to model the solar energy input ($\dot{Q}_{\mathrm{S}}$) and the heat transfer ($\dot{Q}_{\mathrm{T}}$, $\dot{Q}_{\mathrm{V}}$ and $\dot{Q}_{\mathrm{G}}$) in the solar receiver.

The four flow boundary conditions of the model are at:

- station 1: the outlet of the heat sink,
- station 2: the inlet to the cold side of the recuperator,
- station 4: the outlet of the solar receiver, and
- station 5: the inlet to the hot side of the recuperator.

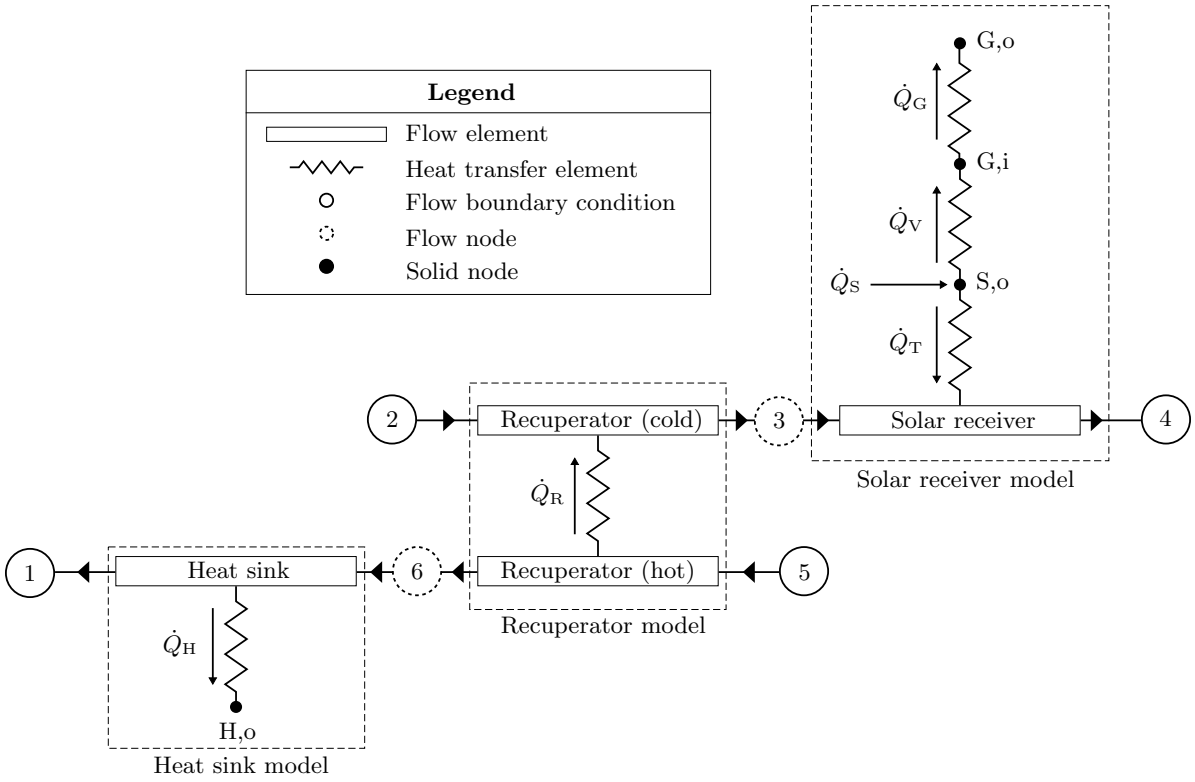

Figure 22: Flownex® model of the thermal system

Stations 3 and 6 are not boundary conditions but are ordinary flow nodes with conditions that are a result of the solution of the network. The model also has four solid nodes:

- one on the outside surface of the solar receiver steel absorber tube (S,o),
- one on the inner surface of the solar receiver glass cover tube (G,i),
- one on the outer surface of the solar receiver glass cover tube (G,o), and
- one on the outer surface of the heat sink tube (H,o).

The three components of the thermal system (i.e. the solar receiver, recuperator and heat sink) form three separate sub-models. Further details about each are provided in the following sections. However, there are a few topics that are common to all three models that are discussed first.

Convection Heat Transfer Correlation

In all cases where convection heat transfer takes place, the convection heat transfer coefficient is calculated using the Dittus-Boelter correlation method, which is available as an option in Flownex®. Although other, more specialized correlations are available, the Dittus-Boelter correlation is appropriate for sCO_2 (Friedman and Anderson, 2017).

Number of Control Volumes

Flownex® has a built-in mechanism to check whether the solution is accurate for the specified number of control volumes. A warning message will be given if it deems that the solution could be improved with more control volumes. The user can then update the number of control volumes if necessary. In general, ten control volumes are sufficient for the solution of the temperature and pressure at the outlet of the heat exchangers to be converged up to three significant figures. In the case of the recuperator however, 30 control volumes (for each side) are used because the temperature profile in the flow channels is considerably steeper compared to the other two heat exchangers.

Surface Roughness

The material roughness must be specified in order to calculate the primary pressure loss. A value of $30\,\mu$m (a typical stainless steel surface in the Flownex® database) is selected.

Secondary Pressure Loss Coefficient

The flow channels of the heat exchangers maintain the same flow area throughout (i.e. they do not converge or diverge) and therefore there are only two secondary pressure loss effects to be considered: an entrance loss as the flow branches from one large channel into several smaller channels in the header, and an exit loss as the flow is collected again from the several parallel channels into a single large channel in the manifold. A conservative value for these two effects combined is $K = 2.0$ (White, 2011). This value is used for the solar receiver and heat sink, but $K = 3.0$ is used for the recuperator because it has significantly more smaller flow channels and thus the branching is expected to cause a greater degree of pressure loss.

5.6. Details of the Solar Receiver Model

Geometry

A cross-sectional view of the solar receiver is presented in Figure 23. The solar receiver is a classical evacuated tube receiver as used in parabolic trough plants.

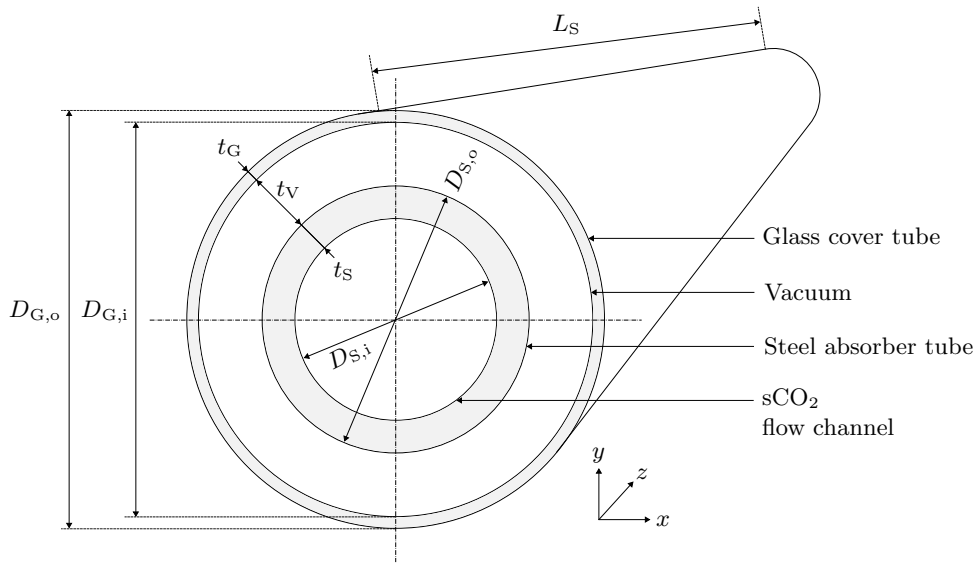

Figure 23: Cross-sectional view of the solar receiver

With the cross-sectional flow area of the channel known from Equation (94), the inner diameter of the flow tube ($D_{S,i}$) can be calculated as

$$A_c = \pi \frac{D^2}{4} \quad \Longrightarrow \quad D = \sqrt{\frac{4A_N}{\pi N}} \, . \tag{96}$$

With constant thicknesses for the steel absorber tube (t_S), vacuum (t_V) and glass cover tube (t_G), the other diameters can be calculated as a function of the inner diameter of the steel tube through

$$D_{S,o} = D_{S,i} + 2\,t_S \, , \tag{97}$$

$$D_{G,i} = D_{S,o} + 2\,t_V \, , \text{ and} \tag{98}$$

$$D_{G,o} = D_{G,i} + 2\,t_G \, . \tag{99}$$

The perimeter (or circumference) of each section can be calculated as

$$p = \pi\, D \, . \tag{100}$$

Multiplying the perimeter of each section by the length of the flow channel gives the surface area over which heat transfer occurs. The total surface area for all the flow channels is therefore

$$A_{\mathrm{s}} = N\,p\,L\ . \tag{101}$$

Flow Channel Element

The inputs for the flow channel element in Flownex® are available in Table 49 in Appendix D.1.

The number of parallel flow tubes is decided based on an existing 50 $\mathrm{MW_e}$ parabolic trough plant (SENER, 2018), which has 180 parallel tubes. Assuming that the plant configuration scales well, if the capacity is five times less (i.e. 10 $\mathrm{MW_e}$), it is assumed that the number of parallel solar receiver tubes would also be five times less (i.e. 36).

Solar Radiation Element $\left(\dot{Q}_{\mathrm{S}}\right)$

In order to model the solar radiation input to the receiver, node (S,o) is specified to be a heat source of magnitude $\dot{Q}_{\mathrm{S}}$, as determined from Equation (93). Node (S,o) is the hottest node in the solar receiver. Heat is transferred from this node both inwards towards the $\mathrm{sCO_2}$ flow channel as well as outwards towards the environment.

Steel Absorber Tube Heat Transfer Element $\left(\dot{Q}_{\mathrm{T}}\right)$

The heat transfer through the steel absorber tube ($\dot{Q}_{\mathrm{T}}$) consists of a conduction heat transfer component ($\dot{Q}_{\mathrm{S,o}}$) and a convection heat transfer component ($\dot{Q}_{\mathrm{S,i}}$), connected in series such that

$$\dot{Q}_{\mathrm{T}} = \dot{Q}_{\mathrm{S,o}} = \dot{Q}_{\mathrm{S,i}}\ . \tag{102}$$

A schematic diagram of the heat transfer in the steel absorber tube is depicted in Figure 24. On the left hand side, in Figure 24(a), the composite heat transfer element as it appears in Flownex® and in Figure 22 is shown. On the right hand side, in Figure 24(b), the full thermal resistance network is shown.

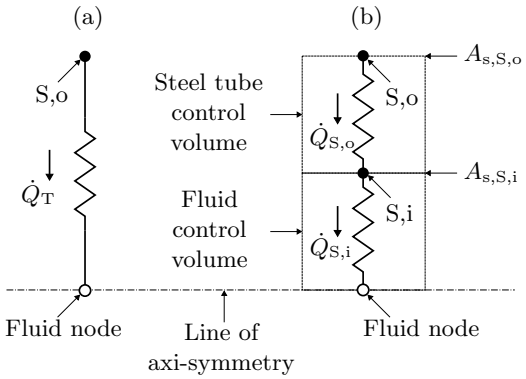

Figure 24: Heat transfer in the solar receiver steel absorber tube: (a) Flownex® model, (b) equivalent thermal resistance network

The heat transfer through the steel absorber tube ($\dot{Q}_{\mathrm{T}}$) is modeled using a *Composite Heat Transfer* element in Flownex®. This element models conduction through a solid and has several options for the heat transfer on the upstream and downstream surfaces. The upstream surface heat transfer option is set to *Adiabatic* because the heat transfer here is included in the $\dot{Q}_{\mathrm{V}}$ element. The downstream surface heat transfer option is set to *Convection*.

The inputs for the steel absorber tube heat transfer element in Flownex® are available in Table 50 in Appendix D.1.

Vacuum Heat Transfer Element $\left(\dot{Q}_{\mathrm{V}}\right)$

Between the outer surface of the steel tube and the inner surface of the glass tube is an evacuated gap (or *vacuum*). The heat transfer through this gap is exclusively by radiation and can be modeled using a *Surface Radiation* element in Flownex®. This element is of the *Two-surface enclosure* type and the form factor (view factor) is one, as is appropriate for two long, concentric cylinders (Çengel and Ghajar, 2015).

A schematic diagram of the heat transfer through the vacuum is presented in Figure 25.

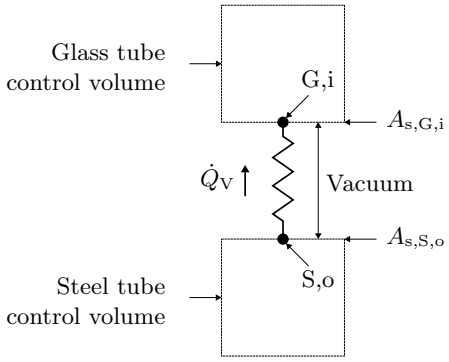

Figure 25: Heat transfer in the solar receiver vacuum

The inputs for the vacuum heat transfer element in Flownex® are available in Table 51 in Appendix D.1.

Glass Cover Tube Heat Transfer Element $\left(\dot{Q}_{\mathrm{G}}\right)$

The heat transfer through the glass cover tube ($\dot{Q}_{\mathrm{G}}$) consists of:

- conduction ($\dot{Q}_{\mathrm{G,i}}$) through the glass from the inner surface at node (G,i) to the outer surface at node (G,o),
- at the outer surface, convection ($\dot{Q}_{\mathrm{G,o,conv.}}$) with V_{wind} to the ambient air at T_{∞}, and
- at the outer surface, radiation ($\dot{Q}_{\mathrm{G,o,rad.}}$) to the environment at the effective sky temperature T_{sky}.

The convection and radiation heat transfers happen parallel to each other, such that

$$\dot{Q}_{\mathrm{G}} = \dot{Q}_{\mathrm{G,i}} = \dot{Q}_{\mathrm{G,o,conv.}} + \dot{Q}_{\mathrm{G,o,rad.}} \,. \tag{103}$$

This heat transfer process can be modeled in Flownex® using a *Composite Heat Transfer* element. As before, the upstream surface heat transfer option is set to *Adiabatic* because the heat transfer here is included in the $\dot{Q}_{\mathrm{V}}$ element. The downstream surface heat transfer option is set to *Convection and Radiation*. The radiation option is specified as *To ambient*.

A schematic diagram of the heat transfer in the glass absorber tube is depicted in Figure 26. On the left hand side, in Figure 26(a), the composite heat transfer element as it appears in Flownex® and in Figure 22 is shown. On the right hand side, in Figure 26(b), the full thermal resistance network is shown.

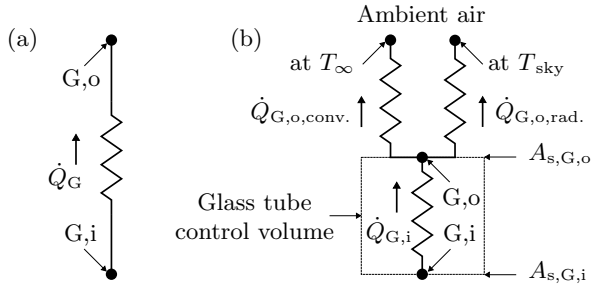

Figure 26: Heat transfer in the solar receiver glass cover tube:
(a) Flownex® model, (b) equivalent thermal resistance network

In the Flownex® model, the terminal element is the solid node (G,o) on the outer surface of the glass as shown in Figure 26(a) because the environment is not modeled as a separate element. However, in the thermal resistance network in Figure 26(b), the network actually terminates at the two environmental nodes (T_∞ for convection and T_{sky} for radiation).

The inputs for the glass absorber tube heat transfer element in Flownex® are available in Table 52 in Appendix D.1.

5.7. Details of the Recuperator Model

Geometry

The recuperator is a *printed circuit heat exchanger* or PCHE. A schematic diagram of a basic heat transfer unit of a PCHE in Figure 27(a) shows two identical rectangular flow channels – one each for the cold and hot side. The two flow channels are geometrically identical, and have a width of w_c and a height of h_c. Separating the channels is a wall of height h_w. The full PCHE *core* consists of many hundreds of these basic heat transfer units stacked horizontally and vertically, as depicted in Figure 27(b).

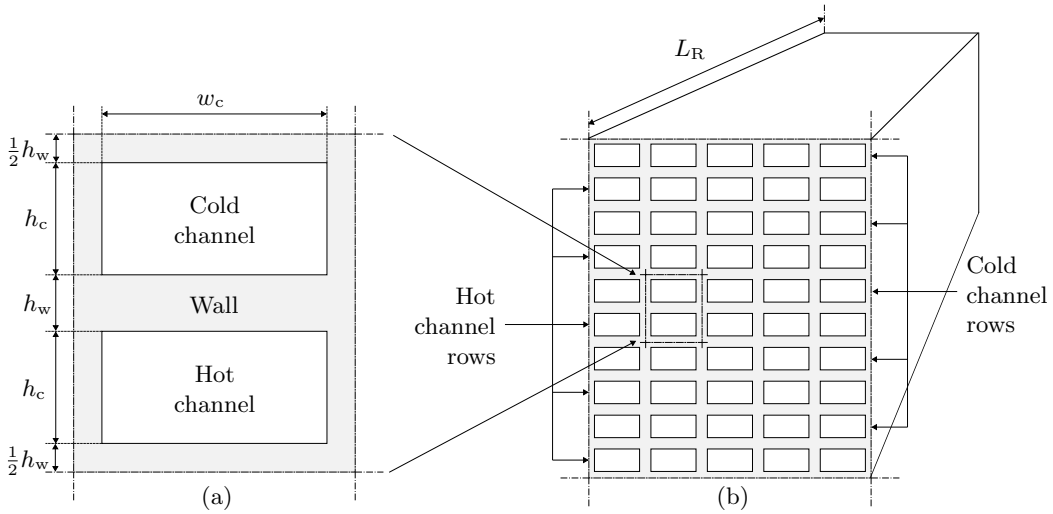

Figure 27: Cross-sectional view of the recuperator:
(a) basic heat transfer unit, (b) full heat exchanger core

The heat transfer analysis can be done for only one basic heat transfer unit, because it is assumed that every cold channel is identical to every other cold channel, and every hot channel is identical to every other hot channel. Therefore, every channel in a particular row of the heat exchanger is the same, with the rows alternating between cold and hot. There is no heat transfer between channels in the same row, because they are all at the same temperature. Heat transfer occurs only in the vertical direction between the channels.

In reality, some of the heat from one hot channel is transferred to the cold channel above it, and some of the heat is transferred to the cold channel below it. However, since this is repeated across the full exchanger, it makes no material difference if it is assumed, as for the current model, that all of the heat from a hot channel is transferred just to one cold control volume.

In order to reduce the number of design variables in the recuperator, the geometric variables of the channels are treated as constants, with the values as specified in Table 53 in Appendix D.2. These values correspond to typical PCHE channel sizes (Çengel and Ghajar, 2015).

For non-circular flow channels, Flownex® requires the perimeter and cross-sectional flow area to be specified. With reference to Figure 27(a), the perimeter is

$$p = 2\,w_\mathrm{c} + 2\,h_\mathrm{c}\ , \tag{104}$$

and the flow area is

$$A_\mathrm{c} = w_\mathrm{c} \times h_\mathrm{c}\ . \tag{105}$$

The number of flow channels for each side of the recuperator (which must be rounded to the nearest natural number to be physically relevant) is calculated as

$$N_\mathrm{R} = \frac{A_\mathrm{N}}{A_\mathrm{c}}\ . \tag{106}$$

The total surface area available for heat transfer on each side of the recuperator is calculated as the width of the flow channel, multiplied by the length of the channel, multiplied by the total number of flow channels per side, or

$$A_\mathrm{s} = w_\mathrm{c}\,L_\mathrm{R}\,N_\mathrm{R}\ . \tag{107}$$

Flow Channel Elements

The inputs for the flow channel elements in Flownex® are available in Table 54 in Appendix D.2.

Heat Transfer Element $\left(\dot{Q}_\mathrm{R}\right)$

The heat transfer in the recuperator ($\dot{Q}_\mathrm{R}$) consists of three parts;

- convection ($\dot{Q}_\mathrm{H}$) from the hot fluid to the surface of the wall at node (H),
- conduction ($\dot{Q}_\mathrm{W}$) through the wall from the hot side to the cold side, and
- convection ($\dot{Q}_\mathrm{C}$) from the surface of the wall at node (C) to the cold fluid.

All three processes occur in series, therefore

$$\dot{Q}_\mathrm{R} = \dot{Q}_\mathrm{H} = \dot{Q}_\mathrm{W} = \dot{Q}_\mathrm{C}\ . \tag{108}$$

This heat transfer process can be modeled in Flownex® using a *Composite Heat Transfer* element, with the heat transfer option on both the upstream and downstream surfaces set to *Convection*.

A schematic representation of the heat transfer in the recuperator is depicted in Figure 28. On the left hand side, in Figure 28(a), the composite heat transfer element as it appears in Flownex® and in Figure 22 is shown. On the right hand side, in Figure 28(b), the full thermal resistance network is shown.

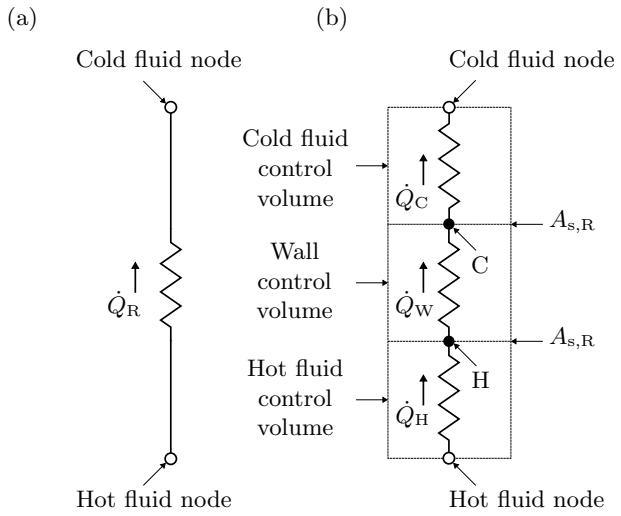

Figure 28: Heat transfer in the recuperator:
(a) Flownex® model, (b) equivalent thermal resistance network

The inputs for the heat transfer element in Flownex® are available in Table 55 in Appendix D.2.

5.8. Details of the Heat Sink Model

Geometry

The heat sink consists of a number of parallel flow channel tubes (N_{H}), each arranged in a serpentine-like fashion as depicted schematically in Figure 29. The total length of the flow channel, including the straight sections and bends, is L_{H}.

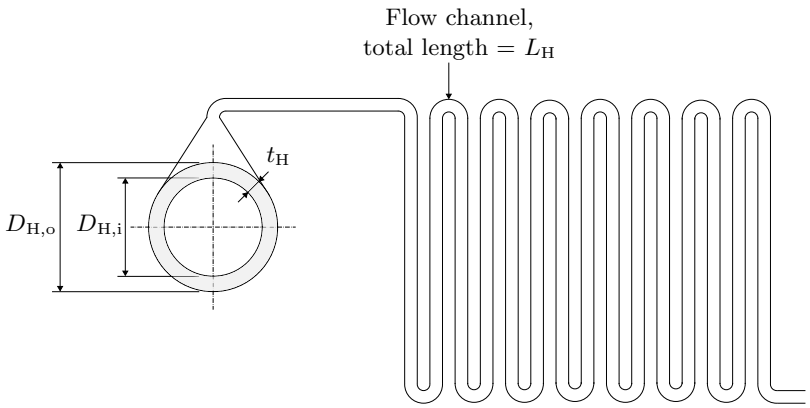

Figure 29: Schematic diagram of a heat sink tube

Annular fins are installed on the outside of the flow channel tube, as shown in Figure 30. If a more detailed heat sink model is required, the work by Kröger (2004) can be considered. For the purposes of this research however, it is assumed that the only effect of the fins is to increase the surface area available for heat transfer on the outside of the heat sink.

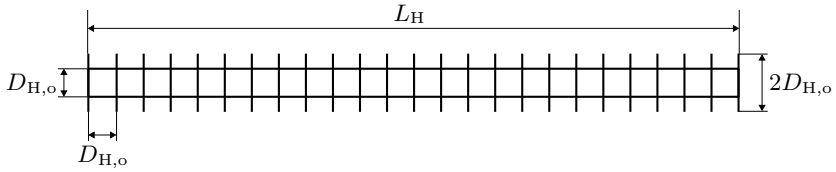

Figure 30: Schematic diagram of the fins on the heat sink

The diameter of each fin is twice the outer diameter of the flow tube (i.e. $2D_{\mathrm{H,o}}$) and the fins are spaced with a distance of one outer diameter (i.e. $D_{\mathrm{H,o}}$) between them, such that the total number of fins on one tube is calculated as

$$N_{\mathrm{F}} = 0.85 \frac{L_{\mathrm{H}}}{D_{\mathrm{H,o}}} , \tag{109}$$

where the 0.85 is an (estimated) factor to account for the reduction in the number of fins that can be installed as a result of the bends in the heat sink.

The surface area added by each fin is the surface area on two sides of an annulus. The total surface area added by all fins on one tube is therefore

$$A_{\mathrm{s,F}} = 2\left[\frac{\pi(2D_{\mathrm{H,o}})^2}{4} - \frac{\pi {D_{\mathrm{H,o}}}^2}{4}\right] N_{\mathrm{F}} = \frac{3\pi {D_{\mathrm{H,o}}}^2 N_{\mathrm{F}}}{2} \ , \tag{110}$$

into which Equation (109) is substituted to yield

$$A_{\mathrm{s,F}} = \frac{(0.85)(3)(\pi)}{2} D_{\mathrm{H,o}} L_{\mathrm{H}} \approx 4\, D_{\mathrm{H,o}} L_{\mathrm{H}} \ . \tag{111}$$

The total surface area of the entire heat sink is therefore

$$A_{\mathrm{s,H}} = N_{\mathrm{H}} \left(\pi\, D_{\mathrm{H,o}} L_{\mathrm{H}} + A_{\mathrm{s,F}}\right) \ , \tag{112}$$

with the outer diameter of the heat sink tube calculated as

$$D_{\mathrm{H,o}} = D_{\mathrm{H,i}} + 2\, t_{\mathrm{H}} \ . \tag{113}$$

The inner diameter of the heat sink tube is calculated from Equation (96).

Flow Channel Element

The inputs for the flow channel element are available in Table 56 in Appendix D.3.

The number of parallel flow tubes in the heat sink is chosen to match the number of parallel flow tubes in the solar receiver.

Heat Transfer Element $\left(\dot{Q}_{\mathrm{H}}\right)$

The heat transfer in the heat sink ($\dot{Q}_{\mathrm{H}}$) consists of four parts:

- convection ($\dot{Q}_{\mathrm{F}}$) from the fluid to the inner surface of the wall,
- conduction ($\dot{Q}_{\mathrm{T}}$) through the tube wall,
- at the outer surface of the wall, convection ($\dot{Q}_{\mathrm{H,conv.}}$) with V_{wind} to the ambient air at T_{∞}, and
- at the outer surface of the wall, radiation ($\dot{Q}_{\mathrm{H,rad.}}$) to the environment at the effective sky temperature T_{sky}.

The convection and radiation heat transfers happen in parallel with each other, such that

$$\dot{Q}_{\mathrm{H}} = \dot{Q}_{\mathrm{F}} = \dot{Q}_{\mathrm{T}} = \dot{Q}_{\mathrm{H,conv.}} + \dot{Q}_{\mathrm{H,rad.}} \ . \tag{114}$$

This heat transfer process can be modeled in Flownex® using a *Composite Heat Transfer* element. The upstream surface heat transfer option is set to *Convection*, and the downstream surface heat transfer option is set to *Convection and Radiation*. The radiation option is specified as *To ambient*.

A schematic diagram of the heat transfer in the heat sink is depicted in Figure 31. On the left hand side, in Figure 31(a), the composite heat transfer element as it appears in Flownex® and in Figure 22 is shown. On the right hand side, in Figure 31(b), the full thermal resistance network is shown.

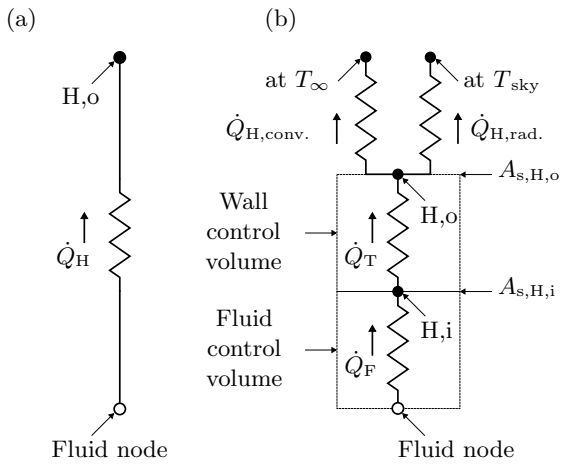

Figure 31: Heat transfer in the heat sink:
(a) Flownex® model, (b) equivalent thermal resistance network

In the Flownex® model, the terminal element is the solid node (H,o) on the outer surface of the heat sink tube as shown in Figure 31(a) because the environment is not modeled as a separate element. However, in the thermal resistance network in Figure 31(b), the network actually terminates at the two environmental nodes (T_∞ for convection and T_{sky} for radiation).

The inputs for the heat transfer element in Flownex® are available in Table 57 in Appendix D.3.

5.9. Model Validation

To validate the model of the thermal system, the following three aspects must be investigated:

- the temperature change ΔT per unit length of heat exchanger,
- the pressure change ΔP per unit length of heat exchanger, and
- the heat loss to the environment.

Temperature and Pressure Change Validation

The first two aspects are investigated by considering the experimental data from the SCARLETT test facility (Straetz *et al.*, 2018), which was developed as part of the sCO_2-HeRo project in Europe. One of the objectives of the facility was to provide experimental data for a printed circuit sCO_2 recuperator.

The experimental setup is described in greater detail by Straetz *et al.* (2018), but essentially it consists of a counter-current printed circuit heat exchanger with water on one side and sCO_2 on the other side. The water is heated up by an electrical heater and is pumped through the recuperator. The sCO_2 flowing in the other channel of the recuperator removes heat from the water.

The SCARLETT recuperator can be modeled similarly to the recuperator of the current research (see Section 5.7) except that, on its own, the recuperator must be given four explicit boundary conditions (stations 2, 3, 5 and 6 in Figure 22). The inlet temperature and pressure of the sCO_2 side is specified at station 2, and the mass flow rate of the sCO_2 side is specified at station 3. At station 6, the mass flow rate of the water side is specified.

To model the heater of the SCARLETT experiment, station 5 is made an interior flow node with a given heat input. Prior to station 5, a frictionless flow channel is added and the inlet temperature and pressure of the water side is then specified at its inlet boundary.

Details of the SCARLETT recuperator flow channel elements (Table 66) and heat transfer element (Table 67) are available in Appendix E.6.

An extensive experimental campaign was conducted by Straetz *et al.* (2018), with several combinations of sCO_2 inlet temperature and pressure values, sCO_2 mass flow rate values, water flow rate values and heater power levels being investigated (although the water mass flow rate and heater power are controlled together so that the water entering the recuperator is always at 286 °C).

The results of the temperature rise validation study are presented in Table 68 in Appendix E.6, and the results of the pressure drop validation study are presented in Table 69 in Appendix E.6. The results of the validation show that the Flownex® model matches the experimental data well, both in terms of temperature rise and in terms of pressure drop.

Heat Loss Validation

The heat loss from the solar receiver to the environment is validated by comparing the results from the developed model (corresponding to the design of the system developed in Chapter 6) with two sets of results from literature. Results of the developed model are detailed in Table 65 in Appendix E.5.

In the first validation study, the heat loss per unit length plotted against the average temperature on the outside of the steel absorber tube ($T_{S,o}$) is compared to experimental results from the commercially-available SCHOTT PTR®70 solar receiver (SCHOTT Solar, 2013). The experimental results are indicated by the square markers in Figure 32, whereas the result of the developed model is indicated by the circular marker. The developed model matches the experimental results well, under-predicting the heat loss by only 6.2%.

In the second validation study, the heat loss per unit length plotted against the inlet temperature of the fluid (T_3) is compared to a reference model of an sCO_2 solar receiver (Qiu *et al.*, 2017). Results from the reference model are indicated by the square markers in Figure 33, whereas the results of the developed model are indicated by the circular markers.

Using the same emissivity of 0.095 as for the previous study and as for the design of the system in the current research, the heat loss is under-predicted; whereas if the emissivity is changed to 0.18 to be consistent with the reference, the heat loss is over-predicted. This result is of minimal consequence however because the temperature of the fluid at the outlet of the solar receiver (T_4) is only 2 °C (less than 1% of 550 °C) lower if the higher emissivity value is used. The heat loss from the developed Flownex® model can therefore be considered as validated.

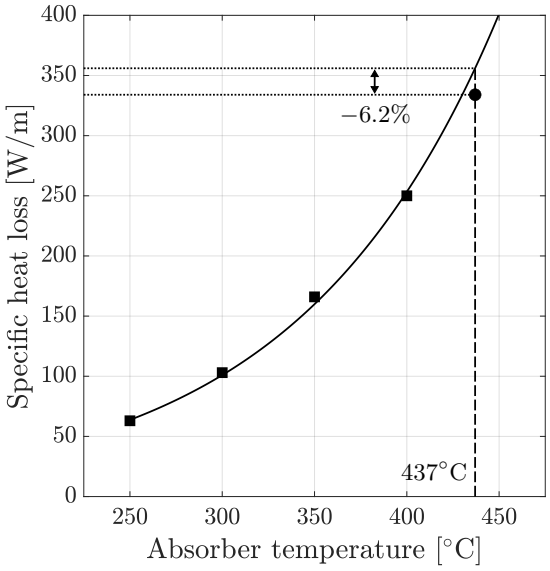

Figure 32: Heat loss from the solar receiver (SCHOTT Solar, 2013)

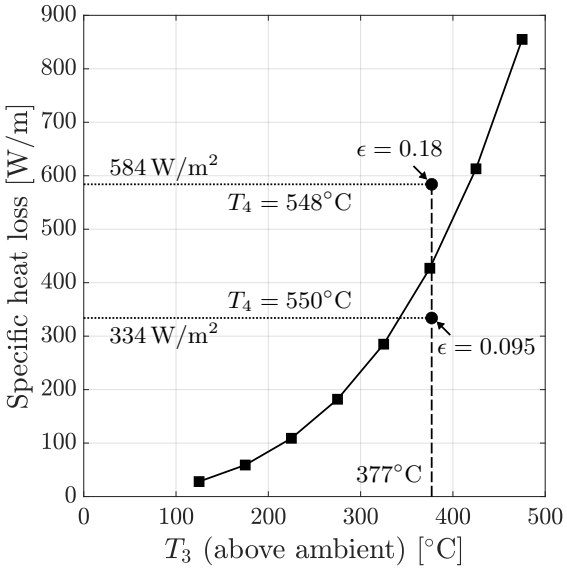

Figure 33: Heat loss from the solar receiver (Qiu *et al.*, 2017)

6. Application

A computational architecture is established (Chapter 2) and the analytical models of the system are available (Chapters 3, 4 and 5). The actual design procedure of the system is discussed in this chapter. It is introduced by way of an example, where the steps of the procedure are demonstrated as the *ab initio* design of the system is performed. The design procedure is divided into four stages: Stage 1 involves analyzing the thermodynamic model with the aim of finding values for many key design variables so that the design space of the system can be reduced before the more computationally expensive power- and thermal system models are analyzed. In Stage 2, the power- and thermal systems are analyzed concurrently with the aim of matching the design spaces of the two sub-systems. Stages 3 and 4 involve completing the detailed designs of the power- and thermal systems.

6.1. Stage 1

In Stage 1 of the design process, values for the turbine and compressor inlet temperatures, the compressor outlet pressure, the cycle mass flow rate and the turbine outlet pressure are selected. These key design variables are fixed in this first stage of the design process because they are optimization objectives themselves (Table 2), or because they have a significant influence on the cycle thermal efficiency (which itself is an optimization objective).

6.1.1. Turbine and Compressor Inlet Temperatures

The most efficient thermodynamic cycle is a reversible cycle operating between two isothermal reservoirs, known as the *Carnot cycle* (Borgnakke and Sonntag, 2014). The thermal efficiency of the Carnot cycle is

$$\eta_{\text{th}} = 1 - \frac{T_{\text{L}}}{T_{\text{H}}} \,, \tag{115}$$

where T_{L} is the absolute temperature of the heat sink reservoir and T_{H} is the absolute temperature of the heat source reservoir.

For a regenerative Brayton cycle, which does not have isothermal reservoirs, Equation (115) no longer holds. However, Borgnakke and Sonntag (2014) derive the efficiency of this cycle and show that

$$\eta_{\text{th}} \propto 1 - \frac{T_{\text{L}}}{T_{\text{H}}} = 1 - \frac{T_1}{T_4} \,, \tag{116}$$

where the numbers refer to the stations of the current system (Figure 1). T_1 is the lowest temperature in the cycle, at the inlet of the compressor, and T_4 is the highest temperature in the cycle, at the inlet of the turbine.

This result indicates that – for both the Carnot cycle and the regenerative Brayton cycle – the heat source temperature must be maximized and the heat sink temperature must be minimized in order to maximize the cycle thermal efficiency.

Considering the system design objectives introduced in Table 2, cycle thermal efficiency should be maximized (f_1) but the cycle maximum temperature T_4 should ideally be minimized in order to reduce the cost of the system (f_3). Without a detailed economic model to make this trade-off between efficiency and cost, for the current research a fixed value of $T_4 = 550\,°\text{C}$ is selected for the design. This temperature also corresponds to the maximum temperature supported by conventional molten salt thermal energy storage systems in CSP plants (Cheang *et al.*, 2015).

With the heat source temperature T_4 fixed, the heat sink outlet temperature T_1 should ideally be as low as possible so that the ratio in Equation (116) can be maximized. In this research, the cycle is designed to remain in the supercritical phase of CO_2 at all times, and therefore the lowest allowable temperature is the critical temperature of CO_2 which is 31 °C. To provide a small buffer to the critical point and to allow for a possible temperature drop in the nozzle section of the compressor, the heat sink outlet temperature for the design is chosen to be $T_1 = 35\,°\text{C}$.

6.1.2. Compressor Outlet Pressure

To investigate the trade-off between objective f_1, which is to maximize cycle thermal efficiency η_{th}, and objective f_2, which is to minimize the maximum pressure P_2 (see Table 2), the thermodynamic model developed in Chapter 3 is analyzed with the fixed values for T_1 and T_4.

To present only the Pareto front of the thermodynamic model as a plot of f_1 and f_2 (or η_{th} and P_2) is not meaningful, because it will not give any insight with regards to how this relationship varies given the true performance of the components. The relationship between η_{th} and P_2 may be different depending on how efficient the turbomachines are or how effective the recuperator is. Therefore, it is more meaningful to present the Pareto front of η_{th} and P_2 with the thermodynamic model analyzed at different constant values of turbomachine efficiency and recuperator effectiveness.

Figure 34 depicts the relationship between η_{th} and P_2 as recuperator effectiveness varies (with a constant value of compressor and turbine efficiency), and Figure 35 depicts the relationship between η_{th} and P_2 as compressor and turbine efficiency varies (with a constant value of recuperator effectiveness).

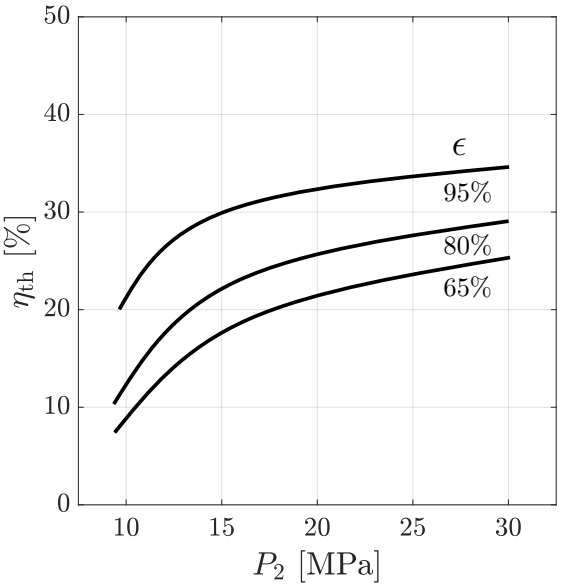

Figure 34: Thermodynamic model[†] results: Pareto front of cycle thermal efficiency and compressor outlet pressure for different recuperator effectiveness values

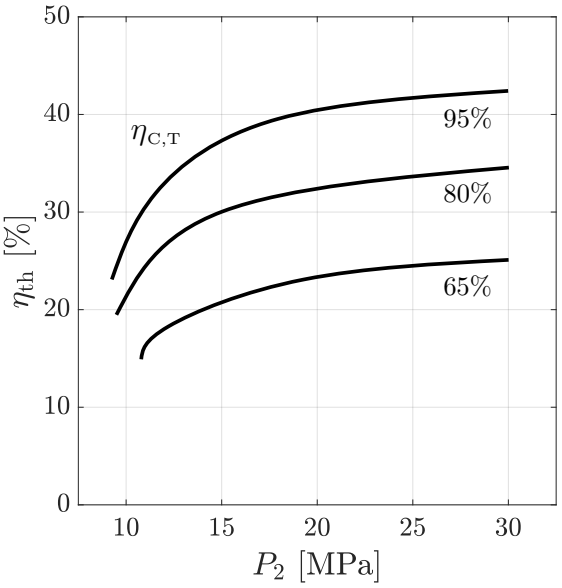

Figure 35: Thermodynamic model[‡] results: Pareto front of cycle thermal efficiency and compressor outlet pressure for different turbomachinery efficiency values

It is evident that regardless of the performance of the components in the cycle, the compressor outlet pressure should be maximized in order to maximize thermal efficiency. Although the gradient of the curves start to flatten out beyond 20 MPa, some improvement in cycle efficiency is still possible – especially if the recuperator effectiveness is low (see the lower two curves in Figure 34).

An earlier study (Dostal *et al.*, 2004) confirmed that the improvement in cycle efficiency is no longer significant beyond about 25 MPa, and therefore there is little value in operating the cycle at higher pressures than this.

Given that supercritical steam power cycles operate at pressures up to 35 MPa (Stein and Buck, 2017), 25 MPa can be regarded as a relatively low maximum pressure. Therefore, a value of $P_2 = 25\,\text{MPa}$ is favorable both for objective f_1 and for objective f_2.

[†] Fixed design variables: $T_4 = 550\,^\circ\text{C}$, $T_1 = 35\,^\circ\text{C}$, $\eta_\text{C} = \eta_\text{T} = 80\%$
[‡] Fixed design variables: $T_4 = 550\,^\circ\text{C}$, $T_1 = 35\,^\circ\text{C}$, $\epsilon = 95\%$

6.1.3. Mass Flow Rate

To investigate the trade-off between objective f_1, which is to maximize cycle thermal efficiency η_{th}, and objective f_5, which is to minimize the cycle mass flow rate $\dot{m}$ (see Table 2), the thermodynamic model developed in Chapter 3 is re-analyzed.

Again, it is is more meaningful to display the Pareto front of f_1 vs f_5 (or η_{th} vs $\dot{m}$) at different constant values of turbomachine efficiency and recuperator effectiveness.

Figure 36 depicts the relationship between η_{th} and $\dot{m}$ as recuperator effectiveness varies (with a constant value of compressor and turbine efficiency), and Figure 37 depicts the relationship between η_{th} and $\dot{m}$ as compressor and turbine efficiency varies (with a constant value of recuperator effectiveness).

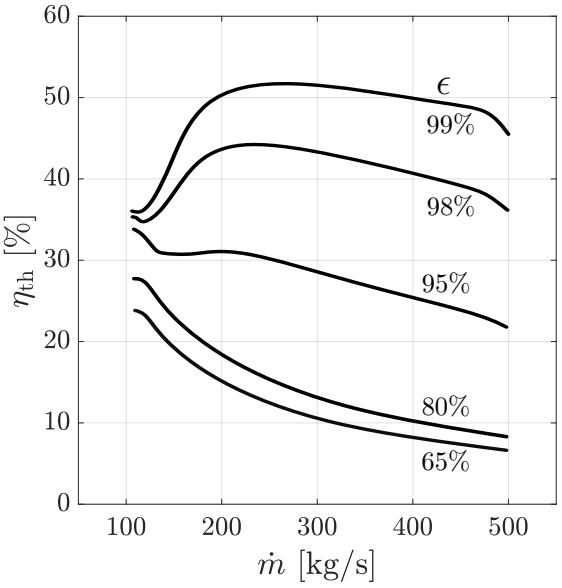

Figure 36: Thermodynamic model† results: Pareto front of cycle thermal efficiency and mass flow rate for different recuperator effectiveness values

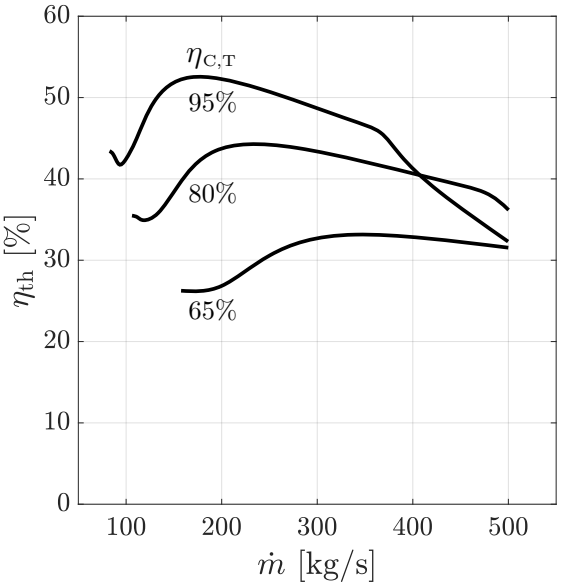

Figure 37: Thermodynamic model‡ results: Pareto front of cycle thermal efficiency and mass flow rate for different turbomachinery efficiency values

Optimal Mass Flow Rate with Variable Recuperator Effectiveness

There is little change in cycle efficiency for a given mass flow rate if the recuperator effectiveness increases from 65% to 80% in Figure 36: a smooth, monotonically-decreasing trend is observed and in both cases the maximum cycle efficiency is achieved if the mass flow rate is minimized.

† Fixed design variables: $T_4 = 550\,^{\circ}\text{C}$, $T_1 = 35\,^{\circ}\text{C}$, $P_2 = 25\,\text{MPa}$, $\eta_{\text{C}} = \eta_{\text{T}} = 80\%$
‡ Fixed design variables: $T_4 = 550\,^{\circ}\text{C}$, $T_1 = 35\,^{\circ}\text{C}$, $P_2 = 25\,\text{MPa}$, $\epsilon = 95\%$

If the recuperator effectiveness is increased to 95%, the maximum cycle efficiency is again achieved when the mass flow rate is minimized, but the trend is no longer smooth and monotonic. As the mass flow rate increases, the cycle efficiency drops from the initial peak and reaches a plateau between 130 kg/s and 220 kg/s, before dropping further.

A significantly different trend is observed when the recuperator effectiveness increases to 98%. No longer is the maximum cycle efficiency achieved at the minimum mass flow rate, but instead the cycle efficiency is low at low mass flow rates and increases with increasing mass flow rate until an optimum is reached at at around 230 kg/s. After this point, the cycle efficiency drops linearly. The same trend is observed if the recuperator effectiveness is 99%, but in this case the optimal mass flow rate is higher at around 260 kg/s.

There are two conclusions to be drawn from this observation. Firstly, the efficiency of the cycle is disproportionately affected by recuperator effectiveness. A 15% increases in recuperator effectiveness from 65% to 80% and again from 80% to 95% yields only about a 5% increase in maximum theoretical cycle efficiency; but a 3% increase in recuperator effectiveness from 95% to 98% yields an increase in maximum theoretical cycle efficiency of 11%, and a 1% increase in recuperator effectiveness from 98% to 99% yields an increase in maximum theoretical cycle efficiency of 7%. A highly effective recuperator is therefore essential for maximizing the thermal efficiency of the cycle.

Secondly, the optimal mass flow rate depends on the effectiveness of the recuperator. If the recuperator effectiveness is less than 95% the mass flow rate should be minimized, but if the recuperator effectiveness exceeds 95% this is no longer true and the optimal mass flow rate increases the more effective the recuperator is.

An appropriate choice for the mass flow rate therefore requires an assumption to be made regarding what level of recuperator effectiveness can be expected from the actual system. Assuming that the recuperator effectiveness of the actual system is at least 98%, a mass flow rate of $\dot{m} = 200\,\text{kg/s}$ is a reasonable choice because the possible increase in maximum cycle efficiency beyond this value is negligible. This value would therefore be a favorable choice both for objective f_1 and for objective f_5 (see Table 2).

Optimal Mass Flow Rate with Variable Turbomachinery Efficiency

The optimal mass flow rate depends not only on the effectiveness of the recuperator but also on the efficiency of the turbomachines. Figure 37 shows that the lower the efficiency of the turbomachines, the higher the minimum cycle mass flow rate is and the higher the optimal mass flow rate is. For example, if the turbomachines are 95% efficient then the minimum mass flow rate at which the cycle can operate is 80 kg/s, and the optimal mass flow rate is around 170 kg/s. Contrast this to the case where the turbomachines are 65% efficient, then the minimum mass flow rate at which the cycle can operate doubles to a value of 160 kg/s and the optimum also doubles to about 350 kg/s.

Assuming that the turbomachines of the real system are at least 80% efficient, a mass flow rate of 200 kg/s remains a reasonable choice because it is near the optimum in both the 80% turbomachine efficiency case and in the 95% turbomachine efficiency case.

6.1.4. Pressure Ratio and Turbine Outlet Pressure

At this point of the design process, the minimum cycle temperature T_1, maximum cycle temperature T_4 and maximum cycle pressure P_2 is known (and also the mass flow rate $\dot{m}$). It would therefore be sensible to choose the minimum cycle pressure P_1 next because this would fix the lower and upper boundaries of the thermodynamic operating conditions of the cycle.

However, the analysis of the thermal system model in Flownex® is unnecessarily complicated if P_1 is a fixed value because it is the *outlet* boundary of the heat rejection side. As discussed in Section 5.2, the Flownex® solver requires temperature and pressure to be specified at the *inlet* boundary. For this reason it is more sensible to choose the turbine outlet pressure P_5 next, instead of the compressor inlet pressure P_1.

The compressor inlet pressure is related to the turbine outlet pressure through

$$P_1 = P_5 - \Delta P_{\text{hot}} \ , \tag{117}$$

where ΔP_{hot} is the pressure drop on the heat rejection (hot) side of the thermal system.

Based on the derivation of the regenerative Brayton cycle efficiency by Borgnakke and Sonntag (2014), it is known that the cycle efficiency is related to the cycle *pressure ratio*,

$$\text{PR} = \frac{P_2}{P_1} \ , \tag{118}$$

with the cycle efficiency increasing with decreasing pressure ratio.

Given that the compressor outlet pressure P_2 is already fixed, it is therefore evident that the value of P_1 should be maximized in order to maximize the cycle efficiency. This can be confirmed by considering the design space of the thermodynamic model in Figure 38, plotted with compressor inlet pressure P_1 on the primary vertical axis, the equivalent pressure ratio PR on the secondary vertical axis, and cycle efficiency on the horizontal axis. Three design spaces are shown in Figure 38, each corresponding to a different value for the efficiency of the turbomachines.

Regardless of what the efficiency of the turbomachines is, it is clear from Figure 38 that the cycle efficiency is maximized if the cycle pressure ratio PR is minimized (or equivalently, if the compressor inlet pressure P_1 is maximized).

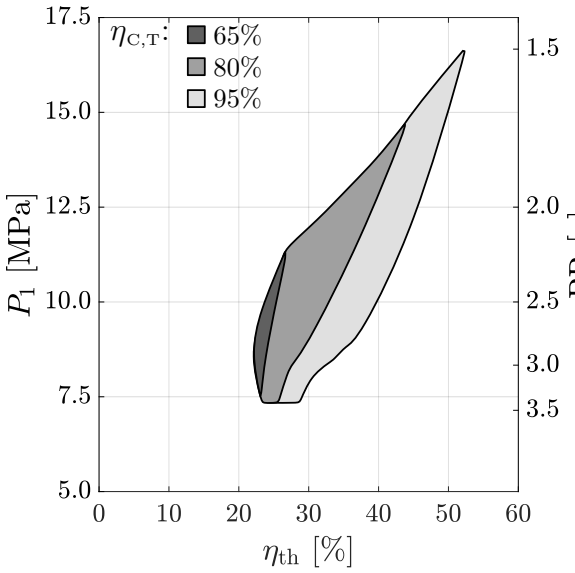

Figure 38: Thermodynamic model† design spaces: compressor inlet pressure and pressure ratio plotted against cycle thermal efficiency for different turbomachinery efficiency values

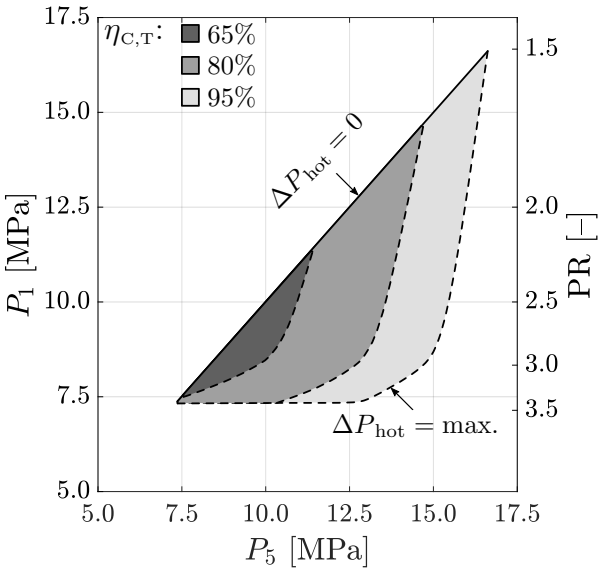

Figure 39: Thermodynamic model† design spaces: compressor inlet pressure and pressure ratio plotted against turbine outlet pressure for different turbomachinery efficiency values

Another interesting observation from Figure 38 is that the 95% turbomachine efficiency design space includes the 80% design space, and the 80% design space includes the 65% design space. The design space of the cycle therefore becomes larger as the turbomachines become more efficient. The cycle is also able to operate at lower pressure ratios and hence higher cycle efficiencies are possible with higher turbomachine efficiencies.

Consider that Equations (117) and (118) can be combined to yield

$$\mathrm{PR} = \frac{P_2}{P_5 - \Delta P_{\mathrm{hot}}} \,, \tag{119}$$

confirming that, in order to maximize cycle efficiency, turbine outlet pressure should be maximized and the pressure drop should be minimized.

With this in mind, Figure 38 becomes more relevant and useful if it is supplemented with Figure 39. This figure shows the same design spaces of the thermodynamic model as Figure 38, except that turbine outlet pressure P_5 replaces cycle efficiency on the horizontal axis.

The relevance of Figure 39 is that it graphically indicates the allowable pressure drop over the hot side of the thermal system. The solid 45° line connects the points where $P_1 = P_5$ and therefore represent the designs for which $\Delta P_{\mathrm{hot}} = 0$. The dotted lines on the opposite ends of the design spaces indicate the minimum allowable value of P_1 and therefore represent the maximum allowable ΔP_{hot} for a given value of P_5.

† Fixed design variables: $T_4 = 550\,^{\circ}\mathrm{C}$, $T_1 = 35\,^{\circ}\mathrm{C}$, $P_2 = 25\,\mathrm{MPa}$, $\dot{m} = 200\,\mathrm{kg/s}$, $\epsilon = 98\%$

Examples of Different Design Points

Figures 38 and 39 should be used in conjunction with each other in order to make an appropriate design decision for the turbine outlet pressure. This is explained by way of the following three examples of possible design choices.

Consider three possible design choices (A, B and C) in Figures 40 and 41.

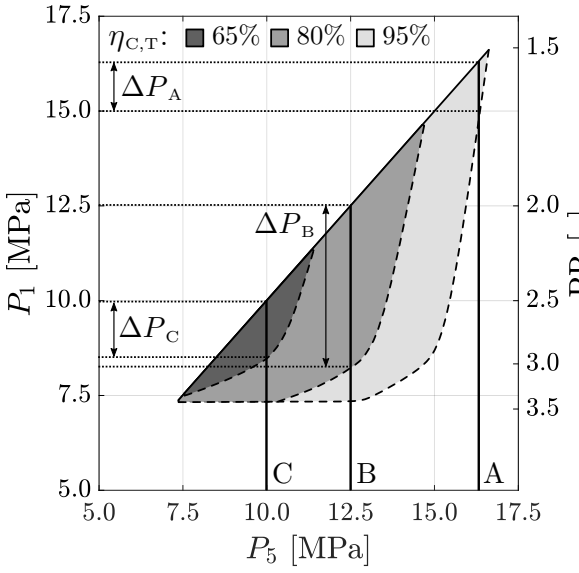

Figure 40: Annotated version of Figure 39 showing three possible designs

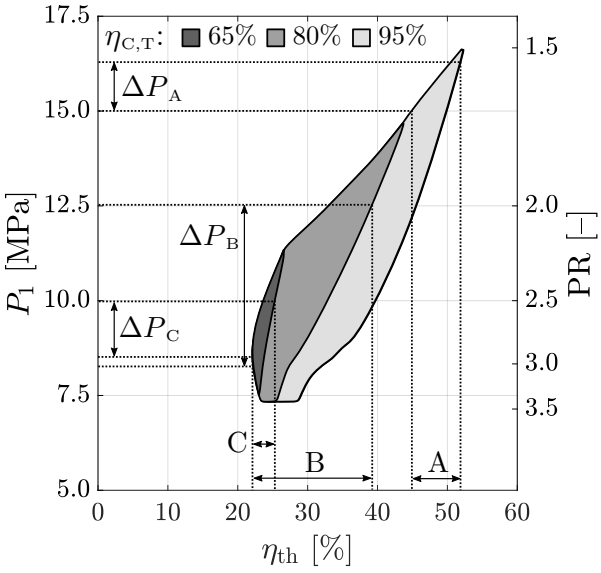

Figure 41: Annotated version of Figure 38 showing three possible designs

Assuming that the turbomachines are 95% efficient, then choice A with $P_5 = 16.3\,\text{MPa}$ is possible. A vertical line drawn upwards from the horizontal axis of Figure 40 at point A to where the dotted line is intercepted shows that the minimum allowable P_1 for this design is 15.0 MPa. The maximum pressure drop is therefore $\Delta P_A = 16.3 - 15.0 = 1.3\,\text{MPa}$.

If the turbomachines are 80% efficient, then the previous choice would no longer be possible because it falls outside of the 80% design space. Instead, a lower value such as $P_5 = 12.5\,\text{MPa}$ at point B in Figure 40 is required. The dotted line is intercepted at $P_1 = 8.2\,\text{MPa}$, which indicates a maximum pressure drop of $\Delta P_B = 12.5 - 8.2 = 4.3\,\text{MPa}$.

For turbomachines that are 65% efficient, the high pressures at point A or B cannot be supported; an even lower value such as $P_5 = 10.0\,\text{MPa}$ at point C in Figure 40 is required. The dotted line is intercepted at $P_1 = 8.5\,\text{MPa}$, which indicates a maximum pressure drop of $\Delta P_C = 10.0 - 8.5 = 1.5\,\text{MPa}$.

Figure 41 is the same as Figure 38 except that the ΔP ranges from Figure 40 are indicated as well. If the horizontal lines are followed from the primary vertical axis of Figure 41 to where they intercept the design spaces, the corresponding cycle thermal efficiency bracket can then be read-off from the horizontal axis of the figure.

Note however that this is just the *estimated* cycle efficiency, based purely on the lowest and highest efficiency values where the design space boundaries are intercepted. This is a graphical approach, and serves only to give a broad indication of the expected efficiency. It is not intended to be precise, because it is based on an analysis of the surrogate model (with assumed component performance levels) and not on the detailed sub-system models (with the actual component performance levels).

The ΔP_{A} range corresponds to a best-case cycle thermal efficiency of 52% and a worst-case cycle efficiency of 45%. Similarly, the ΔP_{B} range corresponds to a best-case cycle efficiency of 39% and a worst-case cycle efficiency of 22%, and the ΔP_{C} range corresponds to a best-case cycle efficiency of 25% and a worst-case cycle efficiency of 22%.

For convenience, the above information is summarized in Table 5.

Table 5: Comparison of three possible design points

Point	P_5 [MPa]	$P_{1,\min}$ [MPa]	$\Delta P_{\max}$ [MPa]	Best PR	Worst PR	Best η_{th} [%]	Worst η_{th} [%]
A	16.3	15.0	1.3	1.53	1.67	52	45
B	12.5	8.2	4.3	2.00	3.05	39	22
C	10.0	8.5	1.5	2.50	2.94	25	22

Based on these three examples, it is evident that in order to choose the turbine outlet pressure P_5 requires two assumptions to be made:

- what the expected minimum efficiency of the turbomachines of the real system are, so that the appropriate design space is used, and
- what the expected maximum magnitude of the pressure drop on the hot side of the real thermal system is, so that a value for P_5 can be chosen in a region of the design space where that pressure drop can be allowed.

The aim should be to have the cycle design point as close as possible to the top right-hand-side corner of Figures 40 and 41 (for example, design point A). A design here corresponds to the minimum pressure ratio and therefore the maximum cycle efficiency.

However, the closer the cycle design point is to the top right-hand-side corner, the more sensitive it becomes to both turbomachine efficiency (because the design spaces of the less efficient turbomachines are excluded) and pressure drop (because the dotted line converges towards the solid line).

Design point B is more practical, because a large pressure drop is supported (i.e. a large vertical distance between the dotted line and the solid line) and also because it includes the design spaces of both the 80% and 95% efficient turbomachines.

Furthermore, if it turns out that the real turbomachines are more efficient than the assumed efficiency, then the vertical distance between the dotted line and the solid lines grow larger and hence a larger pressure drop is supported. For example, if the turbomachines for design point B were 95% efficient instead of 80%, then the dotted line would be intercepted at $P_1 = 7.5\,\mathrm{MPa}$ and therefore the allowable pressure drop is up to $\Delta P_{\mathrm{B}} = 12.5 - 7.5 = 5.0\,\mathrm{MPa}$.

If the designer specifies a high value for P_5 (such as at point A), it will be harder to design a real system that can operate at that specification, because the turbomachines have to be very efficient and the pressure drop in the system must be very low. On the other hand, if the designer specifies a lower value for P_5 (such as at point B), it will be easier to design a real system that can operate at that specification because there is more flexibility regarding the supported turbomachine efficiency and pressure drop; but at the cost of not being able to achieve a high cycle efficiency.

It is up to the designer – based on experience or previous design iterations – to make a selection of the turbine outlet pressure that is optimistic enough (i.e. similar to point A) to allow for a low pressure ratio and therefore high cycle efficiency, but conservative enough (i.e. similar to point B) that allows design flexibility with regards to turbomachine efficiency and pressure drop.

For the current design, a value of $P_5 = 12.5\,\text{MPa}$ (corresponding to point B) is selected.

6.1.5. Review of the Design Space after Stage 1

Stage 1 of the design process is now completed. Decisions have been made on the values of five of the ten shared design variables. The top half of Table 6 summarizes these decisions.

Table 6: Noteworthy updates to the design space in Stage 1

Variable	Type of Update	Details of Update	Unit
T_4	Initial range → Fixed value	32 – 700 → 550	°C
T_1	Initial range → Fixed value	32 – 700 → 35.0	°C
$* P_2$	Initial range → Fixed value	7.38 – 30 → 25.0	MPa
$* \dot{m}$	Initial range → Fixed value	1 – 1 000 → 200	kg/s
$* P_5$	Initial range → Fixed value	7.38 – 30 → 12.5	MPa
$* A_N$	Initial range → Solution-defined range	$1 - 1 \times 10^6 \rightarrow 15.2 \times 10^3 - 1 \times 10^6$	mm^2
$* T_2$	Initial range → Solution-defined range	32 – 700 → 53.4 – 69.6	°C
$* T_5$	Initial range → Solution-defined range	32 – 700 → 473 – 484	°C
P_1	Initial range → Solution-defined range	7.38 – 30 → 8.92 – 12.5	MPa
P_4	Initial range → Solution-defined range	7.38 – 30 → 22.8 – 25	MPa

Each design decision involved choosing a reasonable value for the variable based on the information available from analyzing the thermodynamic model. Once a decision has been made, the lower and upper bounds for that variable is changed to be equal to each other so that the variable is then treated as a constant for the remainder of the design process.

With the five variables in the top half of Table 6 treated as constants, the system has essentially now been given five additional equality constraints. As a result, the design space of the system is expected to change – becoming smaller to account for these new constraints.

The power system on its own is analyzed to see how it is affected by these new equality constraints. Results are presented in the bottom half of Table 6. These variables were all initially bounded by the lower and upper bounds set by the designer as set out in Table 26 in Appendix A.3, but are now bound to the range in which valid solutions are possible.

The following updates to the design space are observed:

- the lower bound on the nominal flow area is considerably higher than the initial lower bound, but the initial upper bound is still allowed,
- the valid compressor outlet temperature range is small ($\sim 15\,°C$),
- the valid turbine outlet temperature range is even smaller ($\sim 10\,°C$),
- the compressor and turbine inlet pressure ranges are relatively small ($\sim 3\,MPa$).

6.2. Stage 2

The aim of Stage 2 is to select an appropriate nominal flow area A_N which would establish geometric compatibility between the components of the system. This requires concurrent analysis of the power system model and the thermal system model.

As discussed in Section 2.4, the MATLAB® model of the power system is relatively straightforward to analyze because it only requires updating the lower bounds and upper bounds to the values set out in Table 6. On the other hand, the Flownex® model of the thermal system is more complicated to analyze because it requires a Monte Carlo simulation if there are any unknown inputs.

The variables indicated with the asterisk ($*$) in Table 6 are the variables that need to be supplied as inputs to the thermal system analysis. Three of these variables have been fixed and can be treated as constants whilst three are still unknown. Given the reasonably small range of values for T_2 and T_5, a Monte Carlo simulation is practical for these two variables. Unfortunately, the range for the nominal flow area A_N still covers two orders of magnitude which means that a Monte Carlo simulation with this variable is not practical.

It is therefore more convenient to estimate a value for the nominal flow area, and to treat it as a constant instead. If the estimated value is appropriate, then the design process can proceed to Stage 3; otherwise a different value needs to be estimated and the power- and thermal systems should be re-analyzed with the new value. What constitutes an appropriate value for the nominal flow is explained by way of three examples in the next sections.

6.2.1. Example of an Appropriate Nominal Flow Area

The first example shows how an appropriate nominal flow area can be identified. It is assumed that a value of $175\,000\,\text{mm}^2$, which is an appropriate value, is estimated for the nominal flow area. An analysis of the thermal system with this nominal flow area value reveals the design space as presented in Figure 42. The shaded band is the design space as plotted with heat sink outlet (compressor inlet) pressure P_1 on the primary vertical axis, against recuperator length L_R on the horizontal axis.

The design space appears as a band because it represents the design space of the complete thermal system, not just the recuperator. The top of the band therefore represents the thermal system designs with the shortest heat sink lengths, hence the outlet pressure is higher for a given length of recuperator; the bottom of the band represents the thermal system designs with the longest heat sink lengths, hence the outlet pressure is lower for a given length of recuperator. The longer the recuperator is, the greater the pressure drop through it is, hence the downward slope of the band.

The curve in Figure 42 is the design space of the thermal system, with the maximum possible recuperator effectiveness ϵ, plotted on the secondary vertical axis, for a given recuperator length on the horizontal axis. The design space appears as a curve rather than as a surface, because the effectiveness of the recuperator is dominated by its length. The effectiveness rises sharply with increasing recuperator length and eventually approaches an asymptote of 100%.

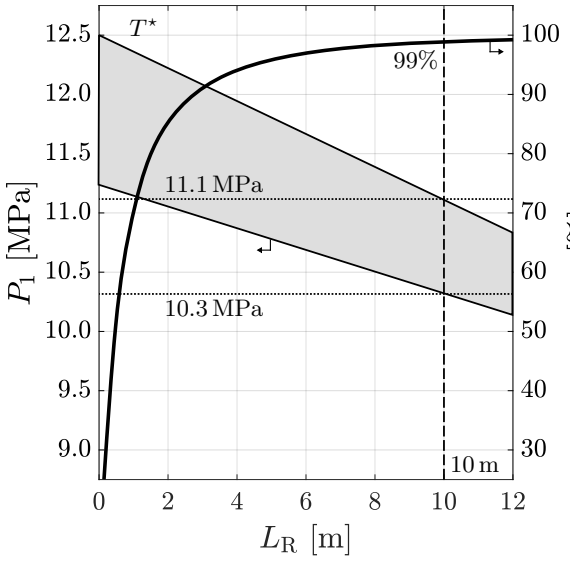

Figure 42: Thermal system† design space: heat sink outlet (compressor inlet) pressure and recuperator effectiveness plotted against recuperator length

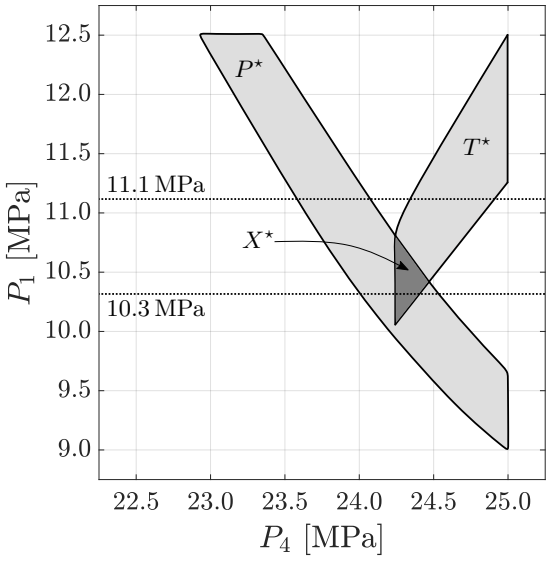

Figure 43: Power system‡ design space and thermal system† design space: heat sink outlet (compressor inlet) pressure plotted against solar receiver outlet (turbine inlet) pressure

Based on the discussion in Section 6.1.3, a recuperator with a high effectiveness is required because:

- it is essential for an efficient overall system, and
- for the selection of the optimal mass flow rate, it was assumed that the real system would have a recuperator with a high effectiveness.

To achieve a high effectiveness, a relatively long recuperator length is required. A recuperator with a length of $L_R = 10\,\text{m}$ is a good choice: it corresponds to a maximum effectiveness of 99% in Figure 42.

A vertical line drawn upwards from the horizontal axis at $L_R = 10\,\text{m}$ in Figure 42 intersects the bottom and top of the pressure band at 10.3 MPa and 11.1 MPa, respectively. This is the range of allowable heat sink outlet pressure values, for the chosen nominal flow area and recuperator length.

The two horizontal lines that indicate these pressures in Figure 42 are duplicated in Figure 43. This figure depicts the power system design space ($P^\star$) and the thermal system design space ($T^\star$), both with a nominal flow area of $175\,000\,\text{mm}^2$ specified. The heat sink outlet (compressor inlet) pressure P_1 is plotted against the solar receiver outlet (turbine inlet) pressure P_4.

† Fixed design variables: $P_2 = 25\,\text{MPa}$, $\dot{m} = 200\,\text{kg/s}$, $P_5 = 12.5\,\text{MPa}$, $A_N = 175\,000\,\text{mm}^2$

‡ Fixed design variables: $T_4 = 550\,°\text{C}$, $T_1 = 35\,°\text{C}$, $P_2 = 25\,\text{MPa}$, $\dot{m} = 200\,\text{kg/s}$, $P_5 = 12.5\,\text{MPa}$, $A_N = 175\,000\,\text{mm}^2$

The two design spaces intersect each other in the small area indicated by the darker shading. This the design space for the complete system ($X^\star$). The fact that the two sub-system design spaces overlap confirms that a valid design for the complete system is possible for the nominal flow area that was chosen (see Figure 7 in Chapter 2 where the concept of design space matching is introduced). A clear sign of an incorrect flow area would be if the two design spaces were mutually exclusive.

Moreover, the intercept between the two design spaces happens within the pressure range indicated by the two horizontal lines. This means that a valid design for the complete system is not only possible for the chosen flow area, but also for the chosen length of recuperator. This is an indication that the nominal flow area that was chosen is appropriate.

Consider that in Figure 43 only a part of the complete system design space falls within the indicated pressure range. This is acceptable; it is not necessary for the full system design space to fall within the indicated pressure range. The expectation is that – given the relatively low required heat sink outlet temperature – the heat sink will in all likelihood be relatively long and therefore the pressure drop through it will be relatively high. This means that the final system design would probably be near the lower of the two P_1 lines, and this is where the design space of the complete system is.

Nevertheless, this is an assumption. If it turns out that that the system design does not need a long heat sink and the pressure drop through it is less, the system design would fall closer to the top P_1 line and therefore a different nominal flow area is required to shift the intercept between the two design spaces upwards towards the top line in Figure 43.

The examples in the following two sections show what happens to the design spaces if the nominal flow area is a different value that is no longer appropriate.

6.2.2. Example of an Excessively Small Nominal Flow Area

The design spaces for a smaller nominal flow area – $125\,000\,\text{mm}^2$ in this case – is depicted in Figures 44 and 45.

Comparing Figure 44 with Figure 42 reveals that a smaller nominal flow area changes the thermal system design space in three ways – the negative gradient of the pressure band becomes steeper, the width of the pressure band increases, and the resulting overall thermal system design space is larger. These effects are attributed to the fact that for a smaller flow area, the velocity of the flow is faster and hence the frictional pressure drop is higher.

The steeper negative gradient indicates that – for the same length of recuperator – the system design with the smaller flow area in Figure 44 has a lower value of P_1 compared to the system design with the larger flow area in Figure 42. The wider pressure band also reveals that the value of P_1 is more sensitive to the length of the heat sink.

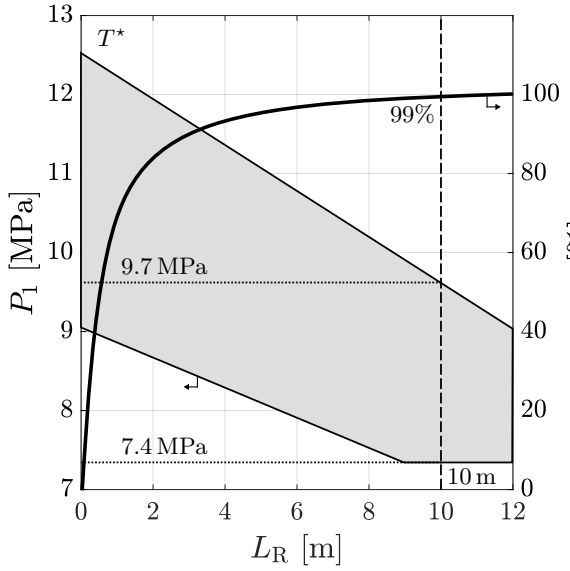

Figure 44: Thermal system† design space: heat sink outlet (compressor inlet) pressure and recuperator effectiveness plotted against recuperator length

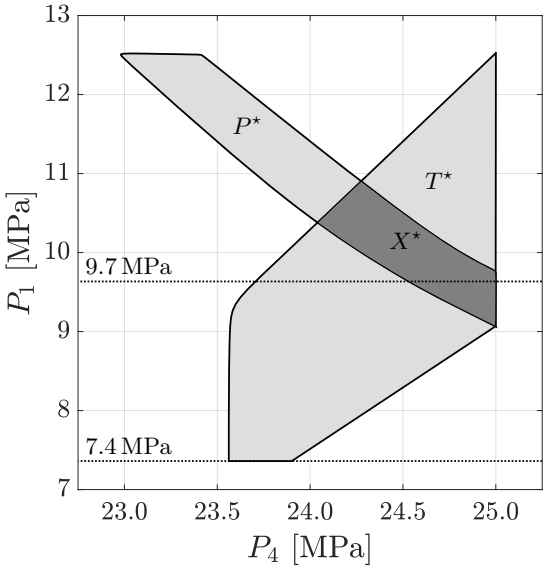

Figure 45: Power system‡ design space and thermal system† design space: heat sink outlet (compressor inlet) pressure plotted against solar receiver outlet (turbine inlet) pressure

The effectiveness curve changes little from Figure 42 to Figure 44. Again, a recuperator length of 10 m would be a good choice because it corresponds to an effectiveness of 99% in Figure 44. The vertical line drawn from the horizontal axis in Figure 44 at this recuperator length intersects the pressure band at 7.4 MPa and at 9.7 MPa.

These two pressure lines are duplicated in Figure 45, which depicts the power system and thermal system design spaces ($P^\star$ and $T^\star$, respectively) at a flow area of 125 000 mm^2. Although the design spaces of the two sub-systems overlap, most of the overlap happens at a higher pressure than the top pressure line. A valid design for the complete system is therefore unlikely to be possible for this combination of flow area and recuperator length, because it is expected that the system design would be close to the lower of the two P_1 lines. It is evident that for this combination, the pressure drop is generally too high and the resulting heat sink outlet pressure is therefore generally too low.

† Fixed design variables: $P_2 = 25$ MPa, $\dot{m} = 200$ kg/s, $P_5 = 12.5$ MPa, $A_N = 125\,000$ mm^2

‡ Fixed design variables: $T_4 = 550$ °C, $T_1 = 35$ °C, $P_2 = 25$ MPa, $\dot{m} = 200$ kg/s, $P_5 = 12.5$ MPa, $A_N = 125\,000$ mm^2

If the recuperator length is chosen to be shorter, say 4 m, then Figure 46 shows that the pressure range would be between 8.3 MPa and 11.4 MPa instead, which is sufficient to encapsulate the complete system design space in Figure 47.

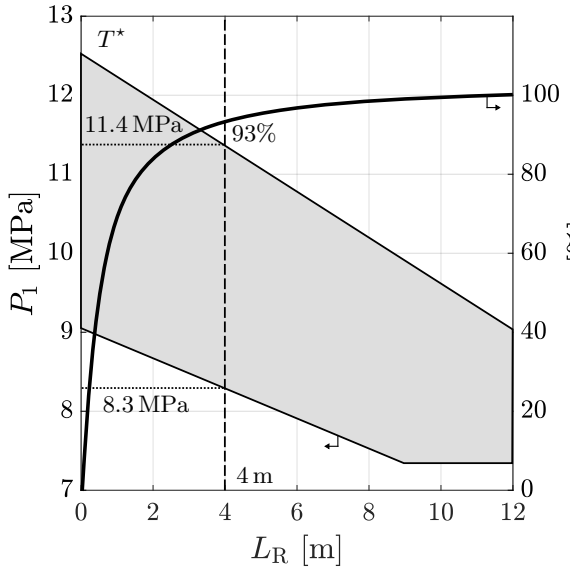

Figure 46: Thermal system† design space: heat sink outlet (compressor inlet) pressure and recuperator effectiveness plotted against recuperator length

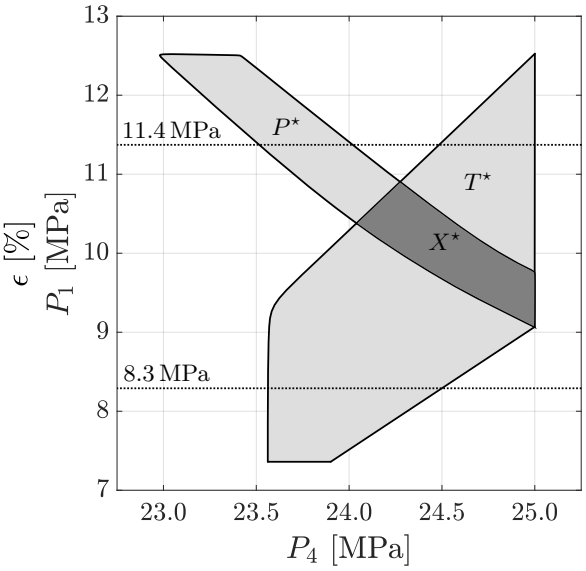

Figure 47: Power system‡ design space and thermal system† design space: heat sink outlet (compressor inlet) pressure plotted against solar receiver outlet (turbine inlet) pressure

A valid design for the complete system for a nominal flow area of 125 000 mm^2 is therefore guaranteed – regardless of heat sink length – but only if the recuperator is shorter. Unfortunately a shorter recuperator length corresponds to a lower effectiveness (93% in Figure 46) and a concomitant reduction in cycle efficiency. For this reason, it is not recommended to design the system with a short heat sink just for the sake of matching the design spaces in the correct pressure range. It is better to keep the desired level of recuperator effectiveness (and therefore recuperator length) and to change the nominal flow area instead.

An interesting observation is that the design space of the power system changes little from Figure 43 to Figure 45 (the axes of the figures are scaled differently, so this may not be obvious at first glance) which suggests that the power system is less affected than the thermal system by changes in the nominal flow area.

† Fixed design variables: $P_2 = 25$ MPa, $\dot{m} = 200$ kg/s, $P_5 = 12.5$ MPa, $A_N = 125\,000$ mm^2

‡ Fixed design variables: $T_4 = 550$ °C, $T_1 = 35$ °C, $P_2 = 25$ MPa, $\dot{m} = 200$ kg/s, $P_5 = 12.5$ MPa, $A_N = 125\,000$ mm^2

6.2.3. Example of an Excessively Large Nominal Flow Area

The design spaces for a larger nominal flow area – 350 000 mm^2 in this case – is depicted in Figures 48 and 49.

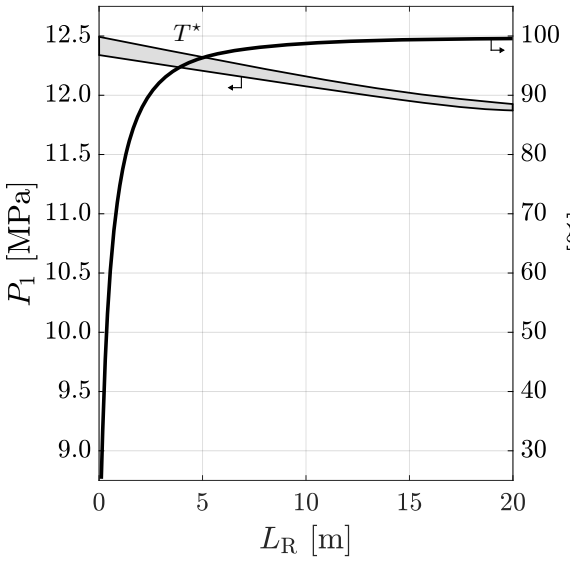

Figure 48: Thermal system† design space: heat sink outlet (compressor inlet) pressure and recuperator effectiveness plotted against recuperator length

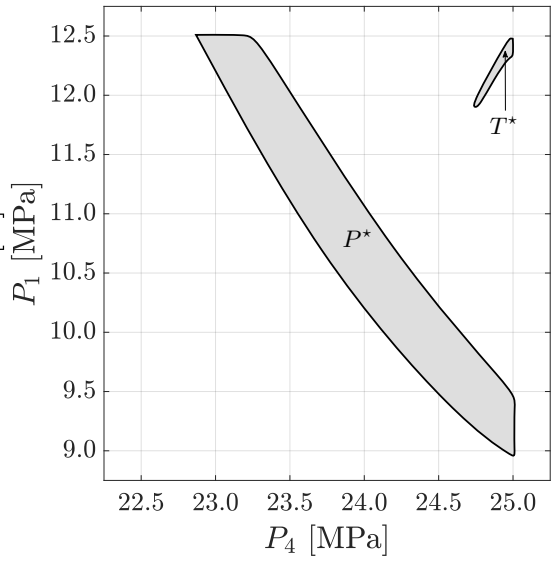

Figure 49: Power system‡ design space and thermal system† design space: heat sink outlet (compressor inlet) pressure plotted against solar receiver outlet (turbine inlet) pressure

Comparing Figure 48 with Figure 42 reveals that a larger flow area makes the negative gradient of the pressure band less steep, indicating that the pressure drop per unit length of recuperator is less. It also makes the band thinner, indicating that the heat sink outlet pressure is less sensitive to heat sink length. Another observation is that for the larger flow area, the recuperator effectiveness reaches the 100% asymptote only at longer lengths. In fact, to reach the 99% effectiveness level, the recuperator needs to be about 50% longer in the 350 000 mm^2 case (Figure 48) as compared to the 175 000 mm^2 case (Figure 42).

The size of the thermal system design space in Figure 49 is also considerably smaller compared to Figures 43 and 45, indicating that the design is less flexible as the nominal flow area is increased.

† Fixed design variables: $P_2 = 25$ MPa, $\dot{m} = 200$ kg/s, $P_5 = 12.5$ MPa, $A_N = 350\,000$ mm^2

‡ Fixed design variables: $T_4 = 550$ °C, $T_1 = 35$ °C, $P_2 = 25$ MPa, $\dot{m} = 200$ kg/s, $P_5 = 12.5$ MPa, $A_N = 350\,000$ mm^2

The consequence of this reduced flexibility on the design of the complete system is clearly visible in Figure 49. The power system design space ($P^\star$) does not intersect the thermal system design space ($T^\star$) at all, which reveals that $350\,000\,\text{mm}^2$ is not a valid choice for the nominal flow area. Regardless of what length of recuperator is chosen, it is not possible to design the complete system with this nominal flow area value.

6.2.4. Review of the Design Space after Stage 2

A recuperator length of $L_\text{R} = 10\,\text{m}$ and a nominal flow area of $A_\text{N} = 175\,000\,\text{mm}^2$ is a good combination for the system because a good recuperator effectiveness can be achieved and the power system and thermal system design spaces intercept each other in the correct P_1 range.

Stage 2 of the design is completed once decisions have been made on these two variables.

The updates to the design space after Stage 2 are set out in Table 7.

Table 7: Noteworthy updates to the design space in Stage 2

Variable	Type of Update	Details of Update	Unit
$*$ A_N	Solution-defined range $\rightarrow$ Fixed value	15.2×10^3 – $1 \times 10^6 \rightarrow 175 \times 10^3$	mm^2
$*$ L_R	Initial range $\rightarrow$ Fixed value	0.01 – $20 \rightarrow 10.0$	m

6.3. Stage 3

The aim of Stage 3 is to complete the detailed design of the other two heat exchangers in the thermal system: the solar receiver and the heat sink. To do this, the thermal system is re-analyzed with the recuperator length and nominal flow area set as constants.

6.3.1. Solar Receiver Design

Figure 50 shows the updated design space of the thermal system with solar receiver outlet (turbine inlet) temperature T_4 plotted against solar receiver length L_S.

To achieve the required turbine inlet temperature of 550 °C, Figure 50 reveals that the solar receiver length needs to be between 60 m and 65 m. The exact value depends on the inlet boundary temperature of the cold side of the thermal system (the compressor outlet temperature T_2) which is still unknown at this point in the design. As indicated in Table 6, this variable can have a value between 53.4 °C and 69.6 °C.

Figure 51 shows the updated design space of the thermal system with solar receiver outlet (turbine inlet) pressure P_4 plotted against solar receiver length L_S. Following the vertical lines upwards at 60 m and 65 m reveals that the outlet pressure P_4 of the solar receiver should be between 24.345 MPa and 24.380 MPa.

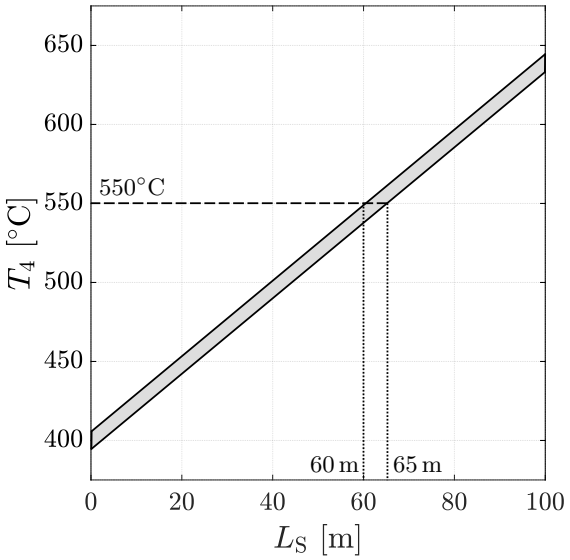

Figure 50: Thermal system† design space: solar receiver outlet (turbine inlet) temperature plotted against solar receiver length

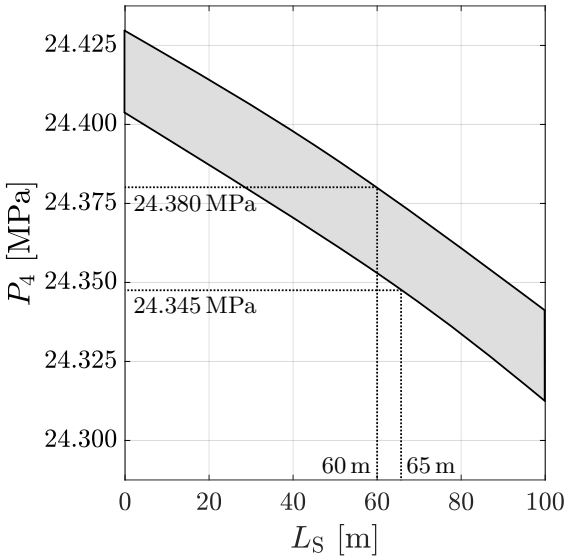

Figure 51: Thermal system† design space: solar receiver outlet (turbine inlet) pressure plotted against solar receiver length

† Fixed design variables: $P_2 = 25\,\text{MPa}$, $\dot{m} = 200\,\text{kg/s}$, $P_5 = 12.5\,\text{MPa}$, $A_N = 175\,000\,\text{mm}^2$, $L_R = 10\,\text{m}$

6.3.2. Heat Sink Design

Figure 52 shows the updated design space of the thermal system with heat sink outlet (compressor inlet) temperature T_1 plotted against heat sink length L_H.

To achieve the required compressor inlet temperature of 35 °C, Figure 52 reveals that the heat sink length needs to be between 1.75 km and 2.05 km. Again, the exact value depends on the inlet boundary temperature. For the hot side of the thermal system, this is the turbine outlet temperature T_5 which Table 6 indicates can vary between 473 °C and 484 °C.

With a heat sink length between these bounds, Figure 53 reveals that the outlet pressure (compressor inlet pressure) P_1 falls between 10.43 MPa and 10.64 MPa.

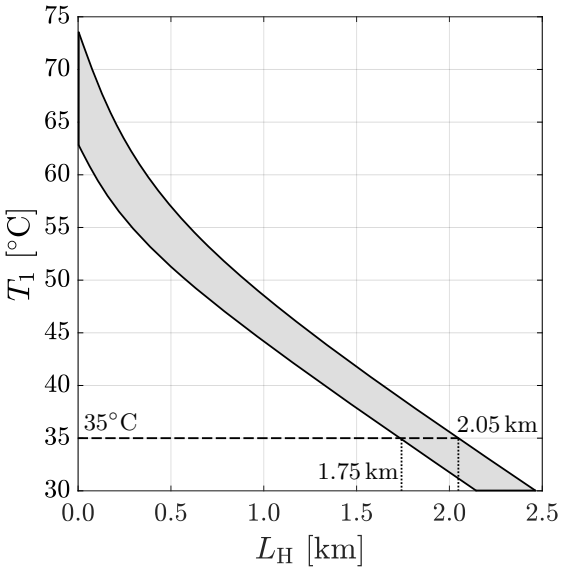

Figure 52: Thermal system† design space: heat sink outlet (compressor inlet) temperature plotted against heat sink length

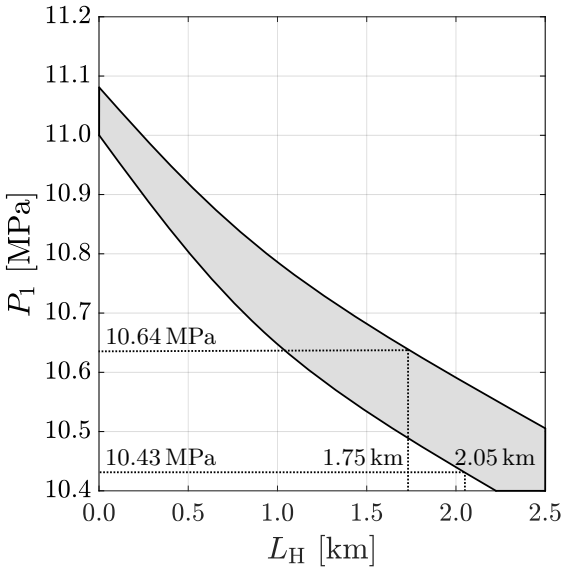

Figure 53: Thermal system† design space: heat sink outlet (compressor inlet) pressure plotted against heat sink length

† Fixed design variables: $P_2 = 25\,\text{MPa}$, $\dot{m} = 200\,\text{kg/s}$, $P_5 = 12.5\,\text{MPa}$, $A_N = 175\,000\,\text{mm}^2$, $L_R = 10\,\text{m}$

6.3.3. Review of the Design Space after Stage 3

With the more restrictive ranges for P_4 and P_1, the power system is re-analyzed to see what the new range for the temperatures T_2 and T_5 are in which the power system would be valid. Table 8 shows these updates.

Table 8: Noteworthy updates to the design space in Stage 3a

Variable	Type of Update	Details of Update	Unit
$*L_S$	Initial range → Solution-defined range	1 – 100 → 60 – 65	m
$*L_H$	Initial range → Solution-defined range	1 – 2 500 → 1 750 – 2 050	m
P_4	Solution-defined range → Solution-defined range	22.8 – 25.0 → 24.345 – 24.380	MPa
P_1	Solution-defined range → Solution-defined range	8.92 – 12.5 → 10.43 – 10.64	MPa
$*T_2$	Solution-defined range → Solution-defined range	53.4 – 69.6 → 59.4 – 59.8	°C
$*T_5$	Solution-defined range → Result	473 – 484 → 479	°C

The valid ranges for the temperatures T_2 and T_5 are evidently very small at this point of the design process, varying within a narrow margin of less than 1 °C. As such, reported up to three significant figures, T_5 is considered fixed.

A re-analysis of the thermal system with the updated range for T_2 and with the fixed value of T_5, produces the set of results as shown in Figures 54 through 57

These results are similar to those presented in Figures 50 through 53, except that now the design space in all of the figures appears as a line (or thin band, depending on the scale of the plot) from which it is simple to read-off the final lengths and outlet pressures of the solar receiver and heat sink.

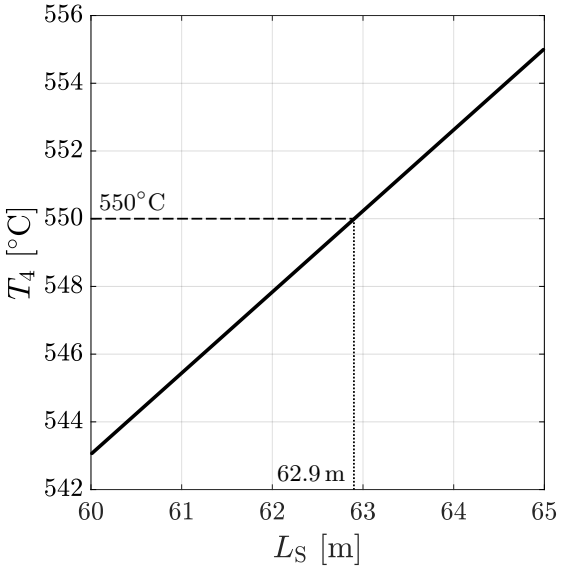

Figure 54: Thermal system† design space: solar receiver outlet (turbine inlet) temperature plotted against solar receiver length

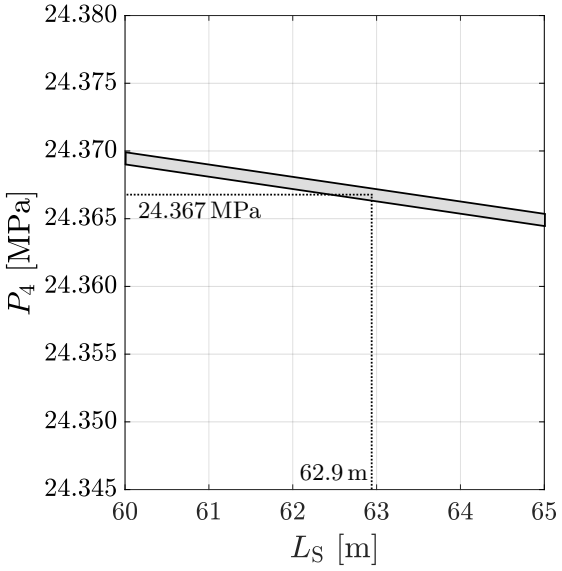

Figure 55: Thermal system† design space: solar receiver outlet (turbine inlet) pressure plotted against solar receiver length

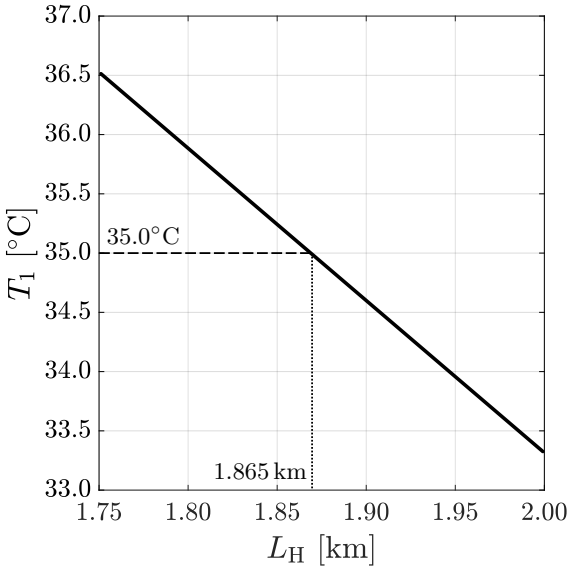

Figure 56: Thermal system† design space: heat sink outlet (compressor inlet) temperature plotted against heat sink length

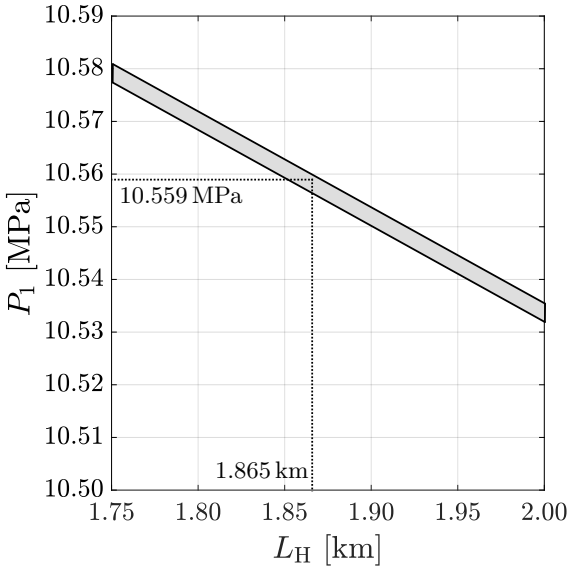

Figure 57: Thermal system† design space: heat sink outlet (compressor inlet) pressure plotted against heat sink length

† Fixed design variables: $P_2 = 25\,\text{MPa}$, $\dot{m} = 200\,\text{kg/s}$, $P_5 = 12.5\,\text{MPa}$, $A_N = 175\,000\,\text{mm}^2$, $L_R = 10\,\text{m}$, $T_5 = 479\,^\circ\text{C}$

The updates to the design space after this re-analysis of the thermal system are presented in Table 9.

Table 9: Noteworthy updates to the design space in Stage 3b

Variable	Type of Update	Details of Update	Unit
$*\,L_S$	Solution-defined range → Result	60 – 65 → 62.9	m
$*\,L_H$	Solution-defined range → Result	1 750 – 2 050 → 1 865	m
P_4	Solution-defined range → Result	24.345 – 24.380 → 24.367	MPa
P_1	Solution-defined range → Result	10.43 – 10.64 → 10.559	MPa

With P_4 and P_1 also fixed, a re-analysis of the power system reveals that the compressor outlet temperature T_2 should be 59.5 °C.

Table 10: Noteworthy updates to the design space in Stage 3c

Variable	Type of Update	Details of Update	Unit
$*\;\; T_2$	Solution-defined range → Result	59.4 – 59.8 → 59.5	°C

With this final update (summarized in Table 10), the design of the system as a whole is completed insofar as the ten shared design variables of the system are concerned (refer to the tables in Appendix A.2 for more details).

Furthermore, the detailed design of the thermal system is also completed because the lengths of the heat exchangers are known (see the tables in Appendix A.4 for more details).

6.4. Stage 4

The final stage of the design process considers the detailed design of the power system. A re-analysis of the power system with the fixed values from Stage 3 results in the design space as shown in Figure 58. The tip radius of each of the turbomachines is plotted against rotational speed.

Figure 58 reveals the following about the turbomachines at this stage of the design:

- A direct relationship between the size and speed of the turbomachines exists: a smaller tip radius necessitates a faster rotational speed and vice versa.
- Once either the rotational speed or the tip speed is selected, the other is fixed.
- For the same rotational speed, the turbine is a larger machine than the compressor.
- The compressor can support a wider range of rotational speeds than the turbine.

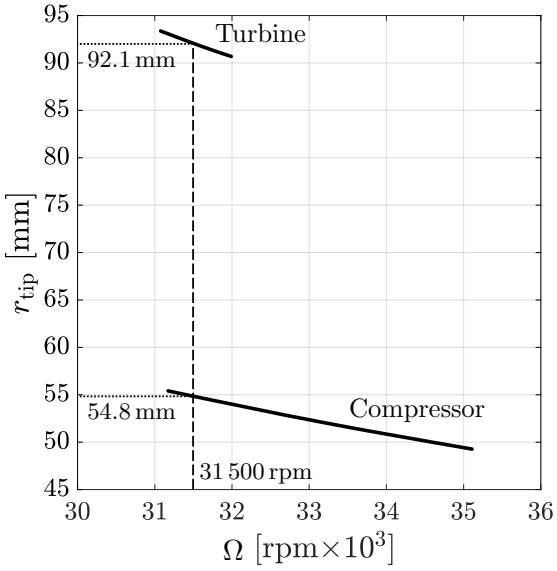

Figure 58: Power system† design space:
turbomachinery tip radii
plotted against rotational speed

It is useful to have both turbomachines operating at the same rotational speed because it allows flexibility with regards to the physical implementation: the compressor could either be powered off the same shaft as the turbine or by an external electrical motor. Figure 58 shows that this is only possible for a small range of rotational speeds; a sensible choice is $\Omega = 31\,500\,\text{rpm}$. If the system is to supply electricity to a grid with a conventional frequency of 50 Hz or 3 000 rpm, a gearbox with a ratio of 10.5:1 would be required.

Once the rotational speed is fixed, the tip radius also becomes fixed, and the remaining design space of the power system is so small that there is little freedom left for the designer to make any decisions. The hub and shroud radii, and blade width of the turbomachines are still free to vary, but the range for each variable is less than one centimeter. This is a relatively small range of variation, given the size of the initial design space, but it should also be taken into account that sCO_2 turbomachinery are inherently small. Therefore, a range of one centimeter could be significant. Nevertheless, a *unique* design of the power system (i.e. with no variation in the values of these variables), can be achieved by exactly fixing the value of a variable, repeating the analysis of the power system to achieve a more reduced design space, exactly fixing the value of another variable, repeating the analysis again, and so forth. This is a trivial and tedious exercise in practice, hence it is not demonstrated here.

After this final step, the design of the system is completed. The final values for the variables of this design (referred to as *Design A*) are listed in the tables in Appendix A.

† Fixed design variables: $T_4 = 550\,^\circ\text{C}$, $T_1 = 35\,^\circ\text{C}$, $P_2 = 25\,\text{MPa}$, $\dot{m} = 200\,\text{kg/s}$, $P_5 = 12.5\,\text{MPa}$, $A_\text{N} = 175\,000\,\text{mm}^2$, $P_4 = 24.367\,\text{MPa}$, $P_1 = 10.559\,\text{MPa}$

7. Design Variations

The design of the system presented in Chapter 6 is conventional: no special constraints are placed on the system and therefore it can be designed with a relatively high degree of freedom and achieve a good level of optimality with regards to all of the objectives. In this chapter, two new design variations of the system are presented to showcase how additional constraints that apply since the start of the design process should be treated. The first design variation is one in which the power system is constrained, the second design variation is one in which the thermal system is constrained. The same system design objectives (Table 2) are maintained.

7.1. Constrained Power System Design

Suppose it is desired that the rotational speed of the turbomachines be significantly reduced from the value of 31 500 rpm specified for the design completed in Chapter 6. Furthermore, the equality constraint,

$$\Omega_{\mathrm{T}} = \Omega_{\mathrm{C}} \implies \Omega_{\mathrm{T}} - \Omega_{\mathrm{C}} = 0 \,, \tag{120}$$

is to be added in order to guarantee the same rotational speed for both machines from the outset of the design process. The following sections deal with the design of this system.

7.1.1. Speed vs Size Trade-off

To see if there is a reasonable possibility for a considerable reduction in rotational speed of both machines concurrently, the power system is analyzed with all design variables free to vary but with the added constraint of Equation (120).

The power system design space with the tip radius of the turbine (which acts as an indication of the size of the machines) plotted against rotational speed is depicted in Figure 59. Figure 60 shows the power system design space with the mass flow rate plotted against rotational speed.

From Figure 59 it is observed that a considerable reduction in speed is possible, but within limits. The design space is bounded with a horizontal asymptote at small tip radius values and a vertical asymptote at small speed values. These asymptotes indicate that the speed cannot be reduced beyond a certain value regardless of size and also that the size cannot be reduced beyond a certain value regardless of speed.

Reducing the speed also impacts the mass flow rate: Figure 60 indicates that a slower rotational speed necessitates a higher mass flow rate.

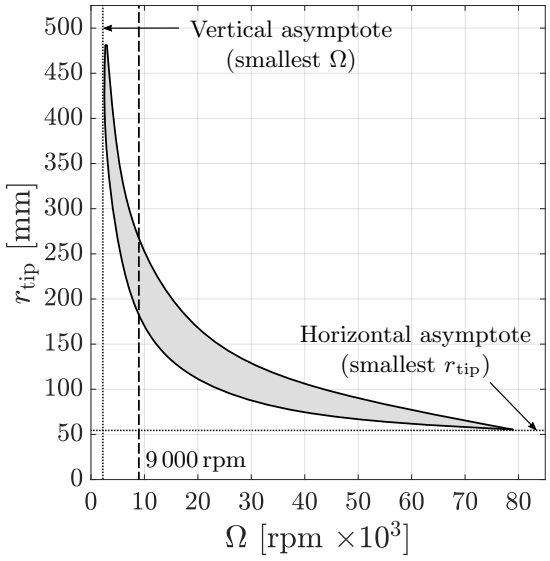

Figure 59: Power system† design space: tip radius plotted against rotational speed

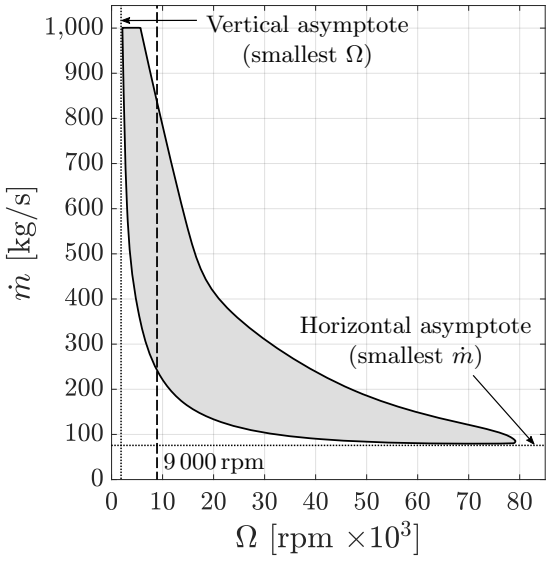

Figure 60: Power system† design space: mass flow rate plotted against rotational speed

Based on the asymptotic behavior of the speed-to-size trade-off, it is not sensible to choose an excessively slow rotational speed because then the size of the turbomachines and the mass flow rate would be excessively large.

Nevertheless, for the sake of demonstration, suppose that it is desired to have the turbomachines rotate at a speed of $\Omega = 9\,000\,\text{rpm}$, or about three times slower than the design of Chapter 6. At this speed, a gearbox with a ratio of only 3:1 is required if the system is to provide electricity to a 50 Hz (3 000 rpm) electrical grid.

7.1.2. Stage 1

Stage 1 of the design process involves choosing the turbine and compressor inlet temperatures, compressor outlet pressure, mass flow rate and turbine outlet pressure.

Based on the earlier discussions in Sections 6.1.1 and 6.1.2, the turbine and compressor inlet temperatures are again chosen to be 550 °C and 35 °C, respectively, and the compressor outlet pressure is again chosen to be 25 MPa.

† All design variables are free to vary.

Mass Flow Rate

An analysis of the power system model reveals that the power system can operate at the stated conditions, and at the required $\Omega = 9\,000\,\text{rpm}$, but provided that the mass flow rate is at least $400\,\text{kg/s}$. This result is depicted in Figure 61, which shows the design space with turbine outlet pressure P_5 plotted against mass flow rate $\dot{m}$, and in Figure 62, which shows the design space with compressor inlet pressure P_1 plotted against mass flow rate.

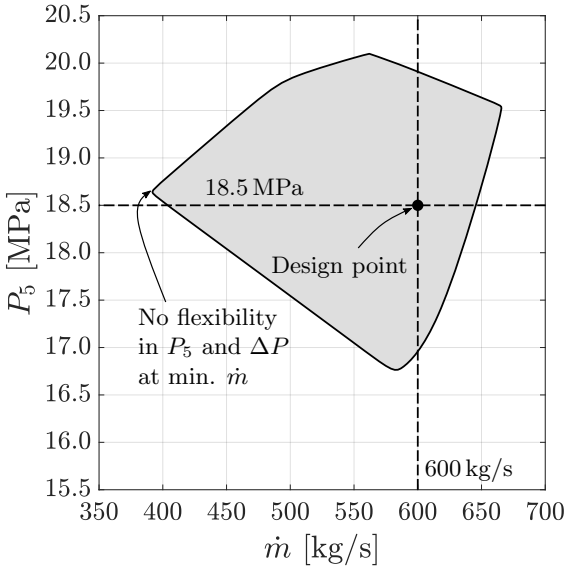

Figure 61: Power system† design space: turbine outlet pressure plotted against mass flow rate

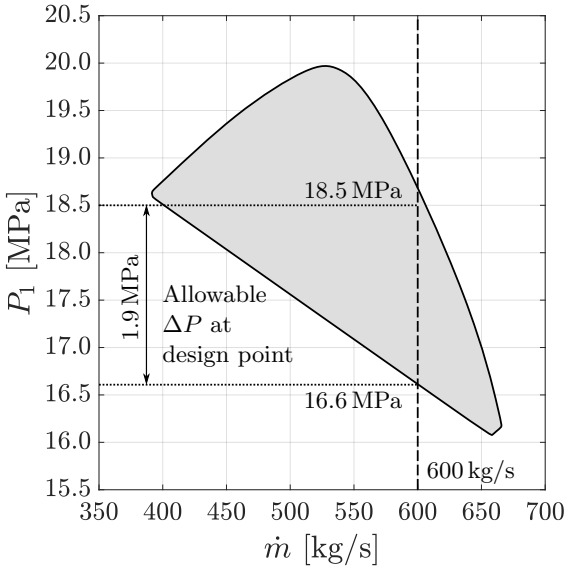

Figure 62: Power system† design space: compressor inlet pressure plotted against mass flow rate

The mass flow rate reaches its minimum value of approximately $400\,\text{kg/s}$ at the left-hand-side corner of the design spaces in Figures 61 and 62. At this point, there is no flexibility with regards to P_5 (i.e. it can only be one value) and the value of P_1 must equal the value of P_5 (hence there can be no pressure drop on the hot side of the thermal system). It is therefore not sensible to design the system with this minimum mass flow rate value.

A more practical choice for the mass flow rate is $\dot{m} = 600\,\text{kg/s}$, because it allows for more flexibility with regards to the value of P_5, and it allows for a large degree of pressure drop ($\Delta P = P_5 - P_1$) if P_5 is sufficiently high.

† Fixed design variables: $T_4 = 550\,^\circ\text{C}$, $T_1 = 35\,^\circ\text{C}$, $P_2 = 25\,\text{MPa}$, $\Omega_\text{C} = \Omega_\text{T} = 9\,000\,\text{rpm}$

Turbine Outlet Pressure

To decide on an appropriate value for the turbine outlet pressure P_5, an analysis of the thermodynamic model with a fixed mass flow rate of 600 kg/s is done. This yields the design spaces as presented in Figures 63 and 64.

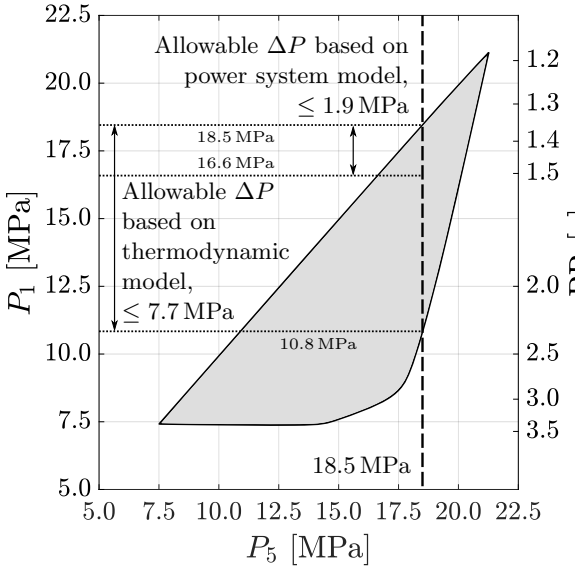

Figure 63: Thermodynamic model† design space: compressor inlet pressure and pressure ratio plotted against turbine outlet pressure

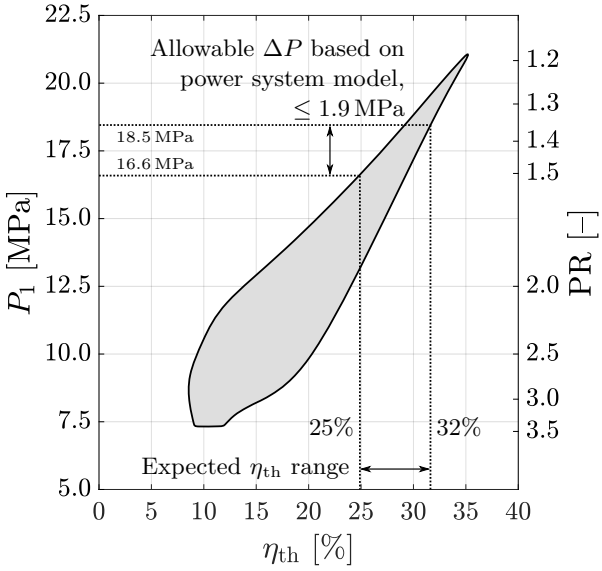

Figure 64: Thermodynamic model† design space: compressor inlet pressure and pressure ratio plotted against cycle efficiency

As discussed in Section 6.1.4, Figures 63 and 64 should be used in conjunction with each other when choosing a value for P_5. It is desirable to choose a relatively high value for P_5 so that the cycle efficiency can be high, but P_5 cannot be too high because then the allowable pressure drop $\Delta P = P_5 - P_1$ would be too low.

Based on Figure 63, a sensible choice for P_5 is a value of 18.5 MPa.

Given that the power system is now specifically constrained, which was not the case for the design in Chapter 6, Figure 63 is not sufficient to check the allowable pressure drop. Figure 62 must be used additionally. If only the thermodynamic model (Figure 63) is considered, the allowable pressure drop would seem to be $18.5 - 10.8 = 7.7$ MPa. On the other hand, if the power system model (Figure 62) is considered, then the allowable pressure drop is significantly less, only $18.5 - 16.6 = 1.9$ MPa at the design point of 600 kg/s and $P_5 = 18.5$ MPa.

Transferring the pressure range corresponding to the power system design point to Figure 64 shows that the corresponding expected range of cycle efficiency values is between 25% and 32%, provided that the assumed component performance level used to generate this design space (i.e. $\epsilon = 98\%$ and $\eta_{\text{C,T}} = 80\%$) is achieved.

† Fixed design variables: $T_4 = 550\,°\text{C}$, $T_1 = 35\,°\text{C}$, $P_2 = 25$ MPa, $\dot{m} = 600$ kg/s, $\epsilon = 98\%$, $\eta_{\text{C,T}} = 80\%$

By analogy to Table 5, Table 11 summarizes the details of this design decision.

Table 11: Details associated with the design decision of $P_5 = 18.5\,\text{MPa}$

P_5 [MPa]	$P_{1,\text{min}}$ [MPa]	ΔP_{max} [MPa]	Best PR	Worst PR	Best η_{th} [%]	Worst η_{th} [%]
18.5	16.6	1.9	1.35	1.51	32	25

Once the five design variables in the top half of the Table 12 have been fixed, the power system model is analyzed to yield the reduced design space of the other variables as reported in the bottom half of Table 12.

Table 12: Noteworthy updates to the design space in Stage 1 for the constrained power system design

Variable	**Type of Update**	**Details of Update**	**Unit**
T_4	Initial range → Fixed value	32 – 700 → 550	°C
T_1	Initial range → Fixed value	32 – 700 → 35.0	°C
* P_2	Initial range → Fixed value	7.38 – 30 → 25.0	MPa
* $\dot{m}$	Initial range → Fixed value	1 – 1 000 → 600	kg/s
* P_5	Initial range → Fixed value	7.38 – 30 → 18.5	MPa
* A_{N}	Initial range → Solution-defined range	$1 - 1 \times 10^6 \rightarrow 76 \times 10^3 - 1 \times 10^6$	mm^2
* T_2	Initial range → Solution-defined range	32 – 700 → 43.4 – 45.5	°C
* T_5	Initial range → Solution-defined range	32 – 700 → 521 – 524	°C
P_1	Initial range → Solution-defined range	7.38 – 30 → 16.6 – 18.5	MPa
P_4	Initial range → Solution-defined range	7.38 – 30 → 23.4 – 24.0	MPa

7.1.3. Stage 2

The aim of Stage 2 is to choose the combination of the nominal flow area and recuperator length of the system. As discussed in Section 6.2, both the power system model and the thermal system model must be analyzed concurrently.

A Monte Carlo simulation of the thermal system must be carried out for its analysis. The inputs are the variables indicated with the asterisk (*) in Table 12. As before, the nominal flow area A_{N} has a large range of possible values and therefore it is more practical to estimate a value and to treat it as a constant instead.

After a few manual iterations with different values for the nominal flow area, it is determined that an appropriate choice is $A_{\text{N}} = 525\,000\,\text{mm}^2$.

Figure 65 shows the design space of the thermal system at this value of the nominal flow area, with heat sink outlet (compressor inlet) pressure P_1 plotted (on the primary vertical axis) against recuperator length, and recuperator effectiveness ϵ plotted (on the secondary vertical axis) against recuperator length.

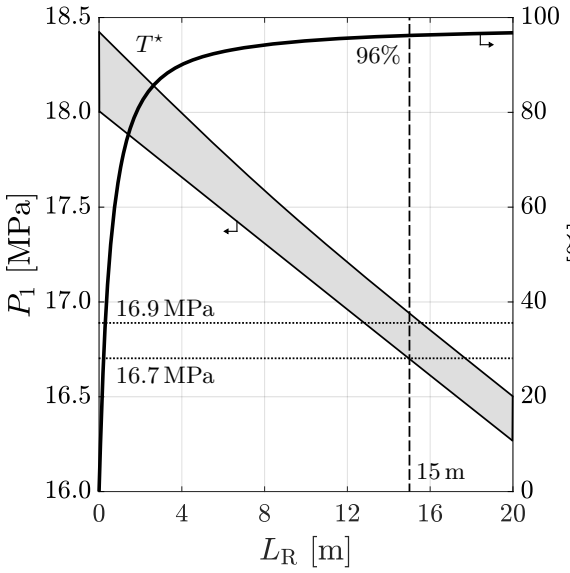

Figure 65: Thermal system† design space: heat sink outlet (compressor inlet) pressure and recuperator effectiveness plotted against recuperator length

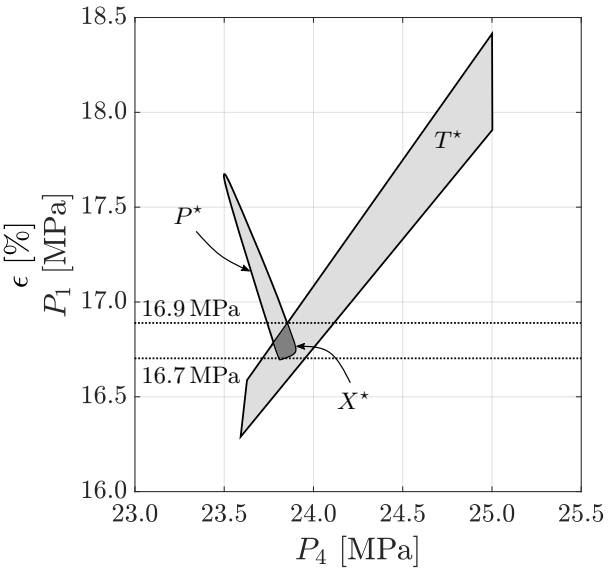

Figure 66: Power system‡ design space and thermal system† design space: heat sink outlet (compressor inlet) pressure plotted against solar receiver outlet (turbine inlet) pressure

A sensible choice for the length of the recuperator is 15 m. The recuperator has reached its maximum effectiveness of 96% at this length, longer lengths do not further increase the effectiveness. For this length of recuperator, as Figure 65 shows, P_1 can vary between 16.7 MPa and 16.9 MPa.

A recuperator effectiveness of 96% is less than the assumed recuperator effectiveness of 98% of the design space in Figure 64. As a result, the cycle efficiency will be lower than the expected range given in Table 11.

Transferring the P_1 range to Figure 66 shows that a valid design for the complete system (X^*) is possible in this pressure range. The valid complete system design space (X^*) is the intersection between the valid power system design space (P^*) and the valid thermal system design space (T^*).

† Fixed design variables: $P_2 = 25\,\text{MPa}$, $\dot{m} = 600\,\text{kg/s}$, $P_5 = 18.5\,\text{MPa}$, $A_N = 525\,000\,\text{mm}^2$

‡ Fixed design variables: $T_4 = 550\,^\circ\text{C}$, $T_1 = 35\,^\circ\text{C}$, $P_2 = 25\,\text{MPa}$, $\Omega_C = \Omega_T = 9\,000\,\text{rpm}$, $\dot{m} = 600\,\text{kg/s}$, $P_5 = 18.5\,\text{MPa}$, $A_N = 525\,000\,\text{mm}^2$

The combination of 525 000 mm^2 for the nominal flow area and 15 m for the recuperator length is appropriate, and Stage 2 of the design is thus completed. The relevant updates to the design space are summarized in Table 13.

Table 13: Noteworthy updates to the design space in Stage 2 for the constrained power system design

Variable	Type of Update	Details of Update	Unit
$*$ A_N	Solution-defined range $\rightarrow$ Fixed value	76.0×10^3 – 1.00×10^6 $\rightarrow$ 525×10^3	mm^2
$*$ L_R	Initial range $\rightarrow$ Fixed value	0.01 – 20 $\rightarrow$ 15.0	m

7.1.4. Stage 3

The aim of Stage 3 is to find the lengths and outlet pressures of the solar receiver and heat sink, and the outlet temperatures of the compressor and turbine. As set out in Section 6.3, this is done through independent analyses of the thermal system and power system, which successively narrow the design space until the results become clear. The specifics of Stage 3 are not repeated here, but the results for the new design of the system are presented in Table 14.

Table 14: Noteworthy updates to the design space in Stage 3 for the constrained power system design

Variable	Type of Update	Details of Update	Unit
$* L_S$	Initial range $\rightarrow$ Result	1 – 100 $\rightarrow$ 54.4	m
$* L_H$	Initial range $\rightarrow$ Result	1 – 2 500 $\rightarrow$ 1 990	m
P_4	Solution-defined range $\rightarrow$ Result	23.4 – 24.0 $\rightarrow$ 23.9	MPa
P_1	Solution-defined range $\rightarrow$ Result	16.6 – 18.5 $\rightarrow$ 16.7	MPa
$* T_2$	Solution-defined range $\rightarrow$ Result	43.4 – 45.5 $\rightarrow$ 45.4	°C
$* T_5$	Solution-defined range $\rightarrow$ Result	521 – 524 $\rightarrow$ 522	°C

7.1.5. Stage 4

Stage 4 of the design process involves finalizing the detailed design of the power system. Unlike the design in Chapter 6, the rotational speed of the turbomachines are already fixed. Therefore, by this point of the design process, the remaining unknown geometrical variables of the power system are only free to vary within a range of less than one centimeter. A unique design with exact values for all of the design variables can be achieved as discussed in Section 6.4

The final values for all of the variables of this new design (referred to as *Design B*) are listed in the tables in Appendix A.

Key differences between this new design and the design developed in Chapter 6 (*Design A*) are: a greater mass flow rate and a greater nominal flow area (Table 25), larger turbomachinery (Table 27), larger heat exchangers and a lower thermal efficiency (Table 31). A more extensive analysis and comparison of the completed designs of the system is carried out in Chapter 8.

7.2. Constrained Thermal System Design

Suppose that the long heat sink (1 865 m) of the system design in Chapter 6 is unacceptable, and that it is desired that the heat sink be 500 m long instead. A new design of the system, taking this constraint into account, is developed in the following sections.

7.2.1. Stage 1

It is to be expected that to accommodate this new constraint, some concessions have to be made regarding some of the design objectives. However, suppose that the maximum temperature in the cycle T_4 should remain at 550 °C and that the maximum pressure in the cycle P_2 should remain at 25 MPa, to be consistent with the discussions in Sections 6.1.1 and 6.1.2.

As with the previous design developed in Section 7.1, one way of accommodating the new constraint on the system is to perform an additional analysis of the detailed sub-system model (which in this case is the thermal system) when making decisions in Stage 1 of the design process. An alternative approach that will be demonstrated here is to use heuristics to predict what the effect of the new constraint on the system would be on the design variables that are decided on in Stage 1.

An argument based on heuristics can be formulated by considering that the length of the heat sink is to be substantially reduced compared to the design in Chapter 6, and therefore the compressor inlet temperature of 35 °C would be not be a reasonable choice for the new design. Instead, a higher compressor inlet temperature should be specified. As demonstration, a value of 65 °C is selected for the new design to be completed in the following sections.

Given that this value is based on a heuristic motivation which cannot be technically substantiated, iteration of the design with different values is recommended. For the purposes of this research however, only one design of the system will be completed following the same, unmodified procedure developed in Chapter 6, but with a compressor inlet temperature of 65 °C. It will be demonstrated that this is a viable and simpler (although less robust) alternative method to the method demonstrated in Section 7.1 for accommodating new constraints on the system.

The first analysis for this new design is the analysis that was done in Section 6.1.3: an analysis of the thermodynamic model with the aim of choosing the cycle mass flow rate. As demonstrated in Section 6.1.3, the optimal mass flow rate depends on the efficiency of the turbomachines and on the effectiveness of the recuperator, therefore assumptions regarding the performance of the components must be made. As before, it is assumed that the turbomachinery would have an isentropic efficiency of at least 80% and that the recuperator would have an effectiveness of at least 98%.

Figure 67 shows the Pareto front between the mass flow rate and the cycle thermal efficiency. The cycle efficiency remains approximately constant between 200 kg/s and 400 kg/s, indicating that any mass flow rate value in this range can be considered as optimal.

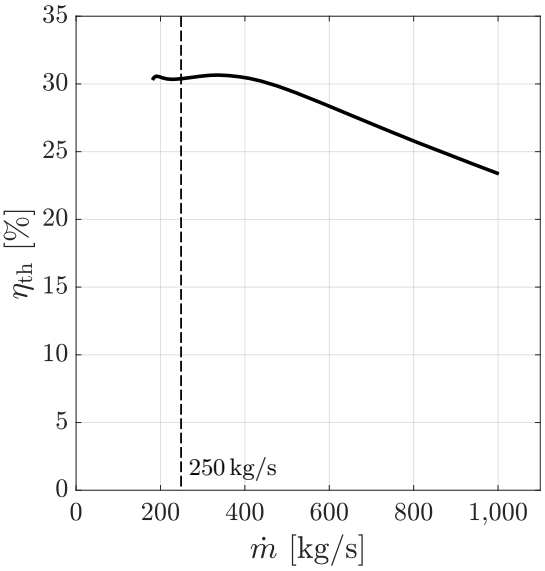

Figure 67: Thermodynamic model† results: Pareto front of cycle thermal efficiency and mass flow rate

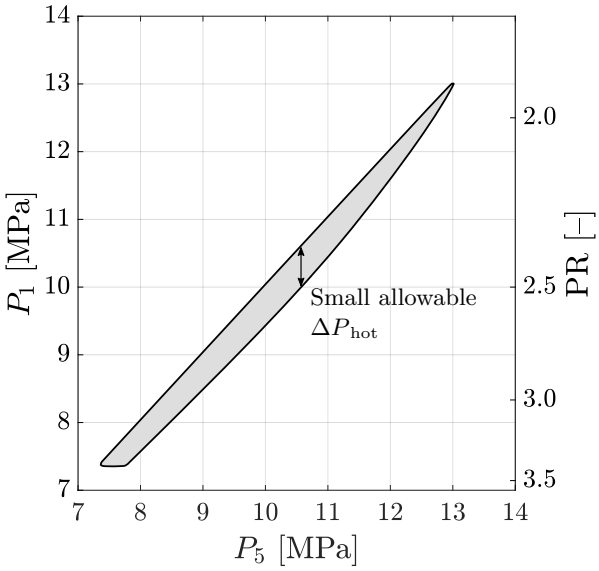

Figure 68: Thermodynamic model‡ design space: compressor inlet pressure and pressure ratio plotted against turbine outlet pressure

In the interest of minimizing the mass flow rate (objective f_5 in Table 2), it would seem as though 200 kg/s is a good choice for the mass flow rate of the new design. However, if this mass flow rate is chosen and the thermodynamic model is analyzed again – this time with the aim of choosing the turbine outlet pressure P_5 as in Section 6.1.4, a potential concern is encountered. This can be seen in Figure 68, which shows the design space of the thermodynamic model with compressor inlet pressure (on the primary vertical axis) and the equivalent pressure ratio (on the secondary vertical axis) plotted against turbine outlet pressure.

The concern is that the design space is narrow across the full range of turbine outlet pressures, which indicates that the allowable pressure drop on the hot side of the thermal system (i.e. $\Delta P_{hot} = P_5 - P_1$) must be small, around 500 kPa at most. This can be compared to the final design of Chapter 6, which had a pressure drop on the hot side of the thermal system of $12.5 - 10.6 = 1.9$ MPa, a value almost four times as much. As a first design iteration, it is therefore more sensible to choose a different mass flow rate so that a larger pressure drop is allowed.

† Fixed design variables: $T_4 = 550\,°C$, $T_1 = 65\,°C$, $P_2 = 25$ MPa, $\eta_C = \eta_T = 80\%$, $\epsilon = 98\%$
‡ Fixed design variables: $T_4 = 550\,°C$, $T_1 = 65\,°C$, $P_2 = 25$ MPa, $\dot{m} = 200$ kg/s, $\eta_C = \eta_T = 80\%$, $\epsilon = 98\%$

A more sensible choice for the mass flow rate is therefore 250 kg/s. Figure 69 shows that the design space corresponding to this new mass flow rate is wider. At a turbine outlet pressure of $P_5 = 14\,\text{MPa}$, the allowable pressure drop ΔP_{hot} is 1.4 MPa, or about three times higher than the 200 kg/s case in Figure 68.

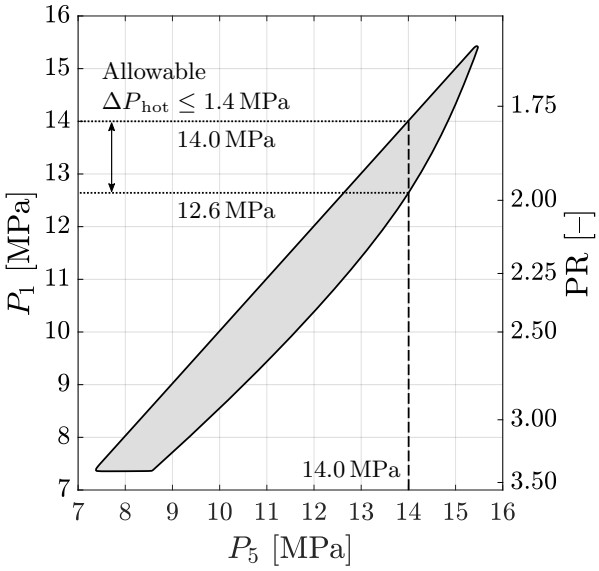

Figure 69: Thermodynamic model† design space: compressor inlet pressure and pressure ratio plotted against turbine outlet pressure

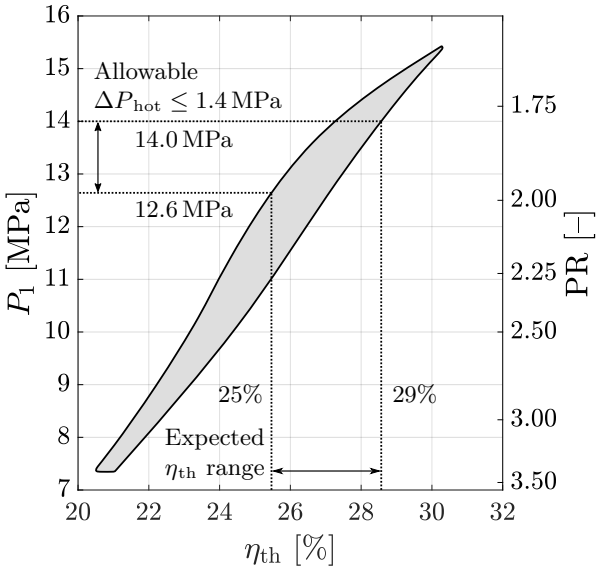

Figure 70: Thermodynamic model† design space: compressor inlet pressure and pressure ratio plotted against cycle thermal efficiency

Figure 70 shows the design space of the thermodynamic model with compressor inlet pressure (on the primary vertical axis) and the equivalent pressure ratio (on the secondary vertical axis) plotted against cycle efficiency.

The allowable heat sink outlet (compressor inlet) pressure P_1 range from Figure 69 intercepts the design space in Figure 70 at an efficiency of just over 25% and at an efficiency of just under 29%. This is the expected cycle efficiency range for a turbine outlet pressure of 14 MPa. Table 15 summarizes this information.

Table 15: Details associated with the design decision of $P_5 = 14\,\text{MPa}$

P_5 [MPa]	$P_{1,\text{min}}$ [MPa]	ΔP_{max} [MPa]	Best PR	Worst PR	Best η_{th} [%]	Worst η_{th} [%]
14.0	12.6	1.4	1.79	1.98	25	29

† Fixed design variables: $T_4 = 550\,^\circ\text{C}$, $T_1 = 65\,^\circ\text{C}$, $P_2 = 25\,\text{MPa}$, $\dot{m} = 250\,\text{kg/s}$, $\eta_{\text{C}} = \eta_{\text{T}} = 80\%$, $\epsilon = 98\%$

With the turbine outlet pressure fixed, the power system is re-analyzed to see how the other variables in the design space have been affected. The noteworthy updates are presented in Table 16.

Table 16: Noteworthy updates to the design space in Stage 1 for the constrained thermal system design

Variable	Type of Update	Details of Update	Unit
T_4	Initial range → Fixed value	32 – 700 → 550	°C
T_1	Initial range → Fixed value	32 – 700 → 65.0	°C
$*\,P_2$	Initial range → Fixed value	7.38 – 30 → 25.0	MPa
$*\,\dot{m}$	Initial range → Fixed value	1 – 1 000 → 250	kg/s
$*\,P_5$	Initial range → Fixed value	7.38 – 30 → 14.0	MPa
$*A_N$	Initial range → Solution-defined range	$1 - 1 \times 10^6 \rightarrow 132 \times 10^3 - 1 \times 10^6$	mm^2
$*\,T_2$	Initial range → Solution-defined range	32 – 700 → 99.3 – 102	°C
$*\,T_5$	Initial range → Solution-defined range	32 – 700 → 486 – 488	°C
P_1	Initial range → Solution-defined range	7.38 – 30.0 → 13.7 – 14.0	MPa
P_4	Initial range → Solution-defined range	7.38 – 30.0 → 24.7 – 25.0	MPa

7.2.2. Stages 2 and 3

The aim of Stage 2 is to choose the combination of the nominal flow area and recuperator length of the system. As discussed in Section 6.2, both the power system model and the thermal system model must be analyzed concurrently.

A Monte Carlo simulation of the thermal system must be carried out for its analysis. The inputs are the variables indicated with the asterisk (*) in Table 16. As before, the nominal flow area A_N has a large range of possible values and therefore it is more practical to estimate a value and to treat it as a constant instead.

After a few manual iterations with different values for the nominal flow area, it is determined that an appropriate choice is $A_N = 750\,000\,mm^2$.

Figure 71 shows the design space of the thermal system at this value of the nominal flow area, with heat sink outlet (compressor inlet) pressure P_1 plotted (on the primary vertical axis) against recuperator length L_R, and recuperator effectiveness ϵ plotted (on the secondary vertical axis) against recuperator length.

A recuperator length of 10 m is chosen for the new design. At this length of recuperator, the effectiveness exceeds 99%.

Unlike the same figure earlier (Figure 42 in Chapter 6), the design space of the thermal system with heat sink outlet (compressor inlet) pressure P_1 in Figure 71 appears as a curve rather than a band. This is because the length of the heat sink is now fixed, and therefore the pressure at the outlet of the hot side of the thermal system is only a function of the recuperator length and not of the heat sink length as well.

Given that the design space is now a curve, for a recuperator length of 10 m, the corresponding value for P_1 can be read-off as an exact value (13.87 MPa) as opposed to a range of values.

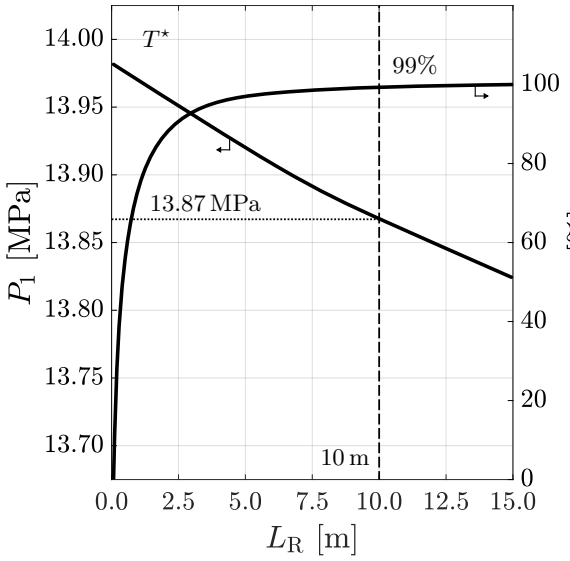

Figure 71: Thermal system† design space: heat sink outlet pressure/ compressor inlet pressure and recuperator effectiveness plotted against recuperator length

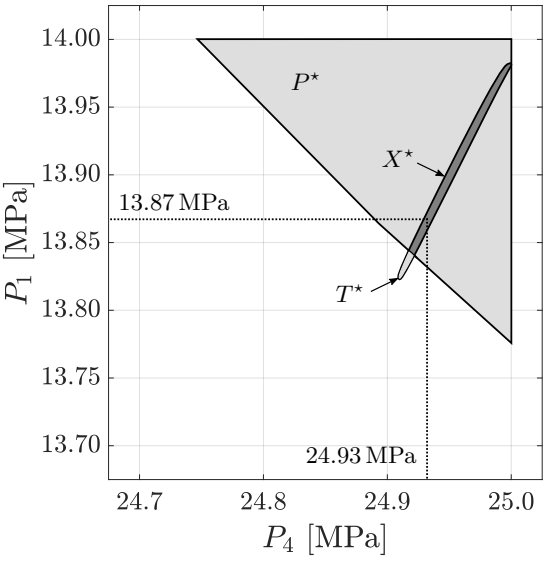

Figure 72: Power system‡ design space and thermal system† design space: heat sink outlet pressure/compressor inlet pressure plotted against solar receiver outlet pressure/turbine inlet pressure

The valid design space of the thermal system ($T^\star$) in Figure 72 is also relatively narrow compared to the valid design space of the power system ($P^\star$). The power system design space almost completely encapsulates the thermal system design space, which shows that the two systems are mutually compatible at this nominal flow area. The intersection between the two design spaces is the design space of the complete system ($X^\star$).

If a horizontal line is drawn from the vertical axis of Figure 72 at $P_1 = 13.87\,\text{MPa}$ to where the design space of the complete system ($X^\star$) is intercepted, then the required solar receiver outlet (turbine inlet) pressure P_4 can be read-off exactly as 24.93 MPa.

As demonstrated in Section 6.3, with the values P_1 and P_4 known, the power system model is re-analyzed, which then fixes the values for T_2 and T_5. With T_2 and T_5 known, the thermal system model is re-analyzed from which the final solar receiver length can be determined. This completes Stage 3 of the design.

† Fixed design variables: $P_2 = 25\,\text{MPa}$, $\dot{m} = 250\,\text{kg/s}$, $P_5 = 14\,\text{MPa}$, $A_N = 750\,000\,\text{mm}^2$

‡ Fixed design variables: $T_4 = 550\,^\circ\text{C}$, $T_1 = 65\,^\circ\text{C}$, $P_2 = 25\,\text{MPa}$, $\dot{m} = 250\,\text{kg/s}$, $P_5 = 14\,\text{MPa}$, $A_N = 750\,000\,\text{mm}^2$

The updates to the design space in Stages 2 and 3 of the design process are summarized in Table 17 and 18, respectively.

Table 17: Noteworthy updates to the design space in Stage 2 for the constrained thermal system design

Variable	Type of Update	Details of Update	Unit
$*$ A_N	Solution-defined range $\rightarrow$ Fixed value	132×10^3 – 1×10^6 $\rightarrow$ 750×10^3	mm^2
$*$ L_R	Initial range $\rightarrow$ Fixed value	0.01 – 20 $\rightarrow$ 10.0	m

Table 18: Noteworthy updates to the design space in Stage 3 for the constrained thermal system design

Variable	Type of Update	Details of Update	Unit
$* L_S$	Initial range $\rightarrow$ Result	1 – 100 $\rightarrow$ 29.4	m
P_4	Solution-defined range $\rightarrow$ Result	24.7 – 25.0 $\rightarrow$ 24.93	MPa
P_1	Solution-defined range $\rightarrow$ Result	13.7 – 14.0 $\rightarrow$ 13.87	MPa
$* T_2$	Solution-defined range $\rightarrow$ Result	99.3 – 102 $\rightarrow$ 100	°C
$* T_5$	Solution-defined range $\rightarrow$ Result	486 – 488 $\rightarrow$ 487	°C

7.2.3. Stage 4

In the final stage of the design process, the combination of rotational speed and tip radius of the turbomachines is selected.

Figure 73 shows that the turbomachines for the new design are slightly larger and rotate slower compared to the design of Chapter 6 (Figure 58). Also, unlike that design, the compressor is the more constrained of the two turbomachines in terms of its allowable range of rotational speeds.

A common rotational speed of 21 000 rpm is a sensible choice for the rotational speed of the turbomachines. This speed is in the middle of the allowable speed range for both machines, and corresponds to a gearbox ratio of 7:1 if the frequency of the electrical grid is 50 Hz (3 000 rpm).

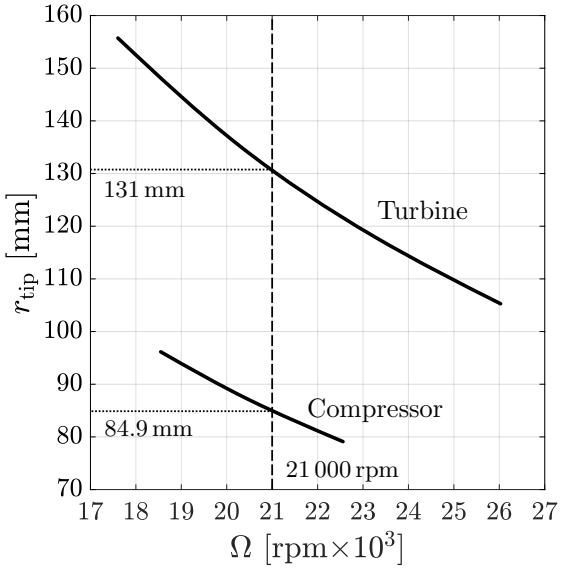

Figure 73: Power system† design space: compressor and turbine tip radius plotted against rotational speed

Once the rotational speeds of the turbomachines are fixed, the tip radius and all the other dimensions are specified to within less than one centimeter. A unique design can be achieved in the same way as discussed in Section 6.4.

This completes the new design of the system. The final values for all of the variables of this new design (referred to as *Design C*) are listed in the tables in Appendix A.

Key differences between this new design and the design developed in Chapter 6 (*Design A*) are: a significantly greater nominal flow area (Table 25), a smaller heat sink and a higher thermal efficiency (Table 31). A more extensive analysis and comparison of the completed designs of the system is carried out in Chapter 8.

† Fixed design variables: $T_4 = 550\,°\text{C}$, $T_1 = 65\,°\text{C}$, $P_2 = 25\,\text{MPa}$, $\dot{m} = 250\,\text{kg/s}$, $P_5 = 14\,\text{MPa}$, $A_\text{N} = 750\,000\,\text{mm}^2$, $P_4 = 24.93\,\text{MPa}$, $P_1 = 13.87\,\text{MPa}$

8. Analysis

The first section of this chapter is a convenient summary of the developed design procedure. The second section is an assessment of this design procedure with regards to the objectives that were identified for it. An in-depth analysis of the three designs of the system is carried out in the third section. The three developed designs of the system are compared to each other from the perspective of where the inefficiencies of each design lies, and following that three additional designs of the system are completed which address these inefficiencies. Finally, a general discussion on a range of topics concludes the chapter.

8.1. Summary of the Design Procedure

A summary of the design procedure developed in Chapter 6 is shown in Figure 74.

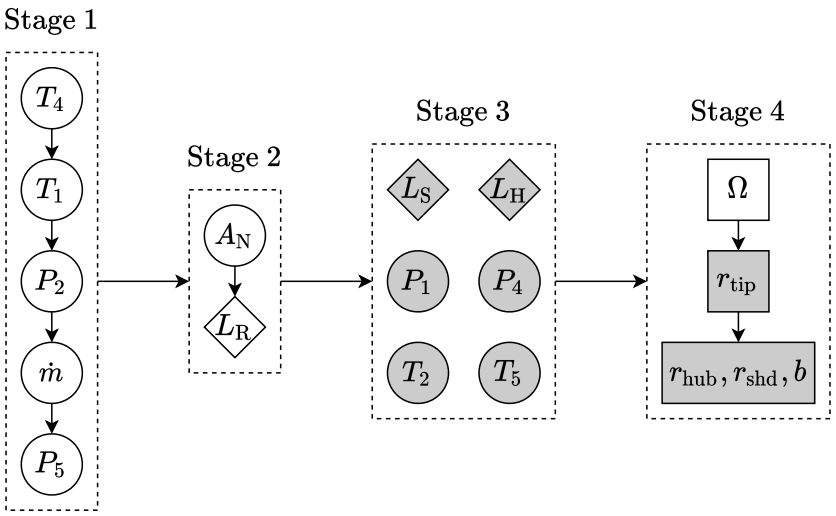

Figure 74: Summary of the design procedure

The circles represent the shared system design variables ($\mathbf{x}_s$), the rectangular boxes represent the power system design variables ($\mathbf{x}_p$) and the diamonds represent the thermal system design variables ($\mathbf{x}_t$). The unfilled shapes represent design variables that must be explicitly chosen by the designer, whereas the filled shapes are fixed (either exactly or to within a narrow range of values) once prior design decisions have been made.

Stage 1

Stage 1 of the design can be completed without requiring analysis of any of the detailed sub-system models. At the start of Stage 1, the basic Carnot theory is used to choose the highest practical turbine inlet temperature T_4 and the lowest practical compressor inlet temperature T_1.

With these two temperatures fixed, the thermodynamic model is analyzed. A plot of cycle efficiency against compressor outlet pressure P_2 is useful for deciding on an appropriate value for P_2. Higher values for P_2 are always preferable from a cycle efficiency perspective, although the efficiency improvement per unit increase in P_2 reduces at higher values.

Once a value for P_2 is known, the thermodynamic model is re-analyzed and a plot of cycle efficiency against mass flow rate $\dot{m}$ is used to decide on an appropriate value for $\dot{m}$. The optimal mass flow rate is dependent on the effectiveness of the recuperator and on the efficiency of the turbomachines. An accurate estimation of the actual performance of the components in the system is therefore essential when choosing the mass flow rate. The design must be iterated if the actual performance turns out to be significantly different from the assumed performance.

Finally, once the mass flow rate is decided upon, the thermodynamic model is re-analyzed in order to choose an appropriate value for the turbine outlet pressure P_5. The value for P_5 is chosen based on a trade-off: it must be high enough to allow the cycle pressure ratio to be low so that the cycle efficiency can be high, but it cannot be so high that the pressure drop in the heat rejection side of the thermal system is not accounted for. As a first iteration, a value for P_5 that allows a reasonably high maximum pressure drop should be chosen. A more optimistic value can be chosen in a next design iteration.

Stage 2

Stage 2 is the most intensive phase of the design. It requires analysis of both the detailed power system model and the detailed thermal system model. Fortunately, with the five design variables from Stage 1 known, the design spaces of the sub-systems are already considerably smaller as compared to the initial design spaces.

A sixth design variable, the nominal flow area A_{N}, must be chosen at the start of the analyses in Stage 2 because the thermal system model would be too computationally expensive to analyze if this is treated as an unknown variable. A value for A_{N} is chosen based on previous experience or by iteration.

The indication that an appropriate nominal flow area is chosen is that the design spaces of the two sub-systems graphically overlap each other when viewed on a plot of compressor inlet pressure P_1 against turbine inlet pressure P_4. The overlap of the design spaces must happen in the correct range of P_1 values. This is the range of outlet pressures for the heat rejection side of the thermal system that corresponds to the chosen length of recuperator L_{R}. The recuperator length must be chosen to ensure that the recuperator has a high effectiveness value.

Stage 2 is completed once a combination of A_{N} and L_{R} is found that allows the sub-system design spaces to overlap in the correct P_1 range.

Stage 3

At the start of Stage 3 the two sub-systems are geometrically compatible, compatible in terms of mass flow rate, and compatible in terms of four shared thermodynamic operating conditions. In Stage 3, independent analyses of the two sub-systems are carried out to complete the compatibility in terms of the other four shared thermodynamic operating conditions, namely the compressor inlet pressure P_1, the turbine inlet pressure P_4, the compressor outlet temperature T_2, and the turbine outlet temperature T_5.

Given the nominal flow area and recuperator length from Stage 2, the thermal system is re-analyzed first. This narrows down the range of values of the solar receiver length L_S that can achieve the known value for T_4 from Stage 1, and the range of values of the heat sink length L_H that can achieve the known value for T_1 from Stage 1. Once the length of the heat exchangers are bounded to a relatively small range of values, the ranges of their outlet pressures P_4 and P_1 are also bounded to a relatively small range of values.

This reduced range of values for P_4 and P_1 are applied to a re-analysis of the power system model, which then reveals the reduced range of values for temperatures T_2 and T_5. The latter is shown to be fixed to within three significant figures at this point of the design.

With the reduced range of values for T_2 and T_5, the thermal system model is re-analyzed which then confirms the final length of the heat exchangers, L_S and L_H, as well as their final outlet pressures, P_4 and P_1. The final value for T_2 is found from one final analysis of the power system model, given the fixed values of P_4 and P_1.

Stage 4

The design of the system, in terms of the shared design variables, and the detailed design of the thermal sub-system is completed after Stage 3. In Stage 4, the detailed design of the power sub-system is completed.

The only major design decision to make in this stage of the design process is with regards to the rotational speed of the turbomachines, Ω_C and Ω_T. Once the speed of a turbomachine is fixed, its tip radius becomes fixed as a result. The other geometrical design variables are then bound within a small range of values. A unique design (with no variation in the values of any of the variables) can be achieved by fixing any one of the remaining free variables and repeating the analysis of the power system model.

8.2. Assessment of the Design Procedure

The developed design procedure can be considered as a *Sequential Design-space Reduction* (SDR) optimization procedure. This design procedure meets all of the stated objectives set out in Section 1.6, as elaborated on in the following sections.

Complete System Design

The design procedure is sufficient to perform the full *ab initio* design of the system, including its thermodynamic operating conditions and the detailed design of all the components.

Multi-objective Extensive Optimization

Multi-objective extensive optimization (as opposed to parametric optimization discussed in Section 1.4) of the system design is possible. In the developed procedure, design decisions regarding objectives f_2, f_3 and f_5 are all made based on a trade-off with objective f_1 (see Table 2) in Stage 1. In all of these cases, a Pareto-optimal solution for the given pair of design objectives is chosen, which therefore guarantees a Pareto-optimal system design. Although the design space of the system is reduced with every design decision, optimal designs are not lost in the process.

Once Pareto-optimal solutions for the other objectives have been determined, objective f_4 is essentially revealed as a result; because the valid remaining design space of the system is small. Objective f_4 can thus not be treated as a primary design objective if the other objectives are also considered. Nevertheless, given the inherent link between objectives f_4 and f_5, a Pareto-optimal solution for f_4 is likely to be a Pareto-optimal solution for objective f_5 as well. Thus it is unnecessary to consider the optimality of objective f_4 additionally.

It should be emphasized that the guarantee on design optimality is reliant on the reasonable assumption that the thermodynamic model is an accurate surrogate model of the system represented by the detailed multidisciplinary sub-system models. Unlike an MDO procedure, the developed design procedure is not based on the analysis of the complete design space of the detailed multidisciplinary sub-system models and therefore a strictly optimal design (either local or global) cannot not found using the developed design procedure. Given that the surrogate model is by its nature an approximation of the actual system, at best a near-optimal system design can be achieved using the developed procedure. Nevertheless, this is an acceptable limitation when considering the advantages that the developed design procedure offers above a standard MDO approach.

Implementation Effort

The implementation effort of the developed procedure is significantly less than classical multidisciplinary optimization procedures because there is no need to develop any type of overarching optimization algorithm that can communicate with both disciplines simultaneously. Explicit bi-directional communication between the two disciplines also need not be facilitated.

The only coupling between the disciplines happens through the sharing of information from the design vector. Whenever a design decision is made, the full design vector (which includes the design variables of both disciplines) is updated, which means that any subsequent analyses of either of the disciplines are done with the same information.

The design vector is updated manually by the designer after each design decision, and it is supplied manually to the discipline solvers before subsequent analyses – in whichever format is appropriate for the particular solver. This can be facilitated by managing the lower and upper bounds of the design variables in a spreadsheet. If the appropriate pre- and post-processing data links are set up, software such as MATLAB® and Flownex® can automatically read and write data to a spreadsheet, but otherwise manually copying values to and from the spreadsheet and the discipline-specific solvers is a viable simple alternative.

Execution Speed

Executing the design procedure is fast: a full *ab initio* design of the complete system can typically be achieved in less than half an hour using a modern (in 2020) mid- to high-end personal computer. This is particularly satisfying, taking into account the dimensionality and scale of the problem, that realistic thermodynamic properties are used in all the analyses, the inherent non-convex and non-linear physics of the problem, and that it is a detailed multidisciplinary design *optimization* problem. The fast execution speed is attributed to four factors:

- A computationally inexpensive surrogate model (the thermodynamic model) is used to make many of the design decisions. This allows the design space of the system to be reduced without requiring the detailed sub-system models to be analyzed. When the detailed sub-system models are analyzed, starting in Stage 2 of the design procedure, their respective design spaces are already much smaller than they would otherwise have been.
- The amount of times that both sub-system models have to be analyzed simultaneously before a decision can be made is minimized. There is only one instance in the design procedure, in Stage 2, in which both sub-system models have to be analyzed simultaneously. In all other cases, the design space is reduced through the analysis of only one of the sub-system models at a time.
- Every analysis – whether it be an analysis of the thermodynamic model or an analysis of one of the detailed sub-system models – has a very specific and deliberate purpose: to make a decision about one design variable only. This decision is based on a trade-off between objectives. Hence, no attempt is made to solve the problem as a single optimization problem, but rather by making a series of Pareto-optimal choices.
- The matching of the values of the shared system design variables between the separate disciplines is not managed by an overarching optimization algorithm like it would be in classical MDO. Instead, the designer manually ensures that these values are within an appropriate level of tolerance (three significant figures in this research). This level of tolerance can be flexible, and can be different and less stringent than the tolerance level of the constraints of the sub-system models.

Model Flexibility

As a result of not requiring explicit communication between the sub-systems or an overarching optimization algorithm, the design procedure is flexible with regards to the sub-system models that are used. In this research, a custom-developed power system model developed in Matlab® was used and the commercial package Flownex® was used to model the thermal system. These sub-system models can be replaced with different models and solvers without requiring any change to the overall design procedure, provided that the new models also feature a way to explore the design space (using one of the methods discussed in Section 2.2.2).

It is preferable that solvers for the sub-system models make use of parallelization so that multi-core computer processors can be effectively utilized.

Constraint Flexibility

It is demonstrated in Chapter 7 how the developed design procedure could be used to design the system if special constraints are placed on the sub-systems. Two examples are demonstrated: a case in which the turbomachines are constrained to rotate at a certain speed, and a case in which the heat sink is constrained to be a certain length.

In the first instance, Stage 1 is amended by adding in an analysis of the detailed power system model when choosing values for $\dot{m}$ and P_5. In the second instance, the same standard design procedure is followed except that a higher value for T_1 is chosen in Stage 1, thus eliminating the need for an additional analysis of the detailed thermal system model.

It is conceivable that any constraint on the sub-systems can be accommodated similarly: either by adding in analyses of detailed sub-system models to check the validity of design decisions, or by anticipating the effect of the added constraint through a heuristic argument and to complete the standard design procedure, iterating if necessary.

8.3. Analysis of the Final System Designs

In the following sections, *Design A* refers to the design of the system which was completed in Chapter 6, *Design B* refers to the system design which had a constraint placed on the rotational speed of the turbomachines (Section 7.1), and *Design C* refers to the system design which had a constraint placed on the length of the heat sink (Section 7.2).

The system design objectives are summarized in Table 2; Table 19 shows the corresponding objective function values, for each of the systems designs that were developed.

Table 19: Objective function values for the final system designs

Objective	Variable	Unit	Target	Design A	Design B	Design C
f_1	η_{th}	%	$\uparrow$	25.9	17.7	27.5
f_2	P_2	MPa	$\downarrow$	25.0	25.0	25.0
f_3	T_4	°C	$\downarrow$	550	550	550
f_4	A_{N}	$\times 10^3\,\text{mm}^2$	$\downarrow$	175	525	750
f_5	$\dot{m}$	kg/s	$\downarrow$	200	600	250

The three system designs that were developed should not be compared without taking into account that the constraints on the system were different in each case. As such, all three of these designs can be considered optimal (or near-optimal) insofar as a weighted combination of the objectives are concerned, and given the constraints under which the designs were developed.

As can be expected based on the fact that it had no special constraints, Design A is the most balanced of the three designs: it achieves a relatively high efficiency whilst requiring a small nominal flow area and a low mass flow rate. Of the three designs, Design A therefore performs well with regards to f_4 and f_5, and moderately well with regards to f_1.

Although Design C is the most efficient of the three designs and therefore performs well with regards to f_1, it requires a nominal flow area that is more than four times as high as the nominal flow area of Design A, as well as a higher mass flow rate. Design C therefore performs poorly with regards to f_4 and f_5.

Design B is arguably the worst design of the three: it has a low efficiency, a large nominal flow area and a high mass flow rate. It therefore performs poorly with regards to f_1, f_4 and f_5.

The three designs have the same values for both compressor outlet pressure P_2 and turbine inlet temperature T_4. The values that were chosen for these variables can be considered to be a good trade-off between efficiency and cost. Higher values for P_2 and T_4 can improve the efficiency of the cycle, but are associated with higher costs. All three designs can therefore be considered as optimal for at least objectives f_2 and f_3.

Thermodynamic Diagrams

Temperature-entropy (Ts) and pressure-specific volume (Pv) diagrams are useful tools to study the characteristics of a thermodynamic cycle. Figure 75 shows the actual Ts and Pv diagrams for the three developed designs.

These diagrams are based on the actual thermodynamics in the cycle. The diagrams are made up of 80 control volumes each (10 for the solar receiver, 10 for the heat sink and 30 for each side of the recuperator); the thermodynamic properties of each control volume are available directly from Flownex®. The main thermodynamic states (i.e. at the interfaces between the components) are indicated by the numbers 1 through 6.

The stations of analysis within the turbomachines (i.e. at the eye and at the tip) can be added as additional "control volumes," but are omitted here in the interest of clarity.

Compression near the Critical Point

The first aspect that the actual Ts diagrams shows is the special variation of the thermodynamic properties near the critical point, which is in the lower left-hand-side corner of the Ts diagram. The isobars become less steep near the critical point, and converge towards each other. This means that less energy is required to compress the fluid from one pressure to another near the critical point. It is one of the main advantages of a supercritical cycle (Musgrove *et al.*, 2017a).

Pressure Ratio

The Ts diagrams also indicate the pressure ratio of the cycle: the width of the Ts diagram of Design A graphically reveals that it operates at a considerably higher pressure ratio as compared to Design B, which has a much narrower Ts diagram.

Pressure Drops

The Pv diagrams are useful to observe the pressure drops in the cycle. Designs A and B clearly experience significant pressure drops, because the lines between states 2, 3 and 4, and between states 5, 6, 1 are slanted downwards. On the other hand, Design C experiences almost no pressure drops, as can be seen by the nearly horizontal lines between states 2, 3 and 4, and between states 5, 6, 1.

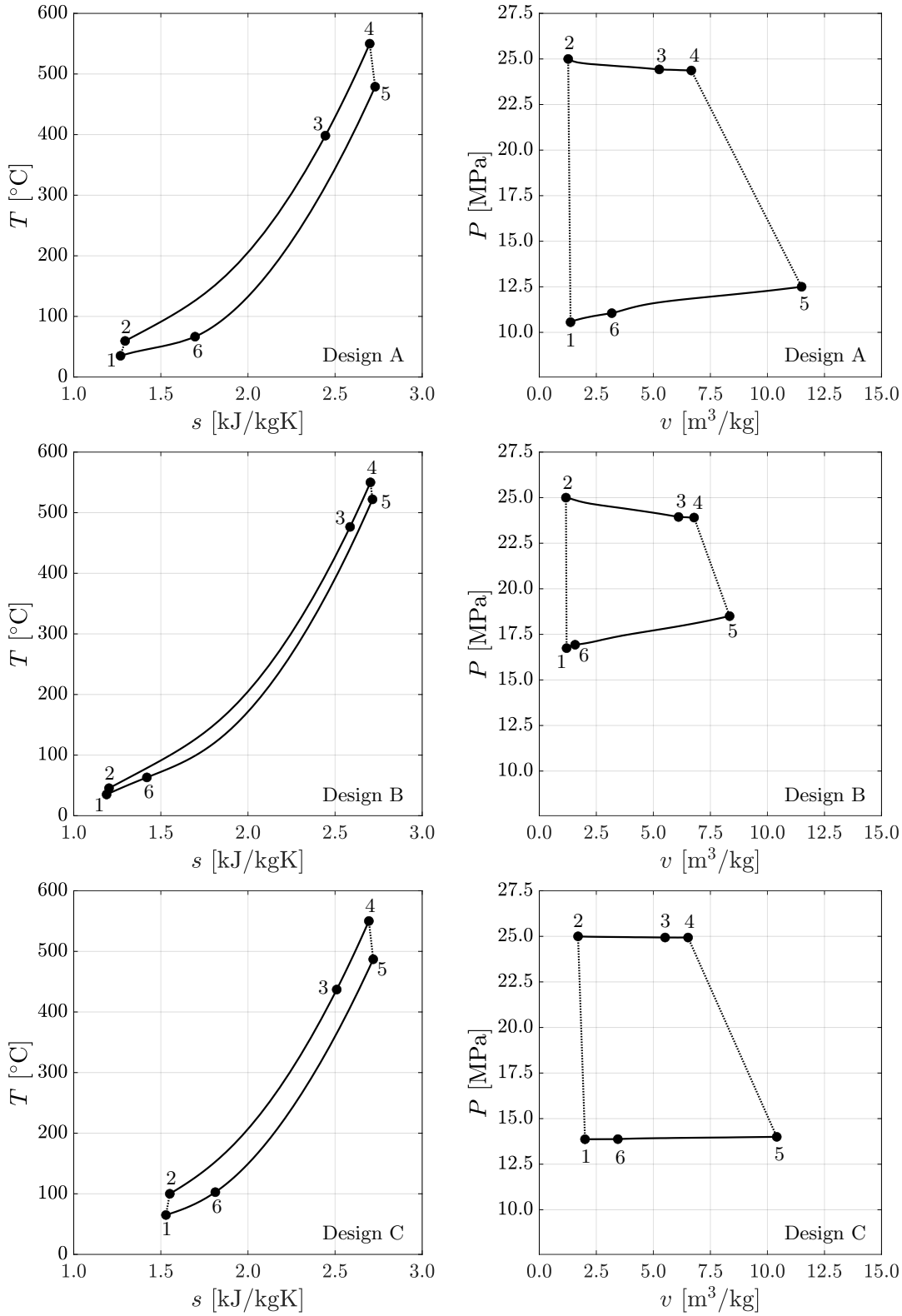

Figure 75: Temperature-entropy and pressure-specific volume diagrams for the final system designs

Back-work Ratio

The ratio between the mechanical work input (in the compressor) and the mechanical work output (in the turbine) is termed the *back-work ratio*,

$$\text{BWR} = \frac{\dot{W}_{\text{C}}}{\dot{W}_{\text{T}}} = \frac{w_{\text{C}}}{w_{\text{T}}} \,. \tag{121}$$

It is preferable to have a small back-work ratio because it means that a smaller fraction of the energy that the turbine supplies is used to drive the compressor.

Based on the values reported in Table 27 in Appendix A.3, the back-work ratio is calculated as 35% for Design A, 46% for Design B, and 42% for Design C. These values are relatively low: traditional Brayton cycles have a back-work ratio of between 40% and 80% (Borgnakke and Sonntag, 2014). A low back-work ratio is thus evidently one of the advantages of an sCO_2 cycle.

Based on the derivation by Borgnakke and Sonntag (2014), it is known that a thermodynamic cycle produces a net mechanical work output because the specific volume is larger in the expansion stage (between states 4 and 5) as compared to the compression stage (between states 1 and 2). As such, there is a link between the specific volume of the fluid and the back-work ratio of the cycle.

By analyzing the Pv diagrams in Figure 75 it is revealed that the specific volume is constant throughout the compression process, and is the same for all three designs ($\sim$2 m^3/kg). However, the expansion process takes place over a range of specific volume values. The starting point of the expansion process is the same for all three designs ($\sim$7 m^3/kg), but the end point is different: $\sim$12 m^3/kg for Design A, $\sim$8 m^3/kg for Design B, and $\sim$10 m^3/kg for Design C. Design A therefore has the highest average specific volume during the expansion phase. It is thus evident why Design A has the lowest back-work ratio of the three designs.

Recuperation

Another aspect revealed by the actual Ts diagrams is the high degree of recuperation for all three designs, as indicated by the clustering of states 1, 2 and 6, and 3, 4 and 5 at the opposite ends of the Ts diagram. Most of the temperature change in the cycle occurs in the recuperator and not in the solar receiver or in the heat sink.

It can also be clearly observed that the recuperator of Design B is less effective than the recuperators of Designs A and C, because of the greater vertical separation between states 2 and 6 in Design B as compared to the other two designs.

By considering the temperature profiles in the recuperators, it is revealed why the recuperator of Design B is less effective than the recuperators in the other two designs. Figure 76 shows the temperature of the fluid in both sides of the recuperator of Design A (which is similar to the recuperator of Design C), at each control volume. The control volumes are numbered from 1 to 30 in the direction of flow of the cold side, or equivalently from 30 to 1 in the direction of flow of the hot side. Figure 77 shows the temperature of the fluid in both sides of the recuperator of Design B at each control volume.

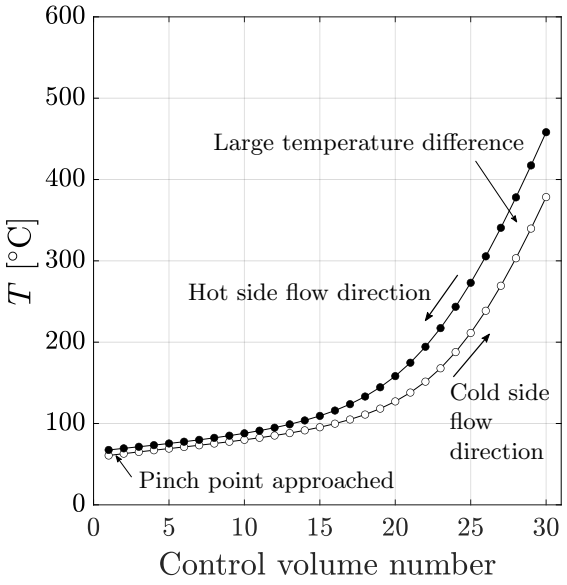

Figure 76: Temperature profile in the recuperator of Design A

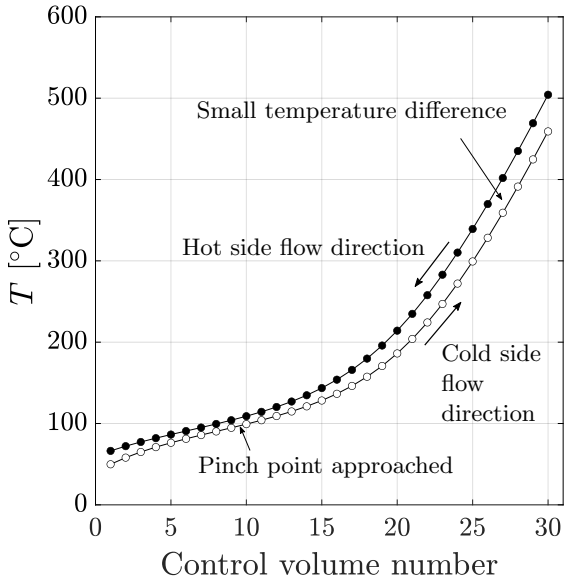

Figure 77: Temperature profile in the recuperator of Design B

In the more effective recuperator (Figure 76), there is a large temperature difference between the two fluid streams for a significant portion of the length of the recuperator, and the minimum temperature difference, or pinch point, is approached only at the end of the recuperator. On the contrary, the less effective recuperator (Figure 77) maintains a relatively small temperature difference throughout the length of the recuperator. Furthermore, the minimum temperature difference is approached in the middle of the recuperator; this is the so-called *internal* pinch point.

As a result of being driven by a temperature difference, the heat transfer rate between the two fluid streams approaches zero in the vicinity of the pinch point. Depending on cycle operating conditions, the pinch point in the recuperator shifts around; the closer the pinch point is to the inlet of the hot side of the recuperator, the lower the effectiveness of the recuperator will be. Dostal *et al.* (2004) estimate that under some conditions the internal pinch point could cause the maximum effectiveness of the recuperator to be as low as 91%.

8.4. Cycle Efficiency Analysis

The final design of the system is a culmination of a series of design decisions; each design decision in some way affects how efficiently the system can convert thermal energy to mechanical energy. It is difficult to independently asses the impact of each design decision on the final efficiency of the system, because each successive design decision must take all the previous design decisions into account. It is therefore more sensible to take a holistic approach by scrutinizing the system after the design has been completed. Santini *et al.* (2016) propose a second-law (entropy-generation) analysis, but for the current research a first-law (thermal efficiency) analysis is more appropriate given the objective function f_1. To this end, several *loss factors* that contribute to the inefficiency of the thermodynamic cycle can be identified. These are introduced, derived and compared to each other in the following sections.

8.4.1. Loss Factors in the Cycle

Operating Temperatures

As elaborated on in Section 6.1.1, the most efficient type of thermodynamic cycle is a Carnot cycle – a reversible cycle operating between two isothermal heat source and heat sink reservoirs. The thermal efficiency of the Carnot cycle can be calculated from Equation (115). As a result of not having an infinitely hot heat source and a heat sink at a temperature of absolute zero, any real thermodynamic cycle will have a Carnot efficiency of less than 100%.

The Carnot efficiency results for the developed designs – calculated using the final maximum and minimum temperatures – are available in Table 41 in Appendix B.5.

Cycle Configuration

In a thermodynamic cycle configuration which does not have isothermal heat source and heat sink reservoirs, Equation (115) can be modified as

$$\eta_{\text{th}} = 1 - \frac{\bar{T}_{\text{L}}}{\bar{T}_{\text{H}}} \,, \tag{122}$$

where $\bar{T}_{\text{L}}$ is the *average* temperature of heat rejection and $\bar{T}_{\text{H}}$ is the *average* temperature of heat addition. This represents the penalty associated with the configuration of the cycle.

Advanced configurations of the Rankine cycle typically approach the Carnot cycle well (Borgnakke and Sonntag, 2014); meaning that the average temperature of heat rejection approaches the lowest temperature in the cycle, and the average temperature of heat addition approaches the highest temperature in the cycle. As a result, the efficiency calculated by Equation (122) approaches the efficiency calculated by Equation (115). The configuration of the cycle thus contributes little to its inefficiency.

On the other hand, simple configurations of the Brayton cycle can deviate substantially from the Carnot cycle (Borgnakke and Sonntag, 2014). The efficiency calculated by Equation (122) can therefore be significantly less than the efficiency calculated by Equation (115), which indicates that the configuration of the cycle contributes considerably to its inefficiency.

For the current system, the average temperature of heat addition is the average between the solar receiver inlet and outlet temperatures. This is calculated as the sum of the temperature of the fluid in each of the control volumes (T_{CV}), divided by the number of control volumes in the solar receiver (n_{S}), i.e.

$$\bar{T}_{\mathrm{H}} = \left(\sum_{i=1}^{n_{\mathrm{S}}} T_{\mathrm{CV,i}} \right) \Big/ n_{\mathrm{S}} \ . \tag{123}$$

Similarly, the average temperature of heat rejection is the average between the heat sink inlet and outlet temperatures. This is calculated as the sum of the temperature of the fluid in each of the control volumes (T_{CV}), divided by the number of control volumes in the heat sink (n_{H}), i.e.

$$\bar{T}_{\mathrm{L}} = \left(\sum_{i=1}^{n_{\mathrm{H}}} T_{\mathrm{CV,i}} \right) \Big/ n_{\mathrm{H}} \ . \tag{124}$$

The values for $\bar{T}_{\mathrm{H}}$ and $\bar{T}_{\mathrm{L}}$ are available in Flownex® and therefore do not need to be calculated manually.

The Carnot efficiency results for the developed designs – calculated using the final average heat source and heat sink temperatures – are available in Table 41 in Appendix B.5.

Operating Pressures

From Figure 34, the higher the compressor outlet pressure is, the higher the cycle efficiency is. Additionally, from the discussion in Section 6.1.4, the lower the pressure ratio in the cycle is, the higher the cycle efficiency is. An efficiency penalty is thus incurred if the compressor outlet pressure is not maximized and if the cycle pressure ratio is not minimized.

Compressor and Turbine Efficiency

The entropy generated during the actual compression and expansion processes is a source of inefficiency for the system.

Pressure Drops

The frictional pressure drop that occurs in the heat exchangers in the direction of fluid flow is another source of inefficiency for the system. The primary effect of the pressure drops in the cycle is that the expansion pressure ratio (over the turbine) is less than the compression pressure ratio (over the compressor). The secondary effect of the pressure drops is entropy generation.

Solar Receiver Heat Loss

As a result of the solar receiver being exposed, a portion of the absorbed solar energy is lost to the environment through convection and radiation. An additional amount of solar energy must therefore be supplied to account for the heat loss. This is associated with a reduction in the thermal efficiency of the system.

Recuperator Effectiveness

A recuperator can only be 100% effective if it has an infinite length and if the thermodynamic operating conditions of the cycle do not cause the occurrence of an internal pinch point. If the recuperator has a finite length (which practically it must have) or if an internal pinch point is encountered, then the effectiveness of the recuperator is less than 100% and the cycle efficiency will be impacted as a result.

8.4.2. Theoretical Thermodynamic Cycles for Loss Factor Analysis

The impact of the first two loss factors (i.e. the operating temperatures and the cycle configuration) on the efficiency of the cycle can be derived from the Carnot theory as discussed; extensive analysis is not required.

Conversely, different theoretical thermodynamic cycles must be analyzed in order to assess the impact of the other loss factors. Each of these theoretical cycles must be ideal with regards to all factors, except for the specific factor which is to be investigated. As such, the assumptions set out in Table 20 are applied.

Table 20: Assumptions applied to the analysis of various theoretical thermodynamic cycles

	Isentropic compressor	Isentropic turbine	No pressure drops	Perfect solar receiver
Cycle for studying the effect of...				
... operating pressures:	✓	✓	✓	✓
... compressor efficiency:		✓	✓	✓
... turbine efficiency:	✓		✓	✓
... pressure drops:	✓	✓		✓
... heat loss from the solar receiver:	✓	✓	✓	

These assumptions give rise to the thermodynamic cycles presented in Table 21. The cycles in Table 21 are based on the thermodynamic states presented in Figure 78, which is a modified version of Figure 12.

Table 21: Thermodynamic states corresponding to various cycles

Actual cycle:	1	→	2	→	3	→	4	→	5	→	6	→	1
Cycle for studying the effect of...													
... operating pressures:	1	→	2s	→	3i	→	4i	→	5is	→	6is	→	1
... compressor efficiency:	1	→	2	→	3i	→	4i	→	5is	→	6i	→	1
... turbine efficiency:	1	→	2s	→	3i	→	4i	→	5i	→	6is	→	1
... pressure drop:	1	→	2s	→	3	→	4	→	5s	→	6s	→	1

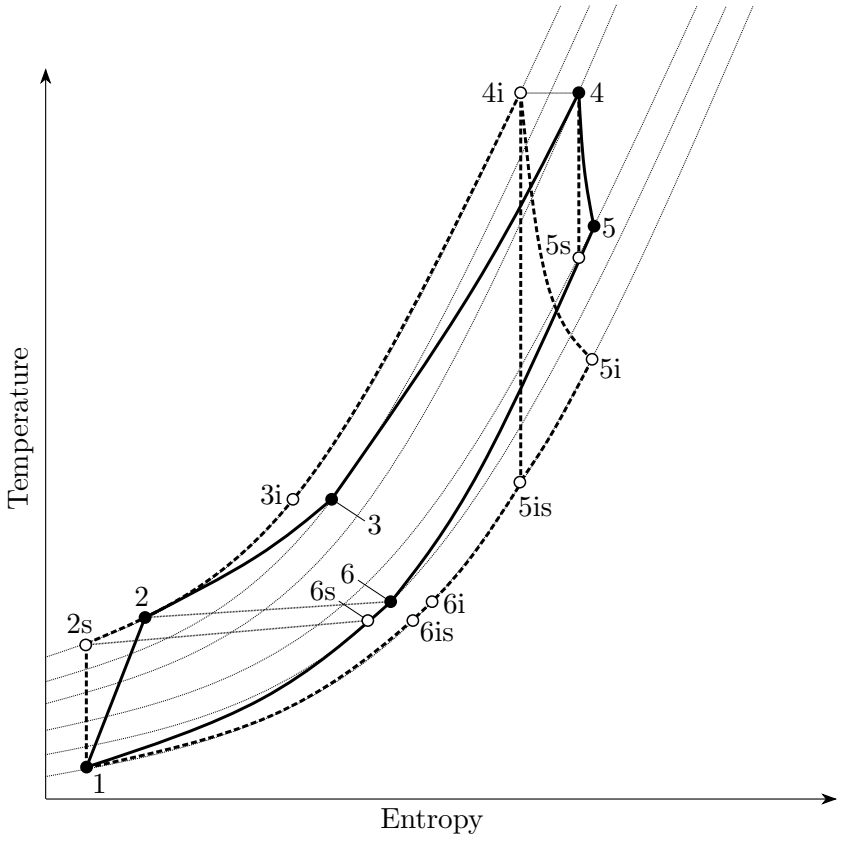

Figure 78: Diagram of actual and theoretical cycle thermodynamics

The specific compressor work input w_C, specific turbine work output w_T and specific heat rejection from the heat sink q_H of the theoretical cycles are calculated using the equations set out in Table 22. These equations are based on the theory presented in Section 3.4. The specific heat input is calculated from the conservation of energy principle using Equation (47), and the thermal efficiency of the cycle is calculated from the definition in Equation (51).

Table 22: Equations for the energy transfer in the theoretical cycles

	w_C	w_T	q_H
Cycle for studying the effect of...			
... operating pressures:	$h_{2s} - h_1$	$h_{4i} - h_{5is}$	$h_{6is} - h_1$
... compressor efficiency:	$h_2 - h_1$	$h_{4i} - h_{5is}$	$h_{6i} - h_1$
... turbine efficiency:	$h_{2s} - h_1$	$h_{4i} - h_{5i}$	$h_{6is} - h_1$
... pressure drop:	$h_{2s} - h_1$	$h_4 - h_{5s}$	$h_{6s} - h_1$

Actual Recuperator Effectiveness Calculations

In all of the newly introduced theoretical cycles, the actual recuperator effectiveness (reported in Table 31 in Appendix A.6) is used. The actual effectiveness is a response variable, calculated using Equation (46) and using the final temperatures of the cycle reported in the tables in Appendix B.4.

Using the actual recuperator effectiveness ensures that a recuperator with an internal pinch point is not inadvertently introduced into the analysis, but makes it impossible to delineate recuperator effectiveness as an independent loss factor. Nevertheless, in all of the system designs, a high recuperator effectiveness was a key focus. Increasing recuperator effectiveness is therefore not expected to be a way in which cycle efficiency can be improved.

With the actual recuperator effectiveness known, Equation (46) is rearranged as

$$\epsilon = \frac{T_5 - T_6}{T_5 - T_2} \implies T_{6\text{i}} = T_{5\text{is}} - \epsilon\left(T_{5\text{is}} - T_2\right) \ , \tag{125}$$

which is used to calculate the temperature at the heat sink inlet for the case with no pressure drops in the cycle (state 6i). Similarly, Equation (46) is rearranged as

$$\epsilon = \frac{T_5 - T_6}{T_5 - T_2} \implies T_{6\text{is}} = T_{5\text{is}} - \epsilon\left(T_{5\text{is}} - T_{2\text{s}}\right) \ , \tag{126}$$

which is used to calculate the temperature at the heat sink inlet for the case where the cycle has an isentropic compressor and no pressure drops (state 6is).

Actual Turbomachinery Efficiency Calculations

The final efficiencies of the turbomachines (reported in Table 31 in Appendix A.6) are also response variables, calculated using Equations (38) and (39) and using with the final thermodynamic states of the cycle reported in the tables in Appendix B.4.

State 5i represents the theoretical turbine outlet state if the cycle has no pressure drops but the actual turbine efficiency is maintained. The enthalpy at state 5i is calculated by rearranging Equation (39) as

$$\eta_{\text{T}} = \frac{h_{4\text{i}} - h_{5\text{i}}}{h_{4\text{i}} - h_{5\text{is}}} \implies h_{5\text{i}} = h_{4\text{i}} - \eta_{\text{T}}\left(h_{4\text{i}} - h_{5\text{is}}\right) \ . \tag{127}$$

Actual Solar Receiver Efficiency Calculations

The efficiency of the solar receiver is a response variable, calculated as

$$\eta_{\text{S}} = \frac{\dot{Q}_{\text{S,absorbed}}}{\dot{Q}_{\text{S,supplied}}} \ , \tag{128}$$

which is the ratio of the absorbed thermal energy input from Equation (36) and the supplied thermal energy input from Equation (93). Results for the system designs are reported in Table 31 in Appendix A.6.

The same thermodynamic cycle that is used for studying the effect of the operating pressures (i.e. 1-2s-3i-4i-5is-6is-1) is used to study the effect of the heat loss from the solar receiver, except that the thermal energy input is divided by the solar receiver efficiency (which makes the thermal energy input a greater amount). The thermal efficiency of the cycle, taking into account the solar receiver efficiency, is therefore

$$\eta_{\text{th}} = \frac{w_{\text{T}} - w_{\text{C}}}{q_{\text{S}}/\eta_{\text{S}}} \, . \tag{129}$$

8.4.3. Cycle Efficiency Breakdown

There is no theoretical basis for claiming that the loss factors are additive (i.e. the sum of the contributions of the loss factors added to the actual cycle efficiency gives an efficiency of 100%), especially since the effectiveness of the recuperator is implicitly taken into account in the calculations of all of the loss factors. Nevertheless, if the theoretical cycle efficiencies of Section 8.4.2 are calculated and appropriately subtracted from each other, a good approximation to the relative contributions of the loss factors can be obtained.

The calculation steps and detailed results are available in Appendix B.6, but a summary of the results is illustrated in Figure 79. This figure shows the relative contribution of each of the loss factors on the cycle efficiency. In order to yield the maximum improvement in cycle efficiency, the greatest contributions should be addressed first in subsequent system design iterations.

The largest source of inefficiency of the system is its operating temperatures – accounting for more than 35% of the total inefficiency. This is purely a limitation of the fundamental physics on which a thermodynamic cycle operates. On the lower end, the temperature of this cycle is limited by the critical temperature of the fluid, and on the upper end it is limited by the technological state-of-the-art and financial considerations.

The next largest contributor to the inefficiency of the system is the operating pressures. This factor can theoretically be reduced by choosing a higher compressor outlet pressure or a lower cycle pressure ratio. Nevertheless, consider that even though Design B has the lowest pressure ratio of all three designs (see Table 25 in Appendix A.2), it has the largest inefficiency associated with the operating pressures. The reason for this is that it also has the lowest recuperator effectiveness (see Table 31 in Appendix A.6). As Figure 34 confirms, as the recuperator effectiveness becomes poorer, the compressor outlet pressure must be increased in order to maintain a given cycle efficiency.

The inefficiency of the compressor and turbine stages together contribute to nearly 15% of the inefficiency in the cycle. Although the compressor stage is less efficient than the turbine stage for all of the designs (see Table 31 in Appendix A.6), the turbine stage contributes a greater proportion to the inefficiency of the cycle. This suggests that it is more important for the system to have an efficient turbine stage as compared to an efficient compressor stage.

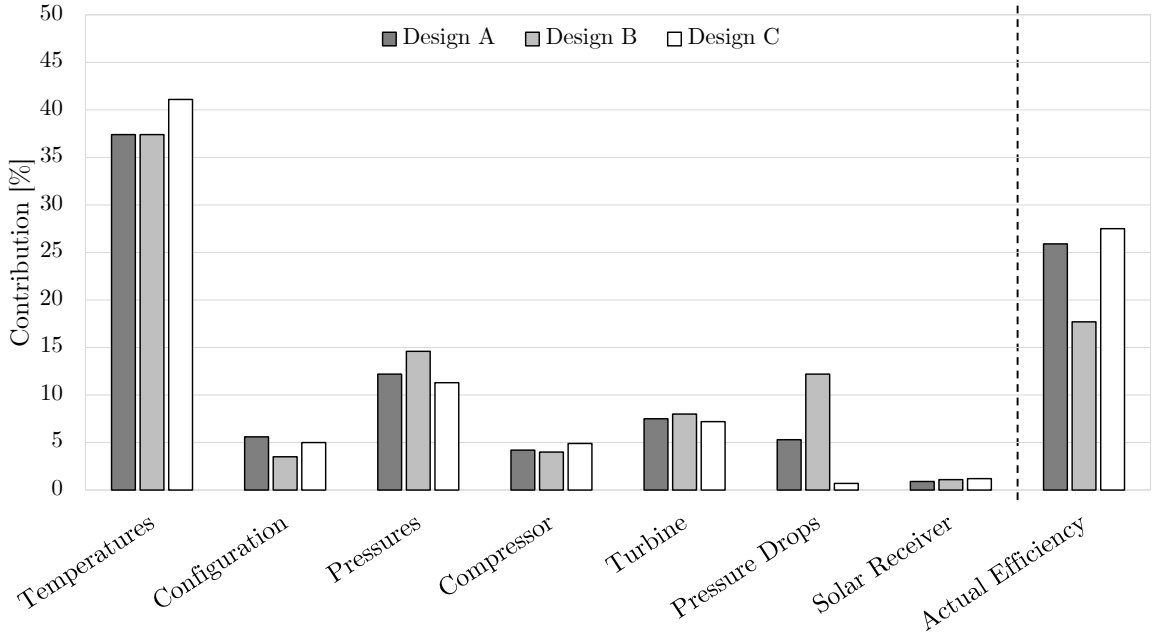

Figure 79: Relative contribution of loss factors to the inefficiency Designs A, B and C

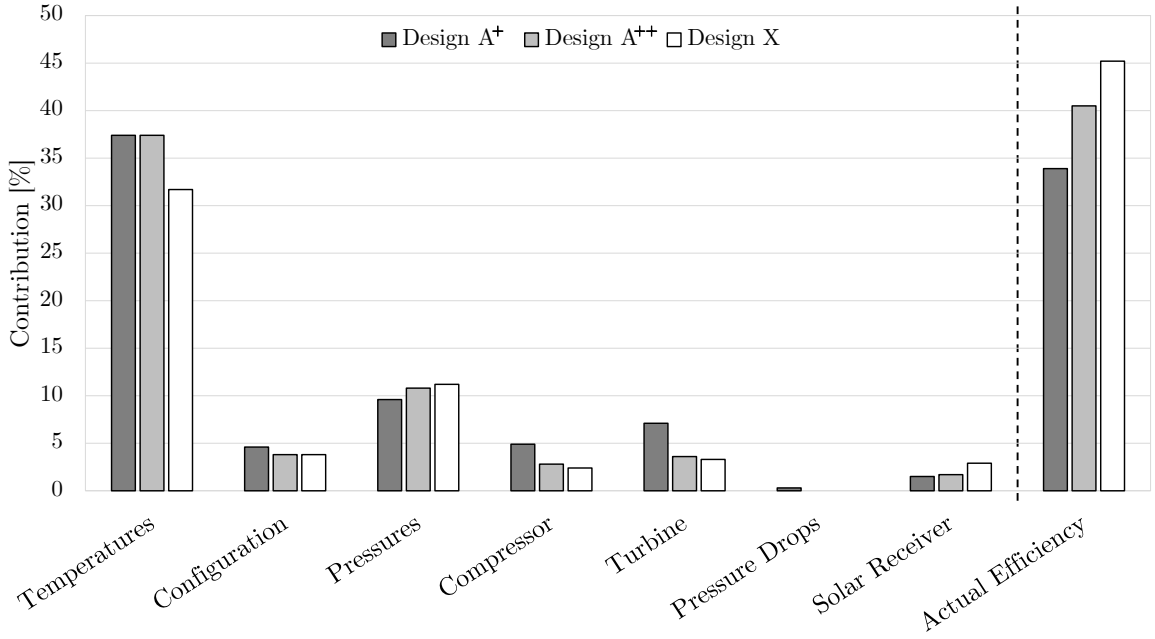

Figure 80: Relative contribution of loss factors to the inefficiency of Designs A^{+}, A^{++} and X

As a consequence of having a large degree of recuperation, the configuration of the cycle is not a significant penalty, contributing only about 5% to the overall inefficiency. This suggests that there is little to gain in terms of efficiency by utilizing a more complicated cycle configuration than the regenerative cycle configuration. Of the three designs, Design B has the lowest configuration penalty. This is because the average temperature of heat addition is higher compared to the other two designs (see Table 41 in Appendix B.5). Figure 75 graphically confirms this, as states 3 and 4 are closer to each other in Design B as compared to the other two designs.

Pressure drops can contribute substantially to the inefficiency of the system. In Design B, the pressure drops cause the system to lose more than 10% of its efficiency. Considering that the actual cycle in Design B is only around 18% efficient, this is extremely high.

Design C is nearly 5% more efficient than Design A, just in terms of the contributions associated with the pressure drops in the two cycles. By having low pressure drops, Design C is able to overcome the disadvantage of operating with a higher compressor inlet temperature; it is actually the most efficient of the three designs.

Heat loss from the solar receiver is only a small source of inefficiency for all of the designs, suggesting that utilizing a point-focus solar receiver would not offer a significant improvement in efficiency for the current system.

8.5. Improved System Designs

Based on the cycle efficiency breakdown, three improved designs are presented. These are referred to as *Design* A^+, *Design* A^{++} and *Design X*.

Design A^+

Without changing the fundamentals of the design (compressor and turbine inlet temperatures, compressor outlet pressure, mass flow rate and cycle configuration), the results of Figure 79 suggest that two basic improvements can be made to Design A: choosing a lower pressure ratio and reducing the pressure drops.

To implement these design changes, Section 6.1.4 is revisited. A more optimistic turbine outlet pressure of $P_5 = 14\,\text{MPa}$ (compared to 12.5 MPa) is chosen and the rest of the design procedure is completed as before.

The new design requires a significantly larger nominal flow area compared to Design A (see Table 25 in Appendix A.2), but the larger nominal flow area means that the flow velocity is less and therefore the pressure drops are also less. Compared to the original Design A, Figure 80 shows that this improved Design A^+ has a slightly smaller inefficiency associated with the operating pressures and a significantly smaller inefficiency associated with pressure drops. As a result, Design A^+ has an efficiency that is eight percentage points higher than Design A. This is a significant improvement in terms of objective f_1, but objective f_4 is impacted as a result of the larger nominal flow area needed in Design A^+.

Design A^{++}

If the turbomachinery stage designs are improved (in this instance by the replacement of the coefficients as set out in Table 30 in Appendix A.5), then a design with an even higher turbine outlet pressure of $P_5 = 15.8\,\text{MPa}$ is possible. Without changing the fundamentals of the design (compressor and turbine inlet temperatures, compressor outlet pressure, mass flow rate and cycle configuration) and continuing the design process as before from Section 6.1.4, the results shown in Figure 80 are achieved.

With the lower inefficiency associated with the inefficiency of the turbomachinery stages, this new Design A^{++} has an efficiency that is more than six percentage points higher than Design A^{+} without needing a larger nominal flow area. Objective f_1 is therefore improved without impeding objective f_4.

Design X

Design X is an example of a more extreme (but nevertheless reasonable) design. Objectives f_1 and f_5 are more optimal, whilst objectives f_2 and f_3 are less optimal. For Design X, the turbine inlet temperature is 700 °C, the compressor outlet pressure is 30 MPa and optimistic coefficients are used for the turbomachinery stages (as set out in Table 30 in Appendix A.5).

Although the nominal flow area of Design X is the same as in Designs A^{+} and A^{++}, the mass flow rate is 35% smaller (see Table 25 in Appendix A.2). As a result, pressure drops are practically eliminated from Design X.

Figure 80 shows that the efficiency gained by operating at a higher turbine inlet temperature is translated almost directly to an increase in cycle efficiency. At 45.2%, the efficiency of Design X is about five percentage points higher than the efficiency of Design A^{++}.

Another aspect to note in Figure 80 is the increased inefficiency associated with the solar receiver in Design X, given the higher turbine inlet temperature and therefore increased heat loss. Bellos and Tzivanidis (2017) show that increased heat loss from the solar receiver could be justified because it corresponds to increased exergetic efficiency, but Design X lies beyond what is considered by the authors to be optimal for a tubular sCO_2 solar receiver.

8.6. General Discussion

The following sections contain meaningful insights and considerations about the final system designs and the design process in general. The first discussion is on what the impact of dry-cooling on the system is. The efficiency of the final designs is then placed into context. Discussions on how to choose the design variables and constants of the problem, the concept of pressure-dominance and how a successful design of the system depends on it, and what to take into account when choosing tolerance levels and units of the variables are presented next. Finally, there are some thoughts about what role the human designer will have as computing power and problem-solving methods continue to evolve.

8.6.1. Dry-cooling

Heat Sink Size and Sensitivity

As demonstrated by the results of Table 29 in Appendix A.4 and Table 31 in Appendix A.6, the heat sink is the largest component of the cycle by a considerable margin. The total surface area of the heat sink ($A_{s,H}$) is two orders of magnitude greater than the total outside surface area of the glass cover tube of the solar receiver ($A_{s,G,o}$). The heat sink tube length (L_H) is also at least an order of magnitude greater than the tube length of the flow channels in the solar receiver (L_S) and recuperator (L_R). The heat sink therefore contributes disproportionately more to the total land-use area and the total cost of materials, compared to the other two heat exchangers.

The heat sink surface area is nearly 40% smaller in Design A^{++} compared to the original Design A, despite the major cycle operating conditions remaining the same. Evidently, the size of the heat sink is sensitive to the design variables (and constants), because it can change substantially even if only minor changes are made elsewhere in the design of the system.

Heat Sink Size and Cycle Efficiency

From the outset of its design, Design C is required to have a short heat sink length, and, compared to Designs A and B, this is indeed the case. However, if Design A is evolved first into Design A^{+} and then into Design A^{++}, not only does the cycle efficiency improve, but the heat sink length surface area is reduced as well. This is to the extent that Design A^{++} and Design C actually have a similar heat sink length and surface area, despite this not being an explicit objective for Design A^{++}. Given that Design A^{++} is significantly more efficient than Design C, Design C cannot be recommended.

It is clear that an efficient cycle confers an advantage in terms of requiring a smaller heat sink area. The conclusion is therefore that a more practical alternative to a design variation where the heat sink length is minimized from the outset (Section 7.2), is to complete the standard design procedure (Chapter 6), review the design and possibly iterate the design so that cycle efficiency is maximized. If the heat sink is still unacceptably long even after optimization of the cycle efficiency, then the approach described in Section 7.2 can be followed.

8.6.2. System Efficiency Review

The overall solar-to-electric efficiency of parabolic trough solar thermal power systems that operate with steam as the working fluid is between 12% and 22% (Patnode, 2006; Breeze, 2014). Assuming a solar-to-thermal conversion efficiency of 75% (Breeze, 2014) and a mechanical-to-electric conversion efficiency of 98% (Patnode, 2006), Design A^{++} would achieve a solar-to-electric efficiency of 30% and Design X a value of 33%.

These results are within the range of efficiency values expected for CSP systems with sCO_2 as working fluid (Muñoz-Antón *et al.*, 2015; Osorio *et al.*, 2016b; Binotti *et al.*, 2017), although it must be emphasized that comparisons to other system designs should take into account the constraints on the system and the modeling assumptions.

Evidently, a considerable improvement in overall system efficiency is possible if an sCO_2 cycle instead of a steam cycle is used in parabolic trough CSP systems. This increase in efficiency is largely as a result of a higher turbine inlet temperature. Parabolic trough systems that use a steam cycle are limited to a maximum turbine inlet temperature of around 400 °C because of the need to use a heat transfer oil in the solar receiver, whereas the sCO_2 working fluid can be heated directly in the solar receiver up to considerably higher temperatures (Muñoz-Antón *et al.*, 2015). Not only does the elimination of the heat transfer oil from the system contribute to improved system efficiency, but it also makes the system simpler.

Design A^{++} achieves more than 90% of the performance level of Design X (30% compared to 33%), yet it has a turbine inlet temperature that is 150 °C lower. This may suggest that operating the current system at a higher turbine inlet temperature than 550 °C is not justifiable in terms of the improvement in system efficiency. Design A^{++} is therefore recommended over Design X.

Design A^{++} also prominently showcases the unique features of the sCO_2 cycle. It operates at a relatively mild maximum temperature and pressure, the cycle configuration is simple, a dry-cooled heat sink is practical, and a parabolic trough solar collector with a linear receiver is suitable. A large improvement in overall system efficiency is also observed when compared to existing parabolic trough plants using steam cycles.

If a higher system efficiency is required, it is recommended that a different basic system is used instead of the system considered in this research. Such a system should have a more advanced configuration, such as the combined cycle analyzed by Milani *et al.* (2017), and use a point-focus receiver to minimize heat loss from the receiver. In order to justify the increased complexity and cost of such a system, the efficiency improvement over a system like Design A^{++} should however be maximized; a turbine inlet temperature at or above 700 °C is therefore recommended.

8.6.3. Choosing Design Variables and Constants

Some variables cannot be calculated as a function of the other variables and therefore they must necessarily be treated as design variables. However, it is also possible to include response variables in the design vector and to treat them as though they were design variables. It is useful to do this for several reasons:

- Explicit control over the lower and upper bounds of these response variables is facilitated. This makes it convenient to control the range of allowable values for these response variables, without having to add explicit constraints to the model(s).
- It could be more convenient to solve for the value of a response variable numerically as part of the overall analysis, rather than to derive an explicit expression for it as a function of the design variables and constants.
- The values of all response variables corresponding to a valid design can be found as a function of the design vector, by analyzing the detailed models with the valid design vector as input. This allows the extended design vector $\mathbf{z}$ to be created.

However, this additional "post-processing" analysis does not have to be done if all the variables of interest (whether they are design variables or response variables) are already in the standard design vector $\mathbf{x}$.

For the current research, there are 12 response variables that are included in the design vector. These are the temperatures and pressures at the tip and at the eye of the turbomachines, and the turbomachine power ratings. These response variables are enclosed in brackets in Table 26 in Appendix A to indicate that they are not actually design variables.

The number of *bona fide* design variables in the problem is therefore 23, even though there are 35 variables in the design vector. In other words, with reference to Equation (4), in this case the problem is 23-dimensional even though $n = 35$.

Choosing which variables to treat as constants from the outset of the design process is another consideration. For example, in the developed system designs, the recuperator flow channel dimensions, wall thicknesses and number of parallel flow channels for the solar receiver and heat sink are treated as constants. This considerably reduces the number of design variables in the problem and therefore makes designing the system easier, but it eliminates some design possibilities from the optimization. It is debatable whether this trade-off between a slightly more optimal design is worth the additional complexity and computational expense associated with introducing more design variables.

8.6.4. The Concept of Pressure-dominance

Muñoz-Antón *et al.* (2015) observed that the efficiency of a solar thermal power system with a linear receiver is highly dependent on the length-to-diameter ratio of the receiver, and concluded that this is because of the impact that the length and diameter have on the pressure drop in the receiver and on the convection heat transfer coefficient. The current research elaborates on this finding and proposes that it should be a fundamental part of the design process of the whole system, not just the solar receiver.

In the following sections, a formal derivation from the fundamental theory of frictional pressure drop and the theory of convection heat transfer is used to demonstrate that the system operates in two distinct regions, depending on the velocity of the flow.

Pressure Change Derivation

The frictional pressure drop in the heat exchangers can be expressed as (Çengel and Ghajar, 2015)

$$\Delta P = f\frac{L}{D}\frac{\rho V^2}{2} \implies \frac{\Delta P}{L} = f\frac{1}{D}\frac{\rho V^2}{2}\,, \tag{130}$$

which shows that the pressure drop per unit length in a heat exchanger is proportional to the square of the flow velocity V, or

$$\frac{\Delta P}{L} \propto V^2\,. \tag{131}$$

Temperature Change Derivation

The temperature change for a fluid flow from the steady-state conservation of energy is

$$\Delta T = \frac{\dot{Q}}{\dot{m}\, c_{\mathrm{p}}} \,, \tag{132}$$

where c_{p} is the specific heat capacity of the fluid (Çengel and Ghajar, 2015). If the definition of the mass flow rate,

$$\dot{m} = \rho\, V A_{\mathrm{c}} \,, \tag{133}$$

is substituted into Equation (132), then it shows that

$$\Delta T = \frac{\dot{Q}}{\rho\, V A_{\mathrm{c}}\, c_{\mathrm{p}}} \,. \tag{134}$$

For convection heat transfer, the heat transfer rate can be expressed as

$$\dot{Q} = h\, A_{\mathrm{s}}\, \tau \,, \tag{135}$$

where A_{s} is the surface area of the flow channel, and τ is the temperature difference between the fluid and the surface of the surrounding channel (Çengel and Ghajar, 2015).

For a circular flow channel, the surface area is

$$A_{\mathrm{s}} = \pi D L \,. \tag{136}$$

Substitution of Equation (135) into Equation (134) reveals

$$\Delta T = \frac{h\, A_{\mathrm{s}}\, \tau}{\rho\, V A_{\mathrm{c}}\, c_{\mathrm{p}}} = \left(\frac{A_{\mathrm{s}}\, \tau}{\rho\, A_{\mathrm{c}}\, c_{\mathrm{p}}}\right)\left(\frac{h}{V}\right) \,, \tag{137}$$

into which Equation (136) is substituted to reveal

$$\Delta T = \left(\frac{\pi D L\, \tau}{\rho\, A_{\mathrm{c}}\, c_{\mathrm{p}}}\right)\left(\frac{h}{V}\right) \implies \frac{\Delta T}{L} = \left(\frac{\pi D\, \tau}{\rho\, A_{\mathrm{c}}\, c_{\mathrm{p}}}\right)\left(\frac{h}{V}\right) \,. \tag{138}$$

Based on the Dittus-Boelter correlation (Çengel and Ghajar, 2015) for *turbulent* flow in a circular flow channel, the convection heat transfer coefficient can be expressed as

$$\begin{aligned} h &= \frac{k}{D}\,\mathrm{Nu} \\ &= \left(\frac{k}{D}\right)\left(0.023\,\mathrm{Re}^{0.8}\,\mathrm{Pr}^{n}\right) \\ &= \left(0.023\,\frac{k}{D}\,\mathrm{Pr}^{n}\right)(\mathrm{Re})^{0.8} \\ &= \left(0.023\,\frac{k}{D}\,\mathrm{Pr}^{n}\right)\left(\frac{\rho V D}{\mu}\right)^{0.8} \,. \end{aligned} \tag{139}$$

This reveals that the convection heat transfer coefficient is proportional to the flow velocity in the relationship

$$h \propto V^{0.8} \,. \tag{140}$$

Finally, Equation (140) is substituted into Equation (138) to show that

$$\frac{\Delta T}{L} \propto \frac{V^{0.8}}{V} = \frac{1}{V^{0.2}} \,. \tag{141}$$

For *laminar* flow, the convection heat transfer coefficient is not a function of the flow velocity (Çengel and Ghajar, 2015), therefore from Equation (138) it is observed that

$$\frac{\Delta T}{L} \propto \frac{1}{V} \,. \tag{142}$$

Dominated Regions

Comparing Equation (131) with Equation (141) – for turbulent flow – or Equation (142) – for laminar flow – reveals that, per unit length of the heat exchanger, at low flow velocities the fluid temperature changes significantly whereas the fluid pressure changes only slightly, whilst at high flow velocities the fluid temperature changes slightly but the fluid pressure changes significantly. This behavior is illustrated in Figure 81 for both the laminar flow and turbulent flow cases.

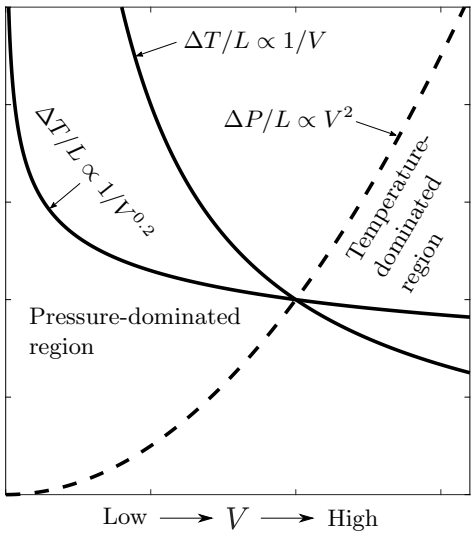

Figure 81: Pressure-dominated and temperature-dominated regions in a heat exchanger

The variable that changes *less* per unit length is referred to as the *dominating* variable. At low flow velocities, pressure dominates temperature, meaning that a large range of temperature change occurs over a small range of pressure change. At high flow velocities, temperature dominates pressure, meaning that a large range of pressure change occurs over a small range of temperature change.

The true relationships of $\Delta P/L$ and $\Delta T/L$ to V are not as simple as Equations (131), (141) and (142) suggest, given that some of the variables are implicit functions of temperature and pressure, but these equations are nevertheless good approximations to highlight the different trends.

It should also be understood that the transition between the pressure-dominated region and the temperature-dominated region is not well-defined and neither does it correspond to a particular flow velocity. It is also not important to know where this transition point is, but rather that it exists and that a successful design of the system depends heavily on which region its heat exchangers operate in.

As illustration of this, consider Figures 50 and 51 in Section 6.3.1, which show the outlet temperature and pressure of the solar receiver as a function of its length. Over the 100 m length, the possible temperature range is large, around 250 °C, and the possible pressure range is small, around 100 kPa. As a result, the length of the solar receiver could be chosen purely by considering the outlet temperature, because the outlet pressure changes so little that it is essentially fixed. Moreover, this is also why the two sub-system design spaces in Figure 43 were matched on pressure only and not on temperature as well. If the system is pressure-dominated, then once the pressure is fixed, the possible temperature range is still large enough that temperature-matching between the sub-system design spaces is essentially guaranteed as well.

For this reason, it is preferred that the system be pressure-dominated. To affect the pressure dominance of the system, consider that pressure-dominance is a function of flow velocity. The easiest way to affect the flow velocity in the heat exchangers without drastically changing any of the other variables is to change the cross-sectional (i.e. the nominal) flow area. From Equation (133) it is clear to see that a larger nominal flow area results in a lower flow velocity and thus greater pressure-dominance, whereas a smaller nominal flow area results in a greater flow velocity and thus greater temperature-dominance.

Its influence on the pressure-dominance of the system means that the nominal flow area is arguably the most important design variable. Moreover, provided that an appropriate nominal flow area is chosen that makes the system pressure-dominated and that allows an overlap of the two sub-system design spaces on heat exchanger outlet pressure (Figure 43), then a complete design of the system can be achieved using only a single once-through execution of the design procedure.

8.6.5. Tolerances and Units

An optimization algorithm considers a design as valid if the constraints are satisfied to within a given tolerance level. In this research, the thermodynamic model and the power system model are both analyzed using optimization algorithms with a tolerance on the constraints of 0.001. This implies that variables are exact up to the second decimal figure. For example, values between 9.999 MW and 10.001 MW are acceptable approximations to 10.00 MW.

Given that the same level of tolerance is applied to all constraints, the choice of units for the variables in the problem must be carefully considered. For example, if the power rating is measured in gigawatt instead of megawatt, then values between 0.009 GW and 0.011 GW would be acceptable approximations to 0.010 GW, or equivalently, values between 9 MW and 11 MW would be acceptable approximations to 10 MW. This demonstrates, from a numerical point-of-view, that 10.00 MW is not the same as 10 MW because the former can include up to 0.002 MW of variation whereas the latter can include up to 2 MW of variation. Such a large variation is likely not sufficiently accurate, and therefore it is necessary to measure the power rating in a unit such as megawatt as opposed to a unit such as gigawatt.

All the design variables of the system have a lower bound of at least one, which means that all variables have at least one non-decimal significant figure. Since the tolerance of the optimization algorithm guarantees an exact solution up to the second decimal figure, it is therefore appropriate to report all results up to three significant figures only. In some cases, for example with the outlet pressures of the heat exchangers in Section 6.3, more figures are indicated to highlight that a unique solution within a small range of values is found. It does not suggest a greater degree of accuracy.

The designer should always apply common sense, and recognize that a unique, converged solution from a computational point of view is a different concept from a solution that is within a practical tolerance level. For example, it is not necessarily meaningful to continue to refine the design space of the power system further in Section 6.4, since all the relevant dimensions of the turbomachines are already known to within a small range of values. Although it is easy for a human designer to recognize (in this example) that geometrical measurements within a small range of values are not necessarily materially different, it is difficult to implement such logic in a computational environment where exact tolerances are applied. This flexibility with regards to tolerances is a distinct advantage of not having an overarching optimization algorithm as part of the design procedure.

8.6.6. The Value of Human Intervention and Insight

Since the early introduction of optimization methods to design applications, maintaining the value of an experienced human designer without it becoming a hindrance to taking full advantage of high-performance computers has been an important consideration (Tong and Gregory, 1992). An optimization method "is not intended to replace [the designer's] intuition and experience but is simply a tool which allows one to arrive at a better end result [as compared to using] a more traditional approach" (von Spakovsky, 1994).

Nevertheless, computing power available to mainstream consumers at present is superior to that which would have been considered state-of-the-art a few years ago. This brings with it the opportunity to solve problems in new and better ways.

As computers become ever faster and more efficient, models that were considered as computationally prohibitively expensive in the past may soon become practical to solve. A system designer could then merely look at several thousands of valid, complete system designs and subsequently choose a suitable one based on the relative performance of the available options, without needing any prior experience or insight.

In fact, if sufficient time is invested to develop customized models that are faster to solve than the current MATLAB® and Flownex® models, if appropriate solution algorithms are used, and if some concessions are made with regards to the accuracy of the solution, tolerances on the constraints, or size of the initial design space to be investigated, then such a scenario is possible at present.

Although it is *possible* to treat the system design optimization problem purely as a mathematical problem to be solved by a computer, it is not necessarily *recommended*. Many of the advantages of the developed design procedure discussed in Section 8.2 is as a result of human intervention in the design process. Taking advantage of human knowledge (such as that the surrogate model can be used to make design decisions), insights (such as that the design space of the system is affected by component performance levels) and heuristics (such as anticipating the effects of pressure drop) has added considerable value to the design procedure.

In addition, there can be no truly optimal design of the system. Even if detailed multidisciplinary design optimization becomes a routine engineering exercise, trade-offs between multiple objectives with subjective relative weightings will remain an inevitable part of the design process. Such trade-offs can only be made by a designer with professional intuition and experience.

9. Conclusion

9.1. Summary

A new procedure for the *ab initio* design of a supercritical carbon dioxide solar thermal power system was developed. At the core of the developed design procedure is a mathematically rigorous computational architecture, which has clear definitions for the variables, constraints and objectives of the system design.

The design space of the complete system is equivalent to the intersection between the valid power sub-system design space and the valid thermal sub-system design space. The design spaces of the sub-systems can be found in a variety of ways; the two ways demonstrated in this research are gradient-based optimization and Monte Carlo simulation. Given that these are numerical techniques, it is necessary to assume that the true design space is approximated well by the pseudo design space with a sufficiently large number of design vectors. The search for more valid design vectors can be terminated by graphical inspection of the evolution of the design space in real-time. The concept of the extended design space is introduced so that design decisions can be made in a consistent manner, regardless of whether the design space is plotted in terms of objective function values or variable values.

A significant portion of the computational expediency of the design procedure is attributed to the use of a surrogate model. This is a computationally-inexpensive model of the thermodynamics of the Brayton cycle. It allows many design decisions to be made without analyzing the computationally-expensive detailed turbomachinery and heat exchanger models. In order to ensure appropriate integration of the surrogate model into the design process, two requirements must be met: key design variables must be the same in both the surrogate problem and the actual problem, and the objective function(s) must behave similarly with regards to the key design variables in both the surrogate problem and the actual problem.

The details of the thermodynamic model which is used as the surrogate model are presented in Chapter 3. The assumptions and theory on which the model is developed are discussed. The surrogate model is developed in MATLAB® and solved using the built-in optimization algorithm. Thermodynamic properties (for this and the other models) are sourced from realistic thermodynamic property tables. The developed model is validated with three different models from literature and is demonstrated to match the published literature well.

Chapter 4 details the power system model. A one-dimensional mean-line analytical modeling approach is chosen because it is flexible, customizable and amenable to computationally-efficient global optimization. The model is developed in MATLAB® and solved using the built-in optimization algorithm.

The turbine and compressor are both modeled using the same fundamental approach that considers the conservation of mass, momentum and energy at different locations within the stage. In the rotor section, velocity diagrams are used to represent the relationships between the velocity vector components and the associated angles between them.

User-specified values of the compressor slip factor and turbine incidence factor are required before the models can be analyzed. Entropy generation in the rotor section is modeled by applying a user-specified isentropic efficiency value. This is an acceptable simplification given that the design space of the turbomachines is restricted to ensure that ratios between variables always remain within the acceptable ranges published in literature. The performance of the nozzle and diffuser sections is modeled using classical loss factors with user-specified coefficients. All coefficients are given typical values from literature.

The power system model is qualitatively verified because the relationships between variables hold true to the relationships that would be expected from an experimental test. Quantitative validation is performed by comparing the models to experimental data from two different projects and data from a computational fluid dynamics study. Results are demonstrated to be in good agreement.

Chapter 5 details the thermal system model. A control-volume-based approach is followed which has the ability to recreate the internal pinch point of the recuperator. The thermal system is modeled in the commercial software package Flownex®. In Flownex®, the heat exchangers are connected to each other in a network, consisting of flow channel elements and heat transfer elements. The conservation of mass, momentum and energy equations are solved for each control volume in the flow channels. Heat transfer is modeled using the thermal resistance concept.

Validation of the thermal system model is performed by comparing a Flownex® model of the recuperator with experimental data, and by comparing the magnitude of heat loss from the solar receiver with two different sets of results published in literature. Results are demonstrated to be in good agreement.

The design procedure itself is introduced and discussed in Chapter 6. It is divided into four stages of decisions that the designer must make. It can be considered as a Sequential Design-space Reduction (SDR) optimization procedure because the design space of the system is successively reduced through a series of Pareto-optimal design decisions.

Chapter 7 demonstrates how the same design procedure can effectively be applied even if special constraints are applied to the system. The analysis of the developed design procedure in Chapter 8 confirms that it achieves all of the stated objectives.

Chapter 8 also includes an analysis of the final system designs that were developed using the design procedure. Several loss factors are identified and derived. The relative contribution of each of the loss factors to the inefficiency of the system is illustrated. This provides a quantitative way to assess a particular design of the system, and highlights the factors which should be addressed first in subsequent design iterations. To demonstrate this, three additional designs of the system are completed.

9.2. List of Novel Contributions

This research makes the following novel contributions:

- A new procedure for the *ab initio* design of a supercritical carbon dioxide solar thermal power system.

  The procedure allows for multi-objective *extensive* optimization, which is an improvement over classical design procedures that only offer the ability to perform *parametric* optimization. The design of the thermodynamic cycle and the detailed design of the components of the system can be performed using the procedure. The procedure is relatively simple to implement and fast to execute. Different types of component models, solution methods and design constraints are supported.

- Detailed models for the turbomachinery and heat exchangers of the system that have been validated with empirical data.

- A robust mathematical computational architecture that can be applied to any single- or multidisciplinary optimization problem, with or without the addition of a surrogate model.

- Derivations of several loss factors that contribute to the thermal inefficiency of the actual system.

  The design of the system can be improved based on comparison of the loss factor contributions. Once the contributions of all of the loss factors have been minimized to within practical limits, the efficiency of the system can be considered as maximized.

- Six optimized designs of a complete supercritical carbon dioxide solar thermal power system, with all thermodynamic-, geometric- and performance variables determined.

9.3. List of Key Findings

A summary of the key findings of this research are as follows:

- The effectiveness of the recuperator and efficiency of the turbomachines have an influence on the optimal mass flow rate of the cycle and on the size of the design spaces in Stage 1 of the design process.

  Although the performance of these components must be estimated in Stage 1 of the design process, their true performance is only calculated in later stages. To achieve an optimal system design therefore requires iteration of the design procedure if the estimated performance differs from the actual performance.

- Based on the cycle efficiency analysis of the final system designs, the combination of a line-focus solar receiver and the simple recuperated cycle configuration is recommended for sCO_2 cycles with turbine inlet temperatures up to 550 °C.

  The recommended system design achieves a thermal-to-mechanical conversion efficiency of 40% and an estimated solar-to-electric conversion efficiency of 30%. This is a considerable improvement compared to line-focus systems that use a classical steam cycle. The higher efficiency is primarily attributed to the higher turbine inlet temperature that is possible in the sCO_2 cycle.

  Higher system efficiency can be achieved with a point-focus solar receiver and a more advanced cycle configuration, but the advantage is arguably only meaningful if the turbine inlet temperature is significantly greater than 550 °C.

- High pressure drops in the heat exchangers may result in a major penalty on cycle efficiency that is of a similar magnitude to, for example, operating the cycle at a high compressor inlet temperature. Pressure drops therefore cannot be assumed to be negligible and, consequently, a thermodynamic analysis alone is not sufficient to accurately predict actual system performance. It can be concluded that the detailed design of the components is essential for any advanced simulation work.

- A naturally-dry-cooled heat sink is not a recommended cooling solution because of the disproportionate physical size (and therefore cost) of the heat sink compared to the other heat exchangers.

- The design of the system is significantly simplified if it is pressure-dominated, because it allows the design spaces of the sub-systems to be matched on pressure only and not on temperature as well. The pressure-dominance of the system can be controlled by changing the value of the nominal flow area A_N.

9.4. Recommendations for Future Work

Once a design of a system has been completed with the developed procedure, it is recommended that the results from the power system model be used to develop a computational fluid dynamics simulation of the turbomachine stages. This is to design the blade profiles, nozzle and diffuser shapes, and to prepare the turbomachines for manufacturing. It may be necessary to further restrict the design space of the turbomachinery to ensure realistic designs. For example, a constraint can be added to check the area ratio of the nozzle and diffuser sections.

Future developments of the design procedure can add additional constraints to account for structural properties where relevant. For example, this can be done to ensure that the shaft diameter of the turbomachines is large enough to support the torque being transferred (which is relevant because the turbomachines of the system are small) and that the flow channel walls are thick enough to support the specified fluid pressure.

A detailed financial model with capital expenditure (CAPEX) and operating expenditure (OPEX) considerations over the lifetime of the system can be added. Such a model will lead to less subjective trade-off decisions. For example, a higher turbine inlet temperature or compressor outlet pressure could be motivated if it can be shown that the additional CAPEX requirement is eventually paid-off because the system is more efficient at producing a unit of electricity and therefore has a lower OPEX.

The relevance of a design procedure that relies on human intervention and insight is bound to be questioned as computing power and problem-solving methods continue to evolve. The developed design procedure is well-suited to take advantage of such developments because it is based on a sound computational architecture that is suitable for automation. Future work could investigate whether automating the logic of the developed design procedure is practical, and if doing so maintains the advantages that the procedure has over classical multidisciplinary design optimization methods.

9.5. Final Remarks

For global economic development to continue, clean and sustainable sources of energy are essential. If an optimized sCO_2 cycle is used in favor of a classical steam cycle in a solar thermal power system, the system can be more efficient, physically smaller and use a simpler cycle configuration. The value proposition of a solar thermal power system is therefore enhanced.

Whether for the purposes of developing a real system, or for developing a theoretical simulation of the system for further analysis, in both cases the foundation is the same. The thermodynamic design of the cycle together with the detailed design of the multidisciplinary components that form the complete system is always a requirement for further work.

Using the procedure that is developed in this dissertation, designers are able to complete an optimized design of the system in a manner that is logical and comprehensive, in a reasonable amount of time, and without needing to implement an overarching multidisciplinary optimization algorithm or explicit bi-directional communication links between the disciplines.

This research contributes to the improvement, standardization, commercialization and ultimately the proliferation of sCO_2 solar thermal power systems. The aspiration is that the application of the developed procedure in practice, whether in its current form or in an adapted form, would accelerate the pace of change in this industry.

Appendices

A. Lists of Variables

This appendix lists the variables of the models in the following groups: the design variables of the thermodynamic model, the design variables of the sub-system models (shared, power-system-exclusive and thermal-system-exclusive), constants and response variables.

A.1. Thermodynamic Model Design Variables

The thermodynamic model is used as a surrogate model, therefore its design variables are collected in the surrogate design vector $\underset{\sim}{\mathbf{x}}$. These variables and their respective lower and upper bounds are set out in Table 23. The underlined variables are the key design variables, i.e. those that also appear in the design vector of the actual problem $\mathbf{x}$.

Table 23: Design variables and default bounds for the thermodynamic model

Variable	Description	Unit	Lower Bound	Upper Bound
General				
$\underline{\dot{m}}$	Mass flow rate	kg/s	1	1 000
ϵ	Recuperator effectiveness	–	0	1
η_{C}	Compressor isentropic efficiency	–	0	1
η_{T}	Turbine isentropic efficiency	–	0	1
η_{th}	Cycle thermal efficiency	–	0	1
Temperatures (static)				
$\underline{T_1}$	Heat sink outlet/Compressor inlet	°C	32	700
$\underline{T_2}$	Compressor outlet/Recuperator cold side inlet	°C	32	700
T_3	Recuperator cold side outlet/Solar receiver inlet	°C	32	700
$\underline{T_4}$	Solar receiver outlet/Turbine inlet	°C	32	700
$\underline{T_5}$	Turbine outlet/Recuperator hot side inlet	°C	32	700
T_6	Recuperator hot side outlet/Heat sink inlet	°C	32	700
$T_{2\mathrm{s}}$	Isentropic compressor outlet	°C	32	700
$T_{5\mathrm{s}}$	Isentropic turbine outlet	°C	32	700
Pressures (static)				
$\underline{P_1}$	Heat sink outlet/Compressor inlet	MPa	7.38	30
$\underline{P_2}$	Compressor outlet/Recuperator cold side inlet	MPa	7.38	30
P_3	Recuperator cold side outlet/Solar receiver inlet	MPa	7.38	30
$\underline{P_4}$	Solar receiver outlet/Turbine inlet	MPa	7.38	30
$\underline{P_5}$	Turbine outlet/Recuperator hot side inlet	MPa	7.38	30
P_6	Recuperator hot side outlet/Heat sink inlet	MPa	7.38	30

A.2. Shared System Design Variables

Table 24 lists the shared system design variables that are collected in the vector $\mathbf{x}_s$, with their bounds. These variables appear both in the model of the power system and in the model of the thermal system. The underlined variables are the key design variables, i.e. those that also appear in the design vector of the surrogate problem $\tilde{\mathbf{x}}$. Table 25 list the values (up to three significant figures) of these variables for the final designs of the system.

Table 24: Shared system design variables and default bounds

Variable	Description	Unit	Lower Bound	Upper Bound
General				
$\underline{\dot{m}}$	Mass flow rate	kg/s	1	1 000
A_N	Nominal flow area	mm^2	1	1×10^6
Temperatures (static)				
$\underline{T_1}$	Heat sink outlet/Compressor inlet	°C	32	700
$\underline{T_2}$	Compressor outlet/Recuperator cold side inlet	°C	32	700
$\underline{T_4}$	Solar receiver outlet/Turbine inlet	°C	32	700
$\underline{T_5}$	Turbine outlet/Recuperator hot side inlet	°C	32	700
Pressures (static)				
$\underline{P_1}$	Heat sink outlet/Compressor inlet	MPa	7.38	30
$\underline{P_2}$	Compressor outlet/Recuperator cold side inlet	MPa	7.38	30
$\underline{P_4}$	Solar receiver outlet/Turbine inlet	MPa	7.38	30
$\underline{P_5}$	Turbine outlet/Recuperator hot side inlet	MPa	7.38	30

Table 25: Final values for the shared system design variables

Variable	Unit	Designs:	A	B	C	A$^+$	A^{++}	X
General								
$\underline{\dot{m}}$	kg/s		200	600	250	200	200	130
A_N	$\times 10^3$ mm^2		175	525	750	800	800	800
Temperatures (static)								
$\underline{T_1}$	°C		35.0	35.0	65.0	35.0	35.0	35.0
$\underline{T_2}$	°C		59.5	45.4	100	50.3	45.8	49.0
$\underline{T_4}$	°C		550	550	550	550	550	700
$\underline{T_5}$	°C		479	522	487	487	493	621
Pressures (static)								
$\underline{P_1}$	MPa		10.6	16.7	13.9	13.9	15.7	16.9
$\underline{P_2}$	MPa		25.0	25.0	25.0	25.0	25.0	30.0
$\underline{P_4}$	MPa		24.4	23.9	24.9	25.0	24.9	30.0
$\underline{P_5}$	MPa		12.5	18.5	14.0	14.0	15.8	16.9

A.3. Power System Design Variables

Table 26 lists the design variables that appear exclusively in the design vector of the power system $\mathbf{x}_\mathrm{p}$, with their bounds. Variables enclosed in brackets are response variables that are included in the design vector for convenience (see Section 8.6.3).

Table 26: Power system design variables and bounds

Variable	Description	Unit	Lower Bound	Upper Bound
Compressor				
Geometry				
$r_{\mathrm{tip,C}}$	Tip radius	mm	1	500
$r_{\mathrm{hub,C}}$	Hub radius	mm	1	500
$r_{\mathrm{shd,C}}$	Shroud radius	mm	2	500
b_C	Blade width	mm	1	500
Temperatures (static)				
$(T_{\mathrm{tip,C}})$	Tip temperature	°C	32	700
$(T_{\mathrm{tip,s,C}})$	Isentropic tip temperature	°C	32	700
$(T_{\mathrm{eye,C}})$	Eye temperature	°C	32	700
Pressures (static)				
$(P_{\mathrm{tip,C}})$	Tip pressure	MPa	7.38	30
$(P_{\mathrm{eye,C}})$	Eye pressure	MPa	7.38	30
Performance				
$(\dot{W}_\mathrm{C})$	Power	kW	1	10×10^3
Ω_C	Rotational speed	$\times 10^3$ rpm	1	100
Turbine				
Geometry				
$r_{\mathrm{tip,T}}$	Tip radius	mm	1	500
$r_{\mathrm{hub,T}}$	Hub radius	mm	1	500
$r_{\mathrm{shd,T}}$	Shroud radius	mm	2	500
b_T	Blade width	mm	1	500
Temperatures (static)				
$(T_{\mathrm{tip,T}})$	Tip temperature	°C	32	700
$(T_{\mathrm{eye,T}})$	Eye temperature	°C	32	700
$(T_{\mathrm{eye,s,T}})$	Isentropic eye temperature	°C	32	700
Pressures (static)				
$(P_{\mathrm{tip,T}})$	Tip pressure	MPa	7.38	30
$(P_{\mathrm{eye,T}})$	Eye pressure	MPa	7.38	30
Performance				
$(\dot{W}_\mathrm{T})$	Power	kW	10×10^3	20×10^3
Ω_T	Rotational speed	$\times 10^3$ rpm	1	100

Table 27 lists the values (up to three significant figures) of the design variables that appear exclusively in the design vector of the power system $\mathbf{x}_\mathrm{p}$ for the final designs of the system. Variables enclosed in brackets are response variables that are included in the design vector for convenience (see Section 8.6.3).

Table 27: Final values for the power system design variables

Variable	**Unit**	**Designs:**	**A**	**B**	**C**	**A$^+$**	**A^{++}**	**X**
Compressor								
Geometry								
$r_{\mathrm{tip,C}}$	mm		54.8	138	84.9	69.1	62.8	58.8
$r_{\mathrm{hub,C}}$	mm		19.0	41.7	22.4	22.1	23.1	18.0
$r_{\mathrm{shd,C}}$	mm		47.5	104	69.4	55.3	57.8	45.1
b_C	mm		15.2	27.5	22.1	17.6	18.8	11.6
Temperatures (static)								
$(T_{\mathrm{tip,C}})$	°C		48.3	40.6	84.9	43.4	40.3	42.0
$(T_{\mathrm{tip,s,C}})$	°C		46.1	39.4	82.7	41.7	39.7	41.2
$(T_{\mathrm{eye,C}})$	°C		33.4	34.7	63.6	34.5	34.6	34.6
Pressures (static)								
$(P_{\mathrm{tip,C}})$	MPa		17.5	20.9	19.4	19.4	19.9	22.8
$(P_{\mathrm{eye,C}})$	MPa		9.74	16.4	13.5	13.5	15.4	16.5
Performance								
$(\dot{W}_\mathrm{C})$	MW		5.49	8.50	7.32	3.88	2.66	2.39
Ω_C	$\times 10^3$ rpm		31.5	9.00	21.0	21.0	18.0	22.6
Turbine								
Geometry								
$r_{\mathrm{tip,T}}$	mm		92.1	203	131	131	137	85.9
$r_{\mathrm{hub,T}}$	mm		31.1	61.3	37.0	42.9	45.5	25.9
$r_{\mathrm{shd,T}}$	mm		77.7	156	112	108	114	65.4
b_T	mm		27.6	60.7	34.1	30.0	28.1	23.2
Temperatures (static)								
$(T_{\mathrm{tip,T}})$	°C		517	537	522	523	522	660
$(T_{\mathrm{eye,T}})$	°C		469	519	484	484	492	614
$(T_{\mathrm{eye,s,T}})$	°C		453	513	470	470	486	606
Pressures (static)								
$(P_{\mathrm{tip,T}})$	MPa		19.2	21.7	20.4	20.4	20.4	23.4
$(P_{\mathrm{eye,T}})$	MPa		11.8	18.2	13.8	13.8	15.7	16.3
Performance								
$(\dot{W}_\mathrm{T})$	MW		15.5	18.5	17.3	13.9	12.7	12.4
Ω_T	$\times 10^3$ rpm		31.5	9.00	21.0	21.0	18.0	35.2

A.4. Thermal System Design Variables

Table 28 lists the design variables that appear exclusively in the design vector of the thermal system $\mathbf{x}_t$, with their bounds. Table 29 lists the values (up to three significant figures) of these variables for the final designs of the system.

Table 28: Thermal system design variables and bounds

Variable	Description	Unit	Lower Bound	Upper Bound
L_S	Solar receiver length	m	1	100
L_H	Heat sink length	m	1	2 500
L_R	Recuperator length	m	0.01	20

Table 29: Final values for the thermal system design variables

Variable	Unit	Designs:	A	B	C	A$^+$	A^{++}	X
L_S	m		62.9	54.4	29.3	23.1	19.3	17.3
L_H	km		1.87	1.99	0.500	0.725	0.568	0.427
L_R	m		10.0	15.0	10.0	16.0	24.0	16.0

A.5. Constants

The coefficient values for the power system model are constant, as summarized in Table 30. Constants for the thermal system model are presented in the tables in Appendix D.

Table 30: Power system coefficient values

Variable	Unit	Designs:	A	B	C	A$^+$	A^{++}	X
$K_{N,C}$	–		0.05	0.05	0.05	0.05	0.03	0.03
$K_{N,T}$	–		0.10	0.10	0.10	0.10	0.07	0.07
η_R	–		0.80	0.80	0.80	0.80	0.90	0.90
η_D	–		0.80	0.80	0.80	0.80	0.90	0.90
σ	–		0.84	0.84	0.84	0.84	0.95	0.95
λ	–		0.84	0.84	0.84	0.84	0.95	0.95

A.6. Response Variables

The final values for a selection of noteworthy response variables are provided in Table 31.

Table 31: Final values for a selection of response variables

Variable	**Unit**	**Designs:**	**A**	**B**	**C**	**A$^+$**	**A^{++}**	**X**
η_{th}	%		25.9	17.7	27.5	33.9	40.5	45.2
η_{C}	%		67.9	71.4	71.4	68.4	78.6	84.2
η_{T}	%		77.0	75.6	79.3	78.4	88.7	89.6
η_{S}	%		98.0	97.5	97.2	96.9	96.5	94.7
ϵ	%		98.3	96.3	99.2	97.1	96.9	97.0
$\dot{Q}_{\text{S,supplied}}$	MW		38.6	56.6	36.3	29.5	24.7	22.1
$A_{\text{s,G,o}}$	m^2		659	925	586	476	398	357
$A_{\text{s,R}}$	$\times 10^3$ m^2		1.75	7.88	7.50	12.8	19.2	12.8
$A_{\text{s,H}}$	$\times 10^3$ m^2		41.6	73.8	22.0	32.8	25.7	19.3
Compressor angles								
α_{tip}	°		71.7	74.7	76.1	75.9	72.1	74.9
α'_{tip}	°		74.5	77.1	78.3	78.1	74.8	75.7
β_{tip}	°		–30.0	–34.8	–37.6	–37.2	–10.4	–11.1
β_{eye}	°		–67.1	–70.1	–69.7	–69.9	–70.1	–68.8
β'_{tip}	°		0.00	0.00	0.00	0.00	0.00	0.00
α_{eye}	°		0.00	0.00	0.00	0.00	0.00	0.00
Turbine angles								
α_{tip}	°		68.6	70.6	74.3	75.7	75.6	74.7
α'_{tip}	°		71.8	73.6	76.7	77.9	76.3	75.5
β_{tip}	°		–25.9	–28.5	–34.1	–36.8	–11.6	–10.9
β_{eye}	°		–50.1	–52.6	–65.4	–67.7	–69.9	–54.1
β'_{tip}	°		0.00	0.00	0.00	0.00	0.00	0.00
α_{eye}	°		0.00	0.00	0.00	0.00	0.00	0.00

B. Thermodynamic Model Details and Results

B.1. Logical Calculations for the Thermodynamic Model

Table 32 presents the logical calculations that occur in the constraints evaluation function of the thermodynamic model. At each step, the input variables are used and a calculation takes place to yield the output variables, which are kept in computer memory for the remainder of the calculations.

Table 32: Logical calculations in the analysis of the thermodynamic model

Step	**Description**	**Equation**	**Input variables**	**Output variables**
1.	Thermodynamic properties			
a.	State 1	*	T_1, P_1	h_1, s_1
b.	State 2	*	T_2, P_2	h_2
c.	State 3	*	T_3, P_3	h_3
d.	State 4	*	T_4, P_4	h_4, s_4
e.	State 5	*	T_5, P_5	h_5
f.	State 6	*	T_6, P_6	h_6
g.	State 2s	*	T_{2s}, P_2	h_{2s}, s_{2s}
h.	State 5s	*	T_{5s}, P_5	h_{5s}, s_{5s}
2.	Specific energy transfers			
a.	Actual work input	(32)	h_2, h_1	w_C
b.	Isentropic work input	(33)	h_{2s}, h_1	$w_{C,s}$
c.	Actual work output	(34)	h_4, h_5	w_T
d.	Isentropic work output	(35)	h_4, h_{5s}	$w_{T,s}$
e.	Heat input	(36)	h_4, h_3	q_S
f.	Heat output	(37)	h_6, h_1	q_H
g.	Cold side recuperation	(45)	h_3, h_2	$q_{R,cold}$
h.	Hot side recuperation	(45)	h_5, h_6	$q_{R,hot}$
3.	Energy transfers			
a.	Compressor power	(49)	$\dot{m}, w_C$	$\dot{W}_C$
b.	Turbine power	(49)	$\dot{m}, w_T$	$\dot{W}_T$
c.	Heat addition rate	(48)	$\dot{m}, q_S$	$\dot{Q}_S$
d.	Heat rejection rate	(48)	$\dot{m}, q_H$	$\dot{Q}_H$

* Interpolated from tables of thermodynamic property data (NIST, 2020). See Section 3.6 for more details.

B.2. List of Equality Constraints

Table 33: Equality constraints of the thermodynamic model

Equation (... = 0)	**Note**
$w_{C,s} - \eta_C\, w_C$	Compressor isentropic efficiency, see Equation (38)
$w_T - \eta_T\, w_{T,s}$	Turbine isentropic efficiency, see Equation (39)
$-10{\times}10^3 + \dot{W}_T - \dot{W}_C$	Specified net power output of cycle (kW), see Equation (50)
$10{\times}10^3 - \eta_{th}\dot{Q}_S$	Thermal efficiency of the cycle, see Equation (51)
$\dot{Q}_H + \dot{W}_T - \dot{Q}_S - \dot{W}_C$	Conservation of energy, see Equation (47)
$s_1 - s_{2s}$	State 2s should have same entropy as state 1
$s_4 - s_{5s}$	State 5s should have same entropy as state 4
$q_{R,cold} - q_{R,hot}$	Recuperation must be equal for both sides, see Equation (45)
$(T_5 - T_6) - \epsilon(T_5 - T_2)$	Recuperator effectiveness, see Equation (46)

B.3. List of Inequality Constraints

Table 34: Inequality constraints of the thermodynamic model

Equation (... $\leq$ 0)	**Note**
$0 - w_C$	Ensures correct sign convention of energy transfers
$P_1 - P_6$	See Equation (30)
$P_6 - P_5$	
$P_5 - P_4$	
$P_4 - P_3$	
$P_3 - P_2$	
$T_1 - T_2$	See Equation (31)
$T_2 - T_6$	
$T_6 - T_3$	
$T_3 - T_5$	
$T_5 - T_4$	

B.4. Final Thermodynamic Property Values

Table 35: Thermodynamic property values at various states for Design A

State	T [°C]	P [MPa]	h [kJ/kg]	s [kJ/kgK]
1	35.0	10.6	286	1.27
2	59.5	25.0	314	1.29
2s	55.3	25.0	305	1.27
3	398	24.4	843	2.44
3i	398	25.0	842	2.44
4	550	24.4	1 032	2.70
4i	550	25.0	1 032	2.69
5	479	12.5	955	2.73
5s	460	12.5	932	2.70
5i	460	10.6	934	2.73
5is	435	10.6	905	2.69
6	66.5	11.1	425	1.69
6s	61.8	11.1	410	1.65
6i	65.9	10.6	431	1.72
6is	61.8	10.6	419	1.68

Table 36: Thermodynamic property values at various states for Design B

State	T [°C]	P [MPa]	h [kJ/kg]	s [kJ/kgK]
1	35.0	16.7	270	1.19
2	45.4	25.0	284	1.20
2s	43.3	25.0	280	1.19
3	477	23.9	941	2.59
3i	477	25.0	941	2.58
4	550	23.9	1 033	2.70
4i	550	25.0	1 032	2.69
5	522	18.5	1 002	2.71
5s	514	18.5	992	2.70
5i	506	16.7	984	2.71
5is	494	16.7	969	2.69
6	63.2	16.9	345	1.42
6s	60.0	16.9	335	1.39
6i	62.0	16.7	342	1.41
6is	60.0	16.7	336	1.40

Table 37: Thermodynamic property values at various states for Design C

State	T [°C]	P [MPa]	h [kJ/kg]	s [kJ/kgK]
1	65.0	13.9	376	1.53
2	100	25.0	404	1.55
2s	96.0	25.0	396	1.53
3	437	24.9	891	2.51
3i	437	25.0	891	2.51
4	550	24.9	1 032	2.69
4i	550	25.0	1 032	2.69
5	487	14.0	963	2.72
5s	472	14.0	945	2.69
5i	485	13.9	961	2.72
5is	470	13.9	943	2.69
6	103	13.9	477	1.81
6s	99.0	13.9	469	1.79
6i	103.0	13.9	477	1.81
6is	99.0	13.9	469	1.79

Table 38: Thermodynamic property values at various states for Design A$^+$

State	T [°C]	P [MPa]	h [kJ/kg]	s [kJ/kgK]
1	35.0	13.9	275	1.22
2	50.3	25.0	294	1.23
2s	47.5	25.0	288	1.22
3	436	25.0	889	2.51
3i	436	25.0	889	2.51
4	550	25.0	1 032	2.69
4i	550	25.0	1 032	2.69
5	487	14.0	963	2.72
5s	471	14.0	944	2.69
5i	486	13.9	962	2.72
5is	470	13.9	943	2.69
6	63.1	13.9	368	1.51
6s	59.8	13.9	356	1.47
6i	62.5	13.9	366	1.50
6is	59.8	13.9	356	1.47

Table 39: Thermodynamic property values at various states for Design A^{++}

State	T [°C]	P [MPa]	h [kJ/kg]	s [kJ/kgK]
1	35.0	15.7	271	1.20
2	45.8	25.0	285	1.21
2s	44.4	25.0	282	1.20
3	455	24.9	913	2.54
3i	455	25.0	913	2.54
4	550	24.9	1032	2.69
4i	550	25.0	1032	2.69
5	493	15.8	969	2.70
5s	487	15.8	961	2.69
5i	493	15.7	969	2.70
5is	487	15.7	961	2.69
6	59.6	15.7	341	1.41
6s	58.1	15.7	336	1.40
6i	59.5	15.7	340	1.41
6is	58.1	15.7	336	1.40

Table 40: Thermodynamic property values at various states for Design X

State	T [°C]	P [MPa]	h [kJ/kg]	s [kJ/kgK]
1	35.0	16.9	269	1.19
2	49.0	30.0	288	1.20
2s	47.4	30.0	285	1.19
3	574	30.0	1059	2.69
3i	574	30.0	1059	2.69
4	700	30.0	1220	2.87
4i	700	30.0	1220	2.87
5	621	16.9	1125	2.88
5s	612	16.9	1114	2.87
5i	621	16.9	1125	2.88
5is	612	16.9	1114	2.87
6	66.1	16.9	354	1.45
6s	64.3	16.9	348	1.43
6i	65.9	16.9	353	1.44
6is	64.3	16.9	348	1.43

B.5. Carnot Efficiencies for the Final System Designs

Table 41: Carnot efficiencies for the final system designs

Based on minimum and maximum temperatures			
Design	T_1 [K]	T_4 [K]	η_{th} [%]
A	308	823	62.6
B	308	823	62.6
C	338	823	58.9
A^+	308	823	62.6
A^{++}	308	823	62.6
X	308	973	68.3
Based on average heat sink and heat source temperatures			
Design	$\bar{T}_L$ [K]	$\bar{T}_H$ [K]	η_{th} [%]
A	321	746	57.0
B	321	785	59.1
C	353	765	53.9
A^+	321	764	58.0
A^{++}	319	774	58.8
X	322	907	64.5

B.6. Cycle Efficiency Breakdown Calculations

The values in Table 42 are calculated as follows:

- The contribution attributed to operating temperatures is 100% minus the Carnot efficiency based on maximum and minimum temperatures from Table 41.
- The contribution attributed to cycle configuration is the above efficiency minus the Carnot efficiency based on average heat sink and heat source temperatures from Table 41.
- The contribution attributed to operating pressures is the above efficiency minus the efficiency calculated as discussed in Section 8.4.2.
- The contributions attributed to compressor efficiency, turbine efficiency, pressure drops and solar receiver heat loss, are calculated by independently subtracting the efficiencies calculated as discussed in Section 8.4.2 from the above efficiency.
- The value in the "cumulative contribution" row is the sum of the seven loss factors.
- The value in the "residual" row is the value that remains after subtracting the actual cycle efficiency and the cumulative contribution from 100%, which occurs because the loss factors are not entirely additive.

Table 42: Cycle efficiency breakdown calculations (values are denoted in %)

	Design A		**Design B**		**Design C**	
	Efficiency	*Contribution*	*Efficiency*	*Contribution*	*Efficiency*	*Contribution*
Perfect cycle	100.0		100.0		100.0	
Operating temperatures	62.6	37.4	62.6	37.4	58.9	41.1
Cycle configuration	57.0	5.6	59.1	3.5	53.9	5.0
Operating pressures	44.8	12.2	44.5	14.6	42.6	11.3
Compressor efficiency	40.6	4.2	40.5	4.0	37.7	4.9
Turbine efficiency	37.3	7.5	36.5	8.0	35.4	7.2
Pressure drops	39.5	5.3	32.3	12.2	41.9	0.7
Solar receiver heat loss	43.9	0.9	43.4	1.1	41.4	1.2
Cumulative contribution		73.1		80.8		71.4
Actual cycle efficiency		25.9		17.7		27.5
Residual		1.0		1.5		1.1
Total contribution		100.0		100.0		100.0

Table 42 (continued)

	Design A$^+$		**Design A^{++}**		**Design X**	
	Efficiency	*Contribution*	*Efficiency*	*Contribution*	*Efficiency*	*Contribution*
Perfect cycle	100.0		100.0		100.0	
Operating temperatures	62.6	37.4	62.6	37.4	68.3	31.7
Cycle configuration	58.0	4.6	58.8	3.8	64.5	3.8
Operating pressures	48.4	9.6	48.0	10.8	53.3	11.2
Compressor efficiency	43.5	4.9	45.2	2.8	50.9	2.4
Turbine efficiency	41.3	7.1	44.4	3.6	50.0	3.3
Pressure drops	48.1	0.3	48.0	0.0	53.3	0.0
Solar receiver heat loss	46.9	1.5	46.3	1.7	50.4	2.9
Cumulative contribution		65.4		60.1		55.3
Actual cycle efficiency		33.9		40.5		45.2
Residual		0.7		–0.6		–0.5
Total contribution		100.0		100.0		100.0

C. Power System Model Details

C.1. Logical Calculations

Table 43 presents the logical calculations that occur in the constraints evaluation function of the power system model. At each step, the input variables are used and a calculation takes place to yield the output variables, which are kept in computer memory for the remainder of the calculations.

The compressor and the turbine follow the same logic, but the equations differ slightly depending on the direction of the flow. If one of the steps is different, the step for the compressor is indicated by (C) and the step for the turbine is indicated by (T) in Table 43.

Table 43: Logical calculations in the analysis of the compressor and turbine

Step	**Description**	**Equation**	**Input variables**	**Output variables**
1.	Thermodynamic properties			
a.	Inlet station	*	$T_{\text{in}}, P_{\text{in}}$	$\rho_{\text{in}}, h_{\text{in}}, c_{\text{in}}$
b. (C)	Eye	*	$T_{\text{eye}},\ P_{\text{eye}}$	$\rho_{\text{eye}},\ h_{\text{eye}},\ s_{\text{eye}},\ c_{\text{eye}}$
b. (T)	Tip	*	$T_{\text{tip}},\ P_{\text{tip}}$	$\rho_{\text{tip}},\ h_{\text{tip}},\ s_{\text{tip}},\ c_{\text{tip}}$
c. (C)	Tip	*	$T_{\text{tip}},\ P_{\text{tip}}$	$\rho_{\text{tip}},\ h_{\text{tip}},\ c_{\text{tip}}$
c. (T)	Eye	*	$T_{\text{eye}},\ P_{\text{eye}}$	$\rho_{\text{eye}},\ h_{\text{eye}},\ c_{\text{eye}}$
d. (C)	Tip (isentropic)	*	$T_{\text{tip,s}},\ P_{\text{tip}}$	$h_{\text{tip,s}},\ s_{\text{tip,s}}$
d. (T)	Eye (isentropic)	*	$T_{\text{eye,s}},\ P_{\text{eye}}$	$h_{\text{eye,s}},\ s_{\text{eye,s}}$
e.	Outlet station	*	$T_{\text{out}},\ P_{\text{out}}$	$\rho_{\text{out}},\ h_{\text{out}},\ c_{\text{out}}$
2.	Geometry			
a.	Radial flow area at tip	(52)	$r_{\text{tip}},\ b$	$A_{\text{tip,r}}$
b.	Axial flow area at eye	(53)	$r_{\text{shd}},\ r_{\text{hub}}$	$A_{\text{eye,x}}$
c.	Mean radius at eye	(54)	$r_{\text{shd}},\ r_{\text{hub}}$	r_{eye}
3.	Meridional velocities			
a.	Inlet station	(55)	$\dot{m},\ \rho_{\text{in}},\ A_{\text{N}}$	V_{in}
b.	Eye	(55)	$\dot{m},\ \rho_{\text{eye}},\ A_{\text{eye,x}}$	$V_{\text{eye,x}}$
c.	Tip	(55)	$\dot{m},\ \rho_{\text{tip}},\ A_{\text{tip,r}}$	$V_{\text{tip,r}}$
d.	Outlet station	(55)	$\dot{m},\ \rho_{\text{out}},\ A_{\text{N}}$	V_{out}

* Interpolated from tables of thermodynamic property data (NIST, 2020). See Section 3.6 for more details.

Table 43 (continued)

Step	Description	Equation	Input variables	Output variables
4.	Velocity triangle at tip			
a.	Blade speed	(63)	ω, r_{tip}	B_{tip}
b.	Ideal absolute tangential velocity	(64)	B_{tip}	$V'_{\text{tip,t}}$
c. (C)	Real absolute tangential velocity	(61)	$V'_{\text{tip,t}}$, σ	$V_{\text{tip,t}}$
c. (T)	Real absolute tangential velocity	(62)	$V'_{\text{tip,t}}$, λ	$V_{\text{tip,t}}$
d.	Real absolute velocity	(65)	$V_{\text{tip,r}}$, $V_{\text{tip,t}}$	V_{tip}
e.	Real relative tangential velocity	(66)	$V_{\text{tip,t}}$, B_{tip}	$R_{\text{tip,t}}$
f.	Real relative radial velocity	(67)	$V_{\text{tip,r}}$	$R_{\text{tip,r}}$
g.	Real relative velocity	(68)	$R_{\text{tip,r}}$, $R_{\text{tip,t}}$	R_{tip}
5.	Velocity triangle at eye			
a.	Blade speed	(57)	ω, r_{eye}	B_{eye}
b.	Absolute velocity	(58)	$V_{\text{eye,x}}$	V_{eye}
c.	Relative tangential velocity	(59)	B_{eye}	$R_{\text{eye,t}}$
d.	Relative axial velocity	(58)	$V_{\text{eye,x}}$	$R_{\text{eye,x}}$
e.	Relative velocity	(60)	$R_{\text{eye,t}}$, $R_{\text{eye,x}}$	R_{eye}
6.	Momentum transfer			
a.	Torque	(69)	$\dot{m}$, $V_{\text{tip,t}}$, r_{tip}	M
b.	Fluid power	(71)	M, ω	$\dot{W}$
7.	Stagnation enthalpy values			
a.	Inlet station	(81)	$h_{\text{in}}, V_{\text{in}}$	$h_{0,\text{in}}$
b.	Eye	(81)	h_{eye}, V_{eye}	$h_{0,\text{eye}}$
c.	Tip	(81)	h_{tip}, V_{tip}	$h_{0,\text{tip}}$
d. (C)	Tip (isentropic)	(81)	$h_{\text{tip,s}}$, V_{tip}	$h_{0,\text{tip,s}}$
d. (T)	Eye (isentropic)	(81)	$h_{\text{eye,s}}$, V_{eye}	$h_{0,\text{eye,s}}$
e.	Outlet station	(81)	h_{out}, V_{out}	$h_{0,\text{out}}$
8.	Stagnation enthalpy differences			
a.	Between tip and eye	(72)	$h_{0,\text{tip}}$, $h_{0,\text{eye}}$	w_0
b. (C)	Between tip and eye (isentropic)	(76)	$h_{0,\text{tip,s}}$, $h_{0,\text{eye}}$	$w_{0,\text{s}}$
b. (T)	Between tip and eye (isentropic)	(77)	$h_{0,\text{tip}}$, $h_{0,\text{eye,s}}$	$w_{0,\text{s}}$
9.	Diffuser performance			
a. (C)	Pressure recovery coefficient	(84)	P_{out}, P_{tip}, ρ_{tip}, V_{tip}	C_{p}
a. (T)	Pressure recovery coefficient	(84)	P_{out}, P_{eye}, ρ_{eye}, V_{eye}	C_{p}
b. (C)	Ideal pressure recovery coefficient	(85)	$A_{\text{tip,r}}$, A_{N}	$C_{\text{p,i}}$
b. (T)	Ideal pressure recovery coefficient	(85)	$A_{\text{eye,x}}$, A_{N}	$C_{\text{p,i}}$
c.	Diffuser efficiency	(87)	C_{p}, $C_{\text{p,i}}$	η_{D}
10.	Nozzle performance			
(C)	Total pressure loss coefficient	(88)	P_{in}, ρ_{in}, V_{in}, P_{eye}, ρ_{eye}, V_{eye}	K_{N}
(T)	Total pressure loss coefficient	(88)	P_{in}, ρ_{in}, V_{in}, P_{tip}, ρ_{tip}, V_{tip}	K_{N}
11.	Mach numbers			
a.	Inlet station	(89)	V_{in}, c_{in}	$\text{Ma}_{\text{V,in}}$
b.	Tip (absolute)	(89)	V_{tip}, c_{tip}	$\text{Ma}_{\text{V,tip}}$
c.	Tip (relative)	(89)	R_{tip}, c_{tip}	$\text{Ma}_{\text{R,tip}}$
d.	Eye (absolute)	(89)	V_{eye}, c_{eye}	$\text{Ma}_{\text{V,eye}}$
e.	Eye (relative)	(89)	R_{eye}, c_{eye}	$\text{Ma}_{\text{R,eye}}$
f.	Outlet station	(89)	V_{out}, c_{out}	$\text{Ma}_{\text{V,out}}$

C.2. List of Equality Constraints

Table 44 lists the equality constraints for the compressor model, Table 45 lists the equality constraints for the turbine model, and Table 46 lists the equality constraints for the power system as a whole.

Table 44: Equality constraints of the compressor

Equation (... = 0)	**Note**
$h_{0,1} - h_{0,\text{eye}}$	Conservation of energy in the nozzle section, see Table 4
$h_{0,2} - h_{0,\text{tip}}$	Conservation of energy in the diffuser section, see Table 4
$w_{0,\text{s}} - \eta_{\text{R}}\, w_0$	Rotor efficiency, see Equation (78)
$\dot{W} - \dot{m}\, w_0$	Equation (72)
$\eta_{\text{D}} - c$	Diffuser efficiency should equal the specified constant
$K_{\text{N}} - c$	Nozzle loss coefficient should equal the specified constant
$s_{\text{eye}} - s_{\text{tip,s}}$	Isentropic state at tip should have same entropy as eye

Table 45: Equality constraints of the turbine

Equation (... = 0)	**Note**
$h_{0,4} - h_{0,\text{tip}}$	Conservation of energy in the nozzle section, see Table 4
$h_{0,5} - h_{0,\text{eye}}$	Conservation of energy in the diffuser section, see Table 4
$w_0 - \eta_{\text{R}}\, w_{0,\text{s}}$	Rotor efficiency, see Equation (79)
$\dot{W} - \dot{m}\, w_0$	Equation (72)
$\eta_{\text{D}} - c$	Diffuser efficiency should equal the specified constant
$K_{\text{N}} - c$	Nozzle loss coefficient should equal the specified constant
$s_{\text{tip}} - s_{\text{eye,s}}$	Isentropic state at eye should have same entropy as tip

Table 46: Equality constraints of the complete power system

Equation (... = 0)	**Note**
$-10{\times}10^3 + \dot{W}_{\text{T}} - \dot{W}_{\text{C}}$	Net mechanical power output of system (kW), see Equation (50)

C.3. List of Inequality Constraints

This section lists the inequality constraints used in the power system model. The compressor and turbine have the same set of inequality constraints, as listed in Table 47. Table 48 lists the inequality constraints for the power system as a whole. Note that these inequality constraints are not applied in the validation of the models.

Table 47: Inequality constraints of the compressor and turbine

Equation (... ≤ 0)	**Note**
$A_{\text{eye,x}} - A_{\text{N}}$ $A_{\text{tip,r}} - A_{\text{N}}$	Converging or diverging area ratios, see Section 4.3.9
$\text{Ma}_{\text{V,in}} - 0.95$ $\text{Ma}_{\text{V,tip}} - 0.95$ $\text{Ma}_{\text{R,tip}} - 0.95$ $\text{Ma}_{\text{V,eye}} - 0.95$ $\text{Ma}_{\text{R,eye}} - 0.95$ $\text{Ma}_{\text{V,out}} - 0.95$	Ensure Mach number does not exceed the specified value, see Equation (90)
$0.927\,V_{\text{tip}} - V_{\text{tip,t}}$ $V_{\text{tip,t}} - 0.971\,V_{\text{tip}}$ $-0.940\,R_{\text{eye}} - R_{\text{eye,t}}$ $R_{\text{eye,t}} + 0.767\,R_{\text{eye}}$	Corresponds to $\alpha_{\text{tip}} \geq 68°$ from Logan (1981) Corresponds to $\alpha_{\text{tip}} \leq 76°$ from Logan (1981) Corresponds to $\beta_{\text{eye}} \geq -70°$ from Logan (1981) Corresponds to $\beta_{\text{eye}} \leq -50°$ from Logan (1981)
$r_{\text{hub}} - 0.4\,r_{\text{shd}}$ $r_{\text{hub}} - 0.7\,r_{\text{tip}}$ $0.53\,r_{\text{tip}} - r_{\text{eye}}$ $r_{\text{eye}} - 0.66\,r_{\text{tip}}$ $0.1\,r_{\text{tip}} - b$ $b - 0.3\,r_{\text{tip}}$ $2\,R_{\text{tip}} - R_{\text{eye}}$ $R_{\text{eye}} - 2.5\,R_{\text{tip}}$ $0.15\,B_{\text{tip}} - V_{\text{eye}}$ $V_{\text{eye}} - 0.5\,B_{\text{tip}}$	All correspond to ratios from Logan (1981)

Table 48: Inequality constraints of the complete power system

Equation (... ≤ 0)	**Note**
$P_1 - P_5$ $P_5 - P_4$ $P_4 - P_2$	See Equation (30)
$T_1 - T_2$ $T_2 - T_5$ $T_5 - T_4$	See Equation (31)

D. Thermal System Model Details

The inputs that appear in the tables in the following sections are divided into three types: design variables (x), response variables (y) and constants (c). For the response variables, the reference equation is provided. For the constants, the value is provided. All design variables have values that are "to be determined," or "TBD."

D.1. Solar Receiver Model

Table 49: Inputs for the solar receiver flow channel element in Flownex®

Variable	Description	Type	Unit	Value
Geometry				
L_S	Length	x	m	TBD
$D_{S,i}$	Diameter	y	mm	Equation (96)
Discretization				
n_S	Number of control volumes	c	—	10
N_S	Number of parallel flow channels	c	—	36
Pressure loss calculation				
ϵ_S	Surface roughness	c	μm	30
K_S	Secondary pressure loss coefficient	c	—	2.0

Table 50: Inputs for the solar receiver steel tube heat transfer element in Flownex®

Variable	Description	Type	Unit	Value
Conduction ($\dot{Q}_{S,o}$)				
$A_{s,S,o}$	Upstream surface area = outside of steel tube	y	m^2	Equation (101)
t_S	Thickness in element direction = thickness of steel tube	c	mm	2*
L_S	Thickness in cross direction = solar receiver length	x	m	TBD
$A_{s,S,i}$	Downstream surface area = inside of steel tube	y	m^2	Equation (101)
Convection on downstream surface ($\dot{Q}_{S,i}$)				
$A_{s,S,i}$	Surface area = inside of steel tube	y	m^2	Equation (101)

* estimated from the dimensions of a commercially-available solar receiver (SCHOTT Solar, 2013)

Table 51: Inputs for the solar receiver vacuum heat transfer element in Flownex®

Variable	Description	Type	Unit	Value
Upstream (S,o)				
$A_{s,S,o}$	Upstream surface area = outside of steel tube	y	m^2	Equation (101)
ε_S	Emissivity of steel	c	—	0.095*
Downstream (G,i)				
$A_{s,G,i}$	Downstream surface area = inside of glass tube	y	m^2	Equation (101)
ε_G	Emissivity of glass	c	—	0.9†
Note: Equation (101) is applied with a vacuum thickness of $t_V = 4\,mm$				

* (SCHOTT Solar, 2013)

† (Çengel and Ghajar, 2015)

Table 52: Inputs for the solar receiver glass tube heat transfer element in Flownex®

Variable	Description	Type	Unit	Value
Conduction ($\dot{Q}_{G,i}$)				
$A_{s,G,i}$	Upstream surface area = inside of glass tube	y	m^2	Equation (101)
t_G	Thickness in element direction = thickness of glass tube	c	mm	1*
L_S	Thickness in cross direction = solar receiver length	x	m	TBD
$A_{s,G,o}$	Downstream surface area = outside of glass tube	y	m^2	Equation (101)
Convection on downstream surface ($\dot{Q}_{G,o,conv.}$)				
$A_{s,G,o}$	Convection area = outside of glass tube	y	m^2	Equation (101)
V_{wind}	Ambient wind speed	c	m/s	1.8†
T_∞	Ambient air temperature	c	°C	21†
P_∞	Ambient air pressure	c	bar	1
$D_{G,o}$	Convection diameter = glass tube outer diameter	y	mm	Equation (99)
Radiation on downstream surface ($\dot{Q}_{G,o,rad.}$)				
$A_{s,G,o}$	Radiation area = outside of glass tube	y	m^2	Equation (101)
ε_G	Emissivity of glass	c	—	0.9‡
ε_{sky}	Effective sky emissivity	c	—	0.8†
T_{sky}	Effective sky temperature	c	°C	–16†

* estimated from the dimensions of a commercially-available solar receiver (SCHOTT Solar, 2013)

† discussed in Section 5.3

‡ (Çengel and Ghajar, 2015)

D.2. Recuperator Model

Table 53: Recuperator channel geometric specifications

Variable	Description	Unit	Value
w_c	Channel width	mm	2
h_c	Channel height	mm	1
h_w	Wall height	mm	0.5

Table 54: Inputs for the recuperator flow channel elements in Flownex®

Variable	Description	Type	Unit	Value
Geometry				
L_R	Length	x	m	TBD
p	Perimeter	y	mm	Equation (104)
A_c	Area	y	mm^2	Equation (105)
Discretization				
n_R	Number of control volumes	c	—	30
N_R	Number of parallel flow channels	y	—	Equation (106)
Pressure loss calculation				
ϵ_R	Surface roughness	c	μm	30
K_R	Secondary pressure loss coefficient	c	—	3.0

Table 55: Inputs for the recuperator heat transfer element in Flownex®

Variable	Description	Type	Unit	Value
Conduction ($\dot{Q}_W$)				
$A_{s,R}$	Surface area	y	m^2	Equation (107)
w_c	Thickness in element direction = wall height	c	mm	Table 53
L_R	Thickness in cross direction = recuperator length	x	m	TBD
Convection on upstream surface ($\dot{Q}_H$)				
$A_{s,R}$	Convection area	y	m^2	Equation (107)
Convection on downstream surface ($\dot{Q}_C$)				
$A_{s,R}$	Convection area	y	m^2	Equation (107)

D.3. Heat Sink Model

Table 56: Inputs for the heat sink flow channel element in Flownex®

Variable	Description	Type	Unit	Value
Geometry				
L_{H}	Length	x	m	TBD
$D_{\mathrm{H,i}}$	Diameter	y	mm	Equation (96)
Discretization				
n_{H}	Number of control volumes	c	—	10
N_{H}	Number of parallel flow channels	c	—	36
Pressure loss calculation				
ϵ_{H}	Surface roughness	c	μm	30
K_{H}	Secondary pressure loss coefficient	c	—	2.0

Table 57: Inputs for the heat sink heat transfer element in Flownex®

Variable	Description	Type	Unit	Value
Conduction ($\dot{Q}_{\mathrm{T}}$)				
$A_{\mathrm{s,H,i}}$	Upstream surface area = inside of tube	y	m^2	Equation (101)
t_{H}	Thickness in element direction = thickness of tube	c	mm	4*
L_{H}	Thickness in cross direction = heat sink length	x	m	TBD
$A_{\mathrm{s,H,o}}$	Downstream surface area = outside of tube	y	m^2	Equation (101)
Convection on upstream surface ($\dot{Q}_{\mathrm{F}}$)				
$A_{\mathrm{s,H,i}}$	Convection area = inside of tube	y	m^2	Equation (101)
Convection on downstream surface ($\dot{Q}_{\mathrm{out,conv.}}$)				
$A_{\mathrm{s,H,o}}$	Convection area = outside of tube	y	m^2	Equation (101)
V_{wind}	Ambient wind speed	c	m/s	1.8†
T_{∞}	Ambient air temperature	c	°C	21†
P_{∞}	Ambient air pressure	c	bar	1
$D_{\mathrm{H,o}}$	Convection diameter = tube outer diameter	y	mm	Equation (113)
Radiation on downstream surface ($\dot{Q}_{\mathrm{out,rad.}}$)				
$A_{\mathrm{s,H,o}}$	Radiation area = outside of tube	y	m^2	Equation (101)
ε_{G}	Emissivity of glass	c	—	0.9‡
$\varepsilon_{\mathrm{sky}}$	Effective sky emissivity	c	—	0.8†
T_{sky}	Effective sky temperature	c	°C	–16†

* arbitrary value

† discussed in Section 5.3

‡ (Çengel and Ghajar, 2015)

E. Validation Data and Results

E.1. Thermodynamic Model Validation

Table 58 presents the details of the thermodynamic model validation study. The variables in Table 58 are sufficient to uniquely characterize the operating point of the cycle in specific (per unit mass) terms. Three different models from literature are investigated, with sufficiently different operating points. Pressure drops in the heat exchangers are included in reference model A (Ahn *et al.*, 2015), but not in reference model B (Bryant *et al.*, 2011) and also not in reference model C (Uusitalo *et al.*, 2019). Pressure drops are specified in the thermodynamic model of the current research through equality constraints or by directly entering the station pressure values. The cycle thermal efficiencies from the models in literature are presented in the second-to-last row of Table 58, whereas the cycle thermal efficiencies calculated by the thermodynamic model of the current research are presented in the last row.

Table 58: Details of the thermodynamic model validation

Variable	**Symbol**	**Unit**	**A**	**B**	**C**
Compressor inlet temperature	T_1	°C	33.2	32	50
Turbine inlet temperature	T_4	°C	500	550	330
Compressor inlet pressure	P_1	MPa	7.78	8.33	7.43
Compressor outlet pressure	P_2	MPa	20	25	30
Primary heat exchanger pressure drop	$P_3 - P_4$	kPa	150	0	0
Heat sink pressure drop	$P_6 - P_1$	kPa	100	0	0
Recuperator heat addition side pressure drop	$P_2 - P_3$	kPa	100	0	0
Recuperator heat rejection side pressure drop	$P_5 - P_6$	kPa	150	0	0
Compressor efficiency	η_C	%	65	89	85
Turbine efficiency	η_T	%	85	90	85
Recuperator effectiveness*	ϵ	%	85	95	70
Reference cycle thermal efficiency	η_{th}	%	25.6	38.8	14.5
Calculated cycle thermal efficiency	η_{th}	%	25.3	38.8	14.5

* using the definition of recuperator effectiveness that corresponds to the reference model

E.2. Compressor Validation Study 1

Table 59: Constants of the sCO_2-HeRo compressor (Hacks *et al.*, 2018a,b)

Variable	Description	Unit	Value
Dimensions			
r_{tip}	Tip radius	mm	19.1
r_{shd}	Shroud radius	mm	8.90
r_{hub}	Hub radius	mm	6.00
b	Blade width	mm	1.25
$A_{D,out}$	Diffuser outlet area	mm^2	330
*Thermodynamics**			
P_{eye}	Pressure at the eye	MPa	7.83
T_{eye}	Temperature at the eye	°C	33
Performance			
$\dot{m}$	Mass flow rate	kg/s	0.65
Ω	Rotational speed	rpm	50 000

* static and stagnation values are equal up to three significant figures

Table 60: Results of the sCO_2-HeRo compressor validation study (Hacks *et al.*, 2018b)

Variable	Description	Unit	Reference	Calculated	Difference
PR*	Pressure ratio	–	1.39	1.31	– 5.76%
$\dot{W}$	Power	kW	5.4†	5.46	+ 1.1%

* static and stagnation ratios are equal up to three significant figures

† This was not measured in the experiment. It is estimated as $7 - 1.6 = 5.4$ kW, which is the difference between the electrical power of the motor (7 kW) (Hacks *et al.*, 2018b) and the windage loss (1.6 kW) (Hacks *et al.*, 2018a).

E.3. Compressor Validation Study 2

Table 61: Constants of the Sandia sCO_2 compressor (Wright *et al.*, 2010)

Variable	Description	Unit	Value
Dimensions			
r_{tip}	Tip radius	mm	18.7
r_{shd}	Shroud radius	mm	9.37
r_{hub}	Hub radius	mm	2.54
b	Blade width	mm	1.71
$A_{D,out}$	Diffuser outlet area	mm^2	402*
Thermodynamics			
P_{eye}	Static pressure at the eye	MPa	7.88†
T_{eye}	Static temperature at the eye	°C	32†,‡
Performance			
$\dot{m}$	Mass flow rate	kg/s	3.39
Ω	Rotational speed	rpm	54 200

* The dimensions of the diffuser were not available, but based on a photograph in the test report (Wright *et al.*, 2010) the diffuser is estimated to have a radius that is double the tip radius of the compressor and a flow channel width that is the same as the compressor blade width, which gives this diffuser outlet area.

† These values are converted from the stagnation properties given by Wright *et al.* (2010) to be consistent with the formulation of the models of this research.

‡ This value varied slightly throughout the course of the experiment. The average value was selected for the validation study.

Table 62: Results of the Sandia sCO_2 compressor validation study (Wright *et al.*, 2010)

Variable	Description	Unit	Reference	Calculated	Difference
$\dot{W}$	Power	kW	32.3*	32.1	– 0.619%
P_{tip}	Static pressure at tip	MPa	10.2	9.92	– 2.75%
$P_{0,2}$	Stagnation pressure at diffuser outlet	MPa	10.7	10.8	+ 0.935%

* The compressor power was measured as 41.0 kW in the motor controller. Wright *et al.* (2010) estimate that only 93% of this power results in motor torque, of which another fraction is lost to windage. The power lost to windage is calculated to be 5.79 kW based on the model by Wright *et al.* (2010). The fluid power is therefore estimated to be $(41.0 \times 0.93) - 5.79 = 32.3$ kW.

E.4. Turbine Validation Study

Table 63: Constants of the turbine for model validation (Zhou *et al.*, 2018)

Variable	Description	Unit	Value
Dimensions			
r_{tip}	Tip radius	mm	52.6
r_{shd}	Shroud radius	mm	40.2
r_{hub}	Hub radius	mm	8.20
b	Blade width	mm	14.0
$A_{\text{N,in}}$	Nozzle inlet area	mm^2	6 582
Thermodynamics			
P_4	Inlet static pressure	MPa	12.9*
T_4	Inlet static temperature	°C	499*
Performance			
$\dot{m}$	Mass flow rate	kg/s	25.8
Ω	Rotational speed	rpm	45 000

* These values are converted from the stagnation properties given by Zhou *et al.* (2018) to be consistent with the formulation of the models of this research.

Table 64: Results of the turbine validation study (Zhou *et al.*, 2018)

Variable	Description	Unit	Reference	Calculated	Difference
$\dot{W}$	Power	MW	1.48	1.33	– 10.1%
P_{eye}	Static pressure at eye	MPa	8.00	7.95	– 0.625%

E.5. Solar Receiver Validation Study

Table 65: Results of the solar receiver validation study

ε_{S}	Emissivity of steel absorber tube	—	0.095	0.18
T_3	Solar receiver fluid inlet temperature (above ambient)	°C	377	377
$T_{\text{S,o}}$	Average temperature on outside of steel absorber tube	°C	437	430
T_4	Solar receiver fluid outlet temperature	°C	550	548
$\dot{Q}'_{\text{G}}$	Heat lost from outside of glass cover tube	W/m	334	584

E.6. Recuperator Validation Study

Table 66: Inputs for the SCARLETT recuperator flow channel elements in Flownex® (Straetz *et al.*, 2018)

Variable	Description	Unit	Value
Geometry			
L_R	Length	mm	150
p	Perimeter	mm	6
A_c	Area	mm^2	2
Discretization			
n_R	Number of control volumes	—	30*
N_R	Number of parallel flow channels	—	15
Pressure loss calculation			
ϵ_R	Surface roughness	μm	30*
K_R	Secondary pressure loss coefficient	—	3.0*

* These values are assumed, but correspond to the values of the developed recuperator model.

Table 67: Inputs for the SCARLETT recuperator heat transfer element in Flownex® (Straetz *et al.*, 2018)

Variable	Description	Unit	Value
Conduction ($\dot{Q}_W$)			
$A_{s,R}$	Surface area	mm^2	4 500
w_c	Thickness in element direction = wall height	mm	1.4
L_R	Thickness in cross direction = recuperator length	mm	150
Convection on upstream surface ($\dot{Q}_H$)			
$A_{s,R}$	Convection area	mm^2	4 500
Convection on downstream surface ($\dot{Q}_C$)			
$A_{s,R}$	Convection area	mm^2	4 500

The first five columns of Tables 68 and 69 are the input conditions for a particular test case. The next column labeled Δ (Exp.) is the value measured in the experiment, and the second-to-last column labeled Δ (Mod.) is the value predicted by the Flownex® model. The last column indicates the percentage difference between the values.

Table 68: Recuperator model temperature rise validation (Straetz *et al.*, 2018)

T_{in} (sCO_2) [°C]	P_{in} (sCO_2) [bar]	$\dot{m}$ (sCO_2) [g/s]	$\dot{m}$ (H_2O)* [kg/h]	$\dot{Q}$ (H_2O) [W]	ΔT (Exp.) [°C]	ΔT (Mod.) [°C]	Diff. [%]
40	110	37	0.651	460	2.4	2.7	+12.5
40	110	37	0.801	560	3.0	3.3	+10.0
40	110	37	0.971	680	3.7	3.9	+5.4
40	110	37	1.171	830	4.6	4.7	+2.2
40	110	37	1.431	1 010	5.5	5.5	0.0
40	110	37	1.742	1 230	6.5	6.5	0.0
40	100	37	0.651	460	1.8	1.9	+5.6
40	100	37	0.801	560	2.2	2.3	+4.5
40	100	37	0.971	680	2.6	2.7	+3.8
40	100	37	1.171	830	3.3	3.2	–3.0
40	100	37	1.431	1 010	3.9	3.8	–2.6
40	100	37	1.742	1 230	4.7	4.5	–4.3
39.5	95	37	0.651	460	1.3	1.4	+7.7
39.5	95	37	0.801	560	1.7	1.7	0.0
39.5	95	37	0.971	680	2.0	2.1	+5.0
39.5	95	37	1.171	830	2.4	2.5	+4.2
39.5	95	37	1.431	1 010	3.0	2.9	–3.3
39.5	95	37	1.742	1 230	3.6	3.5	–2.8

* converted from the given volumetric flow rate

Table 69: Recuperator model pressure drop validation (Straetz *et al.*, 2018)

T_{in} (sCO_2) [°C]	P_{in} (sCO_2) [bar]	$\dot{m}$ (sCO_2) [g/s]	$\dot{m}$ (H_2O)* [kg/h]	$\dot{Q}$ (H_2O) [W]	ΔP (Exp.) [bar]	ΔP (Mod.) [bar]	Diff. [%]
40	110	46	0.651	460	0.16	0.153	–4.4
40	110	56	0.801	560	0.24	0.226	–5.8
40	110	68	0.971	680	0.35	0.334	–4.6
40	100	46	0.651	460	0.17	0.167	–1.8
40	100	56	0.801	560	0.25	0.247	–1.2
40	100	68	0.971	680	0.37	0.363	–1.9
39.5	95	46	0.651	460	0.19	0.176	–7.4
39.5	95	56	0.801	560	0.27	0.260	–3.7
39.5	95	68	0.971	680	0.39	0.384	–1.5

* converted from the given volumetric flow rate

References

Achkari, O. and El Fadar, A. Latest developments on TES and CSP technologies – energy and environmental issues, applications and research trends. *Applied Thermal Engineering*, 167:114806, 2020.

Ahn, Y., Lee, J., Kim, S.G., Lee, J.I., Cha, J.E., and Lee, S.-W. Design consideration of supercritical CO_2 power cycle integral experiment loop. *Energy*, 86:115–127, 2015.

Alshammari, F., Karvountzis-Kontakiotis, A., Pesiridis, A., and Giannakakis, P. Off-design performance prediction of radial turbines operating with ideal and real working fluids. *Energy Conversion and Management*, 171:1430–1439, 2018.

Angelino, G. Carbon dioxide condensation cycles for power production. *Journal of Engineering for Power*, 90(3):287–295, 1968.

Ashcroft, J., Kimball, K., and Corcoran, M. Overview of Naval Reactors Program development of the supercritical carbon dioxide Brayton system. In *Supercritical CO_2 Power Cycle Symposium*, Troy, NY, 29-30 April 2009.

Aungier, R.H. *Centrifugal Compressors: A Strategy for Aerodynamic Design and Analysis*. American Society of Mechanical Engineers, New York, NY, 2000.

Aungier, R.H. *Turbine Aerodynamics: Axial-Flow and Radial-Inflow Turbine Design and Analysis*. American Society of Mechanical Engineers, New York, NY, 2006.

Ausiello, G., Crescenzi, P., and Protasi, M. Approximate solution of NP optimization problems. *Theoretical Computer Science*, 150:1–55, 1995.

Avadhanula, V.K. and Held, T.J. Transient modeling of a supercritical CO_2 power cycle and comparison with test data. In *ASME Turbo Expo 2017*, Charlotte, NC, 26-30 June 2017.

Balje, O.E. *Turbomachines – A guide to Design, Selection and Theory*. Wiley, New York, NY, 1981.

Barton, R.R. Simulation metamodels. In *Proceedings of the 1998 Winter Simulation Conference*, Washington D.C., December 1998.

Battisti, F.G., Cardemil, J.M., Miller, F.M., and da Silva, A.K. Normalized performance optimization of supercritical, CO_2-based power cycles. *Energy*, 82:108–118, 2015.

Battisti, F.G., Cardemil, J.M., and da Silva, A.K. A multivariate optimization of a Brayton power cycle operating with CO_2 as working fluid. *Energy*, 112:908–916, 2016.

Bejan, A., Tsatsaronis, G., and Moran, M. *Thermal Design and Optimization*. Wiley, Hoboken, NJ, 1996.

Bellos, E. and Tzivanidis, C. Parametric investigation of supercritical carbon dioxide utilization in parabolic trough collectors. *Applied Thermal Engineering*, 127:736–747, 2017.

Bellos, E., Tzivanidis, C., Antonopoulos, K.A., and Daniil, I. The use of gas working fluids in parabolic trough collectors – an energetic and exergetic analysis. *Applied Thermal Engineering*, 109:1–14, 2016.

Bennett, J.A., Moisseytsev, A., and Sienicki, J.J. Modeling and cycle optimization. In Brun, K., Friedman, P., and Dennis, R., editors, *Fundamentals and Applications of Supercritical Carbon Dioxide (sCO_2) Based Power Cycles*. Woodhead, Duxford, United Kingdom, 2017.

Berthet Couso, G., Barraza Vicencio, R., Vasquez Padilla, R., Soo Too, Y.C., and Pye, J. Dynamic model of supercritical CO_2 Brayton cycles driven by concentrated solar power. In *ASME 11th International Conference on Energy Sustainability*, Charlotte, NC, 26-30 June 2017.

Biencinto, M., González, L., Valenzuela, L., and Zarza, E. A new concept of solar thermal power plants with large-aperture parabolic-trough collectors and sCO_2 as working fluid. *Energy Conversion and Management*, 199:112030, 2019.

Binotti, M., Astolfi, M., Campanari, S., Manzolini, G., and Silva, P. Preliminary assessment of sCO_2 cycles for power generation in CSP solar tower plants. *Applied Energy*, 204:1007–1017, 2017.

Bird, R.B., Stewart, W.E., and Lightfoot, E.N. *Transport Phenomena*. Wiley, New York, NY, 2nd edition, 2002.

Bolton, H.P.J., Groenwold, A.A., and Snyman, J.A. The application of a unified Bayesian stopping criterion in competing parallel algorithms for global optimization. *Computers and Mathematics with Applications*, 48:549–560, 2004.

Borgnakke, C. and Sonntag, R.E. *Fundamentals of Thermodynamics*. Wiley, Singapore, 8th edition, 2014.

Boyce, M.P. *Gas Turbine Engineering Handbook*. Butterworth-Heinemann, Waltham, MA, 4th edition, 2012.

Breeze, P. *Power Generation Technologies*. Newnes, Oxford, United Kingdom, 2nd edition, 2014.

Brooks, M.J., du Clou, S., van Niekerk, J.L., Gauche, P., Leonard, C., Mouzouris, M.J., Meyer, A.J., van der Westhuizen, N., van Dyk, E.E., and Vorster, F. SAURAN: A new resource for solar radiometric data in Southern Africa. *Journal of Energy in Southern Africa*, 26:2–10, 2015. `www.sauran.ac.za`.

Bryant, J.C., Saari, H., and Kourosh, Z. An analysis and comparison of the simple and recompression supercritical CO_2 cycles. In *Supercritical CO_2 Power Cycle Symposium*, Boulder, CO, 24-25 May 2011.

Çengel, Y.A. and Ghajar, A.J. *Heat and Mass Transfer: Fundamentals and Applications*. McGraw-Hill, New York, NY, 5th edition, 2015.

Cheang, V.T., Hedderwick, R.A., and McGregor, C. Benchmarking supercritical carbon dioxide cycles against steam Rankine cycles for concentrated solar power. *Solar Energy*, 113:199–211, 2015.

Cho, J., Shin, H., Ra, H.-S., Lee, G., Roh, C., Lee, B., and Baik, Y.-J. Development of the supercritical carbon dioxide power cycle experimental loop in KIER. In *ASME Turbo Expo 2016*, Seoul, South Korea, 13-17 June 2016.

Clementoni, E.M., Cox, T.L., and Sprague, C.P. Startup and operation of a supercritical carbon dioxide Brayton cycle. *Journal of Engineering for Gas Turbines and Power*, 136(7):071701, 2014.

Coco-Enríquez, L., Muñoz-Antón, J., and Martínez-Val, J.M. New text comparison between CO_2 and other supercritical working fluids (ethane, Xe, CH_4 and N_2) in line-focusing solar power plants coupled to supercritical Brayton power cycles. *International Journal of Hydrogen Energy*, 42:17611–17631, 2017.

Dennis, R.A., Musgrove, G., Rochau, G., Fleming, D., Carlson, M., and Pasch, J. Overview. In Brun, K., Friedman, P., and Dennis, R., editors, *Fundamentals and Applications of Supercritical Carbon Dioxide (sCO_2) Based Power Cycles*. Woodhead, Duxford, United Kingdom, 2017.

Dixon, S.L. and Hall, C.A. *Fluid Mechanics and Thermodynamics of Turbomachinery*. Butterworth-Heinemann, Oxford, United Kingdom, 7$^{\text{th}}$ edition, 2014.

DOE/Sandia National Laboratories. Supercritical carbon dioxide Brayton cycle turbines promise giant leap in power generation. `www.sciencedaily.com/releases/2011/03/110304090459.htm`, 2011.

Dostal, V., Driscoll, M.J., and Hejzlar, P. A supercritical carbon dioxide cycle for next generation nuclear reactors. Technical Report MIT-ANP-TR-100, Massachussets Institute of Technology, 2004.

Dunbar, W.R., Moody, S.D., and Lior, N. Exergy analysis of an operating boiling-water-reactor nuclear power station. *Energy Conversion and Management*, 36(3):149–159, 1995.

Dyreby, J.J. *Modeling the Supercritical Carbon Dioxide Brayton Cycle with Recompression*. PhD Dissertation, University of Wisconsin-Madison, Madison, WI, 2014.

European Commission. The supercritical CO_2 heat removal system. `cordis.europa.eu/project/id/662116`, 2017.

European Commission. Supercritical CO_2 cycle for flexible and sustainable support to the electricity system. `cordis.europa.eu/project/id/764690`, 2019.

Feher, E.G. The supercritical thermodynamic power cycle. *Energy Conversion*, 8:85–90, 1968.

Flownex Simulation Environment. version 8.10.0.3799. `www.flownex.com`, 2020a.

Flownex Simulation Environment. sCO2. `www.flownex.com/industry-application/power-generation/co2-cycle`, 2020b.

Forrester, A.I.J. and Keane, A.J. Recent advances in surrogate-based optimization. *Progress in Aerospace Sciences*, 45:50–79, 2009.

Friedman, P. and Anderson, M. Thermodynamics. In Brun, K., Friedman, P., and Dennis, R., editors, *Fundamentals and Applications of Supercritical Carbon Dioxide (sCO_2) Based Power Cycles*. Woodhead, Duxford, United Kingdom, 2017.

Garey, M.R. and Johnson, D.S. *Computers and Intractability: A Guide to the Theory of NP-Completeness*. W.H. Freeman, New York, NY, 1979.

Gas Technology Institute. 10 MWe supercritical carbon dioxide (sCO_2) pilot power plant. `www.gti.energy/wp-content/uploads/2019/01/STEP-Project-Detailed-Description-Dec2018.pdf`, 2018.

Gavic, D.J. Investigation of water, air, and hybrid cooling for supercritical carbon dioxide Brayton cycles. MSc Thesis, University of Wisconsin-Madison, Madison, WI, 2012.

Ginley, D. and Chattopadhyay, K., editors. *Solar Energy Research Institute for India and the United States (SERIIUS): Lessons and Results from a Binational Consortium*. Springer, 2020.

Gray, J.S., Hwang, J.T., Martins, J.R.R.A., Moore, K.T., and Naylor, B.A. OpenMDAO: an open-source framework for multidisciplinary design, analysis and optimization. *Structural and Multidisciplinary Optimization*, 59:1075–1104, 2019.

Hacks, A., Schuster, S., Dohmen, H.J., Benra, F.-K., and Brillert, D. Turbomachine design for supercritical carbon dioxide within the sCO2-HeRo.eu project. *Journal of Engineering for Gas Turbines and Power*, 140:121017, 2018a.

Hacks, A.J., Vojacek, A., Dohmen, H.J., and Brillert, D. Experimental investigation of the sCO2-HeRo compressor. In *2nd European supercritical CO_2 Conference*, Essen, Germany, 30-31 August 2018b.

Haftka, R.T. and Gürdal, Z. *Elements of Structural Optimization*. Springer, 3rd edition, 1992.

Hannapel, S. and Vlahopoulos, N. Implementation of set-based design in multidisciplinary design optimization. *Structural and Multidisciplinary Optimization*, 50:101–112, 2014.

Haseli, Y. Optimization of a regenerative Brayton cycle by maximization of a newly defined second law efficiency. *Energy Conversion and Management*, 68:133–140, 2013.

Held, T.J. Initial test results of a megawatt-class supercritical CO_2 heat engine. In *4th International Symposium - Supercritical CO_2 Power Cycles*, Pittsburgh, PA, 9-10 September 2014.

Hexemer, M.J. and Rahner, K. Supercritical CO_2 Brayton cycle Integrated System Test (IST) TRACE model and control system design. In *Supercritical CO_2 Power Cycle Symposium*, Boulder, CO, 24-25 May 2011.

Holaind, N., Bianchi, G., De Miol, M., Saravi, S.S., Tassou, S.A., Leroux, A., and Jouhara, H. Design of radial turbomachinery for supercritical CO_2 systems using theoretical and numerical CFD methodologies. In *1st International Conference on Sustainable Energy and Resource Use in Food Chains*, Berkshire, United Kingdom, 19-20 April 2017.

Hu, X.-B., Wang, M., and Di Paolo, E. Calculating complete and exact Pareto front for multiobjective optimization: A new deterministic approach for discrete problems. *IEEE Transactions on Cybernetics*, 43(3):1088–1101, 2013.

Inkscape. Inkscape vector graphics editor. `www.inkscape.org`, 2020.

International Energy Agency. Electricity generation by source, World 1990-2018. `www.iea.org`, 2020.

Iverson, B.D., Conboy, T.M., Pasch, J.J., and Kruizenga, A.M. Supercritical CO_2 Brayton cycles for solar-thermal energy. *Applied Energy*, 111:957–970, 2013.

Japikse, D. Assessment of single- and two-zone modeling of centrifugal compressors. In *Gas Turbine Conference and Exhibit*, Houston, TX, 18-21 March 1985.

Japikse, D. *Centrifugal Compressor Design and Performance*. Concepts ETI, Wilder, VT, 1996.

Japikse, D. and Baines, N.C. *Introduction to Turbomachinery*. Concepts ETI, Norwich, VT, 1994.

Kim, M.S., Oh, B.S., Kwon, J.S., Jung, H.-Y., and Lee, J.I. Transient simulation of critical flow with thermal-hydraulic system analysis code for supercritical CO_2 applications. In *ASME Turbo Expo 2017*, Charlotte, NC, 26-30 June 2017.

Kler, A.M., Zharkov, P.V., and Epishkin, N.O. Parametric optimization of supercritical power plants using gradient methods. *Energy*, 189:116230, 2019.

Kler, A.M., Potanina, Y.M., and Marinchenko, A.Y. Co-optimization of thermal power plant flowchart, thermodynamic cycle parameters, and design parameters of components. *Energy*, 193:116679, 2020.

Korpela, S.A. *Principles of Turbomachinery*. Wiley, Hoboken, NJ, 2011.

Kröger, D.G. *Air-Cooled Heat Exchangers and Cooling Towers: Thermal-Flow Performance Evaluation and Design*. PennWell, Tulsa, OK, 2004.

Le Moullec, Y., Jinyi, Z., Zijiang, Y., Pan, Z., Neveux, T., Mendoza, T., Brau, J.F., Zhipeng, Q., Wenlong, C., Xihua, W., and Chengtao, J. Retrofit of Dunhuang 10 MW molten salt plant with a high temperature supercritical CO_2 cycle. `www.solarpaces.org/wp-content/uploads/study-Retrofit-of-Dunhuang-10MW-molten-salt-plant-with-a-high-temperature-supercritical-CO2-cycle.pdf`, 2018.

Le Roux, W.G., Bello-Ochende, T., and Meyer, J.P. A review on the thermodynamic optimisation and modelling of the solar thermal Brayton cycle. *Renewable and Sustainable Energy Reviews*, 28: 677–690, 2013.

Li, H., Fan, G., Cao, L., Yang, Y., Yan, X., Dai, Y., Zhang, G., and Wang, J. A comprehensive investigation on the design and off-design performance of supercritical carbon dioxide power system based on the small-scale lead-cooled fast reactor. *Journal of Cleaner Production*, 256:120720, 2020.

Li, Z. and Zheng, X. Review of design optimization methods for turbomachinery aerodynamics. *Progress in Aerospace Sciences*, 93:1–23, 2017.

Liang, Y., Chen, J., Luo, X., Chen, J., Yang, Z., and Chen, Y. Simultaneous optimization of combined supercritical CO_2 Brayton cycle and organic Rankine cycle integrated with concentrated solar power system. *Journal of Cleaner Production*, 266:121927, 2020.

Llorente García, I., Álvarez, J.L., and Blanco, D. Performance model for parabolic trough solar thermal power plants with thermal storage: Comparison to operating plant data. *Solar Energy*, 85:2443–2460, 2011.

Logan, E. *Turbomachinery: Basic Theory and Applications*. Marcel-Dekker, New York, NY, 1981.

Luu, M.T., Milani, D., McNaughton, R., and Abbas, A. Analysis for flexible operation of supercritical CO_2 Brayton cycle integrated with solar thermal systems. *Energy*, 124:752–771, 2017a.

Luu, M.T., Milani, D., McNaughton, R., and Abbas, A. Dynamic modelling and start-up operation of a solar-assisted recompression supercritical CO_2 Brayton power cycle. *Applied Energy*, 199:247–263, 2017b.

Manninen, J. and Zhu, X.X. Thermodynamic analysis and mathematical optimisation of power plants. *Computers and Chemical Engineering*, 22(Supplement 1):S537–S544, 1998.

Martins, J.R.R.A. and Lambe, A.B. Multidisciplinary design optimization: A survey of architectures. *American Institute of Aeronautics and Astronautics Journal*, 51(9):2049–2075, 2013.

MathWorks. MATLAB, version R2019b Update 1 (9.7.0.1216025). `www.mathworks.com/products/matlab.html`, 2019.

McKay, M.D., Beckman, R.J., and Conover, W.J. A comparison of three methods for selecting values of input variables in the analysis of output from a computer code. *Technometrics*, 21(2):239–245, 1979.

Meas, M.R. and Bello-Ochende, T. Thermodynamic design optimisation of an open air recuperative twin-shaft solar thermal Brayton cycle with combined or exclusive reheating and intercooling. *Energy Conversion and Management*, 148:770–784, 2017.

Milani, D., Luu, M.T., McNaughton, R., and Abbas, A. Optimizing an advanced hybrid of solar-assisted supercritical CO_2 Brayton cycle: a vital transition for low-carbon power generation industry. *Energy Conversion and Management*, 148:1317–1331, 2017.

Mills, A.F. *Heat Transfer*. Pearson, 2nd edition, 1999.

Muñoz-Antón, J., Rubbia, C., Rovira, A., and Martínez-Val, J.M. Performance study of solar power plants with CO_2 as working fluid. A promising design window. *Energy Conversion and Management*, 92:36–46, 2015.

Musgrove, G. and Wright, S. Introduction and background. In Brun, K., Friedman, P., and Dennis, R., editors, *Fundamentals and Applications of Supercritical Carbon Dioxide (sCO_2) Based Power Cycles*. Woodhead, Duxford, United Kingdom, 2017.

Musgrove, G., Ridens, B., and Brun, K. Physical properties. In Brun, K., Friedman, P., and Dennis, R., editors, *Fundamentals and Applications of Supercritical Carbon Dioxide (sCO_2) Based Power Cycles*. Woodhead, Duxford, United Kingdom, 2017a.

Musgrove, G., Sullivan, S., Shiferaw, D., Fourspring, P., and Chordia, L. Heat exchangers. In Brun, K., Friedman, P., and Dennis, R., editors, *Fundamentals and Applications of Supercritical Carbon Dioxide (sCO_2) Based Power Cycles*. Woodhead, Duxford, United Kingdom, 2017b.

Neises, T. and Turchi, C. Supercritical carbon dioxide power cycle design and configuration optimization to minimse levelized cost of energy of molten salt power towers operating at 650 °C. *Solar Energy*, 181:27–36, 2019.

NIST. Chemistry WebBook. In Linstrom, P.J. and Mallard, W.G., editors, *Standard Reference Database Number 69*. National Institute of Standards and Technology, Gaithersburg, MD, 2020. DOI: `10.18434/T4D303`.

Nocedal, J. and Wright, S.J. *Numerical Optimization*. Springer, New York, NY, 2nd edition, 2006.

O'Connor, P.D.T. and Kleyner, A. *Practical Reliability Engineering*. Wiley, Chichester, United Kingdom, 5th edition, 2012.

Osorio, J.D., Hovsapian, R., and Ordonez, J.C. Effect of multi-tank thermal energy storage, recuperator effectiveness, and solar receiver conductance on the performance of a concentrated solar supercritical CO_2-based power plant operating under different seasonal conditions. *Energy*, 115:353–368, 2016a.

Osorio, J.D., Hovsapian, R., and Ordonez, J.C. Dynamic analysis of concentrated solar supercritical CO_2-based power generation closed-loop cycle. *Applied Thermal Engineering*, 93:920–934, 2016b.

Owen, M.T.F. *Air-cooled condenser steam flow distribution and related dephlegmator design considerations*. PhD Dissertation, Stellenbosch University, Stellenbosch, South Africa, 2013.

Papalambros, P.Y. and Wilde, D.J. *Principles of Optimal Design: Modeling and Computation*. Cambridge University Press, Cambridge, United Kingdom, 3rd edition, 2017.

Patnode, A.M. Simulation and performance evaluation of parabolic trough solar power plants. MSc Thesis, University of Wisconsin-Madison, Madison, WI, 2006.

Peinado Gonzalo, A., Pliego Marugán, A., and García Márquez, F.P. A review of the application performances of concentrated solar power systems. *Applied Energy*, 255:113893, 2019.

Persky, R. and Sauret, E. Loss models for on and off-design performance of radial inflow turbomachinery. *Applied Thermal Engineering*, 150:1066–1077, 2019.

Pinker, S. *Enlightenment Now*. Penguin Random House, 2018.

Qiu, X.-w., Anderson, M., and Japikse, D. An integrated design system for turbomachinery. In *9th International Conference on Hydrodynamics*, Shanghai, China, 11-15 October 2010.

Qiu, Y., Li, M.-J., He, Y.-L., and Tao, W.-Q. Thermal performance analysis of a parabolic trough solar collector using supercritical CO_2 as heat transfer fluid under non-uniform solar flux. *Applied Thermal Engineering*, 115:1255–1265, 2017.

Rao, S.S. Game theory approach for multiobjective structural optimization. *Computers and Structures*, 25(1):119–127, 1987.

Rao, Z., Xue, T., Huang, K., and Liao, S. Multi-objective optimization of supercritical carbon dioxide recompression Brayton cycle considering printed circuit recuperator design. *Energy Conversion and Management*, 201:112094, 2019.

Richter, P., Ábrahám, E., and Morin, G. Optimisation of concentrating solar thermal power plants with neural networks. In Dobnikar, A., Lotrič, U., and Šter, B., editors, *Adaptive and Natural Computing Algorithms*. Springer, Berlin, Germany, 2011.

Saeed, M., Khatoon, S., and Kim, M.-H. Design optimization and performance analysis of a supercritical carbon dioxide recompression Brayton cycle based on the detailed models of the cycle components. *Energy Conversion and Management*, 196:242–260, 2019.

Sandia National Laboratories. Dakota, a multilevel parallel object-oriented framework for design optimization, parameter estimation, uncertainty quantification, and sensitivity analysis. `dakota.sandia.gov`, 2020.

Santini, L., Accornero, C., and Cioncolini, A. On the adoption of carbon dioxide thermodynamic cycles for nuclear power conversion: A case study applied to Mochovce 3 Nuclear Power Plant. *Applied Energy*, 181:446–463, 2016.

Sarkar, J. and Bhattacharyya, S. Optimization of recompression S-CO_2 power cycle with reheating. *Energy Conversion and Management*, 50:1939–1945, 2009.

Schichl, H., Neumaier, A., Markót, M.C., and Domes, F. On solving mixed-integer constraint satisfaction problems with unbounded variables. In Gomes, C. and Sellmann, M., editors, *Integration of AI and OR Techniques in Constraint Programming for Combinatorial Optimization Problems*. Springer, Berlin, Germany, 2013.

SCHOTT Solar. PTR®70 Receiver Dataheet, 2013.

Schuster, S., Benra, F.-K., and Brillert, D. Small scale sCO_2 compressor impeller design considering real fluid conditions. In *5th International Symposium - Supercritical CO2 Power Cycles*, San Antonio, TX, 28-31 March 2016.

SENER. Bokpoort parabolic trough plant datasheet, 2018.

Sienicki, J.J., Moisseytsev, A., Fuller, R.L., Wright, S.A., and Pickard, P.S. Scale dependencies of supercritical carbon dioxide Brayton cycle technologies and the optimal size for a next-step supercritical CO_2 cycle demonstration. In *SCO_2 Power Cycle Symposium*, Boulder, CO, 24-25 May 2011.

Singer, D.J., Doerry, N., and Buckley, M.E. What is set-based design? *Naval Engineers Journal*, 121 (4):31–43, 2009.

Singh, R., Miller, S.A., Rowlands, A.S., and Jacobs, P.A. Dynamic characteristics of a direct-heated supercritical carbon-dioxide Brayton cycle in a solar thermal power plant. *Energy*, 50:194–204, 2013.

Snyman, J.A. *Practical Mathematical Optimization*. University of Pretoria, Pretoria, South Africa, 2004.

Sobieszczanski-Sobieski, J. and Haftka, R.T. Multidisciplinary aerospace design optimization: survey of recent developments. *Structural Optimization*, 14:1–23, 1997.

Span, R. and Wagner, W. A new equation of state for carbon dioxide covering the fluid region from the triple-point temperature to 1100 K at pressures up to 800 MPa. *Journal of Physical and Chemical Reference Data*, 25(6):1509–1596, 1996.

Stein, W.H. and Buck, R. Advanced power cycles for concentrated solar power. *Solar Energy*, 152: 91–105, 2017.

Stine, W.B. and Geyer, M. *Power From The Sun* book. `http://www.powerfromthesun.net`, 2001.

Straetz, M., Mertz, R., and Starflinger, J. Experimental investigation on the heat transfer between condensing steam and sCO_2 in a compact heat exchanger. In *2nd European supercritical CO_2 Conference*, Essen, Germany, 30-31 August 2018.

The World Bank and Solargis. Solar resource maps. `www.solargis.com`, 2019.

Tong, S.S. and Gregory, B.A. Turbine preliminary design using artificial intelligence and numerical optimization techniques. *Journal of Turbomachinery*, 114(1):1–7, 1992.

Tosserams, S., Etman, L.F.P., and Rooda, J.E. Multi-modality in augmented Lagrangian coordination for distributed optimal design. *Structural and Multidisciplinary Optimization*, 40:329–352, 2010.

Trinh, T.Q. Dynamic response of the supercritical CO_2 Brayton recompression cycle to various system transients. MSc Thesis, Massachussets Institute of Technology, Boston, MA, 2009.

Tucker, P.G. Computation of unsteady turbomachinery flows: Part 1 – progress and challenges. *Progress in Aerospace Sciences*, 47:522–545, 2011.

Tucker, P.G. Trends in turbomachinery turbulence treatments. *Progress in Aerospace Sciences*, 63: 1–32, 2013.

United Nations. Climate change. `www.un.org/en/sections/issues-depth/climate-change/`, 2020.

Utamura, M., Hasuike, H., and Yamamoto, T. Demonstration test plant of closed cycle gas turbine with supercritical CO_2 as working fluid. *Strojarstvo*, 52(4):459–465, 2010.

Uusitalo, A., Ameli, A., and Turunen-Saaresti, T. Thermodynamic and turbomachinery design analysis of supercritical Brayton cycles for exhaust gas heat recovery. *Energy*, 167:60–79, 2019.

Versteeg, H.K. and Malalasekera, W. *An Introduction to Computational Fluid Dynamics*. Pearson, Harlow, United Kingdom, 2nd edition, 2007.

von Backström, T.W. The effect of specific heat ratio on the performance of compressible flow turbomachines. In *Proceedings of ASME Turbo Expo 2008*, Berlin, Germany, 9-13 June 2008.

von Spakovsky, M.R. Application of engineering functional analysis to the analysis and optimization of the CGAM problem. *Energy*, 19(3):343–364, 1994.

Wang, D., Wu, Z., Fei, Y., and Zhang, W. Structural design employing a sequential approximation optimization approach. *Computers and Structures*, 134:75–87, 2014a.

Wang, K. and He, Y.-L. Thermodynamic analysis and optimization of a molten salt solar power tower integrated with a recompression supercritical CO_2 Brayton cycle based on integrated modeling. *Energy Conversion and Management*, 135:336–350, 2017.

Wang, K., Li, M.-J., Guo, J.-Q., Li, P., and Liu, Z.-B. A systematic comparison of different S-CO_2 Brayton cycle layouts based on multi-objective optimization for applications in solar power tower plants. *Applied Energy*, 212:109–121, 2018.

Wang, L., Yang, Y., Dong, C., Morosuk, T., and Tsatsaronis, G. Multi-objective optimization of coal-fired power plants using differential evolution. *Applied Energy*, 115:254–264, 2014b.

White, F.M. *Fluid Mechanics*. McGraw-Hill, New York, NY, 7th edition, 2011.

Whitfield, A. and Baines, N.C. *Design of Radial Turbomachines*. Longman, New York, NY, 1990.

Wright, S. and Scammell, W. Economics. In Brun, K., Friedman, P., and Dennis, R., editors, *Fundamentals and Applications of Supercritical Carbon Dioxide (sCO_2) Based Power Cycles*. Woodhead, Duxford, United Kingdom, 2017.

Wright, S.A. and Anderson, M. Supercritical CO_2 cycle for advanced NPPs. In *Workshop on New Cross-cutting Technologies for Nuclear Power Plants*, Cambridge, MA, 30-31 January 2017.

Wright, S.A., Radel, R.F., Vernon, M.E., Rochau, G.E., and Pickard, P.S. Operation and analysis of a supercritical CO_2 Brayton cycle. Technical Report SAND2010-0171, Sandia National Laboratories, 2010.

Zhou, A., Song, J., Li, X., Ren, X., and Gu, C. Aerodynamic design and numerical analysis of a radial inflow turbine for the supercritical carbon dioxide Brayton cycle. *Applied Thermal Engineering*, 132: 245–255, 2018.